Isotope Effects in Chemical Processes of Atmospheric Interest

Thesis by

Wei-Chen Chen

In Partial Fulfillment of the Requirements
for the Degree of
Doctor of Philosophy

California Institute of Technology
Pasadena, California

2009
(Defended January 20, 2009)

Acknowledgments

First and foremost I offer my sincerest gratitude to my research advisor, Professor Rudy Marcus, who has always been available for consultations and guidance. I have been enormously fortunate in working with Professor Marcus, who amazes me with his wisdom in making the best decisions, his boundless energy in studying science, and his relentless effort to uncover the principles behind the research puzzles. I attribute my graduate study to his advising and encouragement. Without him this thesis would not have been completed or written. I simply could not wish for a better or friendlier mentor.

I would like to thank my committee members: Professor Aron Kuppermann, Professor Rudy Marcus, Professor Geoffrey A. Blake, and Professor Harry B. Gray for their patience and insightful comments during the examinations. It is my honor to have them on my committee.

I would also like to thank the past and present members of the Marcus group. Hollis Evans is a respectful and helpful member of the staff, who helps me to facilitate my research, to obtain extra benefits from the group, and to communicate with Professor Marcus while I was hiding in some national parks or visiting some natural wonders. Professor Yi Qin Gao is a brilliant scientist, and I benefit a lot from his many insightful discussions and suggestions. Zhaoyan Zhu is a smart and excellent office-mate, who listened to my complains when I was in bad moods. Other colleagues in our group, Dr. Meher Prakash Ayalasomayujula, Dr. Jau H. Tang, Professor Katsumi Niki, Dr. Nima Ghaderi, Dr. Yousung Jung, Evans Booney, Dr. Maksym Kryvohuz, Dr. Shachi S. Gosavi, Dr. Thomas Renger, Ruth DeSilveira, Dr. Pavel Frantsuzov, and Dr. Jason Weibel are wonderful working company for teaching, supporting, and helping me and making my stay at Caltech a pleasant and comfortable place. I benefit greatly as being a member of Marcus group.

During these years of my graduate study, I have also been fortunate to have some very fine friendships with people outside of my research group. My roommate, Ding-Shyue Jerry Yang, is a genius and was always ready to discuss everything. My friends, I-Ren Lee and Dr. Chi-Yuan Victor Shih, were always there for me to bother. My friend, Wei-Guang Liu, always forgave me and my girlfriend for our teasing. My master's advisor, Professor Chin-Hui Yu, and my former colleague in Taiwan, Professor Jen-Shiang Kenny Yu, made me feel that I was not far away from Taiwan.

My grandparents and parents have given me tremendous love and support in every aspect and stage of my life. Without their support, the life of my graduate study would not be so colorful. I also want to express my warmest thanks to my sister, Wei-Inn Chen. Although she is in Taiwan, she is always there to counsel me. (Thanks for the Skype and MSN.) My girlfriend, Yu-Chieh Doris Chen, is an amazing lady. She always finds a way to make me laugh. We share many best memories and sweetest moments in my graduate study.

Abstract

The thesis is focused on the theoretical study of the isotope effects in three atmospheric reactions, the CO+OH reaction, the photolysis of N_2O, and the ozone formation. The CO+OH reaction is investigated by using both Rice-Ramsperger-Kassel-Marcus theory and its nonstatistical modification, which was prompted by existing molecular-beam data on incomplete intramolecular energy transfer in the HOCO* intermediate. The resulting calculations show reasonable agreement with most experimental data, except the O isotope effect. Two predictions are made: the temperature dependence of the OD+CO reaction; and the rate constant k_v decreasing with increasing CO vibrational quantum number v from $v = 0$ to $v = 1$. In both experiments and our calculation, the kinetic oxygen isotope effect is different from the expected value (i.e. the mass-dependent slope), which may be due to the H-tunneling. An experiment that avoids a possible role of vibrationally excited OH radicals as reactants in the O isotope effect is also suggested to remove the discrepancy in the O isotope effect between the experiments and calculations.

The UV photolysis of the greenhouse gas N_2O and its isotope effects are important in atmospheric chemistry. Based on the multidimensional reflection principle using the available *ab initio* data on the molecule for the potential energy surfaces and the transition dipole moments, we provide an accurate but not computationally intensive method in obtaining the absorption cross section. The present calculated fractionation gives good agreement with the experimental absorption cross section in the low-energy region, where the experimentally observed isotopic fractionation occurs. We also suggest a single effective mass, a linear combination of two main coordinates for the photolysis, to determine the slope of a multi-element isotope plot and to yield approximate agreement between the experimental data and a "mass-dependent" fractionation, which range from 0.47 to 3.28.

A modified *ab initio* potential energy surface is used for calculations of ozone recombination and isotopic exchange rate constants. The calculated low-pressure isotopic effects on the ozone formation reaction are consistent with the experimental results and with the theoretical results obtained earlier [J. Chem. Phys. **116**, 137 (2002)]. This result showed that they are relatively insensitive to the properties of the PES.

Table of Contents

Chapter 1

On the Theory of the CO+OH Reaction, Including H and C Kinetic Isotope Effects

[This chapter appeared in the *Journal of Chemical Physics* **123**, 094307 (2005).]

THE JOURNAL OF CHEMICAL PHYSICS **123**, 094307 (2005)

On the theory of the CO+OH reaction, including H and C kinetic isotope effects

Wei-Chen Chen and R. A. Marcus[a)]
Noyes Laboratory, 127-72 California Institute of Technology, Pasadena, California 91125

(Received 1 February 2005; accepted 15 July 2005; published online 8 September 2005)

The effect of pressure, temperature, H/D isotopes, and C isotopes on the kinetics of the OH +CO reaction are investigated using Rice-Ramsperger-Kassel-Marcus theory. Pressure effects are treated with a step-ladder plus steady-state model and tunneling effects are included. New features include a treatment of the C isotope effect and a proposed nonstatistical effect in the reaction. The latter was prompted by existing kinetic results and molecular-beam data of Simons and co-workers [J. Phys. Chem. A **102**, 9559 (1998); J. Chem. Phys. **112**, 4557 (2000); **113**, 3173 (2000)] on incomplete intramolecular energy transfer to the highest vibrational frequency mode in $HOCO^*$. In treating the many kinetic properties two small customary vertical adjustments of the barriers of the two transition states were made. The resulting calculations show reasonable agreement with the experimental data on (1) the pressure and temperature dependence of the H/D effect, (2) the pressure-dependent $^{12}C/^{13}C$ isotope effect, (3) the strong non-Arrhenius behavior observed at low temperatures, (4) the high-temperature data, and (5) the pressure dependence of rate constants in various bath gases. The kinetic carbon isotopic effect is usually less than 10 per mil. A striking consequence of the nonstatistical assumption is the removal of a major discrepancy in a plot of the k_{OH+CO}/k_{OD+CO} ratio versus pressure. A prediction is made for the temperature dependence of the OD+CO reaction in the low-pressure limit at low temperatures. © *2005 American Institute of Physics*. [DOI: 10.1063/1.2031208]

I. INTRODUCTION

The reaction of CO with the OH radical plays a major role in both atmospheric and combustion chemistry.[1,2] The reaction is known to be the principal oxidation which converts CO to CO_2 in the atmosphere,[1] and is also the key reaction controlling the OH radical concentration in the lower atmosphere.[1] Reflecting its importance and the unusual temperature and pressure dependence of its rate constant, the $CO+OH \rightarrow CO_2+H$ reaction has been examined extensively in many experimental[3–17] and theoretical studies,[17–28] including experimental studies over a very wide range of temperatures and pressures.[4–13,17] Nevertheless, carbon and oxygen isotope effects have been observed[29–33] and the anomalous effects for these heavy-atom isotopes have not yet been treated in the literature. Again, Simons and co-workers[63–65] observed in their molecular-beam study of the reverse reaction, $H+CO_2 \rightarrow OH+CO$, that the vibrational excitation of the CO product was far below that expected from statistical theory for the $HOCO^*$ intermediate. While the energies in their experiments are higher than those normally occurring in the OH+CO reaction, it is interesting to look for other anomalies in that reaction which may be better explained by a nonstatistical modification of the Rice-Ramsperger-Kassel-Marcus (RRKM) theory. Furthermore, there is a discrepancy in the H/D isotope effect in the literature.[27] The present work treats these various observations.

The radical intermediate HOCO has been observed both in the gas phase and in a matrix.[16,34–36] The ionization potential, energy of formation, and vibrational and rotational spectroscopy of the radical have also been characterized.[3,35] Studies of the kinetics of HOCO formation have firmly established the connection between the reactants (OH+CO) and the products ($H+CO_2$).[16] The currently accepted reaction mechanism includes an OH and CO bimolecular association step producing a vibrationally excited *trans*-HOCO, followed by *cis-trans* isomerization. The final reaction steps in competition with each other are dissociation to H and CO_2, back reaction to OH and CO, and collisional stabilization.[5,13,16,17,21,22] As the pressure increases, the collisional stabilization of the *cis*- and *trans*-HOCO intermediates competes favorably with the dissociation channel and the back reaction. When OH and CO react in oxygen, both the dissociation channel and the collision stabilization lead to HO_2 and CO_2, because of the follow-up reactions of H and HOCO with O_2.[37–39] The present paper treats the dependence of the rate constants on temperature, pressure, foreign gases, and H/D and $^{12}C/^{13}C$ isotope effects. Interpretation of the oxygen isotope effects[31–33] is complex and is discussed in a second paper.

The experimental study of the OH+CO reaction covers a temperature range from 80 to 3150 K.[4–13,17] A marked change of activation energy occurs near 500 K. The pressure and bath gas dependence of the reaction rate have also been measured,[11–15,17,40] as has the pressure and temperature dependence of the OD+CO reaction.[11,17,41] The k_{OH+CO}/k_{OD+CO} ratio shows a pressure-dependent H/D isotope effect. Further

---

[a)] Electronic mail: ram@caltech.edu

TABLE I. Calculated geometries and vibrational frequencies of normal isotopes by CC. The units are in Å for bond length, in degree for angles and dihedral angles, and in cm^{-1} for vibrational frequencies.

	OH+CO′	TS_a	cis-HOCO′	trans-HOCO′	TS_d	CO_2
R_{OH}	0.976	0.975	0.976	0.967	1.345	
R_{CO}	1.148	2.033	1.342	1.358	1.227	1.177
$R_{CO'}$		1.150	1.199	1.194	1.184	1.177
θ_{HOC}		94.86	107.74	107.37	116.27	
$\theta_{OCO'}$		123.52	129.61	126.38	155.28	180.00
$d_{HOCO'}$		180.00	0.00	180.00	0.00	
ν_1	2154[a]	312*i*	596	533	2125*i*	639
ν_2	3763[b]	197	594	606	518	639
ν_3		244	1091	1090	640	1345
ν_4		752	1321	1262	945	2410
ν_5		2122	1868	1903	1298	
ν_6		3784	3707	3869	2157	

[a] ν_{OH}

[b] ν_{CO}

experimental kinetic isotopic studies with ^{18}OH, ^{13}CO, $C^{17}O$, and $C^{18}O$ have also been performed. These results provide a body of data for tests of *ab initio* or other potential-energy surfaces and of reaction-rate theory. In particular, there is a serious discrepancy between the observed and calculated plot of OH/OD rates versus pressure.

Stevens *et al.* appear to be the first group to study experimentally the kinetic isotope effects for carbon and oxygen in the reaction.[29] They measured the isotopic ratios of the unreacted CO and of the CO_2 formed in the reaction mass spectrometrically and obtained pressure-dependent fractionation of $^{13}C/^{12}C$ and $^{18}O/^{16}O$ at pressures from 150 to 800 torr. In a similar but independent study Smit *et al.*[30] obtained results for the fractionation between carbon isotopes, which were consistent with those of Stevens *et al.* Their investigations were prompted by the need for understanding the global budget of atmospheric ^{12}CO and ^{13}CO. The enrichment of oxygen isotopes in CO was found to be nonconventional in its mass dependence, i.e., it did not obey the usual "mass-dependent" theoretically based and usually applicable rule of Bigeleisen and Mayer.[42]

Results similar to those of Stevens *et al.*[29] were obtained by Röckmann *et al.*[31] Laboratory studies of isotope effects were also made by Feilberg *et al.*,[32,33] whose results do not agree with those of Röckmann *et al.* and Stevens *et al.* The experimental precursors generating the OH radicals are different. The experimental conditions of Röckmann *et al.* are simpler in that ozone was not added and so there were fewer chemical reactions in the overall scheme. While HO_2 may be a dominant product in the studies of Stevens *et al.* and Röckmann *et al.*, due to the reaction of the source material H_2O_2 with OH, the rate constant for the reaction of CO with HO_2 is extremely small, less than 10^{-27} cm^3 $molecule^{-1}$ s^{-1} at room temperature,[43] and so is about 14 orders of magnitude smaller than that of CO with OH. The HO_2 is therefore not expected to interfere in the analysis.

Dynamical and statistical treatments of the CO+OH reactions have been made with various theoretical methods,[17,20–25] including quasiclassical trajectories, quantum dynamics, transition state theory, and RRKM theory. In the present article we focus on the statistical and nonstatistical aspects of the reaction over a wide temperature region for the different experimental conditions, as well as the hydrogen and carbon isotope effects.

The carbon isotope effect is typically less than 10 per mil at these pressures and temperatures. In the present study, RRKM theory and a nonstatistical modification are used, together with nuclear tunneling corrections and a step-ladder model for collision stabilization. Like the previous study by Senosiain *et al.*,[27] the resulting theory reproduces a large body of experimental data, apart from the potentially complex O-isotope effect discussed elsewhere. In addition, we treat the C-isotope effect and the large OH/OD rate constant discrepancy described in Ref. 27.

The paper is organized as follows: The potential-energy surface used is summarized in Sec. II A. The kinetic scheme for RRKM calculations, approximate tunneling probabilities, step-ladder model for pressure effects, and a possible nonstatistical distribution model for energy transfer at the exit channel are treated in Secs. II B–II E, respectively. Results are given in Sec. III and discussed in Sec. IV.

II. CALCULATION METHODS

A. Potential-energy surface

An *ab initio* potential-energy surface (PES) was calculated by Zhu *et al.*,[21] who used the modified GAUSSIAN-2 method (G2M). To obtain the more accurate vibrational frequencies and rotational constants of all stable and TS structures for various isotopes we use a coupled-cluster method,[44,45] abbreviated as CC. The calculated geometries and vibrational frequencies of normal isotopes are listed in Table I. To test the robustness of certain calculations, particularly of the H/D isotope effects, the results are compared in Appendix A with another modified *ab initio* potential [Lakin-Troya-Schatz-Harding (LTSH) by Lakin *et al.*],[24,46] and with two other *ab initio* methods, the MP2 method and a density-functional method (B3LYP), for the vibrational and rotational constants. The GAUSSIAN 98 program[47] was employed for all *ab initio* calculations to obtain the principal stable and TS equilibrium structures and their rotational and vibrational constants.

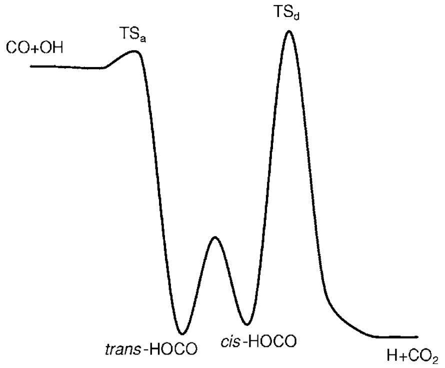

FIG. 1. Schematic profile of potential-energy surface of the CO+OH reaction.

A major candidate for the origin of the strong non-Arrhenius effect in the rate constant is the tunneling at the transition state TS_d in Fig. 1 for forming $H+CO_2$ from *cis*-HOCO. This interpretation is consistent with there being a large imaginary frequency at TS_d, $2126i\ \mathrm{cm}^{-1}$ calculated by CC. The RRKM rate constant in the low-pressure limit at room temperature calculated with this PES was larger than the experimental value by a factor of about 2. Accordingly, to match the experimental and calculated rate constants, the potential energy of TS_a and TS_d were shifted vertically slightly by two independent constants, E_1 at TS_a and E_2 at TS_d. (Vertical shifts are commonly used in conjunction with *ab initio* surfaces.) E_1 and E_2 were determined from the rate constants for the CO+OH reaction at 100 and 300 K in the low-pressure limit (Sec. III A). At lower temperatures the barrier at TS_a dominates the rate constant due to the large tunneling at TS_d. At room temperature the barriers in both exit and entrance channels of HOCO^* influence the rate constant. With these two constants, E_1 and E_2, and an energy-transfer parameter α per collision (Sec. II D), all the remaining properties of the reaction were calculated and compared with the experimental data. When different methods of varying accuracy were used and the shifts E_1 and E_2 were made to fit two pieces of data above, the resulting calculated rate constants are similar in all methods, as shown in Appendix A.

B. Kinetic scheme and rate constants

Microcanonical RRKM theory is used with tunneling corrections[48] for each quantum state of the two transition state structures. The steady-state equation for pressure effects is then solved. The coordinate assumed for the transition structures is the reaction path with minimal energy. The vibration frequencies of the transition state (TS) structures are fixed in the vicinity of the TS when counting the number of states along the reaction path with variation of the HO…CO center-to-center distance, and hence, of the two largest moments of inertia. (A more elaborate variational calculation of selected points will be given elsewhere.) There are van der Waals complexes of CO and OH and the loose transition structures to form the TS_a, but calculations show that they have only a minor effect on the reaction rates.[49] Thus, TS_a is the only transition state structure for the entrance channel included in the kinetic scheme. The potential-energy barrier between *trans*- and *cis*-HOCO is much lower than the potential energies of the entrance and exit channels, and so the two isomers interconvert in the energetic HOCO^* intermediate. The density of states of HOCO^* is therefore evaluated by summing $\rho_{\text{cis-HOCO}}(EJ)$ and $\rho_{\text{trans-HOCO}}(EJ)$, which includes the hindered rotation as one of the coordinates in the calculation. In the kinetic scheme, we can simply write HOCO^* for the sum of cis-HOCO^* and trans-HOCO^*. At zero pressure, the following scheme for the reaction of CO+OH is used for reaction at any energy E and total angular momentum J:

$$\mathrm{CO}+\mathrm{OH} \underset{k_{-1}(EJ)}{\overset{k_1(EJ)}{\rightleftharpoons}} \mathrm{HOCO}^*(EJ), \tag{1}$$

$$\mathrm{HOCO}^*(EJ) \overset{k_2(EJ)}{\rightarrow} \mathrm{H}+\mathrm{CO}_2. \tag{2}$$

At finite pressures an additional series of kinetic equations are added to the scheme:

$$\mathrm{HOCO}^*(EJ)+M \overset{\omega(EJ\to E'J')}{\rightarrow} \mathrm{HOCO}(E'J')+M, \tag{3}$$

where M is a third body and E and J are conserved in reaction steps (1) and (2). The rate constants $k_i(EJ)$ are all E and J dependent. The $\omega(EJ\to E'J')$ is the rate constant per unit E for forming HOCO at $(E'J')$ from HOCO(EJ) by collision with a third body M.

The rate equation for the distribution function, $g(EJ)$, for HOCO^* at any specified (EJ) per unit energy is

$$\begin{aligned}\frac{dg(EJ)}{dt} &= k_1(EJ)-[k_{-1}(EJ)+k_2(EJ)+\omega]g(EJ)\\ &\quad +\sum_{J'}\int_{E'}\omega(E'J'\to EJ)g(E'J')\mathrm{d}E',\end{aligned} \tag{4}$$

where $g(EJ)$ denotes $[\mathrm{HOCO}(EJ)]/[\mathrm{CO}][\mathrm{OH}]$. The latter has units of $(\text{energy concentration})^{-1}$. The total collision frequency ω is

$$\omega=\sum_{J'}\int_{E'}\omega(EJ\to E'J')\mathrm{d}E'. \tag{5}$$

This $\omega(EJ\to E'J')$ is described by a step-ladder model employed in Sec. II D.

In the dissociation of the intermediate via TS_d, the RRKM rate constant $k_2(EJ)$ appearing in Eqs. (2) and (4) is

$$k_2(EJ)=\frac{N_d(EJ)}{h\rho(EJ)}, \tag{6}$$

where $\rho(EJ)$ is the density of states of the corresponding dissociating energetic molecules and $N_d(EJ)$ is the sum of states of TS_d, with the tunneling correction[50,51] for a microcanonical ensemble of

$$N_d(EJ) = \int_{-\infty}^{E} \kappa_d(E')\rho_d((E-E')J)\mathrm{d}E' . \qquad (7)$$

Here, $\kappa_d(E')$ is the tunneling transmission probability of TS_d when the energy in the H-tunneling coordinate is E', and $\rho_d((E-E')J)$ denotes the density of states of TS_d at an energy $E-E'$ and at total angular momentum J.

Harmonic vibrational frequencies and rotational constants for counting $N(EJ)$ or $\rho(EJ)$ were obtained by electronic structure calculations described in Sec. II A. To account approximately for the anharmonicity of the energetic intermediates, the density of states of *trans*- and *cis*-HOCO were increased by a constant factor, 1.5.[52] For TS, a "loose" TS was assumed. Anharmonicity effects for the vibrations of OH and CO are minor. In the calculation of quantum states of the internal rotation about the HO–CO bond in TS_a,[53] *cis*- and *trans*-HOCO were treated as one-dimensional hindered rotors.

C. Tunneling calculations with statistical and nonstatistical models

All *ab initio* calculations show a sharp potential-energy barrier in the product channel.[18,21] However, the magnitude of the imaginary frequency of TS_d depends on the electronic structure method used. Although these values are substantially different from each other (they are tabulated later), all of them indicate that the tunneling must be included in calculating the low-temperature reaction rates.[54] In these systems, in mass-weighted coordinate space the tunneling through the potential barrier occurs entirely in the products' channel and so there is no "corner cutting."[55] As a first approximation to reduce computational time, the tunneling probability $\kappa(E)$ was estimated for passage through an Eckart potential.[56] The potential was fitted to the paths of steepest ascent and descent through the saddle point. The Eckart-fitted approximation was checked with a sampling of more accurate calculations for selected points. In general, the Eckart barrier provides a more accurate but still simple representation than an inverted parabolic potential. However, the tunneling probability in the significant tunneling regions calculated by the Wigner approximation with an inverted parabolic potential is very similar to that calculated using the Eckart approximation. The difference of tunneling probabilities is less than 10%. However, compensation by barrier-height adjustment almost completely removes this discrepancy. Therefore, the bottom shape of the barrier in the exit channel only has a minor effect in the tunneling effect. With a slightly different vertical shift E of TS_d, such difference have only a minor effect over the final results.

D. Pressure effects with statistical and nonstatistical models

At high temperatures the effect of pressure on all properties in the present region of focus, below 1000 torr, is minor both experimentally and theoretically. However, at low temperatures in this pressure region both the pressure and the nature of the foreign gas affect the reaction rate. The collision frequency for the transition from EJ to $E'J'$, $\omega(EJ \to E'J')$, is approximated as the product of the total collision frequency ω, the energy transfer probability $P_{E\to E'}$, and the rotational angular momentum transfer probability $P_{J\to J'}: \omega(EJ \to E'J') = \omega P_{E\to E'} P_{J\to J'}$. For angular momentum transfer a strong collision is assumed. Thereby, the transfer probability $P_{J\to J'}$ from J to state J' equals the thermal distribution of J' states of the intermediate, HOCO, at the given temperature.

In the step-ladder model used for the energy-transfer probability $P_{E\to E'}$,[57] a certain amount of energy α is transferred in each collision, in the present case between HOCO^* and a bath molecule. The energy-transfer parameter α (α is positive) is dependent on the bath gas, but is independent of pressure. The α value of each bath gas, determined by best agreement with experimental results[11,13,14,17,40] of the CO +OH reaction at pressures below 800 torr, are given later in Table III.

By microscopic reversibility the ratio of activating collisions divided by the deactivating collisions in a step is equal to $[\rho(E)/\rho(E-\Delta E)]e^{-\alpha/k_BT}$, where $\rho(E)$ is the density of states of the intermediate at a total energy E. When $\rho(E)$ is approximated by a constant for a range of energies near the dissociation threshold,[58] the probabilities can then be written as

$$P_{E\to E'} = \begin{cases} \frac{e^{-\alpha/k_BT}}{1+e^{-\alpha/k_BT}}, & E' = E + \alpha \\ \frac{1}{1+e^{-\alpha/k_BT}}, & E' = E - \alpha \\ 0, & \text{otherwise}. \end{cases} \qquad (8)$$

The Lennard-Jones potential was used for interaction between a bath molecule and HOCO. The ϵ and σ parameters for the various bath gases in the Lennard-Jones potential are the same as those calculated by Zhu *et al.*[21] The lower limit for the energy range in the present calculations is 3000 cm^{-1} below the dissociation limit of CO and OH formation at the given temperature and pressure; even energies below $-2500\ \mathrm{cm}^{-1}$ are sufficiently lower than the dissociation threshold that the probability of the intermediate reacquiring enough energy to dissociate is negligible. To ensure convergence in the high-temperature and high-pressure region, the upper limit of the energy used in the calculations was 12 000 cm^{-1} above the dissociation limit, and the total angular momentum J covered the range from 0 to 220 in the E, J-resolved calculation. The energy grain size used for the energy integration in computing the pressure effect on the reaction rate constant was 1 cm^{-1}.[59] (For calculations restricted to 500 K or less, an upper limit of 5000 cm^{-1} in E and of 100 in J would have sufficed.)

E. OH energy partitioning and nonstatistical modification

In the RRKM theory it is assumed that the rate of energy redistribution in the intramolecular states of the intermediate is much faster than that of the dissociation. The molecular-beam results of Simons and co-workers for the reaction H $+\mathrm{CO}_2 \to \mathrm{HOCO}^* \to \mathrm{OH}+\mathrm{CO}$ show, albeit at higher energies than the present, that the CO formed has less energy than would be expected from statistical microcanonical behavior,

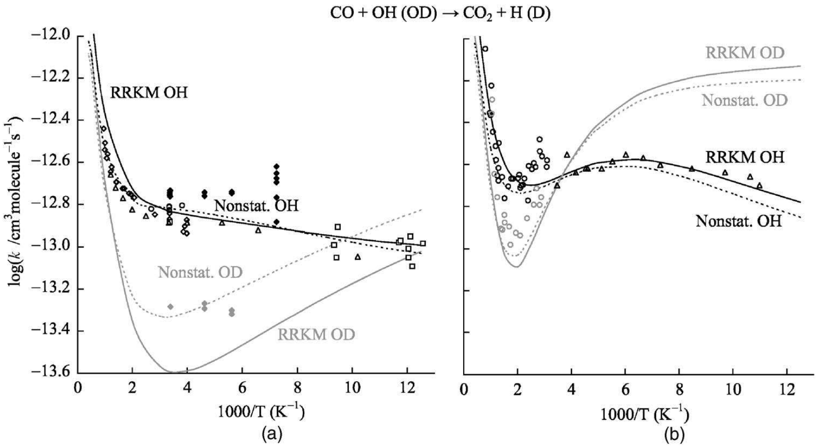

FIG. 2. Arrhenius plots for CO+OH (blacks) and CO+OD (grays). The solid and dashed lines are calculated using the RRKM and nonstatistical model, respectively. (a) The open squares and solid diamonds are experimental results obtained for 2–10 torr by Frost *et al.* (Refs. 11,12). The open diamonds and circles are obtained at 100 and 50–92 torr, respectively, by Ravishankara and co-workers (Refs. 6 and 13). The open triangles are the extrapolated rate constants CO+OH at zero pressure obtained by Fulle *et al.* (Ref. 5). The lines are the calculations at the low-pressure limit. (b) The open circles are the experimental data of Jonah *et al.* (Ref. 4) for a bath gas of 760 torr of Ar and 15 torr of H_2O. The open triangles are for 760 torr of He obtained by Fulle *et al.* (Ref. 5). The lines are the present calculations at 785 torr of Ar.

i.e., that there was a limited energy exchange between the newly formed OH bond and the other coordinates in $H\cdots OCO^*$. The reaction of $CO+OH\rightarrow H+CO_2$ requires a concentration of energy in the OH bond stretch in the *cis* intermediate (Fig. 1). Since the exit channel for the $CO_2+H\rightarrow CO+OH$ reaction is flat (no sharp repulsive drop), there is no major dynamical effect in this exit channel and so the energy distribution of the CO and OH products should reflect that expected from statistical theory,[60–62] applied now to HOCO, with relatively minor corrections for dynamics.

Although the formation of $HOCO^*$ from OH+CO is a highly exothermic reaction, the OH group would still be present largely in its vibrational ground state in a microcanonical distribution $\rho(EJ)$ at room temperature, because of the high OH-stretching vibrational frequency. However, since the potential-energy barriers in the entrance and exit channels are similar, a large amount of internal energy in an energetic HOCO molecule needs to be transferred into the OH bond in order for the HOCO to dissociate into CO_2+H. After this barrier at exit channel is overcome, the H atom then dissociates from the OCO. The harmonic energy steps of OH stretching in HOCO are about 3600 cm^{-1}, which is larger by 1700 cm^{-1} than that for the other vibrational modes. Because of this large frequency difference between OH stretching and the other modes, the internal energy transfer to OH-stretching motion via internal resonances with the other modes may be less rapid than needed for internal equilibration. (A higher-order resonance is possible.) Prompted by the experimental results of Brouard *et al.*[63–65] and other results, we have explored, with details in Appendix C, the effect of a reduced intramolecular energy transfer between the OH-stretching-mode motion and the other coordinates.

In this first trial calculation, an intramolecular energy-transfer parameter ξ in HOCO is defined in Eq. (C2) for the transfer to and from an OH vibration and is assumed to be 4000 cm^{-1}. It is somewhat larger than the vibrational frequency of the OH stretching in the $HOCO^*$, so allowing the intramolecular transfer of roughly one OH vibrational quantum. The nonstatistical modification significantly improves the agreement with the data for the rate constants of CO+OH at high temperatures, the rate constants of CO+OD at low pressures at room temperature, and the k_{OH+CO}/k_{OD+CO} ratio at room temperature. The ε ^{13}C values at around 1 atm are also improved. The results are given and discussed in the following sections.

III. RESULTS

A. Temperature effect

The experimental values of the rate constants at 100 and 300 K in the low-pressure limit are about 1.1×10^{-13} and 1.5×10^{-13} cm^3 $molecule^{-1}$ s^{-1}, respectively.[6,12,13,17,40,66] The two parameters E_1 and E_2 used to adjust potential energies of TS_a and TS_d to obtain agreement with these two low-pressure rate constants are 0 and 340 cm^{-1}, respectively, using the usual RRKM theory. When the nonstatistical modification is employed, they are instead 10 and 30 cm^{-1}, respectively. (Since the low-pressure rates are independent of the parameter α, we used them for this purpose.) The *classical* barrier with zero-point energy added for TS_a is about 280 cm^{-1} in both RRKM theory and the nonstatistical modification. For TS_d it is 965 and 655 cm^{-1}, respectively. Although there are some differences between the barriers of the unmodified and modified RRKM theory, their temperature-dependent rate constants at low pressures shown in Fig. 2(a) are similar. The calculations in Figs. 2(a) and 3 show that the slopes of the calculated Arrhenius plot are comparable to those of the experiment, and the change in the slopes occurs in both cases between 300 and 500 K. However, as seen in Fig. 3, the nonstatistical modification significantly improves

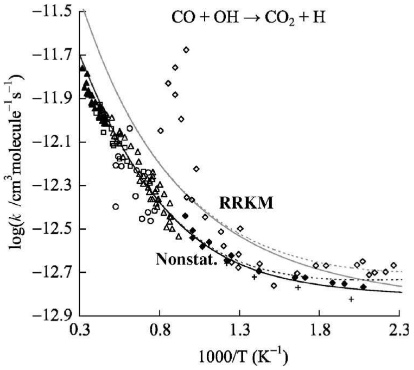

FIG. 3. Arrhenius plots for the CO+OH reaction in the high-temperature region. The gray and black lines are obtained with the RRKM and the nonstatistical model, respectively. The solid lines are for the low-pressure limit and the dashed lines are at 785 torr Ar. The solid triangles are obtained by Lissianski *et al.* (Ref. 7). The open squares are for 1178–2379 torr obtained by Golden *et al.* (Ref. 17), open triangles for 682–1168 torr by Wooldridge *et al.* (Refs. 8,9), open circles for 682–1168 torr by Brabbs *et al.* (Ref. 10), open diamonds for 785 torr Ar by Jonah *et al.* (Ref. 4), and solid diamonds for 100 torr Ar by Ravishankara and Thompson (Ref. 6). The plus signs refer to the results at the low-pressure limit extrapolated by Fulle *et al.* (Ref. 5).

the agreement between experimental and calculated results of the rate constants for CO+OH in the high-temperature region.

B. Pressure effect

Low- and high-pressure rate constants k^0 and k^∞ were studied experimentally by Fulle *et al.* at various temperatures.[5] Their fitted values are summarized in Table II, together with the present calculations and the step-down energy-transfer model. The effect of bath gases on the reaction of CO+OH has been investigated for He, N_2, air,CF_4, and SF_6.[11,13,14,17,40] The calculated rate constants are compared with the experimental data in Fig. 4(a). The α values obtained by unmodified and modified RRKM theory are similar and are listed in Table III.

C. OD and OH

Pressure-dependent rate constants were measured for the OD+CO reaction with different bath gases by Paraskevopoulos and Irwin,[41] Golden *et al.*,[17] and Frost *et al.*[11] The three sets of measurements and the calculations for He, Ar, N_2, air, CF_4, and SF_6 are compared in Fig. 4(b). For simplicity, the α's for OD+CO are assumed to be the same as those for OH+CO. The fitted curves for OD+CO using the nonstatistical modification, shown in Fig. 5, agree well with experiment, except for N_2, which is similar to the results of Golden *et al.*[17] and Senosiain *et al.*[27] and are discussed later. Unmodified RRKM theory underestimates the rate constant of OD+CO at low pressures at room temperature, and so the fitted RRKM curves in Fig. 4(b) do not agree well in the low-pressure region. However, the nonstatistical modification significantly improves the agreement, as seen in Fig. 5.

The ratio $k_{\text{OH+CO}}/k_{\text{OD+CO}}$ calculated using RRKM theory is plotted in Fig. 6 as a function of the pressure of He. The theoretical results agree with the experimental data relatively well at pressures higher than 300–500 torr, but the nonstatistical modification significantly improves the rate constant ratios in the low-pressure region and agrees with the experimental data in the entire pressure region, as seen by the dashed line in Fig. 6. The pressure-dependent rate constants for the OD+CO reaction with different bath gases calculated with the nonstatistical model in Fig. 5 also improve the agreement with experimental data in the low-pressure region. [cf. RRKM theory used in Fig. 4(b)].

The OH+CO and OD+CO systems in Fig. 2(a) show a marked difference in their dependence on temperature at low pressures and are calculated both for the RRKM theory and the nonstatistical modification. The OD+CO rate is predicted to have a minimum value around $1000/T=4$. Only Frost *et al.* appear to have studied the OD+CO reaction at low pressures.[11] The present calculation is in general agreement with their experimental results.

Jonah *et al.* measured the temperature dependence of the OH+CO and OD+CO rate constants at pressures ~760 torr at moderate and low temperatures.[4] Fulle *et al.* did a similar experiment of the OH+CO reaction at the lower-temperature

TABLE II. Comparison of the calculated k^0's and k^∞'s at several temperatures with the extrapolated values by Fulle *et al.* (Ref. 5). The rate constants are in units of 10^{-13} cm^3 molecule^{-1} s^{-1}.

T	k^0			k^∞		
(K)	RRKM	Nonstatistical	Expt.[a]	RRKM	Nonstatistical	Expt.[a]
100	1.1	1.1	0.9[b]	2.5	2.2	4.0[b]
200	1.4	1.4	1.3[c]	7.3	6.8	7.0[c]
300	1.5	1.5	1.3	13.2	13.6	9.6
400	1.7	1.6	1.4	20.2	19.5	12.6
500	1.9	1.7	1.5	28.4	27.5	16.2
600	2.2	1.8	1.7	37.8	36.9	20.3
700	2.6	2.0	1.9[d]	48.5	47.5	25.1[d]
800	3.1	2.3	2.2[e]	60.3	59.3	30.0[e]

[a] Results extrapolated to $p=0$ and $p=\infty$ by Fulle *et al.*

[b] Measured at 98 K.

[c] Measured at 190 K.

[d] Measured at 717 K.

[e] Measured at 819 K.

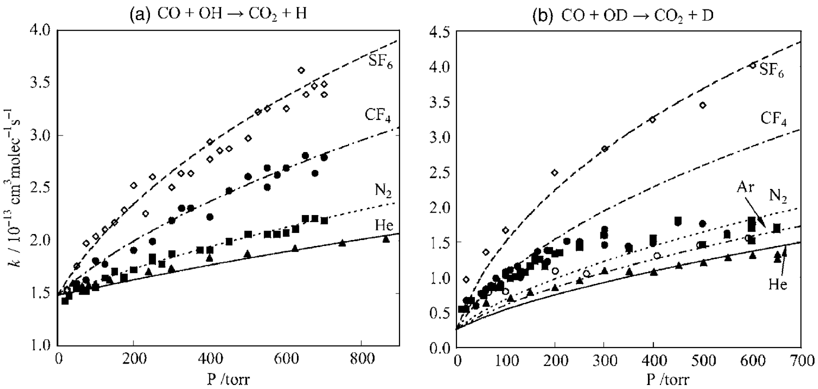

FIG. 4. Calculated and experimental pressure-dependent rate constants of (a) CO+OH and (b) CO+OD at 298 K for various bath gases. The RRKM method with the fitted energy-transfer parameter α listed in Table III is used in calculating rate constants. (a) The solid triangles are for He by Golden *et al.* (Ref. 17) and solid squares, solid circles, and open diamonds for N_2, CF_4, and SF_6, respectively, by Paraskevopoulos and Irwin (Ref. 40). (b) The open circles and open diamonds are for Ar and SF_6, respectively, by Golden *et al.* (Ref. 17). The solid triangle, solid squares, and solid circles are for He, N_2, and CF_4, respectively, by Paraskevopoulos and Irwin (Ref. 40).

region.[5] The temperature dependence of the calculated rate constants for both OH+CO and OD+CO reactions at 785 torr of Ar in Fig. 2(b) are similar in both RRKM theory and its nonstatistical modification models and are in good agreement with experiment.

D. Kinetic isotope effect for carbon

The isotopic fractionation of ^{13}C, $\varepsilon\ ^{13}$C, is defined as

$$\varepsilon\ ^{13}\mathrm{C} = \left(\frac{^{12}k}{^{13}k} - 1 \right) \times 1000 \text{ per mil}, \tag{9}$$

where ^{12}k and ^{13}k are the rate constants for the reaction of ^{12}CO and ^{13}CO with OH, respectively. Pressure-dependent $\varepsilon\ ^{13}$C's from 75 to 840 torr at room temperature were measured by Stevens *et al.*,[29] Smit *et al.*,[30] and Röckmann *et al.*[31] The data of Stevens *et al.* and Röckmann *et al.* show that $\varepsilon\ ^{13}$C depends slightly on bath gases.[29,31] Our calculations for the pressure dependence of the $\varepsilon\ ^{13}$C values by both RRKM and the nonstatistical models, shown in Fig. 7, agree reasonably well with the experimental data. As the pressure is increased, the calculated $\varepsilon\ ^{13}$C values also increase and depend slightly on bath gases. We discuss these results in Sec. IV.

IV. DISCUSSION

A. The barriers at TS$_a$ and TS$_d$

1. RRKM theory

As noted in Sec. III A two parameters E_1 and E_2 are needed to adjust the potential energies of TS$_a$ and TS$_d$, to fit the experimental values[6,12,13,17,40,66] of the rate constants at 100 and 300 K. The results of the barrier adjustments are consistent with recent previous estimates, the literature values varying from 100 to 380 cm^{-1} for TS$_a$ and from 0 to 1000 cm^{-1} for TS$_d$.[5,17–19,21,24] The fitted barriers for TS$_d$ in the literature are more scattered than those for TS$_a$ because of the difference in tunneling arising from large differences in imaginary frequencies at TS$_d$. In most theoretical calculations,[17–19,21,24,27] including the present, the exit channel barrier, ΔE_d, including zero-point energy, is higher than that for the entrance channel, ΔE_a, when the same calculational method is applied to both TSs.

TABLE III. The α values of several bath gases. The units are in cm^{-1}.

	G2M	Nonstatistical[a]	Zhu *et al.* (Ref. 21)[b]	Golden *et al.* (Ref. 22)[b]	Senosiain *et al.* (Ref. 27)[b]
He	140	140	150	150[c]	80
Ar[d]	190	190	450	300	110
N_2	200	210	250	300[e]	100[f]
CF_4	300	310	450	680	160[g]
SF_6	400	410	1000	800	190[h]

[a] The nonstatistical model is used.
[b] The pressure effect is calculated using the exponential down model.
[c] 180 cm^{-1} for OD+CO in He.
[d] Fitted to the data from OD+CO reaction.
[e] 480 cm^{-1} for OD+CO in N_2.
[f] 140 cm^{-1} for OD+CO in N_2.
[g] 150 cm^{-1} for OD+CO in CF_4.
[h] 200 cm^{-1} for OD+CO in SF_6.

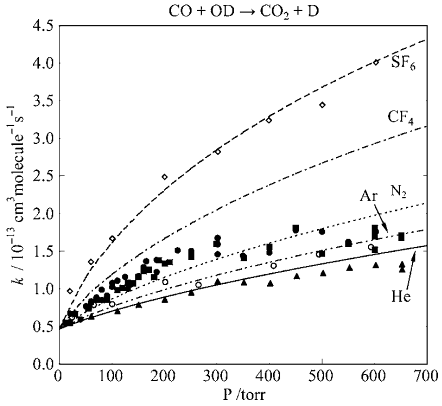

FIG. 5. Comparison of the experimental pressure-dependent rate constants of CO+OD at 298 K for various bath gases with the calculated rate constants using the nonstatistical modification. The energy-transfer parameter α assumed is listed in Table III. The open circles and open diamonds are for Ar and SF_6, respectively, obtained by Golden *et al.* (Ref. 17) and the solid triangle, solid squares, and solid circles are for He, N_2, and CF_4, respectively, by Paraskevopoulos and Irwin (Ref. 40).

Because of the large width and low barrier of TS_a, tunneling through TS_a at the low-pressure limit is important only at temperatures below 400 K. The calculated tunneling effects at TS_a increase the rate constant by about 10% in the low-pressure limit for a temperature of 400 K and less at higher temperatures. When any tunneling at TS_a is neglected, the reaction rate at room temperature in the low-pressure limit is less by about 20%. This effect is much smaller than that at TS_d, where the neglect of tunneling reduces the rate constant by a factor of 20.

The rate constants calculated with variation of rotational constants along the minimum reaction path near both TSs reduced the rate constants at low pressure by less than 1% at room temperature, as compared with fixing the position of TS_a at the local potential-energy maximum along this reaction coordinate. In the low-pressure limit the rate constant was reduced by 5% and 10% at 1000 and 2500 K, respectively. At high pressures this effect of varying the rotational constants along the reaction coordinate reduced the rate constant by 10% at 1000 K and 20% at 2500 K. The variational effects by Senosiain *et al.*[27] reduced the rate constants by 23% at 1000 K and 42% at 2500 K at low pressures, and by 11% at 1000 K and 21% at 2500 K at high pressures. The decrease is smaller in our calculations, presumably due to their taking into account the changing hindering rotation of OH and CO in TS_a along the reaction path.

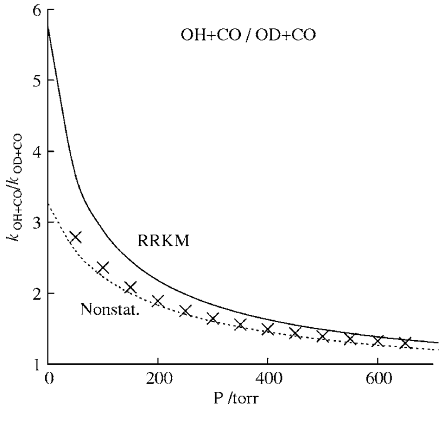

FIG. 6. Comparison of calculated and experimental results for the H/D kinetic isotope effect as a function of pressure at 300 K. The experimental data (×'s) are taken from a fit to Paraskevopoulos' results. The solid line is calculated using the conventional RRKM theory, and the dashed line is obtained using the nonstatistical modification.

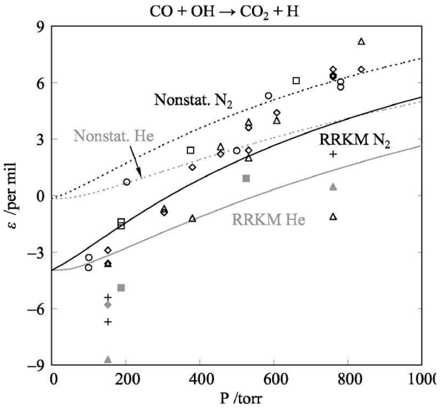

FIG. 7. The ε ^{13}C values for the system of CO+OH given as a function of the total pressure at room temperature. The solid lines are calculated using the conventional RRKM theory, and the dashed line is obtained with the nonstatistical model. The black and gray lines indicate the pressure dependence in N_2 and He gases, respectively. The open circles are obtained for N_2 by Smit *et al.* (Ref. 30). The gray solid and black open squares are obtained in He and N_2 (or N_2+O_2), respectively, by Röckmann *et al.* (Ref. 31). The gray solid triangles, black open triangle, open diamond, and plus symbols are obtained in Ar, air (by measuring products), air, and O_2, respectively, by Stevens *et al.* (Ref. 29).

2. Nonstatistical modification

The barrier of TS_a in the modification is similar to that used for the usual theory, reflecting the small sensitivity of the rate to TS_a. The barrier of TS_d now needed is about 300 cm^{-1} less than before. This lowering compensates for the constraint placed on the intramolecular energy transfer in the $HOCO^*$ when it passes through the TS_d in this nonstatistical modification.

B. Non-Arrhenius behavior

1. RRKM theory

The strongly non-Arrhenius behavior of the CO+OH reaction in Fig. 2 was observed in many earlier studies, both experimentally[5,6,11–13,15] and theoretically.[17,20–22,25] The experimental rate constants are slightly temperature dependent at low pressures in the temperature range 100–500 K, but increase steeply at higher temperatures.[5,6,11] Because the barriers to form products ($H+CO_2$) or revert to reactants (OH +CO) from $HOCO^*$ are similar, the competition between k_{-1} in Eq. (1) and k_2 in Eq. (2) for $HOCO^*$ disappearance serves to explain the change of slope of $\ln k$ versus $1/T$ of the reaction in Fig. 2(a); in the present calculations at high temperatures the k_{-1} in Eq. (1) is much larger than the k_2 in Eq. (2). So the barrier in the exit channel TS_d then dominates the rate. However, at temperatures below ~500 K k_{-1} and k_2 are comparable. Due to a large tunneling through TS_d at lower energies, k_2/k_{-1} ultimately increases as the temperature is decreased and so the contribution to the barrier from the rate at the entrance channel TS_a increases. In summary, the change in slope in Fig. 2(a) is due to the similar barrier heights of both entrance and exit channels together with a large tunneling effect in the exit channel TS_d.

2. Nonstatistical modification

The results calculated using the modification are similar to those obtained with the unmodified theory. However, as seen in Fig. 3, the modification describes the experiments at the high temperatures better than before.

C. Pressure effect

1. RRKM theory

The calculated low- and high-pressure rate constants, k^0 and k^∞, at the various temperatures listed in Table II, were compared with the extrapolated experimental values of Fulle *et al.*[5] As mentioned earlier, the calculated rate constants in the low-pressure limit are very similar to the extrapolated experimental values. The rate constants at the high-pressure limit are largely controlled by the properties of TS_a, and the extent of agreement with the extrapolated experimental values by Fulle *et al.*[5] in the high-pressure limit is seen in Table II. Any difference may reflect a shortcoming of the calculation of TS_a.

The effect of bath gases on the reaction of CO+OH has been studied for He, N_2, air, CF_4, and SF_6.[11,13,14,17,40] It has been repeatedly documented that polyatomic bath gases are better energy-transfer agents than monatomic gases. Possible reasons include higher densities of intramolecular energy states for the collisional energy transfer, larger collision radii, and more attractive interactions leading to a closer and so more steeply repulsive interaction. The fitted energy-transfer parameter α for He, Ar, N_2, CF_4, and SF_6 is 140, 190, 200, 300, and 400 cm^{-1}, respectively. The calculated rate constants and the experimental data are compared in Fig. 4(a). The α values listed in Table III are close to the fitted α values of Zhu *et al.*[21] and Senosiain *et al.*,[22] especially for monatomic and diatomic gases, but are larger than the fitted values of Senosiain *et al.*[27] Strictly speaking the α values are not exactly equivalent since the exponential down model is used by all other groups. In the results of other groups and ours the somewhat larger deviations of the α values for the polyatomic gases may arise from the different pressure models employed.

The pressure-dependent measurements of OD reacting with CO in various bath gases, He, Ar, N_2, air, CF_4, and SF_6,[11,17,41] are compared in Fig. 4(b) with calculations using the unmodified RRKM theory. Assuming the α's for OD+CO to be similar to those used for OH+CO, the fitted curves for OD+CO are in general agreement with experiment. The results indicate that α depends not only on the bath gas but also on whether the isotope is D or H. Senosiain *et al.*[22,27] optimized their calculations to agree with the experimental data by adjusting the α values for both OD+CO and OH+CO. Their α's for OD+CO are somewhat higher than those for OH+CO, but the difference is small, except for N_2, for which the results are similar to ours. For simplicity, the same α value for the C-isotope-substituted OH+CO reactions in each bath gas is assumed in the study of the kinetic C-isotopic effect discussed in Sec. IV F.

2. Nonstatistical modification

The k^0 values at high temperatures obtained with the RRKM modified theory are smaller than those obtained with conventional theory and are closer to the extrapolated experimental results. The k^∞ values are similar in both treatment, because they are mainly determined by the properties of TS_a, which is treated in the same way in both models. The energy-transfer parameter α for various bath gases by both models are similar and are listed in Table III. The nonstatistical theory improves the agreement of the pressure dependence of OD reacting with CO in various bath gases significantly, especially for the extrapolated values at zero pressure, as shown in Fig. 5. The most important improvement arising from the nonstatistical model is in the plot of k_{OH+CO}/k_{OD+CO} ratios versus pressure, especially at lower pressures, as in Fig. 6. In that figure, the large discrepancy between experiment and the conventional RRKM theory is clear. This discrepancy with conventional RRKM theory was also seen in Fig. 9 of Ref. 27 and is now removed by the nonstatistical modification (Fig. 6). The robustness of this result is shown in Appendix A 4 (Fig. 10).

D. Negative temperature effect in OD+CO

1. RRKM theory

The calculated rate constants for OD+CO in Fig. 2(a) display a minimum around 250 K. Only Frost *et al.* appear to have studied the OD+CO reaction as a function of temperature at low pressures.[11] In their study at 178, 216, and 295 K, Fig. 2(a), they observed nearly temperature-independent reaction rates. Their RRKM calculations also showed a slight decrease in rate in going from 80 to 300 K. There is general agreement between the experimental and calculated results.

The relatively large negative temperature effects observed in the OD+CO reaction, shown in Fig. 2(a), can be explained by the lowered barrier at TS_a and the increased height of the TS_d barrier in OD+CO relative to that in OH+CO. The energy with the zero-point corrections of TS_a in OD+CO is around 150 cm^{-1} and that of TS_d is around 1320 cm^{-1}. Although the value of the imaginary frequency of OD at TS_d is smaller than that of OH, the barrier change increases the tunneling window (energy difference between TS_d and TS_a) by about 500 cm^{-1} in OD+CO. The decreased barrier in the entrance channel allows the formation of more intermediates at low temperatures. At low pressures, the intermediates can only tunnel through TS_d to products or revert to reactants. The number of states is approximately independent of temperature, but the partition function of the collision pair decreases as temperatures increase. From our calculations in Fig. 2(a), the negative temperature effect is significant at temperatures lower than 250 K. The experiments on OD+CO at low pressures and temperatures would permit a test of the prediction of a negative temperature effect in the present calculation.

When different *ab initio* theories are used there is a difference of imaginary frequency at TS_d in various force constants. As a result, the temperature where the minimum in the calculated rate constant occurs is spread from 200 to 400 K, as shown in Appendix A 2, the higher temperature occurs with the larger value of the imaginary frequencies. The studies on OD+CO at low pressures and low temperatures would help determine better the value of the imaginary frequency at TS_d and so determine more precisely the magnitude of tunneling effects.

2. Nonstatistical modification

Comparing the Arrhenius plot of the OD+CO reaction at low pressures for the unmodified and modified theories, the former has a weaker temperature dependence in the low-temperature region. This result is consistent with the results in the experiment of Frost *et al.* There are only two measurements of the rate constants below 250 K. More measurements at low temperatures would permit a test of the trend predicted in Fig. 2(a).

E. OH and OD

1. RRKM theory

In the measurements of Paraskevopoulos and Irwin,[40] Frost *et al.*,[11] and Golden *et al.*,[17] the pressure-dependent kinetic H/D isotope effect is given at about 300 K. At low pressures their experimental values for $k_{\mathrm{OH+CO}}/k_{\mathrm{OD+CO}}$ are 3.6, 2.7, and 2.3, respectively. This kinetic effect can be understood in terms of tunneling, together with the zero-point energy difference of TS_a and TS_d. Compared with the ratios in the data of Paraskevopoulos and Irwin, the ratio $k_{\mathrm{OH+CO}}/k_{\mathrm{OD+CO}}$ calculated using the unmodified theory, the solid line in Fig. 6, significantly overestimates it at pressures below 500 torr, but is comparable with experiments at higher pressures. The robustness of this result is seen later in Appendix A.

Jonah *et al.* measured the rates of OH+CO and OD+CO from 340 to 1250 K at 1 atm of Ar and 15 torr of water vapor.[4] Both rates have minima around 600 K [Fig. 2(b)]. This negative dependence on temperature was also observed by Fulle *et al.*[5] in the rates of OH+CO from 91 to 288 K at 750 torr of He. The rate constants measured by the latter group showed a maximum around 170 K. Our calculations in Fig. 2(b) for both OH+CO and OD+CO reactions at 785 torr of Ar are close to their results. The minimum rate of OH and OD occurs at about 400 and 500 K, respectively, which are slightly lower than the measured values. The calculated negative temperature dependence of the CO+OH reaction rate between 200 and 400 K has a maximum around 160 K, which is close to the maximum in the measurements of Fulle *et al.*

2. Nonstatistical modification

When the intramolecular energy-transfer restriction is introduced using the modified theory, the agreement of the rate constant ratios at the low-pressure region is significantly improved, as seen by the dashed line in Fig. 6. The modified theory also improves agreement with experiment for the pressure dependence of the low-pressure rate constants of OD+CO as in Fig. 5. The temperature dependence of the rate constants at pressures ~1 atm are similar to these in the unmodified theory and in the experiment. At temperatures higher than 1000 K, the rate constants in Fig. 3 obtained using the modified theory agree better with the experiment than before and are lower than the conventional RRKM result by about 60%.

The calculations for the unmodified theory tend to underestimate the rate constants of OD+CO in the low-pressure region, perhaps because any difference in the energy-transfer ability between HOCO^* and DOCO^* is not considered. The vibrational frequency of the OD stretching in DOCO, about $2700\ \mathrm{cm}^{-1}$, is much less than the OH-stretching frequency. Accordingly, the energy transfer between the OD stretching and other modes in energetic DOCO^* may well be easier than in HOCO^*. In the nonstatistical modification, the relation between the energy-transfer parameter ξ in HOCO and that in DOCO is simply assumed to be

$$\xi_D = \frac{\nu}{\nu_D}\xi, \tag{10}$$

where ν is the OH (OD) stretching frequency in the intermediate, the subscript D and no subscript indicating the DOCO and HOCO systems, respectively. Equation (10) implies that the energy redistribution in the energetic DOCO is faster than that in HOCO. In counting the number of states for TS_d, with a tunneling correction using Eq. (C2), the range of integration used for DOCO is about 30% larger than that for HOCO due to the ν_D in Eq. (10) being smaller than ν.

F. Kinetic isotope effect for carbon

1. RRKM theory

The reaction at atmospheric pressure was found to favor a positive $\varepsilon\ {}^{13}\mathrm{C}$ by 6 per mil, while negative values were observed at pressures below ~300 torr. These experimental data also show that $\varepsilon\ {}^{13}\mathrm{C}$ depends slightly on the bath gas.[29,31] The values in monatomic gases, such as He or Ar, are lower than those in diatomic gases, such as air, O_2, and N_2. Our calculations in Fig. 7 for $\varepsilon\ {}^{13}\mathrm{C}$ agree reasonably well with these data. The calculated $\varepsilon\ {}^{13}\mathrm{C}$ at low pressures is negative, around −4 per mil. As the pressure increases, the calculated $\varepsilon\ {}^{13}\mathrm{C}$ increases to positive values, similar to the pressure dependence observed in the experiment. Although the values of collision stabilization energy, the α's for He and N_2 are different, the trend in pressure dependence of $\varepsilon\ {}^{13}\mathrm{C}$ in Fig. 7 is similar. As pressure increases, the $\varepsilon\ {}^{13}\mathrm{C}$ in N_2 increases faster than in He, but the difference is small.

The calculated negative $\varepsilon\ {}^{13}\mathrm{C}$ at low pressures can be understood in terms of the higher density of the vibrational and rotational states for heavier isotopic molecules. The

TABLE IV. Parameters for fitting the rate constants at 100 and 300 K in the low-pressure limit for various PES's and *ab initio* methods.[a] All units are cm^{-1}.

PES	G2M				LTSH			
ab initio	DFT-CC	DFT-MP	CC	MP2	DFT-CC	DFT-MP	CC	MP2
E_1	−10	−10	0	10	−280	−280	−270	−260
E_2	60	10	340	580	330	290	620	850
				OH+CO				
ΔE_a	269	349	275	359	273	353	280	363
ΔE_d	714	664	965	1318	704	664	964	1308
ν_a^i	312*i*	449*i*	312*i*	449*i*	312*i*	449*i*	312*i*	449*i*
ν_d^i	1526*i*	1526*i*	2126*i*	3176*i*	1526*i*	1526*i*	2126*i*	3176*i*
				OD+CO				
ΔE_a	135	194	150	221	139	199	154	226
ΔE_d	1067	1017	1322	1665	1057	1017	1322	1655
ν_a^i	310*i*	447*i*	310*i*	447*i*	310*i*	447*i*	310*i*	447*i*
ν_d^i	1219*i*	1219*i*	1686*i*	2547*i*	1219*i*	1219*i*	1686*i*	2547*i*

[a] ν_a^i and ν_d^i denote the imaginary frequencies of TS_a and TS_d, respectively.

pressure dependence of $\varepsilon\ ^{13}\mathrm{C}$ can be explained in terms of the difference of vibrational energies at the TSs and of the collision frequencies, ω, for the $^{12}\mathrm{C}$ and $^{13}\mathrm{C}$ intermediates; due to the lower barrier and higher number of states in both TS_a and TS_d when $^{13}\mathrm{C}$ is substituted for $^{12}\mathrm{C}$, ^{13}k is larger than ^{12}k in the low-pressure region, causing $\varepsilon\ ^{13}\mathrm{C}$ to be negative in the present theory. The collision frequencies are proportional to $\mu^{-1/2}$, where μ is the reduced mass of the bath gas and HOCO^*. As the pressure is increased the rate of collision stabilization of intermediates is larger due to the larger collision frequency. Therefore, the presently calculated $\varepsilon\ ^{13}\mathrm{C}$ values in Fig. 7 vary from slightly negative at low pressures to about +5 per mil at 1000 torr, which is similar to the experimental data. The collision factor can introduce a maximum of +7 per mil when the bath gas is N_2 and the rate is proportional to the collision frequency.

2. Nonstatistical modification

Our calculations in Fig. 7 for $\varepsilon\ ^{13}\mathrm{C}$ in both the unmodified and the modified theory agree reasonably well with the experimental data. The $\varepsilon\ ^{13}\mathrm{C}$ calculated using the modified theory are a little larger than the values obtained before. It increases from −4 per mil to about 0 per mil at 100 torr, which is higher than the independent experimental results of Stevens *et al.*[29] and Smit *et al.*[30] given in Fig. 7. Even though the values obtained using the model in the low-pressure region tend to overestimate the carbon fractionation, as compared with experiment, they are still in good overall agreement with the data, especially for pressures higher than 500 torr. Similar to the results obtained for the pressure dependence of the $\varepsilon\ ^{13}\mathrm{C}$ values of two bath gases with the unmodified theory, the values in N_2 using the modified theory increase faster than those in He, again in agreement with experiments.

V. CONCLUSIONS

The use of a nonstatistical modification of the RRKM theory significantly improves the agreement with experiment for (1) the pressure-dependent $k_{\mathrm{OH+CO}}/k_{\mathrm{OD+CO}}$ ratio, (2) the pressure dependence of the OD+CO reaction rate, and (3) the non-Arrhenius behavior at high temperatures. In (1) a major discrepancy between experiment and theory has been removed, assuming the validity of the nonstatistical effect. A negative temperature effect at low temperatures in the OD+CO reaction is predicted in both unmodified and modified RRKM theories. The measured $\varepsilon\ ^{13}\mathrm{C}$ effect is very small and pressure dependent. The calculations with unmodified and modified RRKM theories are in reasonable agreement with $^{13}\mathrm{C}$ rate, considering the extremely small magnitude of the effect (from −4 per mil at low pressures to 6 per mil at ~1 atm).

ACKNOWLEDGMENTS

It is a pleasure to acknowledge the support of this research by the National Science Foundation. We also thank Dr. Muckerman for providing the F matrix for the structures in their paper,[18] which were used to check the accuracy of rate constant calculation with our previous vibrational frequencies.

APPENDIX A: RESULTS FOR DIFFERENT PES'S

Calculations with different and less accurate force constant methods were used to test the sensitivity of certain aspects of the calculations and are discussed in this Appendix. The results for the $k_{\mathrm{OH+CO}}/k_{\mathrm{OD+CO}}$ ratios between 200 and 800 torr and for the non-Arrhenius effect and the pressure effect below 1000 torr all show a robustness toward the different calculations. Apart from the transition state structure of the entrance channel (TS_a),[67] the vibrational frequencies and rotational constants of all structures for the various isotopes were calculated by three methods in this comparison,

TABLE V. k^0's and k^∞'s at temperatures obtained from values extrapolated to $p=0$ by Fulle *et al.* (Ref. 5) and calculated with various PESs. The rate constants have units of 10^{-13} cm^3 molecule^{-1} s^{-1}.

PES	G2M				LTSH				
ab initio	DFT-CC	DFT-MP	CC	MP2	DFT-CC	DFT-MP	CC	MP2	Expt.[a]
					k^0				
100 K	1.1	1.1	1.1	1.1	1.1	1.1	1.1	1.0	0.9[b]
200 K	1.3	1.3	1.4	1.3	1.3	1.2	1.3	1.3	1.3[c]
300 K	1.5	1.5	1.5	1.5	1.5	1.5	1.5	1.5	1.3
400 K	1.7	1.8	1.7	1.6	1.7	1.8	1.6	1.6	1.4
500 K	2.0	2.1	1.9	1.8	2.1	2.1	1.9	1.8	1.5
600 K	2.4	2.5	2.2	1.9	2.5	2.5	2.2	2.0	1.7
700 K	2.9	3.0	2.6	2.2	3.0	3.0	2.6	2.2	1.9[d]
800 K	3.5	3.6	3.1	2.5	3.5	3.6	3.1	2.5	2.2[e]
					k^∞				
100 K	2.9	1.8	2.5	1.5	2.7	1.8	2.4	1.5	4.0[b]
200 K	8.0	4.5	7.3	4.0	7.8	4.3	7.1	3.9	7.0[c]
300 K	14.1	8.0	13.2	7.4	13.9	7.9	13.0	7.2	9.6
400 K	21.5	12.4	20.2	11.5	21.2	12.2	19.9	11.3	12.6
500 K	30.1	17.5	28.4	16.3	29.7	17.4	28.0	16.2	16.2
600 K	40.0	23.5	37.8	21.9	39.6	23.3	37.5	21.8	20.3
700 K	51.2	30.2	48.5	28.3	50.8	30.0	48.1	28.1	25.1[d]
800 K	63.7	37.7	60.3	35.4	63.3	37.5	59.9	35.2	30.0[e]

[a] Extrapolated results to $p=0$ and $p=\infty$ by Fulle *et al.* (Ref. 5).
[b] Measured at 98 K.
[c] measured at 190 K.
[d] Measured at 717 K.
[e] Measured at 819 K.

CCSD(T) with 6-31G(d,p), B3LYP with cc-pVTZ, and MP2 with 6-31++G(d,p). The properties of TS$_a$ are obtained only from the results of MP2 or CC. The acronym DFT will denote the calculation by B3LYP. DFT-MP will denote the calculations combining the structure data of TS$_a$ from MP2 and the other statures from B3LYP, while DFT-CC is similar but with the data for TS$_a$ obtained from CCSD(T). The LTSH potential, given by Lakin *et al.*,[24] involves an analytical function based on recent high-level *ab initio* methods and was also used to explore the robustness.

1. Temperature and pressure effects

Some robustness is expected to occur partly because there are two adjustable parameters E_1 and E_2 of the potential energy of TS$_a$ and TS$_d$ determined from the two rate constants. These E_1 and E_2 adjustments are listed for each specific PES in Table IV. Although the parameters differ between G2M and LTSH, the resulting *classical* barriers (i.e., no tunneling) with zero-point corrections of TS$_a$ and TS$_d$ are similar at the same *ab initio* level. All the barriers of TS$_a$ with zero-point corrections in our fitted results agree well with the recent estimates derived from kinetic measurements and from barrier theoretical calculations.[17–19,21,24] Due to the difference of the imaginary frequencies of TS$_d$, the E_2 parameter differs most among *ab initio* methods. All of them are, as expected, within or near the range of earlier theoretical studies.[17–19,21,24] The calculated temperature dependence of rate constants has a non-Arrhenius effect at low temperatures and is quite robust in the present calculations.

The extrapolated low- and high-pressure rate constants k^0 and k^∞ from the data of Fulle *et al.*[5] and the calculations

TABLE VI. α values of several bath gases with various PESs. The units are cm^{-1}.

PES	G2M				LTSH					
ab initio	DFT-CC	DFT-MP	CC	MP2	DFT-CC	DFT-MP	CC	MP2	Ref. 21	Ref. 22
He	130	150	140	180	120	140	130	170	150	150[a]
Ar[b]	180	200	190	220	160	180	180	210	450	300
N_2	190	240	200	300	170	230	190	280	250	300[c]
CF_4	270	380	300	460	250	340	270	440	450	680
SF_6	350	500	400	700	320	450	360	650	1000	800

[a] 180 cm^{-1} for OD+CO in He.
[b] Fitted to the data from the OD+CO reaction.
[c] 480 cm^{-1} for OD+CO in N_2.

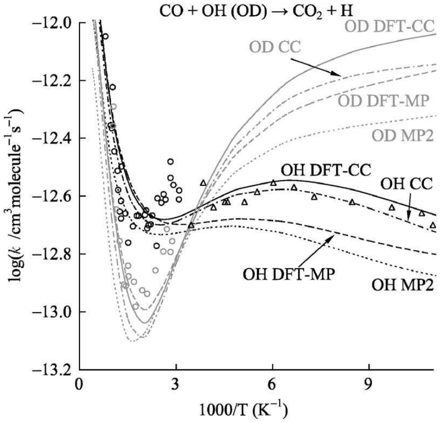

FIG. 8. Arrhenius plots for the reaction of CO+OH (black lines) and CO+OD (gray lines) in Ar at 785 torr. All curves in the plot are obtained with G2M, and the LTSH potentials show similar curves. The black and gray open circles are the experimental data of OH and OD reacting with CO, respectively (Ref. 4). The bath gas in the experiment consists of 760 torr of Ar and 15 torr of H_2O. The open triangles are Fulle's experiments at 760 torr of He. The solid, dot-dashed, dashed, and dotted lines are calculated with DFT-CC, CC, DFT-MP, and MP2, respectively.

with the step-down model are summarized in Table V. At the high-pressure limit, the rate constants are largely controlled by the properties of TS_a. Since there are two kinds of *ab initio* calculation levels, CC and MP2, for TS_a, the high-pressure rate constants k^{∞}'s in the calculations can be divided into two groups. The properties of TS_a described by MP2 and DFT-MP reproduce better the extrapolated experimental k^{∞} values by Fulle *et al.*, but on the whole there is reasonable agreement.

The α values obtained using various PESs for various bath gases, listed in Table VI, form two groups. The force constants and structure of TS_a in DFT-CC and CC are the same and form a group, and those in DFT-MP and MP2 are the same and form a second group. Both sets of α are close to the α values independently fitted by Zhu *et al.*[21] and Senosiain *et al.*[22] (A caveat in comparing the step ladder α with the exponential down α was noted earlier.) The pressure-dependent rates in various bath gases calculated by various *ab initio* methods are similar to those in Fig. 4(a). Using the same force constants, the fitted α values from the G2M potential are slightly larger than those from LTSH, since the intermediate in the latter is stabler by about 1.5 kcal mol^{-1}. The last observation is similar to the results of Senosiain *et al.*[22] Their fitted α value for He was reduced from 150 to 100 cm^{-1} when they lowered the energy of the HOCO* intermediates by 5.5 kcal mol^{-1}. Thus, the pressure dependence of the rate constants is controlled by the properties of both TS_a and the stability of the HOCO* intermediate.

2. OH and OD

The calculated k_{OH+CO}/k_{OD+CO} ratio decreases to about 2 at 200 torr and about 1.2 at 700 torr using the various force constants for the various PESs. DFT-CC, DFT-MP, and CC overestimate the ratio at pressures lower than 100 torr.

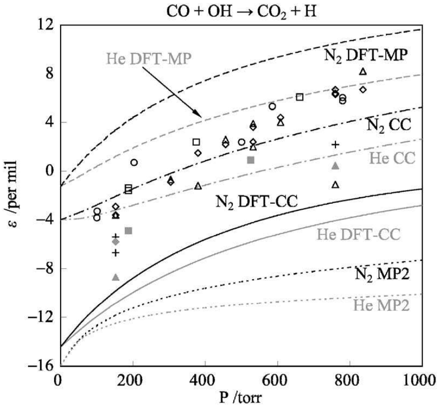

FIG. 9. The ε ^{13}C values for the system of OH+CO as a function of total pressure at room temperature. Both G2M and LTSH potentials give similar results, only the calculations with G2M are shown in the plot. The gray and black lines are for He and N_2 gases, respectively. The solid, dot-dashed, dashed, and dotted lines are calculated with DFT-CC, CC, DFT-MP, and MP2, respectively. The open circles are obtained for N_2 by Smit *et al.* (Ref. 30). The gray solid and black open squares are obtained by Röckmann *et al.* (Ref. 31) for He, and N_2 (or N_2+O_2), respectively. Others are obtained by Stevens *et al.* (Ref. 29), where the gray and black indicate that the bath gases are He or Ar, and N_2, O_2, or air, respectively.

The negative temperature effects in the OD+CO reaction in the low-pressure limit are obtained for all PESs. The temperature for the minimum rate strongly depends on the imaginary frequency of TS_d. The temperature with the minimum rate is around 400 K in MP2, 300 K in CC, and 200 K in DFT-CC and DFT-MP, and is higher the higher the imaginary frequency. All Arrhenius plots of the OH and OD reacting with CO in Ar at 785 torr, shown in Fig. 8, are similar.

3. Kinetic isotope effect for carbon

Since the fractionation of ^{13}C is very small, the different sets of force constants yield slightly different results. However, all the calculated results show similar trends of the pressure dependence of the ε ^{13}C values between different bath gases, in agreement with the experimental data. The calculated pressure dependence of fractionation of ^{13}C is shown in Fig. 9. All calculations except MP2 give similar

TABLE VII. Parameters for fitting the rate constants at 100 and 300 K in the low-pressure limit. DFT-CC and CC methods are used with the G2M potential by nonstatistical model with ξ at 4000 cm^{-1}. The energy-transfer parameters α for various bath gases are also listed. The units are cm^{-1}.

Ab initio	DFT-CC	CC
E_1	0	10
E_2	−280	30
	α	
He	120	140
Ar[a]	170	190
N_2	190	210
CF_4	280	310
SF_6	360	410

[a]Fitted to the data from the OD+CO reaction.

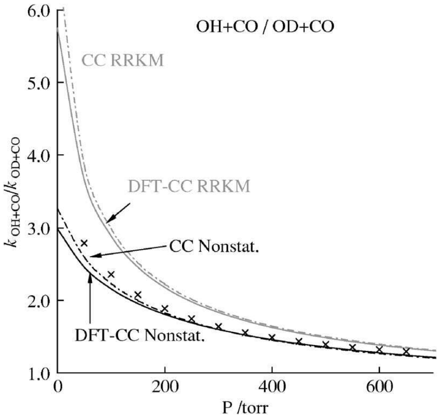

FIG. 10. Comparison of calculated and experimental results for the kinetic OH/OD isotope effect as a function of pressure at room temperature. The experimental data (×'s) are taken from the fit to the data of Paraskevopoulos. The modified and unmodified RRKM theories are used in the calculation. The solid and dot-dashed lines are calculated with DFT-CC and CC, respectively.

pressure dependence. The reason for the inadequate pressure dependence calculated with MP2 is probably due to an overestimation of the imaginary frequency in TS_d.

4. Nonstatistical effect

Since Eq. (C4) is used to approximate ξ in the isotope-substituted HOCO, it decreases the ratio of the rate for OH+CO relative to OD+CO. In the nonstatistical effect only the two most accurate methods were used to test the accuracy of the nonstatistical modification, namely, the CC and DFT-CC methods together with the G2M potential. The value of ξ in HOCO in both CC and DFT-CC is assumed to be 4000 cm^{-1}. The parameters E_1 and E_2 adjusted to fit the rates of OH+CO at 100 and 300 K at low pressures and the energy-transfer parameter α in various bath gases are listed in Table VII. The α values for the model are also similar to those for the conventional RRKM model, hence the pressure dependence of rate constants in both models are similar. However, for both CC and DFT-CC methods the nonstatistical model describes better the rate constant ratios between OH and OD reacting with CO, as seen in Fig. 10. The negative temperature effect of the OD+CO reaction is also observed in the model, shown in Fig. 11.

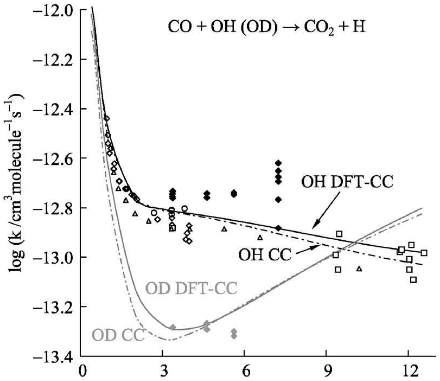

FIG. 11. Arrhenius plots for CO+OH (black lines) and CO+OD (gray lines) at the low-pressure limit. The solid and dot-dashed lines are calculated with DFT-CC and CC, respectively, at this limit. The open squares and solid diamonds are experimental results obtained for 2–10 torr by Frost *et al.* (Refs. 11,12). The open diamonds and circles are obtained at 100 and 50–92 torr, respectively, by Ravishankara and co-workers (Refs. 6 and 13). The open triangles are the extrapolated rate constants at zero pressure obtained by Fulle (Ref. 5).

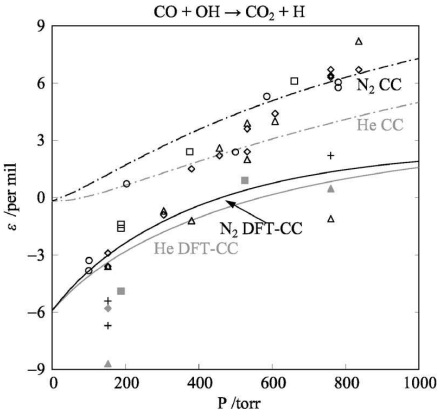

FIG. 12. The ε ^{13}C values for the system of CO+OH by the nonstatistical model as a function of the total pressure. The solid and dot-dashed lines are calculated with DFT-CC and CC, respectively. The black and gray lines indicate the pressure dependence in N$_2$ and He gases, respectively. The open circles are obtained for N$_2$ by Smit *et al.* (Ref. 30). The gray solid and black open squares are obtained for He and N$_2$ (or N$_2$+O$_2$), respectively, by Röckmann *et al.* (Ref. 31). Others are obtained in by Smit *et al.* (Ref. 29). The gray and black indicate the bath gases as He or Ar, and N$_2$, O$_2$, or air, respectively.

The kinetic isotope effects of carbon of DFT-CC are in better agreement with experiment at pressures under 400 torr when this nonstatistical correction is used, as seen in Fig. 12. Although the values obtained with CC agree better at pressures higher than 500 torr, both DFT-CC and CC give a similar trend for the pressure dependence of ε ^{13}C.

APPENDIX B: THE TUNNELING PROBABILITY FOR AN ECKART BARRIER

For the Eckart potential, frequently used to estimate the tunneling probability of the reaction,[68] the transmission probability as a function of energy E is

$$\kappa(E) = 1 - \frac{\cosh(a-b) + \cosh(c)}{\cosh(a+b) + \cosh(c)}, \tag{B1}$$

where

$$a = \frac{4\pi E^{1/2}}{h\nu^*(V_1^{-1/2} + V_2^{-1/2})}, \quad b = \frac{4\pi(E - V_1 + V_2)^{1/2}}{h\nu^*(V_1^{-1/2} + V_2^{-1/2})},$$

$$c = 4\pi\left(\frac{V_1 V_2}{(h\nu^*)^2} - \frac{1}{16}\right)^{1/2}, \tag{B2}$$

V_1 is the barrier height relative to the beginning of the barrier and V_2 is the barrier height relative to the products. The

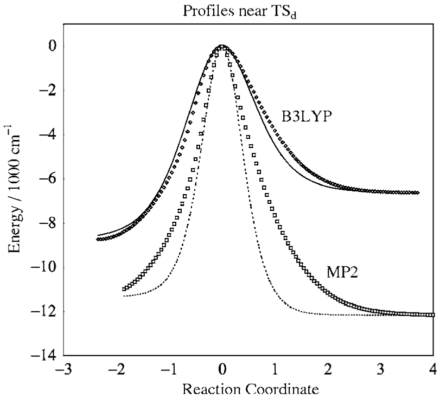

FIG. 13. Comparison of different barrier profiles with Eckart potential functions and with IRC calculations. The open diamonds and open squares denote the IRC calculations at TS$_d$ calculated with B3LYP and MP2, respectively. The solid and dotted lines were obtained using the Eckart potential for the exit channel using B3LYP and MP2, respectively.

potential is written for an exoergic reaction, i.e., $V_1 \leqslant V_2$, and ν^* is the absolute value of the imaginary frequency.

The GAUSSIAN 98 program supports the intrinsic reaction coordinate (IRC) calculation for the MP2 and DFT methods, but not for the CC method. Since the value of the imaginary frequency of TS$_d$ by CC is intermediate between those obtained using the other methods, the difference between the barrier profiles estimated by the Eckart potential functions and calculated by the IRC method with DFT or MP2, shown in Fig. 13, would be expected to reflect the nature of any error in using the Eckart potential to approximate calculations by CC. The Eckart potential is sharper than that obtained by the IRC calculation, especially when the imaginary frequency is large. (The imaginary frequency is $1526i$ cm^{-1} in DFT and $3372i$ cm^{-1} in MP2.) However, most of the tunneling region occurs between the top of the barrier at TS$_d$ and about 1500 cm^{-1} below it. In comparing the tunneling probabilities through Eckart and parabolic barriers, the shape of the bottom of the barrier has a negligible effect on the reaction rate constants. We infer that an Eckart potential is a reasonable barrier to approximate the tunneling effect in the current study.

APPENDIX C: EQUATION FOR THE NONSTATISTICAL MODEL

In a trial intramolecular energy-transfer model, we assume that only a limited amount of energy, ξ, can be transferred into or out of OH stretching just before the HOCO* passes through TS$_d$. The dissociation rate of HOCO* at a total energy E, rotational quantum state J, and quantum number n of OH stretching in HOCO* is then

$$k_n(EJ) = \frac{N_n(EJ)}{h\rho_n(EJ)}, \tag{C1}$$

where

$$N_n(EJ) = \int_{\mathrm{Max}[E_0,E_0+nh\nu-\xi]}^{\mathrm{Min}[E,E_0+nh\nu+\xi]} \kappa_d(E')\rho_d((E-E')J)\mathrm{d}E'. \tag{C2}$$

The definitions of $\kappa_d(E')$ and $\rho_d((E-E')J)$ are the same as in Eq. (7). ν is the OH-stretching frequency of *cis*-HOCO, and the lower and upper bounds of the integral correspond respectively to the maxima value between E_0 and $E_0+nh\nu-\xi$ and the minima value between E_0 and $E_0+nh\nu+\xi$. The dissociation rate of HOCO* at total energy E and rotational state J can be expressed from Eq. (C1) as

$$k(EJ) = \frac{1}{1+n_{\mathrm{max}}} \sum_{n=0}^{n_{\mathrm{max}}} \frac{\rho_n(EJ)}{\rho(EJ)} k_n(EJ), \tag{C3}$$

where n_{max} is the maximum allowed quantum number of the OH stretching in the energetic intermediate at (E,J), $\rho_n(EJ)$ is the density of states of the intermediate at OH vibrational state n, and $\rho(EJ)$ is the total density of states at total energy E and rotational state J.

The energy-transfer parameter ξ depends on the difference in resonances of the OH-stretching vibration with other modes and on the anharmonic coupling of the PES. It can also influence the isotope effects. As a first approximation, and similarly as in Eq. (10) in the deuterium case, ξ_{iso} is written as

$$\xi_{\mathrm{iso}} = \frac{\nu}{\nu_{\mathrm{iso}}}\xi, \tag{C4}$$

where ν is the OH-stretching frequency in the intermediate and the subscript "iso" and no subscript indicates the isotope-substituted HOCO and normal isotopologue of HOCO, respectively. Although a very crude approximation, the equation includes the fact that the internal energy transfer would be more rapid when the stretching frequency is closer to that of the other modes. For example, the ξ value in DOCO calculated from the approximation is about 40% larger than that in HOCO.

[1] R. P. Wayne, *Chemistry of Atmospheres*, 3rd ed. (Oxford University Press, New York, 2000).

[2] *Combustion Chemistry*, edited by W. C. Gardiner, Jr. (Springer, New York, 1984).

[3] A. Miyoshi, H. Matsui, and N. Washida, J. Chem. Phys. **100**, 3532 (1994).

[4] C. D. Jonah, W. A. Mulac, and P. Zeglinski, J. Phys. Chem. **88**, 4100 (1984).

[5] D. Fulle, H. F. Hamann, H. Hippler, and J. Troe, J. Chem. Phys. **105**, 983 (1996).

[6] A. R. Ravishankara and R. L. Thompson, Chem. Phys. Lett. **99**, 377 (1983).

[7] V. Lissianski, H. Yang, Z. Qin, M. R. Mueller, and K. S. Shin, Chem. Phys. Lett. **240**, 57 (1995).

[8] M. S. Wooldridge, R. K. Hanson, and C. T. Bowman, Int. J. Chem. Kinet. **28**, 361 (1996).

[9] M. S. Wooldridge, R. K. Hanson, and C. T. Bowman, *25th International Symposium on Combustion, University of California at Irvine, Irvine, CA, 13 July–5 August 1994* (The Combustion Institute, Pittsburgh, PA, 1994), pp. 741–748.

[10] T. A. Brabbs, F. E. Belles, and R. S. Brokaw, *13th International Symposium on Combustion, University of Utah, 23–29 August 1970* (The Combustion Institute, Pittsburgh, PA, 1971), pp. 129–136.

[11] M. J. Frost, P. Sharkey, and I. W. M. Smith, J. Phys. Chem. **97**, 12254 (1993).

[12] M. J. Frost, P. Sharkey, and I. W. M. Smith, Faraday Discuss. Chem. Soc. **91**, 305 (1991).

[13] A. J. Hynes, P. H. Wine, and A. R. Ravishankara, J. Geophys. Res. **91**, 11815 (1986).

[14] A. Hofzumahaus and F. Stuhl, Ber. Bunsenges. Phys. Chem. **88**, 557 (1984).

[15] R. Forster, M. Frost, D. Fulle, H. F. Hamann, H. Hippler, A. Schlepegrell, and J. Troe, J. Chem. Phys. **103**, 2949 (1995).

[16] N. F. Scherer, C. Sipes, R. B. Bernstein, and A. H. Zewail, J. Chem. Phys. **92**, 5239 (1990).

[17] D. M. Golden, G. P. Smith, A. B. McEwen *et al.*, J. Phys. Chem. A **102**, 8598 (1998).

[18] H. G. Yu, J. T. Muckerman, and T. J. Sears, Chem. Phys. Lett. **349**, 547 (2001).

[19] T. V. Duncan and C. E. Miller, J. Chem. Phys. **113**, 5138 (2000).

[20] R. Valero and G. J. Kroes, J. Chem. Phys. **117**, 8736 (2002).

[21] R. S. Zhu, E. G. W. Diau, M. C. Lin, and A. M. Mebel, J. Phys. Chem. A **105**, 11249 (2001).

[22] J. P. Senosiain, C. B. Musgrave, and D. M. Golden, Int. J. Chem. Kinet. **35**, 464 (2003).

[23] R. Valero, D. A. McCormack, and G. J. Kroes, J. Chem. Phys. **120**, 4263 (2004).

[24] M. J. Lakin, D. Troya, G. C. Schatz, and L. B. Harding, J. Chem. Phys. **119**, 5848 (2003).

[25] D. M. Medvedev, S. K. Gray, E. M. Goldfield, M. J. Lakin, D. Troya, and G. C. Schatz, J. Chem. Phys. **120**, 1231 (2004).

[26] K. L. Feilberg, G. D. Billing, and M. S. Johnson, J. Phys. Chem. A **105**, 11171 (2001).

[27] J. P. Senosiain, S. J. Klippenstein, and J. A. Miller, Proc. Combust. Inst. **30**, 945 (2005).

[28] J. Troe, Proc. Combust. Inst. **27**, 167 (1998).

[29] C. M. Stevens, L. Kaplan, R. Gorse, S. Durkee, M. Compton, S. Cohen, and K. Bielling, Int. J. Chem. Kinet. **12**, 935 (1980).

[30] H. G. J. Smit, A. Volz, D. H. Ehhalt, and H. Knappe, in *Stable Isotopes*, edited by H. Schmidt, H. Förstel, and K. Heinzinger (Elsevier, New York, 1982), pp. 147–152.

[31] T. Röckmann, C. A. M. Brenninkmeijer, G. Saueressig, P. Bergamaschi, J. N. Crowley, H. Fischer, and P. J. Crutzen, Science **281**, 544 (1998).

[32] K. L. Feilberg, S. R. Sellevag, C. J. Nielsen, D. W. T. Griffith, and M. S. Johnson, Phys. Chem. Chem. Phys. **4**, 4687 (2002).

[33] K. L. Feilberg, M. S. Johnson, and C. J. Nielsen, Phys. Chem. Chem. Phys. **11**, 2318 (2005).

[34] B. Ruscic, M. Schwarz, and J. Berkowitz, J. Chem. Phys. **91**, 6780 (1989).

[35] B. Ruscic and M. Litorja, Chem. Phys. Lett. **316**, 45 (2000).

[36] M. E. Jacox, J. Chem. Phys. **88**, 4598 (1988).

[37] J. T. Petty, J. A. Harrison, and C. B. Moore, J. Phys. Chem. **97**, 11194 (1993).

[38] J. Nolte, J. Grussdorf, E. Temps, and H. G. Wagner, Z. Naturforsch., A: Phys. Sci. **48**, 1234 (1993).

[39] G. Poggi and J. S. Francisco, J. Chem. Phys. **120**, 5073 (2004).

[40] G. Paraskevopoulos and R. S. Irwin, J. Chem. Phys. **80**, 259 (1984).

[41] G. Paraskevopoulos and R. S. Irwin, Chem. Phys. Lett. **93**, 138 (1982).

[42] J. Bigeleisen and M. G. Mayer, J. Chem. Phys. **15**, 261 (1947).

[43] D. H. Volman, J. Photochem. Photobiol., A **100**, 1 (1996).

[44] The vibrational frequencies and rotational constants of all stationary structures are calculated by the CCSD(T) method with the 6-31G(d,p) basis set.

[45] With the same values of α for various bath gases, the difference of calculated rates by using the rotational constants and vibrational frequencies between CC and Yu *et al.* (Ref. 18) is less than 1% as pressure is under 1000 torr. The values of carbon-isotope fractionation by CC is higher than the other by around 1 per mil at low pressure and around 2.5 per mil at 1 atm. Thus, the structures and vibrational frequencies by CC is good enough for this study.

[46] Recent high-level *ab initio* calculations are considered in the energies of stationary points in the LTSH potential. Since the imaginary frequency of TS_d in the LTSH potential is too low, the vibrational frequencies and rotational constants of all stationary structures are calculated by *ab initio* methods. Only the energies without ZPE corrections of the stationary structures are obtained from the LTSH potential.

[47] M. J. Frisch, G. W. Trucks, H. B. Schlegel *et al.*, GAUSSIAN 98, revision A.11.3, Gaussian, Inc., Pittsburgh, PA, 2002.

[48] The tunneling corrections for microcanonical systems were described by Marcus (Ref. 50). Instead of the usual sum over states $N(EJ)$, $\Sigma 1$, one sums over the TS-dependent tunneling over probabilities $\Sigma\kappa(\epsilon J)$ for $\epsilon < E$. A similar prescription is given by Miller (Ref. 51). The details about evaluating the tunneling probability are described in Sec. II C.

[49] Including the loose transition structure forming $\mathrm{OH}\cdots\mathrm{CO}$, the rates are decreased by about 5% at room temperature. It has negligible effects on the rate constant ratios for OH and OD reacting with CO at pressures below 1000 torr. The difference in fractionation of the carbon isotope calculated with and without the additional loose transition structure in the calculation for the present pressures 0–1000 torr and room-temperature regions is about 0.5 per mil.

[50] R. A. Marcus, J. Chem. Phys. **45**, 2138 (1966).

[51] W. H. Miller, J. Am. Chem. Soc. **101**, 6810 (1979).

[52] J. Troe, J. Chem. Phys. **79**, 6017 (1983).

[53] The rotational barrier was obtained from the high-level *ab initio* calculations by Yu *et al.* (Ref. 18).

[54] The sharp barrier at TS_d is not included in any analytical potential functions by Schatz *et al.* (Refs. 25 and 46).

[55] R. A. Marcus, J. Chem. Phys. **45**, 4500 (1966).

[56] C. Eckart, Phys. Rev. **35**, 1303 (1930).

[57] Y. Q. Gao and R. A. Marcus, J. Chem. Phys. **114**, 9807 (2001).

[58] Y. Q. Gao and R. A. Marcus, J. Chem. Phys. **116**, 137 (2002).

[59] As the exponential model is used to test the convergence, the results of grain size in 5 and 10 cm^{-1} are the same.

[60] R. A. Marcus, J. Chem. Phys. **62**, 1372 (1975).

[61] G. Worry and R. A. Marcus, J. Chem. Phys. **67**, 1636 (1977).

[62] S. J. Klippenstein and R. A. Marcus, J. Chem. Phys. **93**, 2418 (1990).

[63] M. Brouard, D. W. Hughes, K. S. Kalogerakis, and J. P. Simons, J. Phys. Chem. A **102**, 9559 (1998).

[64] M. Brouard, D. W. Hughes, K. S. Kalogerakis, and J. P. Simons, J. Chem. Phys. **112**, 4557 (2000).

[65] M. Brouard, I. Burak, D. W. Hughes, K. S. Kalogerakis, J. P. Simons, and V. Stavros, J. Chem. Phys. **113**, 3173 (2000).

[66] The experimental rate constants at low pressure near 300 K are in the range of $(1.3-1.8)\times 10^{-13}\ \mathrm{cm}^3\ \mathrm{molecule}^{-1}\ \mathrm{s}^{-1}$. The rate constant is chosen by a best fit to the pressure dependence at 300 K.

[67] The HO–CO distance of TS_a optimized by B3LYP is too long, which is around 2.99 Å in B3LYP, so doubtful frequencies would be expected. A similar result happened when Lin used B3LYP/6-311G(d,p) to calculate TS_a. (Ref. 21).

[68] H. S. Johnston and J. Heicklen, J. Phys. Chem. **66**, 532 (1962).

Chapter 2

On the Theory of the Reaction Rate of Vibrationally Excited CO Molecules with OH Radicals

[This chapter appeared in the *Journal of Chemical Physics* **124**, 024306 (2006).]

THE JOURNAL OF CHEMICAL PHYSICS **124**, 024306 (2006)

On the theory of the reaction rate of vibrationally excited CO molecules with OH radicals

Wei-Chen Chen and R. A. Marcus[a)]
Noyes Laboratory 127-72, California Institute of Technology, Pasadena, California 91125

(Received 13 October 2005; accepted 10 November 2005; published online 10 January 2006)

The dependence of the rate of the reaction $CO+OH \rightarrow H+CO_2$ on the CO-vibrational excitation is treated here theoretically. Both the Rice-Ramsperger-Kassel-Marcus (RRKM) rate constant k_{RRKM} and a nonstatistical modification k_{non} [W.-C. Chen and R. A. Marcus, J. Chem. Phys. **123**, 094307 (2005).] are used in the analysis. The experimentally measured rate constant shows an apparent (large error bars) decrease with increasing CO-vibrational temperature T_v over the range of T_v's studied, 298–1800 K. Both $k_{RRKM}(T_v)$ and $k_{non}(T_v)$ show the same trend over the T_v-range studied, but the $k_{non}(T_v)$ vs T_v plot shows a larger effect. The various trends can be understood in simple terms. The calculated rate constant k^v decreases with increasing CO vibrational quantum number v, on going from $v=0$ to $v=1$, by factors of 1.5 and 3 in the RRKM and nonstatistical calculations, respectively. It then increases when v is increased further. These results can be regarded as a prediction when v state-selected rate constants become available. © *2006 American Institute of Physics*. [DOI: 10.1063/1.2148408]

I. INTRODUCTION

The conversion of CO to CO_2 by reaction with an OH radical is one of the principal oxidation reactions in the atmosphere[1] and has been the subject of many experimental[2–16] and theoretical studies.[16–28] The currently accepted reaction mechanism involves a CO and OH bimolecular association to form a vibrationally excited *trans*-$HOCO^*$ radical, followed by a *cis-trans* isomerization. There are also the back reaction to reform the reactants, the forward reaction leading to $H+CO_2$ and the collisional stabilization of $HOCO^*$. In the presence of oxygen both the $H+CO_2$ and the stabilized HOCO form the same products, HO_2 and CO_2.[29–31]

The non-Arrhenius behavior for the thermal rate constant has been extensively studied in experiments and theory.[3–12,16,20,21,26–28] It involves a nearly activationless barrier in the entrance channel $CO+OH \rightarrow HOCO^*$ and also in the exit channel $HOCO^* \rightarrow H+CO_2$. There is a large H-tunneling effect in the latter, and at low temperatures there is even tunneling in the former. In the Arrhenius plot of $\ln k_{rate}$ vs $1/T$ the slope increases significantly at temperatures higher than 500 K, reflecting the actual energy barrier that exists when H-tunneling becomes less important.

In a novel experiment Dreier and Wolfrum[32] formed vibrationally excited CO molecules by collision of CO with vibrationally excited N_2. The latter was obtained by microwave discharge in an N_2/Ar mixture to form excited $N(^4S)$, which then reacted with NO. The vibrational temperature T_v of the CO molecules was determined from the optical absorption spectrum of the vibrational-rotational states of $CO(v,J)$ at or below 1800 K. On the other hand, the rotational and translational temperatures remained at room temperature. The OH radicals were obtained from a discharge in H_2/Ar to yield H, which then further reacted with NO_2 to form OH.

Under these conditions the rate constant appeared to decrease by about 15% from its room-temperature value when T_v was increased to 1800 K, though with large error bars (the results of many measurements). We treat this behavior in the present article and make predictions for v state-selected experiments, where the effects would be considerably larger.

The calculational method is summarized in Sec. II, and the results are given and discussed in Sec. III.

II. THEORY AND CALCULATION METHOD

The key aspects of the calculations are noted below, with more details being given in the earlier paper.[28]

A. Kinetic scheme and rate constants

Because the energy barrier between *cis*- and *trans*-HOCO is much lower than the energy barriers in the entrance and exit channels, we can assume as before that the *cis* and *trans* energetic intermediates $HOCO^*$ easily interconvert. The pressure in the experiments was about 4 mbars,[32] and so collisional stabilization by bath gases can be neglected. At zero pressure, the kinetic scheme for the vibrationally excited CO molecules reacting with the OH radicals at an energy E and total angular momentum J is given by

$$CO^v + OH \xrightarrow{k_1^v(EJ)} HOCO^*(EJ), \tag{1}$$

$$HOCO^*(EJ) \xrightarrow{k_{-1}(EJ)} CO + OH, \tag{2}$$

[a)] Electronic mail: ram@caltech.edu

$$\mathrm{HOCO}^*(EJ) \xrightarrow{k_2(EJ)} \mathrm{H}+\mathrm{CO}_2. \tag{3}$$

The rate constant for the forward reaction in Eq. (1) is denoted by $k_1^v(EJ)$ when the CO vibration is initially in the quantum state v. The rate constant $k_{-1}(EJ)$ in Eq. (2) yields CO having any CO vibrational quantum number and not necessarily having the initial v. The rate constants $k_1^v(EJ), k_{-1}(EJ)$, and $k_2(EJ)$ are E and J dependent. The limiting low-pressure steady-state rate constant k^v for any specified initial CO vibrational quantum state v is given by

$$k^v = \sum_J \int_E \frac{k_1^v(EJ)k_2(EJ)}{k_{-1}(EJ)+k_2(EJ)} dE. \tag{4}$$

In terms of numbers of quantum states of the two transition states, this low-pressure rate constant at any given v is

$$k^v = \sum_J \int_E \frac{N_1^v(EJ)N_2(EJ)}{hQ[N_1(EJ)+N_2(EJ)]} dE, \tag{5}$$

where Q is the partition function of the OH and CO when CO is in the specified initial vibrational state v. $N_1^v(EJ), N_1(EJ)$, and $N_2(EJ)$ denote the sums of quantum states of the transition states for the entrance at specified v, entrance at all accessible v's, and exit channels, respectively, for the energy E and total angular momentum J. When $v \geqslant 1$ the $N_1(EJ)$ for the backward reaction in the entrance channel is larger than $N_1^v(EJ)$ because the energy redistribution in the intermediate HOCO* yields a large number of quantum states in $N_1(EJ)$. Each sum of states includes a tunneling correction for a microcanonical ensemble[33,34]

$$N_i(EJ) = \int_{E_{\min}}^{E} \kappa_i(E')\rho_i((E-E')J)dE' \quad (i=1,2) \tag{6}$$

and

$$N_1^v(EJ) = \int_{E_{\min}}^{E} \kappa_1(E')\rho_1^v((E-E')J)dE', \tag{7}$$

where $E_{\min}$ denotes the energy minimum in HOCO*. In Eq. (7) for $N_1^v(EJ)$, unlike Eq. (7) for $N_1(EJ)$ and $N_2(EJ)$, only an energy $E-vh\nu$ is available for energy redistribution in the ρ_1^v in this transition state: We note that for the E in $N_1^v(EJ)$ in Eq. (7) one writes $E-vh\nu$. $\kappa_i(E')$ is the tunneling transmission probability at an energy E' in the tunneling coordinate. As in Ref. 28, κ_i is estimated by tunneling through a fitted Eckart potential, and $\rho_i((E-E')J)$ denotes the density of rovibrational states of the transition state i at an energy $E-E'$ and total angular momentum J.

The rate constant at the vibrational temperature T_v is then given by

$$k(T_v) = \frac{1}{Q_{\mathrm{CO}}^{\mathrm{vib}}(T_v)} \sum_v k^v \exp\left(\frac{-vh\nu}{k_B T_v}\right), \tag{8}$$

where $Q_{\mathrm{CO}}^{\mathrm{vib}}$ is the vibrational partition function of the CO molecules at a vibrational temperature T_v.

The potential-energy surface used is the same as that employed in the earlier paper,[28] with the same two adjusted parameters and the same refined vibrational frequencies of all stationary structures. In the calculation the number of quantum states of the internal rotation about the HO–CO bond in the entrance channel was treated as before as a one-dimensional hindered rotor.

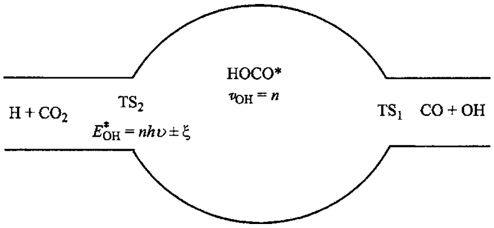

FIG. 1. Formation of CO+OH from H+CO$_2$. All n's are possible but the difference in energy in the OH coordinate between TS$_2$ and HOCO* is $\pm\xi$. In TS$_2$ the OH bond stretching energy is $nh\nu\pm\xi$. In HOCO* it is $nh\nu$ for each n.

B. Nonstatistical modification of RRKM

We recall previous studies where the reaction CO+OH $\rightarrow$CO$_2$+H showed a nonstatistical behavior[35–40] in both bulk gas-phase and molecular-beam studies of the reverse reaction, H+CO$_2\rightarrow$OH+CO. It was observed that the vibrational excitation of the CO product of that reaction was below that expected from statistical theory for the HOCO* intermediate. There appear to be various nonstatistical components. In the present nonstatistical modification of the Rice-Ramsperger-Kassel-Marcus (RRKM) theory, as in Ref. 28, we simply assume that the intramolecular energy transfer between the high-frequency OH-stretching vibration in the HOCO* and the other (lower-frequency) modes is not rapid enough to yield an intramolecular statistical distribution during the typical lifetime of the HOCO* before the latter dissociates into H+CO$_2$.

In our earlier study[28] a nonstatistical modification of the RRKM theory was also used to treat the reaction, a treatment which included H- and C-isotope effects. The nonstatistical modification removed an existing discrepancy in the literature[26,41] between results of experiment and the RRKM theory for the H-/D-isotope effect at low pressures. It reproduced the non-Arrhenius behavior for the rate constants at high and low temperatures.

In this nonstatistical modification[28] of the RRKM theory, it was assumed that only a limited amount of energy ξ can be transferred into or out of the OH-stretching vibration just before the HOCO* enters the transition state TS$_2$, from which it dissociates into H+CO$_2$. That is, there is restricted energy transfer between the HOCO* phase space and the phase space of TS$_2$, as depicted schematically in Fig. 1 for the reverse reaction. The value assumed[28] for ξ, 4000 cm^{-1}, is a little larger than the energy of one OH-stretching quantum. Therefore, the amount of energy in the H-dissociation motion in the TS$_2$ produced from an intermediate HOCO* with n quanta in the OH vibration is limited in TS$_2$ to an energy in $nh\nu\pm\xi$ interval, as shown in Fig. 2. The dissociation rate constant $k_2(EJ)$ at a total energy E and angular momentum J of HOCO* thus includes a partitioning over the quantum number n of the OH-stretching vibration in

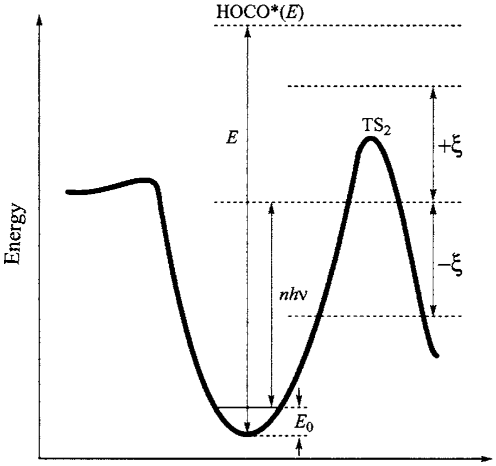

FIG. 2. Schematic profile of the relation between the HOCO* with total energy E including n quanta in the OH stretching and the OH energy interval $nh\nu \pm \xi$, permitting the entrance into TS$_2$ in the nonstatistical model.

HOCO*. The allowed values of n are $0, 1, \ldots, n_{\max}$, a total of $(n_{\max}+1)$ values, where $n_{\max}$ is the maximum allowed quantum number of the OH-stretching vibration in the HOCO* at the given E and J. The $N_2(EJ)$ in Eq. (5) is thus replaced by the weighted sum,

$$N_2^{\text{non}}(EJ) = \frac{1}{(n_{\max}+1)} \sum_{n=0}^{n_{\max}} N_2^n(EJ), \tag{9}$$

where in virtue of the definition of ξ we have

$$N_2^n(EJ) = \int_{\max[E_0+nh\nu-\xi,E_0]}^{\min[E_0+nh\nu+\xi,E]} \kappa_2(E')_{\rho_2}((E-E')J)dE'. \tag{10}$$

The $\kappa_2(E')$ and $\rho_2((E-E')J)$ are the same as those in Eq. (6), ν in Eq. (10) is the OH-stretching frequency of *cis*-HOCO, and the lower and upper bounds of E are as indicated. E_0 is the potential energy plus the zero-point energy in HOCO*. The upper and lower bounds of E in Eq. (10) limit the amount of energy ξ transferring between other modes and the OH-stretching motion in TS$_2$. When ξ approaches infinity, the energy transfer between modes is much faster than the lifetime of intermediates and the number of states used in the conventional RRKM is obtained at any n, i.e., $N_2^n(EJ) = N_2(EJ)$.

Using Eq. (9) and the rate constants $k_2^n(EJ)$ for the reaction from the intermediate HOCO* with n quanta in the OH-stretching mode, the conventional RRKM rate constant at specified E and J can be expanded as

$$k(EJ) = \frac{N_2(EJ)}{h\rho(EJ)} = \frac{1}{n_{\max}+1} \sum_{0}^{n_{\max}} \frac{\rho^n(EJ)}{\rho(EJ)} k_2^n(EJ), \tag{11}$$

since $k_n(EJ) = N_2^n(EJ)/h\rho^n(EJ)$, where $\rho^n(EJ)$ is the density of states of the HOCO* at OH vibrational state n. Equation (11) is Eq. (C3) (Ref. 42) in Ref. 28. The rate constant with nonstatistical modification can be obtained by using Eqs. (10) and (11) with a finite value of ξ.

TABLE I. The rate constants at the CO vibrational quantum number v at 298 K. The unit is 10^{-13} cm^3 molecule^{-1} s^{-1}.

k^v	RRKM	Nonstatistical	$K_{\text{non}}^v / K_{\text{RRKM}}^v$	Expt. (Ref. 32)
$v=0$	1.49	1.53	1.03	⋯
$v=1$	0.97	0.54	0.56	⋯
$v=2$	1.50	0.96	0.64	⋯
$v=3$	2.16	1.21	0.56	⋯
$v=4$	2.96	1.48	0.50	⋯
$k_{\text{total}}(T_v=298\ K)$	1.49	1.53		1.51 ± 0.6
$k_{\text{total}}(T_v=1400\ K)$	1.44	1.42		1.36 ± 0.5
$k_{\text{total}}(T_v=1800\ K)$	1.41	1.37		1.30 ± 0.5

III. RESULTS AND DISCUSSION

The calculated rate constants are listed in Table I as a function of the initial CO vibrational quantum state v. In the RRKM theory and the nonstatistical modification, the rate constant first decreases by about factors of 1.5 and 3, respectively, on going from $v=0$ to $v=1$ and then increases with further increase in v. It is seen that v state-selected experiments, particularly $v=0$ and 1, would be helpful in clarifying the importance of nonstatistical effects in the reaction.

This calculated dependence of the rate constants on v can be understood as follows: When $v=0$ at 298 K we have $N_1(EJ) > N_2(EJ)$ for a typical E (about 500 cm^{-1} at room temperature for $v=0$) and J, as seen in Fig. 3, because the effective barrier in the exit channel is slightly higher than that in the entrance channel. That is, the low-pressure reaction-rate constant in Eq. (5) has its main bottleneck in the exit channel transition state. We also have $N_1^{v=0}(EJ) \approx N_1(EJ)$since very few CO's are vibrationally excited in returning to CO+OH via the entrance channel transition state TS$_1$. We note next that integration over E for any v begins at $E = vh\nu$, i.e., it is an integration over E' from 0 to ∞, where $E' = E - vh\nu$. When $v=1, N_1^{v=1}(EJ)$ is about equal to

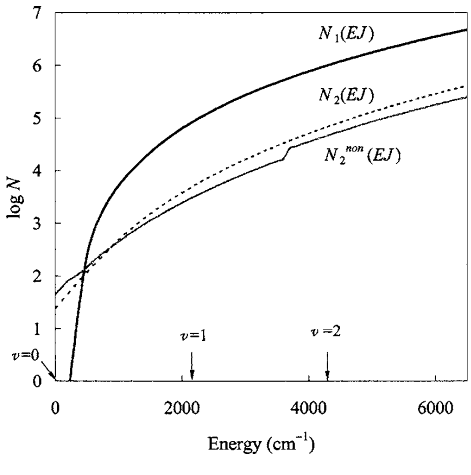

FIG. 3. The sums of states $N_1(EJ)$, $N_2(EJ)$, and $N_2^{\text{non}}(EJ)$ are plotted vs E. The chosen J state shown on this plot is the most probable J at room temperature. The plots of $N_1^{v=0}(EJ)$ and of $N_1(EJ)$ overlap in the energy range at current interest. The vibrational energy of CO at $v=1,2$ is indicated in the abscissa. In $N_2^{\text{non}}(EJ)$ the bump around 3600 cm^{-1} is due to the increase of accessible OH-vibrational states in $N_2^{\text{non}}(EJ)$.

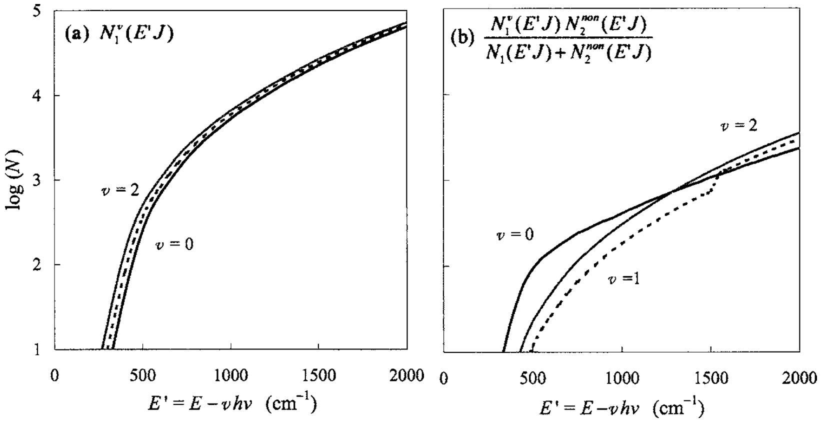

FIG. 4. The sums of states $N_1^v(E'J)$ and $[N_1^v(E'J)N_2^{\text{non}}(E'J)]/[N_1(E'J)+N_2^{\text{non}}(E'J)]$ obtained with the nonstatistical theory are plotted vs E', total energy E minus $vh\nu$ at the specified v. The solid black, dotted black, and the solid gray lines denote the plots for $v=0,1$, and 2, respectively. The chosen J state shown on this plot is the most probable J at room temperature. In (b) the small bump for $v=1$ around 1500 cm^{-1} is due to the increase of accessible OH-vibrational states in $N_2^{\text{non}}(EJ)$.

$N_1^{v=0}((E-h\nu)J)$, as seen in Fig. 4(a), but $N_1(EJ)$ and $N_2(EJ)$ are enhanced significantly over their values at $E-h\nu$. The increase in $N_1(EJ)$ is larger than that in $N_2(EJ)$, as seen in Fig. 3, because much of the energy in TS_2 goes into overcoming the need for tunneling rather than only in increasing the number of quantum states. Thereby, the key quantity in Eq. (5), $[N_1^v N_2]/[N_1+N_2]$, decreases when v is increased from 0 to 1, as seen in Fig. 4(b). At higher v, and hence higher energies, $N_2(EJ)$ increases with E more rapidly than does $N_1(EJ)$ (Fig. 5), perhaps because TS_1 has more rotations (hindered) than TS_2, and the number of quantum states increases less rapidly for rotations (one squared term per coordinate) than for vibrations (two squared terms per coordinate). Thus, for $v=1,2,\ldots$, the ratio $N_2(EJ)/[N_1(EJ)+N_2(EJ)]$ increases with energy (Fig. 5), and so the rate constants also increase with increasing v.

The present calculated result for $v=1$ compared with $v=0$ is different from the classical trajectory results of Lakin *et al.*,[23] but the trend from $v=1$ to $v=2$ is in the same direction: Their calculation showed a cross section for the reaction that increased monotonically when v was increased from 0 to 2. The difference may have several origins, one being the absence of the quantum-mechanical tunneling in the exit channel transition state when classical trajectories are used. The consequences of this tunneling effect produce the decrease in k^v on going from $v=0$ to $v=1$.

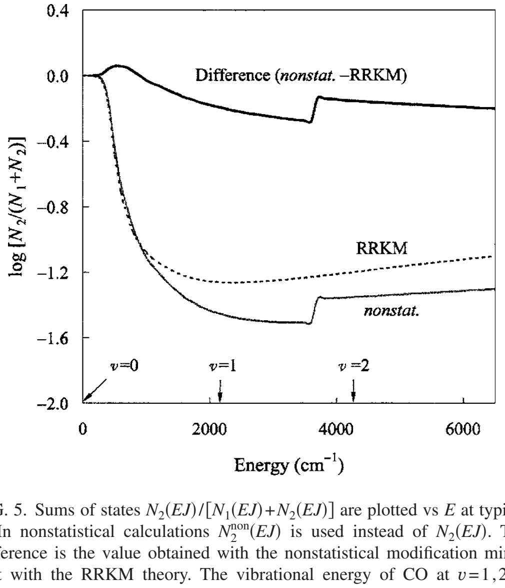

FIG. 5. Sums of states $N_2(EJ)/[N_1(EJ)+N_2(EJ)]$ are plotted vs E at typical J. In nonstatistical calculations $N_2^{\text{non}}(EJ)$ is used instead of $N_2(EJ)$. The difference is the value obtained with the nonstatistical modification minus that with the RRKM theory. The vibrational energy of CO at $v=1,2$ is indicated in the abscissa. In the nonstatistical calculations and the difference, the small bump around 3600 cm^{-1} is due to the increase of accessible OH-vibrational states in $N_2^{\text{non}}(EJ)$.

Because of the limited amount of internal energy transfer in the exit channel in the nonstatistical model [Eqs. (9) and (10)], the energy dependence of $N_2^{\text{non}}(EJ)$ is smaller than that of $N_2(EJ)$ of the RRKM theory. Thereby, the nonstatistical model has a weaker energy dependence of $[N_1^v N_2^{\text{non}}]/[N_1+N_2^{\text{non}}]$ on v, and so the enhancement of $N_2^{\text{non}}(EJ)$ noted above with increase in v is less than that of $N_2(EJ)$, as seen in Fig. 3, and so the decrease in the k^v value from $v=0$ to $v=1$ is larger.

Since the calculated $k^{v=1}$ value is smaller than $k^{v=0}$, the rate constants at higher vibrational temperatures are lower than the value at room temperature for the vibrational temperatures studied, 298, 1400, and 1800 K, as seen in Fig. 6. In the experiment[32] the rate constant in this range of T_v's is smaller than the room-temperature value by 10% at 1400 K and 15% at 1800 K (but with large error bars). The calculated rate constants at the two temperatures, $k_{\text{total}}(T_v=1400)$ and $k_{\text{total}}(T_v=1800)$, are lower than $k_{\text{total}}(T_v=298)$ by 7% and 12%, respectively, in the modified statistical theory and by 3% and 5% in the unmodified RRKM theory. The trend is seen in Fig. 6.

We also note that quantum-mechanical calculations or perhaps classical trajectories can test the validity of the simple nonstatistical model assumed in Fig. 2. In passing we also note one property seen in Fig. 3 not needed in the discussion of the effect of v at room temperature but of interest at low temperature: At energies below ~300 cm^{-1} we have $N_1 < N_2$. Its origin is that although the barrier at TS_2 is somewhat higher than at TS_1 there is so much tunneling at TS_2 that the bottleneck at these low energies now occurs at TS_1, i.e., $N_1 < N_2$.

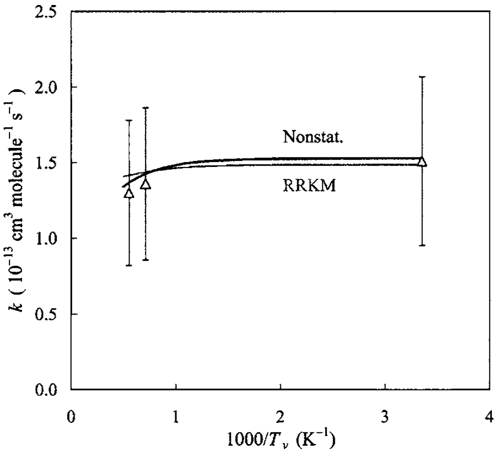

FIG. 6. Plot of rate constants vs CO-vibrational temperature T_v. The temperature for the other coordinates is 298 K. The calculated rate constants obtained with the RRKM theory and with the nonstatistical modification are shown by the gray and black lines, respectively. The open triangles and error bars are taken from the experimental data of Dreier and Wolfrum (Ref. 32).

IV. CONCLUSIONS

Both the RRKM and the nonstatistical modified theory yield a decrease in rate constant for the $OH+CO \rightarrow H+CO_2$ reaction at higher CO-vibrational temperatures. Because of the limited energy transfer rate in the nonstatistically modified theory, the effect is stronger in the modified theory than in the standard RRKM theory and is also closer to the apparent experimental results.[32] State-selected experiments as a function of v are predicted (Table I) to first decrease and then increase with increasing v and, of course, yield much larger effects than vibrationally averaged results.

ACKNOWLEDGMENT

It is a pleasure to acknowledge the support of this research by the National Science Foundation.

[1] R. P. Wayne, *Chemistry of Atmospheres*, 3rd ed. (Oxford University Press, New York, 2000).

[2] A. Miyoshi, H. Matsui, and N. Washida, J. Chem. Phys. **100**, 3532 (1994).

[3] C. D. Jonah, W. A. Mulac, and P. Zeglinski, J. Phys. Chem. **88**, 4100 (1984).

[4] D. Fulle, H. F. Hamann, H. Hippler, and J. Troe, J. Chem. Phys. **105**, 983 (1996).

[5] A. R. Ravishankara and R. L. Thompson, Chem. Phys. Lett. **99**, 377 (1983).

[6] V. Lissianski, H. Yang, Z. Qin, M. R. Mueller, and K. S. Shin, Chem. Phys. Lett. **240**, 57 (1995).

[7] M. S. Wooldridge, R. K. Hanson, and C. T. Bowman, Int. J. Chem. Kinet. **28**, 361 (1996).

[8] M. S. Wooldridge, R. K. Hanson, and C. T. Bowman, *25th International Symposium on Combustion, University of California at Irvine, Irvine, CA, 13 July-5 August 1994* (The Combustion Institute, Pittsburgh, PA, 1994), pp. 741–748.

[9] T. A. Brabbs, F. E. Belles, and R. S. Brokaw, *13th International Symposium on Combustion, University of Utah, Salt Lake City, UT, 23–29 August 1970* (The Combustion Institute, Pittsburgh, PA, 1971), pp. 129–136.

[10] M. J. Frost, P. Sharkey, and I. W. M. Smith, J. Phys. Chem. **97**, 12254 (1993).

[11] M. J. Frost, P. Sharkey, and I. W. M. Smith, Faraday Discuss. Chem. Soc. **91**, 305 (1991).

[12] A. J. Hynes, P. H. Wine, and A. R. Ravishankara, J. Geophys. Res. **91**, 11815 (1986).

[13] A. Hofzumahaus and F. Stuhl, Ber. Bunsenges. Phys. Chem. **88**, 557 (1984).

[14] R. Forster, M. Frost, D. Fulle, H. F. Hamann, H. Hippler, A. Schlepegrell, and J. Troe, J. Chem. Phys. **103**, 2949 (1995).

[15] N. F. Scherer, C. Sipes, R. B. Bernstein, and A. H. Zewail, J. Chem. Phys. **92**, 5239 (1990).

[16] D. M. Golden, G. P. Smith, A. B. McEwen, C. L. Yu, B. Eiteneer, M. Frenklach, G. L. Vaghjiani, A. R. Ravishankara, and F. P. Tully, J. Phys. Chem. A **102**, 8598 (1998).

[17] H. G. Yu, J. T. Muckerman, and T. J. Sears, Chem. Phys. Lett. **349**, 547 (2001).

[18] T. V. Duncan and C. E. Miller, J. Chem. Phys. **113**, 5138 (2000).

[19] R. Valero and G. J. Kroes, J. Chem. Phys. **117**, 8736 (2002).

[20] R. S. Zhu, E. G. W. Diau, M. C. Lin, and A. M. Mebel, J. Phys. Chem. A **105**, 11249 (2001).

[21] J. P. Senosiain, C. B. Musgrave, and D. M. Golden, Int. J. Chem. Kinet. **35**, 464 (2003).

[22] R. Valero, D. A. McCormack, and G. J. Kroes, J. Chem. Phys. **120**, 4263 (2004).

[23] M. J. Lakin, D. Troya, G. C. Schatz, and L. B. Harding, J. Chem. Phys. **119**, 5848 (2003).

[24] D. M. Medvedev, S. K. Gray, E. M. Goldfield, M. J. Lakin, D. Troya, and G. C. Schatz, J. Chem. Phys. **120**, 1231 (2004).

[25] K. L. Feilberg, G. D. Billing, and M. S. Johnson, J. Phys. Chem. A **105**, 11171 (2001).

[26] J. P. Senosiain, S. J. Klippenstein, and J. A. Miller, Proc. Combust. Inst. **30**, 945 (2005).

[27] J. Troe, *Proceedings of the Combustion Institute*, 27, 167 (1998).

[28] W.-C. Chen and R. A. Marcus, J. Chem. Phys. **123**, 094307 (2005).

[29] J. T. Petty, J. A. Harrison, and C. B. Moore, J. Phys. Chem. **97**, 11194 (1993).

[30] J. Nolte, J. Grussdorf, E. Temps, and H. G. Wagner, Z. Naturforsch., A: Phys. Sci. **48**, 1234 (1993).

[31] G. Poggi and J. S. Francisco, J. Chem. Phys. **120**, 5073 (2004).

[32] D. Dreier and J. Wolfrum, *18th International Symposium on Combustion, University of Waterloo, Canada, 17–22 August 1980* (The Combustion Institute, Pittsburgh, PA, 1981), pp. 801–809.

[33] R. A. Marcus, J. Chem. Phys. **45**, 2138 (1966).

[34] W. H. Miller, J. Am. Chem. Soc. **101**, 6810 (1979).

[35] J. K. Rice and A. P. Baronavski, J. Chem. Phys. **94**, 1106 (1991).

[36] A. Jacobs, H. -R. Volpp, and J. Wolfrum, Chem. Phys. Lett. **218**, 51 (1994).

[37] S. L. Nickolaisen, H. E. Cartland, and C. Wittig, J. Chem. Phys. **96**, 4378 (1992).

[38] M. Brouard, D. W. Hughes, K. S. Kalogerakis, and J. P. Simons, J. Phys. Chem. A **102**, 9559 (1998).

[39] M. Brouard, D. W. Hughes, K. S. Kalogerakis, and J. P. Simons, J. Chem. Phys. **112**, 4557 (2000).

[40] M. Brouard, I. Burak, D. W. Hughes, K. S. Kalogerakis, J. P. Simons, and V. Stavros, J. Chem. Phys. **113**, 3173 (2000).

[41] J. Troe, Proc. Combust. Inst. **30**, 952 (2005).

[42] There is a typographical error in Eq. (C3) in Ref. 28. The denominator in the right-hand side of the equation should read $(n_{max}+1)$ instead of n_{max}.

Chapter 3

On the Theory of the CO+OH Reaction: Tunneling Effect and the O-isotope Anomaly

[This chapter submitted to the *Journal of Chemical Physics*.]

Abstract

The kinetic oxygen isotope effect (KIE) in the $HO+CO$ reaction is different from the value expected in the Bigeleisen-Mayer formula. The possible factors influencing the small KIE in $H^{18}O+CO$ are discussed. Since these factors can differ in their sign, the calculation results are sensitive to the theoretical input. Qualitative features are described for comparing with the experimental results. An experiment that avoids a possible role of vibrationally excited OH radicals as reactants is also suggested. The effect of H-tunneling on the well-known Bigeleisen-Mayer formula for the KIE is also discussed. The results reduce to the expected from that B-M result when the tunneling is omitted.

I. INTRODUCTION

The $CO+OH \rightarrow CO_2+H$ reaction is known to be the principal reaction for oxidizing CO in the atmosphere and controlling the OH radical concentration.[1] It has been extensively studied both by experiments[2–16] and by theoretical calculations.[16–24] Our own interest in the reaction from: it having been occasionally identified as a reaction showing a "mass-independent" oxygen isotope fraction. This result appeared strange since it is unlike ozone fractionation that has a symmetry effect and whose mass-independent fractionation (MIF) has this origin. We shall see that, in fact, a three-isotope plot points to an isotopic anomaly rather than an MIF.

In our previous papers,[25,26] many experimental observations, including the pressure and temperature dependence of the reaction rate constants, and the H- and C-isotope effects, were treated using the RRKM theory and a nonstatistical modification and agreed with the experimental data. Previous evidence for a nonstatistical behavior of the reverse reaction at higher energies was seen in the molecular beam experiments of Simons and coworkers[27,28] Experimentally there is an anomalous oxygen kinetic isotope effect (KIE),[29,30] anomalous in the sense of not obeying the Bigeleisen-Mayer rule.[31,32] The present study was undertaken to explore this issue, as well as to study another aspects of the Bigeleisen-Mayer rule, namely the effect of molecular tunneling, here of H and D.

The currently accepted mechanism for the reaction is that an OH radical reacts with CO, producing a vibrationally excited energetic *trans*-HOCO*.[4,12,15,16,20,21] This step is followed by *cis*-*trans* isomerization, and the final competitive steps are the dissociation to

H and CO_2, the back reaction to OH and CO, and a collisional stabilization of HOCO*. When the pressure is increased, collisional stabilization of the energetic HOCO* competes increasingly favorably with the forward dissociation channel and the back reaction. When OH and CO react in air or oxygen, both the dissociation channel and collision stabilization lead to the same products, HO_2 and CO_2, due to the follow-up reactions of the H and HOCO with O_2.[33–35]

A theoretical treatment of the oxygen KIE has not been given previously. Kurylo and Laufer appear to be the first group who used heavy oxygen isotopes to study the reaction experimentally.[36] They produced ^{18}OH radicals photochemically photolyzing $H_2{}^{18}O$ with 184.9 nm radiation, then leaving them reacting with CO in a static cell. They reported that $C^{18}O$ was produced at low pressure, and disappeared in the presence of 760 torr of SF_6, suggesting that there was isotopic exchange between the $C^{16}O$ and the ^{18}OH, but did not report a rate constant. Using a thermal source of ^{18}OH, namely from H atoms reacting with NO_2 or F atoms reacting with H_2O in a flow tube, Greenblatt and Howard[37] did not observe a measurable isotopic exchange and concluded that the rate constant for the isotopic exchange of ^{18}OH with $C^{16}O$ was no larger than 10^{-15} cm^3 $molecule^{-1}$ s^{-1}. Thus, there are two different observations of the O-exchange although it has been suggested by the latter group that other reactions on the walls of the static cell may have caused the exchange in the Kurylo and Laufer study.[37] However, the issue has not yet been resolved in the literature. Whereas these two groups of authors studied isotopic exchange, Stevens and co-workers used mass spectroscopy and, importantly, used a photolytic source of OH radicals to study the oxygen KIE in $C^{18}O$.[29] They measured the isotopic ratios of the unreacted CO, and obtained pressure-dependent enrichment of the $^{18}O/^{16}O$ ratio over the pressure range of 150 to 800 torr.

Later experimental studies of the heavy oxygen KIE using $C^{18}O$, were made by Röckmann et al. using a photolytic source of OH radicals[30] and by Feilberg et al. using photolytic ozone reacting with water to form OH radicals.[38] The pressure-dependent fractionation results of ^{18}O by Röckmann et al. are comparable to those by Stevens et al., but differ from those of Feilberg et al.[38] The precursors generating the OH radicals differed in the two studies. The experimental conditions by Röckmann et al. are simpler, in that no ozone is added and many fewer chemical reactions contribute to the overall reaction scheme. While HO_2 may be a dominant product in the studies of Röckmann et al.[30] and Stevens et al.[29] due to the reaction of the source material H_2O_2 with OH and in principle could have interfered, the rate constant for the reaction of CO with HO_2 is extremely small, about 10^{-27} cm^3 molecule^{-1} s^{-1} at room temperature.[39] Thus, it is about 14 orders of magnitude smaller than that of CO with OH and would not interfere in the studies in references 29 and 30.

The anomalous oxygen KIE in the CO+OH reaction is examined in the present work. Our calculated result shows that the KIE in this reaction is a compromise between two opposing effects: (1) a heavy isotope favors the formation of TS_2 (the transition state from HOCO* to CO_2+H) due to an increase the number of states of a transition state relative to the partition of reactants, and (2) a light isotope (^{12}C and ^{16}O) favors the formation of TS_2 because of the reduced imaginary frequency in the tunneling reaction coordinate. The present article discusses the dominance of these two effects in various isotopomers. The calculation result shows that the carbon KIE is dominated qualitatively by the former and the oxygen KIE at CO by the latter.

The article is organized as follows: The calculational methods are outlined in section II. The results are given in section III and discussed in section IV.

II. CALCULATIONAL METHODS

The calculational methods are the same as those described previously,[25,26] and are briefly summarized here. At any energy E and total angular momentum J, we have

$$\mathrm{CO} + \mathrm{OH} \underset{k_{-1}(EJ)}{\overset{k_1(EJ)}{\rightleftharpoons}} \mathrm{HOCO}^*(EJ), \tag{1}$$

$$\mathrm{HOCO}^*(EJ) \overset{k_2(EJ)}{\longrightarrow} \mathrm{H} + \mathrm{CO}_2. \tag{2}$$

The transition states for reactions (1) and (2) are abbreviated as TS_1 and TS_2, respectively. In the kinetic scheme, the density of states of the energetic intermediate HOCO* includes density of states of the both *cis*-HOCO* and *trans*-HOCO*, since the rotational barrier for *cis-trans* conversion is far lower than the energy of reactants and a rapid conversion can be assumed. At finite pressures an additional series of kinetic equations is added:

$$\mathrm{HOCO}^*(EJ) + \mathrm{M} \overset{\omega(EJ \to E'J')}{\longrightarrow} \mathrm{HOCO}(E'J') + \mathrm{M}, \tag{3}$$

where M is a third body. The total rotational-vibrational energy E and the total angular momentum J are conserved in reaction steps (1) and (2). The rate constants are all E- and J-dependent; $\omega(EJ \to E'J')$ is the rate constant per unit E for forming HOCO at $(E'J')$ from (EJ) by collision with a third body M. The collision frequency

$\omega(EJ \rightarrow E'J')$ is factored approximately into the total collision frequency ω, the energy transfer probability $P_{E \rightarrow E'}$, and the rotational angular momentum transfer probability $P_{J \rightarrow J'}$. Thereby, the energy transfer probability is $\omega(EJ \rightarrow E'J') = \omega P_{E \rightarrow E'} P_{J \rightarrow J'}$. $P_{E \rightarrow E'}$ is approximated by a stepladder model,[40,41] in which a certain amount of energy α is transferred between the intermediate HOCO* and a bath molecule in each collision. Because of the smallness of the C and O isotope effect, it is necessary to use a fine division of energies. The use of the stepladder instead of a continuous model in this treatment of very small isotope effects saves a factor of 10 in computational time and resources, as discussed in reference 41. The α value is taken as dependent on the bath gas but independent of pressure and isotopic substitution in HOCO. The α values of various bath gases were obtained in our previous paper by best fit to the experimental data.[25] For angular momentum transfer a strong collision was assumed. Thereby, the transfer probability $P_{J \rightarrow J'}$ equals the thermal distribution of rotational states of the intermediate HOCO*, at the given temperature,[40] i.e., $P_{J \rightarrow J'} = (2J'+1)\exp(-B_J[J'(J'+1) - J(J+1)]/k_B T)/(2J+1)$, where B_J is the rotational constant of J.

The rate constants of the CO+OH reaction were calculated as a function of pressure by solving the rate equations for reactions (1)–(3) using microcanonical RRKM calculations. Tunnelling corrections for both TS$_1$ and TS$_2$, and a steady-state equation for pressure effects were included. The H-tunneling correction was estimated from a transmission through an Eckart potential[42] passing through the saddle-point. (For the given *ab initio* potential energy surfaces the TS$_2$ lies in the exit channel, and so there is little or no "corner cutting.") At room temperature the tunneling at TS$_1$ contributes about 20%

of the total rate constant.[25] An *ab initio* potential energy for the important equilibrium structures was calculated by Lin and co-workers,[20] who used the modified Gaussian-2 method (G2M). To obtain the more accurate vibrational frequencies and rotational constants for all equilibrium structures for the various isotopes we used, as before,[25,26] a coupled-cluster method,[43,44] abbreviated as CC.[45] The optimized structures and vibrational frequencies of all stationary structures are given in Table I of reference 25. In our earlier work,[25] the potential energy of TS_1 and TS_2 were shifted vertically slightly by two independent constants to match the experimental rate constants with the non-Arrhenius effect at low temperature and the energy transfer parameters used to described the pressure effect at room temperature in various bath gases. We made no further change here.

The above results are compared in appendix A with another potential energy surface for all stationary structures (LTSH by Schatz and co-workers[23,46]). The robustness was tested using other methods, as discussed in appendix A.

III. RESULTS

A. Slopes of the Three-Isotope Plot and "Mass-Independent" Fractionation

Apparently not mentioned before in the isotope reaction-rate literature is the effect of H-tunneling on the well-known three-isotope plot and the Bigeleisen-Mayer laws.[31,32] The enrichment or depletion is defined as

$$\delta\mathrm{Q} \equiv \left(\frac{(\mathrm{Q}/^{16}\mathrm{O})_{\mathrm{sample}}}{(\mathrm{Q}/^{16}\mathrm{O})_{\mathrm{standard}}} - 1 \right) \times 1000 \text{ per mil}, \tag{4}$$

where the “Q” in the equations denotes ^{17}O or ^{18}O. A plot of δ^{17}O vs δ^{18}O constitutes the well known three-isotope plot for O isotopes. According to the usual “mass-dependent” theory of Bigeleisen and Mayer,[31,32] the slope is about 0.52 for oxygen isotopes, a result well established in the experimental literature for systems with no mass-anomaly. A MIF has been defined in two ways. A technically rigorous definition is a slope of unity for the 3-isotope δ^{17}O vs δ^{18}O plot (“mass-independent”). In a second definition the deviation from mass-dependence often used is when a Δ^{17}O defined in equation (5) differs from zero:

$$\Delta^{17}\mathrm{O} \equiv \delta^{17}\mathrm{O} - 0.52 \times \delta^{18}\mathrm{O} \neq 0. \tag{5}$$

The Δ^{17}O is popularly used since it requires only a pair of (δ^{17}O, δ^{18}O) measurements, whereas a 3-isotope plot requires a whole series of measurements.

Two fractionation properties for the KIE of oxygen, εCQ and εHQ, can be defined, according as the heavy oxygen is in the CO or in the OH:

$$\varepsilon\mathrm{CQ} \equiv \left(\frac{k_{\mathrm{CO+OH}}}{k_{\mathrm{CQ+OH}}} - 1\right) \times 1000 \text{ per mil;} \tag{6}$$

$$\varepsilon\mathrm{HQ} \equiv \left(\frac{k_{\mathrm{CO+OH}}}{k_{\mathrm{CO+QH}}} - 1\right) \times 1000 \text{ per mil.} \tag{7}$$

In a kinetic-controlled reaction with a small amount of reaction, the enrichment defined in equations (6) and (7) approximately equals the fractionation defined in equation (4), i.e., $\varepsilon\mathrm{CQ} \cong \delta\mathrm{CQ}$ and $\varepsilon\mathrm{HQ} \cong \delta\mathrm{HQ}$. The experimental and calculated slopes of the three-isotope plots in the present study are listed in Table I, together with the range of fractionations Δ^{17}O of the CQ+OH reaction in two bath gases, He and N_2, at total pressures below 1000 torr. The slope of εH^{17}O vs εH^{18}O in He obtained by RRKM the-

TABLE I: Calculated and experimental slopes of the three-isotopes plots and range of Δ^{17}Os in He or N_2 at pressures between 0 and 1000 torr[a]

	RRKM (no tunneling)	RRKM	Nonstatistical	Expt.[30]
		He		
$\varepsilon C^{17}O$ vs $\varepsilon C^{18}O$	0.45	0.39	0.39	1.1[b]
$\varepsilon H^{17}O$ vs $\varepsilon H^{18}O$	0.52	0.56	0.56	—
Δ_{CQ}	0.13 to 0.75	0.20 to 0.92	0.29 to 0.98	2.3 to 3.0[b]
Δ_{QH}	1.58 to 2.11	−0.79 to −1.11	−0.96 to −1.25	—
			N_2	
$\varepsilon C^{17}O$ vs $\varepsilon C^{18}O$	—	0.36	0.36	1.6[c]
$\varepsilon H^{17}O$ vs $\varepsilon H^{18}O$	—	0.60	0.58	—
Δ_{CQ}	—	0.20 to 1.02	0.27 to 1.07	2.8 to 4.5[c]
Δ_{QH}	—	−0.80 to −1.22	−0.97 to −1.39	—

[a] The R-squared values of the linear fits are better than 0.95. The units are per mil.

[b] There are only two experimental points at 188 and 525 torr.

[c] The bath gas is N_2 or N_2+O_2. The pressures are at 188, 375, and 660 torr.

ory without including tunneling has the usual mass-dependent value, as seen in Table I. All other slopes of the fractionation show an “anomalous” mass effect, i.e., they differ from the Bigeleisen and Mayer rule. The calculated εHQ is larger than the εCQ. The deviation of the experimental result from the Bigeleisen-Mayer rule is consistent with the importance of H-tunneling in TS_2. The importance of TS_2 at low pressure supported by the H/D effect.

B. KIE for Oxygen

Only the εCQ values have been measured experimentally thus far. The $\varepsilon C^{18}O$ values in Fig. 1 calculated by the RRKM method and by a nonstatistical modification are about +4 and +3 per mil, respectively, at low pressure. As the pressure is increased, the values calculated by both models decrease monotonically to around −2 per mil at 1000 torr (Fig. 1). The calculated pressure dependence of the ^{18}O KIE in different bath gases (N_2 and He) is very similar. The robustness of the calculated ^{18}O values is seen in appendix A. All the calculated results made with the different *ab initio* methods give similar $\varepsilon C^{18}O$ values, all positive and 5 to 7 per mil, at low pressure. We consider in section IV C a qualitative explanation for the sign of this result rather than focusing on small differences in quantitative. The agreement largely rests on one key assumption; the same argument explaining why the KIE of ^{18}O and ^{13}C have opposite signs at low pressure (The possible reasons are given in appendix B.).

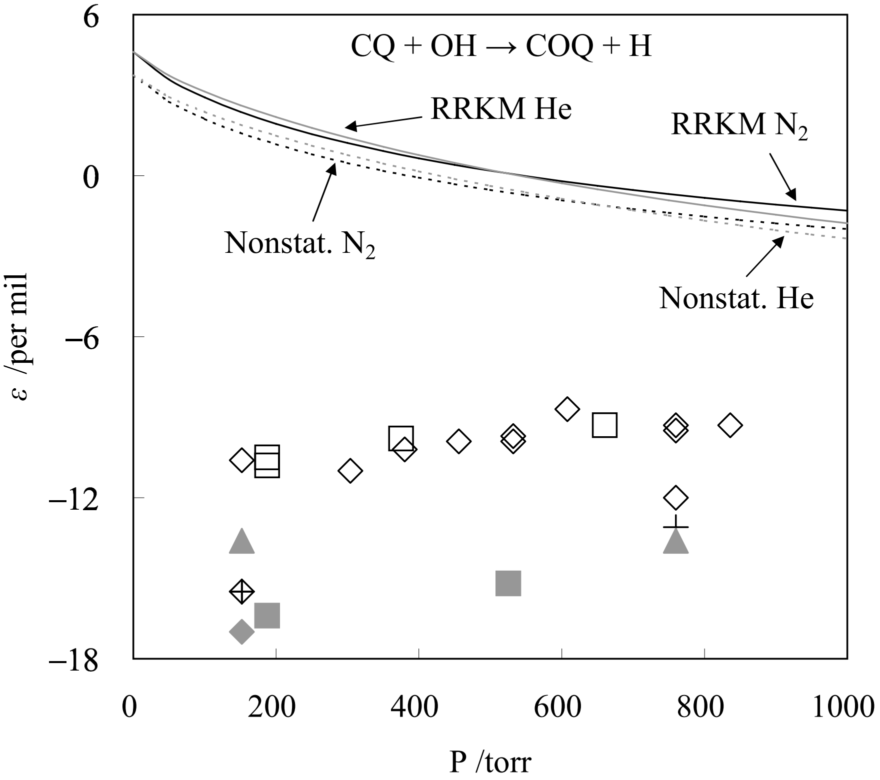

FIG. 1: $\varepsilon C^{18}O$ calculated using the RRKM method and the nonstatistical model for the OH+CO reaction as a function of total pressure. The data given by gray closed and black open squares were obtained in He (or Ar), and N_2 (or N_2+O_2), respectively, by Röckmann.[30] and by Stevens.[29]

IV. DISCUSSION

A. Mass-Dependent Effect and the Three-Isotope Plot

According to Bigeleisen's and Mayer's "mass-dependent" rule,[31,32] the expected slope of a three-isotope plot of oxygen isotopes is ~0.52. When the reaction is either a single step or consists of a preequilibrium followed by a rate determining step in the absence of H-tunneling, the usual mass-dependent Bigeleisen-Mayer isotope behavior is expected to occur. However, when there are competitive processes in a mechanism or when there is nuclear tunneling, there is no requirement that the slope have this value. The calculated slopes of $\varepsilon C^{17}O$ vs $\varepsilon C^{18}O$ and $\varepsilon H^{17}O$ vs $\varepsilon H^{18}O$ at various pressures in Table I without H-tunneling effect are seen to have smaller deviations from 0.52 than those with tunneling. The large tunneling effect in the dissociation reaction (2) thus introduces a larger anomalous mass effect in the CO+OH reaction. Such potential sources of breakdown of the rule for mass-dependent behavior, tunneling or complexity of mechanism, do not appear to have been mentioned in the literature.

The magnitude of the fractionation $\Delta^{17}O$, equation (5), is sometimes used to identify a "mass-independent" effect in reactions. However, $\Delta^{17}O$ can differ from zero for a variety of reasons, some having nothing to do with the mass-independent effect seen in ozone, as noted earlier. In Table I the calculated Δ_{OH} using RRKM without tunneling has incidentally the largest value, even though the corresponding slope in the three-isotope plot is 0.52, the "ideal" value of mass-dependent slope for the oxygen isotopes. Hence, the magnitude of $\Delta^{17}O$ appears here in the intercept of the plot. Using only

$\Delta^{17}O$ as a criterion for a "mass-independent fractionation" is convenient, but does not distinguish among alternative sources of the deviation, H-tunneling and complexity of mechanism, and is different from the current (symmetry-based) molecular basis of the mass-independent effect. In fact, even when $\Delta^{17}O$ is appreciable in Table I, the slope of the three-isotope plot can still be far from the real *mass-independent* value of unity. As a generic term, values of $\Delta^{17}O$ different from zero can be termed "*mass-anomalous,*" rather than a special class of which–those with unit slope–"*mass-independent.*"

B. The Major Facts in the KIE

The enrichment of the ^{13}C and ^{18}O at low pressure is the result of two opposing effects, as mentioned earlier and as we now elaborate on: (1) the heavy isotope tends to increase the number of states at the transition states relative to the thermally averaged partition function of the reactants and so favors the heavier isotope; (2) the tunneling through transition states favors the lighter isotope, because of its greater participation in the H-dominated tunneling coordinate. To assess the relative importance of these two factors for any set of computations, we consider also the case where transition state TS_2 is regarded as rate controlling but where tunneling is neglected. In that case only the first factor is present and the enrichment is seen in Table II to be negative. When tunneling is included, the participation of heavier oxygen isotopes in the tunneling coordinate favors the positive enrichment of the lighter oxygen isotopes in the products. However, the carbon atom is able to form more bonds with the surrounding atoms. Since the heavier carbon reduces the vibrational and rotational constants, it causes a favor of the heavier

TABLE II: Comparison between calculated RRKM fractionation with and without tunneling in the low-pressure limit[a]

	Without Tunnelling[b]	With Tunnelling
$C^{17}O$+OH	−2.30	2.60
$C^{18}O$+OH	−5.54	4.62
CO+^{17}OH	−24.62	8.58
CO+^{18}OH	−50.38	18.32
^{13}CO+OH	−59.25	−3.97

[a] Units are in per mil.

[b] There are few changes of the enrichment values as the barrier of TS_2 is lowered by 340 cm^{-1}. It shows that the enrichment is insensitive to the exact value of barrier high as long as the TS_2 is the rate-determining step.

carbon isotopomer in the reaction constant at low pressure.

C. Sources for the Oxygen KIE

To analyze the theoretically calculated $C^{18}O$ KIE, we are focusing on zero pressure, since the physical interpretation is the most transparent there. The essence of the result for the ^{18}O KIE at zero pressure is seen using the following ratio that appears in the integral over E and J for the zero-pressure rate constant:

$$k_{\mathrm{rate}}(EJ) = \frac{k_1 k_2}{k_{-1} + k_2} = \frac{N_1 N_2}{Q(N_1 + N_2)} e^{-E/k_B T}. \tag{8}$$

The variables N_1 and N_2 are the number of states of TS_1 and TS_2, respectively; and Q is the partition function for the reactants' collision pair in the center of mass system. The expression has the form of an effective number of TS states, $1/N_{eff} = 1/N_1 + 1/N_2$, a "sum of resistances." The potential energy of TS_1 and TS_2 were constrained by the non-Arrhenius behavior in a wide temperature range (83–3300 K). As discussed in reference 25, the rate constant at high temperatures is dominated by the barrier of TS_2. At room temperature the calculated thermally weighted $N_1 \simeq 3.8 N_2$.[47] Thus, in equation (8) the ratio of $N_1/(N_1 + N_2)$ is roughly unity, and then the low pressure limit of the rate constant of the reaction is given approximately by

$$k_{N_2}^{\mathrm{approx}} = \int_E \mathrm{d}E \sum_J \frac{N_2}{Q} e^{-E/k_B T}, \tag{9}$$

and so is dominated by TS_2, in which tunneling plays an important role, as discussed in the above section. The importance of TS_2 is seen in the H/D isotope effect at room temperature, which tends to a value slightly greater than 3 as the pressure tends to zero. (Theory and experiments discussed in reference 25.)

Table III it is shown that the calculated ε for ^{18}O is similar to the $\varepsilon_2^{\text{approx}}$. (The definition of the latter is similar to equations (6) and (7) but using the ratio of $k_{N_2}^{\text{approx}}$s for the two isotopomers.) Because of the dominant calculated role of N_2 in contributing to the rate constant, the calculated sign of εC^{18}O reflects primarily the effect of the heavier mass in reducing the effective tunneling mass at TS$_2$. It reduces the tunneling frequencies in TS$_2$ and hence reduces the rate constant, thus causing a positive values of the calculated εC^{18}O at low pressure in Fig. 1. Because all masses in the HOCO* contribute to the effective tunneling mass, the products tend to be enriched in the lighter isotope. Calculations in appendix C illustrate the robustness of the calculated result, a robustness understood if the key hypothesis is valid, namely that TS$_2$ is rate controlling at low pressure and room temperature. If H/D tunneling were unimportant then the calculated isotope effect would be of opposite sign, as shown in Table II.

D. Comparison of Experiments and Calculations

In both Stevens's and Röckmann's independent measurements,[29,30] the εC^{18}O values in He, Ar, or O$_2$ are about −15 per mil, while those in N$_2$ or air are about −10 per mil, as seen in Fig. 1. The pressure dependence of the εC^{18}Os is seen there to be minor. The experimental ΔCQ values obtained by Röckmann et al. are about 2.5 per mil at 200 torr and increase to about 3 per mil at 500 torr in He and to about 4.5 per mil at 900 torr in N$_2$. In an application to atmospheric problems, the effect of such an enrichment

TABLE III: Comparison between calculated fractionation $\varepsilon_1^{\text{approx}}$, $\varepsilon_2^{\text{approx}}$ and ε in the low-pressure limit[a]

	$\varepsilon_1^{\text{approx}}$	$\varepsilon_2^{\text{approx}}$	ε
^{13}CO+OH	16.33	−10.24	−3.97
C^{17}O+OH	1.50	3.35	2.60
C^{18}O+OH	−0.77	7.17	4.62
CO+^{17}OH	14.34	8.51	8.58
CO+^{18}OH	33.20	17.35	18.32

[a] Units are in per mil.

on the seasonal fractionation changes in the oxygen isotopes of the atmospheric carbon monoxide was discussed in reference 30. The calculated Δ_{CQ} values are in the range 0.2–1.1 per mil, as seen in Table I, which is slightly smaller than experimental values, 2.3–3.0 per mil.

In our calculations using both the RRKM and the nonstatistical models, the results for the calculated $\varepsilon \mathrm{C}^{18}\mathrm{O}$ values are offset from the experimental values by about +15 per mil, as seen in Fig. 1. As discussed in the above section and in the additional information in appendix C, the compact structure of TS_2 leads a well-defined transition state and to a calculated $\varepsilon \mathrm{C}^{18}\mathrm{O}$ at low pressure that is dominated by TS_2 and is positive. This calculational result is different from experiment. A possible origin of this discrepancy is discussed in the section IV E. Although the sign of $\varepsilon \mathrm{C}^{18}\mathrm{O}$ in low-pressure limit are different in calculation and experiments, both calculated and experimental of $\varepsilon \mathrm{C}^{18}\mathrm{O}$ show minor pressure dependence as pressure is varied from 0 to 1000 torr, as seen in Fig. 1.

E. A Possible Explanation of the $^{16}\mathrm{O}/^{18}\mathrm{O}$ Discrepancies and a Proposed Experiment

One possible explanation of this $^{16}\mathrm{O}/^{18}\mathrm{O}$ discrepancy is in the theory. Another possibility is that this discrepancy in the $\varepsilon \mathrm{C}^{18}\mathrm{O}$ in the CO+OH reaction is experimental, due to a nonthermal effect. In particular the OH radicals in the experiments in references 29 and 30 are formed photochemically and if they are vibrationally hot, the mass dependence of heavier oxygen isotopes in CO in the reaction would be affected, since intramolecular H-transfer reaction in the energetic HOCO* may occur. This isotope exchange effect would not change the mass dependence of carbon isotopes, and so our previous work that reproduced the sign and pressure dependence of latter would be unaffected.[25] It would also be consistent with the experiments in reference 36.

When the HOCO* has a large excess energy, an isotopic exchange of the oxygen atoms between CO and OH in the vibrationally excited HOCO* molecule becomes possible. This reorganization can reform the reactants without forming products. Two possibilities for the intramolecular H-transfer are:

$$\textit{trans}\text{-HOCQ}^* \longrightarrow \text{HCO}_2 \longrightarrow \textit{trans}\text{-OCQH}^*, \tag{10}$$

$$\textit{cis}\text{-HOCQ}^* \longrightarrow \textit{cis}\text{-OCQH}^*. \tag{11}$$

In reaction (10) the intermediate HCO_2 has the hydrogen atom close to the carbon atom instead of an oxygen atom, but might occur by "roaming." Reaction (10) recalls the new "roaming" H-atom mechanism seen in the photodissociation of formaldehyde.[48–50] Although when zero-point energy is not included reaction (10) had a shallow well, calculated as 840 cm^{-1}, but the zero-point energy of HCO_2 makes the effective well disappear.[20] Reaction (11) is a direct intramolecular H-transfer reaction from one oxygen atom to the other, possible for the *cis* geometry but not for the *trans*.

The calculated geometries and vibrational frequencies of the structures in reactions (10) and (11) are listed in Table IV. In our *ab initio* CC calculations, relative to the separated reactants, the barrier of reaction (10) without zero-point corrections is about 3500 cm^{-1}, and that of reaction (11) is more than 8000 cm^{-1}, so only reaction (10) needs to be considered in an intramolecular mechanism. The barrier in reaction (10)

TABLE IV: CC-calculated geometries and vibrational frequencies of the transition structures of normal isotopes in Reactions (10) and (11)[a]

	Reaction (10)	Reaction (11)
R_{OH}	1.242	1.337
R_{CO}	1.318	1.266
R_{CQ}	1.191	1.266
θ_{HOC}	61.30	68.25
θ_{OCQ}	142.69	116.35
d_{HOCQ}	180.0	0.0
ν_1	$1952i$	$2257i$
ν_2	496	840
ν_3	666	1049
ν_4	1147	1328
ν_5	1862	1658
ν_6	2233	2044

[a] The units are in Å for bond length, in degree for angles and dihedral angles, and in cm^{-1} for vibrational frequencies.

has a large value of the imaginary frequency with H-transfer, and so both tunneling and dynamic effects would be important when the internal energy of HOCO* is high enough for reaction (10) to occur. When thermalized OH radicals at room temperature are used, the calculated rate constant for forming HCO_2 is less than 10^{-17} cm^3 $molecule^{-1}$ s^{-1}, reaction (10) would contribute only about 0.1 per mil to the ε of the CO+OH reaction so be negligible.

In the experiments of Kurylo and Laufer,[36] oxygen isotopic exchange of OH and CO was reported in the depleted reactants at low pressure. Due to the photolysis used to generate OH radicals, some of the radicals may be vibrationally hot when they react later with CO. Since HOCO* is now at a higher energy, the reaction rate of the intramolecular hydrogen exchange, reaction (10), could be enhanced. This presumption is consistent with Kurylo and Laufer's observation,[36] which implies H-transfer reaction involving in the CO+OH reaction at low pressure. In contrast to Kurylo and Laufer's experiment, there was no observable H-transfer reaction in Greenblatt and Howard's study,[37] but in the latter the OH radicals were generated by chemical reactions rather than by photolysis.

The OH radicals in both Stevens's and Röckmann's experiments were generate by photolysis of H_2O_2 with an Hg or Xe lamp,[29,30] so the resulting OH radicals may have excess vibrational energy. Even if the excess energy results in the reaction rates of hydrogen transfer of only about 1.5% of the rate of the ordinary CO+OH reaction, namely has a rate constant of 2×10^{-15} to 3×10^{-15} cm^3 $molecule^{-1}$ s^{-1}, it would decrease the $\varepsilon C^{18}O$ values in the present calculations to values nearly the same as those in the experimental results, and would also change the Δ_{CO} value to about 7 per mil, and so be of the same order as the experimental value. Thus, new measurements of the $\varepsilon C^{18}O$ and Δ_{CO} using a thermalized source of OH could offer useful insight into this issue and also resolve the difference between the experiments of Stevens and Röckmann on one hand and those of Kurylo and Laufer on the other.

F. Oxygen KIE in QH

Using a spectroscopic detection of OH, Greenblatt and Howard measured rate coefficients for the reaction of ^{18}OH and ^{16}OH with CO to be $(1.49 \pm 0.15) \times 10^{-13}$ and $(1.44 \pm 0.15) \times 10^{-13}$ cm^3 molecule^{-1} s^{-1}, respectively.[37] This kind of measurement of absolute rather than relative values of the rate constants for the different isotopes gives too large an error to compare with the present calculations. However, using mass-spectroscopy, such as in Stevens's and Röckmann's measurements,[29,30] the accuracy of measuring KIE is sufficient to determine the oxygen isotope effect.

Although the KIE in QH is not the main focus of this paper does not appear in the literature yet, we compare it with the KIE in CQ. The reduction in the imaginary frequency due to heavier oxygen leads to a decreased tunneling. The effect is seen in Table V to be greater when the heavier oxygen is in OH than when it is in CO, a result qualitatively expected because the O in OH is closer to the H in HOCO* than when it is in CO, and so contributes more dynamically to the effective tunneling mass. Accordingly the calculated εHQ is larger than the calculated εCQ at all pressures, a result seen in both the RRKM and the nonstatistical models, as seen in Fig. 2. The effect of the imaginary frequency of TS_2 dominating the difference between εHQ and εCQ is also

TABLE V: Calculated imaginary frequency of TS_2 by CC for different oxygen isotopes[a]

	H···OCQ	H···QCO
Q = ^{16}O	2126i	2126i
Q = ^{17}O	2125i	2116i
Q = ^{18}O	2123i	2107i

[a] The units are cm^{-1}.

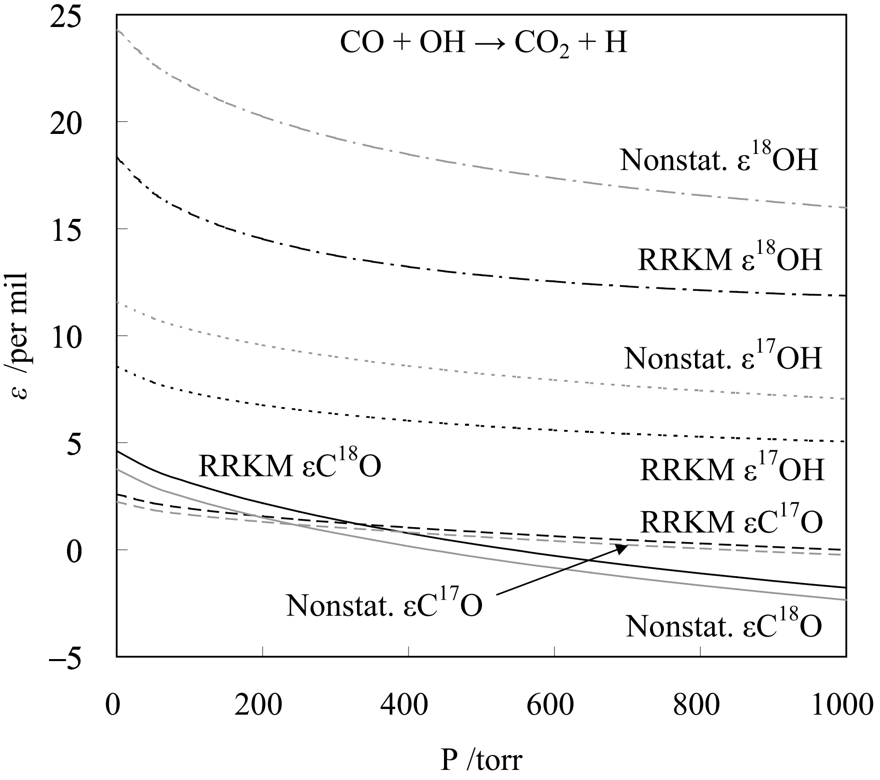

FIG. 2: Pressure dependence of the calculated εCQ and εHQ values for the OH+CO reaction. The black and gray lines are obtained using the RRKM method and the nonstatistical model, respectively. Since both N_2 and He bath gases give similar results, only the calculations with N_2 are shown in the plot.

seen in the calculations made with other *ab initio* methods (Appendices). Therefore, using thermalized source of QH could be helpful in comparing with this prediction and so testing further the importance of the H-tunneling effect in the reaction.

V. CONCLUSIONS

The mass-independent character in a reaction is better defined by the slope in a three-isotope plot, instead the magnitude of fractionation, Δ, since a reaction such as CO+OH may have peculiar mass-dependence with nonzero Δ value. The CO+OH reaction is better described as a mass-anomalous reaction, instead of mass-independent. Since it involves an energetic HOCO intermediate without a preequilibrium followed by a rate-determinate step, the slope in a three-isotope plot is expected to be different from the ideal mass-dependent value, $\sim$0.52.

Its oxygen KIE is a compromise between two opposing effect: (1) a heavy isotope tends to increase the ratio between the number of state at transition states and the thermally average partition function of reactants; (2) a light isotope tends to increase the tunneling effect at transition states. Their importance in the reaction at room temperature and at pressures below 1000 torr was studied with RRKM theory and with a nonstatistical modification, both including and excluding the nuclear tunneling of H at the TSs, using a potential energy surface and the parameters that are the same as those used previously.[25] The reaction in the current calculation favors lighter oxygen isotope since tunneling dominates the calculated fractionation, which is different in the heavier carbon isotopomer. The different dominated effect between the carbon and oxygen KIE is qualitatively explained by the bond-order properties in these two elements. Although the same treatment as that given in our previous paper[25] reproduced a large body of experimental data discussed there, there is a discrepancy between the measured and calculated anomalous mass dependence of oxygen isotopes in the reaction. The calculated sign of ^{18}O enrichments at low pressure and room temperature rests on only one key assumption, namely that the TS_2 with tunneling dominate TS_1.

The discrepancy for oxygen from experiments may instead be due to an intramolecular hydrogen transfer reaction (10) arising from vibrationally hot OH radicals. This hypothesis can be tested by measuring the O-isotope effect using thermalized OH radicals, perhaps such as those used in the work of Greenblatt and Howard.[37] Since the OH radicals in Stevens's and in Röckmann's experiments were produced by photolysis,[29,30] the OH radicals may have had excess vibrational energy, introducing the possibility of the intramolecular H-atom transfer "roaming" reaction (10), with an immediate consequence for the O-isotope effect discussed in Section IV E. Using thermalized OH radicals to study the kinetic oxygen isotope effects would eliminate such a high-energy mechanism and so be an appropriate for testing the present theory regarding the dominance of TS_2 at low pressure and room temperature.

Acknowledgments

It is a pleasure to acknowledge the support of this research by the National Science Foundation. We also thank Dr. Muckerman for providing the F matrix for the structures in their paper,[17] which were used to check the accuracy of rate-constant calculation with

our previous vibrational frequencies.

APPENDIX A: CALCULATED RESULTS FOR DIFFERENT PES'S

The robustness of the results of the present calculations was explored using other electronic structure methods. In particular, to test the sensitivity of certain aspects of the calculations, different, albeit less accurate, methods were used. They are discussed in this appendix. Apart from the transition state structure of the entrance channel TS_1,[51] the vibrational frequencies and rotational constants of all structures for the various isotopes were calculated by three methods, CCSD(T) with 6-31G(d,p), B3LYP with cc-pVTZ, and MP2 with 6-31++G(d,p). The properties of TS_1 are obtained only from the results of MP2 or CC, since DFT gives an unrealistic structure.[51] The acronym DFT denotes the calculation by B3LYP, DFT-MP denotes the calculations combining the structure data of TS_1 from MP2 and the structures from B3LYP, while DFT-CC is similar but with the data for TS_1 obtained from CCSD(T). The GAUSSIAN 98 program[52] was employed for all three *ab initio* calculations (CC, MP2, and B3LYP) to obtain the principal equilibrium structures and their rotational and vibrational constants.

With the force constants and rotational constants at the same *ab initio* level, both G2M and LTSH potentials give very similar calculated results for the oxygen isotope effect. At the low pressure limit at room temperature, the calculated $\varepsilon C^{18}O$ values are about 6, 7, 5, and 2 per mil for DFT-CC, DFT-MP, CC, and MP2, respectively, with G2M or LTSH potentials. The RRKM and nonstatistical modification give similar results. In the pressure range from 0 to 1000 torr the values for all PESs except MP2 are greater than -2 per mil, as shown in Fig. 3. The imaginary frequency of TS_2 by MP2 is unreasonably large, $3176i$, and so gives lower calculated values of $\varepsilon C^{18}O$, monotonically decreasing from 2 to -6 per mil as the pressure changes from 0 to 1000 torr. Because of the unreasonable OH frequency in MP2, the MP2 results are omitted in Fig. 3.

The calculated fractionation for the oxygen atom in OH, $\varepsilon H^{18}O$ at low pressure is again positive and is about 4, 11, 18, and 39 per mil with force constants obtained by using DFT-CC, DFT-MP, CC, and MP2, respectively. The large difference in $\varepsilon H^{18}O$ and $\varepsilon C^{18}O$ is similar to the trend of the values of the imaginary frequency in TS_2 obtained for various calculational levels.[53] This trend is also similar to the trend of the difference between $\varepsilon H^{18}O$ and $\varepsilon C^{18}O$ at low pressure.

APPENDIX B: COMPARISON OF O AND C KIE

Compared oxygen KIE with the carbon's in reference 25, both calculation and experiments shows that the $\varepsilon^{13}CO$ values have a larger pressure dependence than $\varepsilon C^{18}O$ when the pressure is varied from 0 to 1000 torr. At low pressure limit, the $\varepsilon^{13}CO$ value is negative, as discussed in the above two sections, because the TS_2 still dominates the reaction and the heavier isotope decreases the vibrational and rotational constants, its number of states in ^{13}C increases more than that in normal isotope, shown in Table III. Although reducing tunneling effect due to ^{13}C also contributes to reducing the number of states in TS_2, similar to that in heavier oxygen isotope, increasing number of states of TS_2 by reducing vibrational and rotational constants dominates in the ^{13}C isotopomer. The dominance effect in number of states in ^{13}C is different from that in heavy oxygen

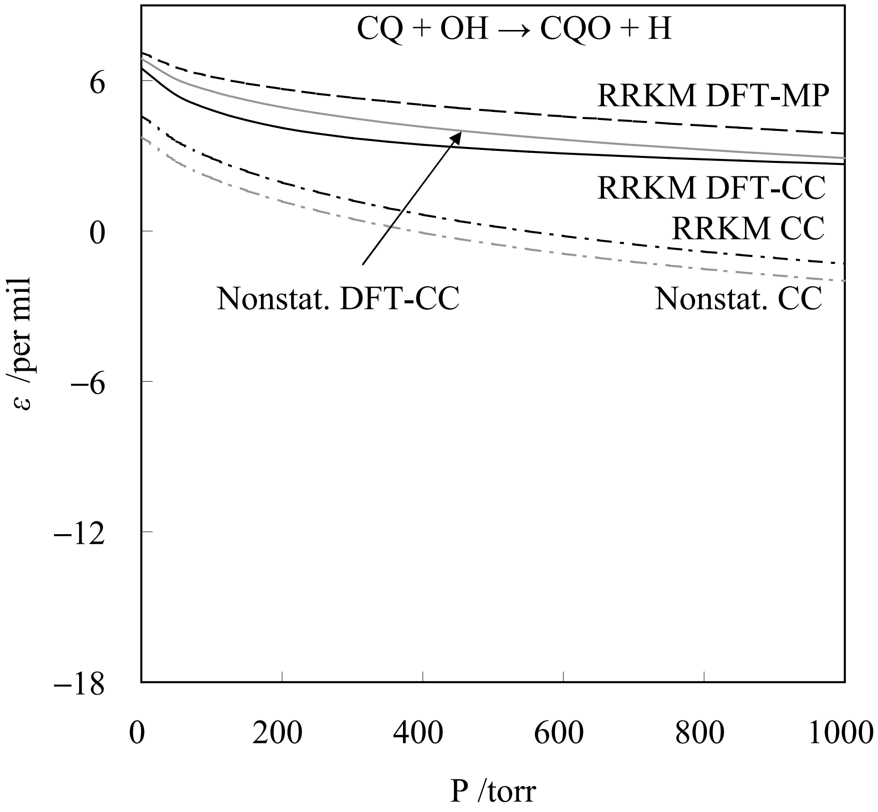

FIG. 3: Calculated $\varepsilon C^{18}O$ values for the OH+CO reaction as a function of total pressure. The G2M and LTSH potentials and He and N_2 bath gases all give results similar to those plotted, namely the results with G2M in N_2 are shown in the plot. The black and gray lines are obtained with the RRKM method and the nonstatistical model, respectively. The solid, dashed-dot, and dashed lines are calculated with DFT-CC, CC, and DFT-MP, respectively. (The reason for not showing MP2 results is given in appendix A.)

isotopomers because the carbon atom can form more bond with surrounding atoms than oxygen atom. This crucial difference leads to the different fractionation behavior at low pressure limit in our present calculation.

As the discussion in our previous article of the non-Arrhenius behavior,[25] the barrier of TS_2 dominates rate constants at high temperature regions, and both barriers contribute rate constants at low temperature regions. Although the usual KIE is smaller at higher temperature, due to the non-Arrhenius behavior the absolute value of the calculated $\varepsilon\mathrm{C}^{18}\mathrm{O}$ and $\varepsilon^{13}\mathrm{CO}$ at low pressure limit show that as increasing temperature, instead of monotonic decreasing in the usual KIE, they reach a maximum at $\sim$400 K, as seen in Table VI.

Another parameter is introduced here to show the robustness in the fractionation at low pressure limit, especially the oxygen KIE. Since TS_2 involves dissociation of a hydrogen atom from HOCO^*, the imaginary frequencies is difficult to obtain precisely using *ab initio* methods.[20,25] The imaginary frequency of TS_2 is scaled by a factor. Using the same fitting procedures of the two vertical shifted parameters of TS_1 and TS_2 described in reference 25, The scaling factor to best represent the calculated pressure dependence of carbon KIE, as shown in Fig. 4, is 0.95 and 0.85 for RRKM and nonstatistical modification, respectively. Although changing the value of imaginary frequency has some improvements on the carbon KIE, Table VII shows that the scaling factor has negligible effect on the oxygen KIE. This result is expected since, as discussed in section IV C and shown in Table III, both $\varepsilon_1^{\mathrm{approx}}$ and $\varepsilon_2^{\mathrm{approx}}$ have contribution on the carbon fractionation, but the oxygen fractionation is mainly dominated by $\varepsilon_2^{\mathrm{approx}}$ in our present calculation.

TABLE VI: Temperature dependence of $\varepsilon C^{18}O$ and $\varepsilon^{13}CO$ at low-pressure limit [a]

	$\varepsilon C^{18}O$	$\varepsilon^{13}CO$
200 K	1.29	0.89
298 K	4.62	−3.97
400 K	5.38	−4.94
500 K	5.28	−4.53
600 K	4.87	−3.56

[a] Units are in per mil.

TABLE VII: $\varepsilon C^{18}O$ and $\varepsilon^{13}CO$ at low pressure limit [a]

	Scaling Factor[b]	$\varepsilon^{13}CO$	$\varepsilon C^{18}O$
RRKM	1.00	−3.97	4.62
RRKM	0.95	−5.47	4.43
Nonstatistical	1.00	−0.18	3.76
Nonstatistical	0.85	−3.67	3.62

[a] Units of fractionation are in per mil.

[b] A scaling factor of the imaginary frequency of TS_2, see text.

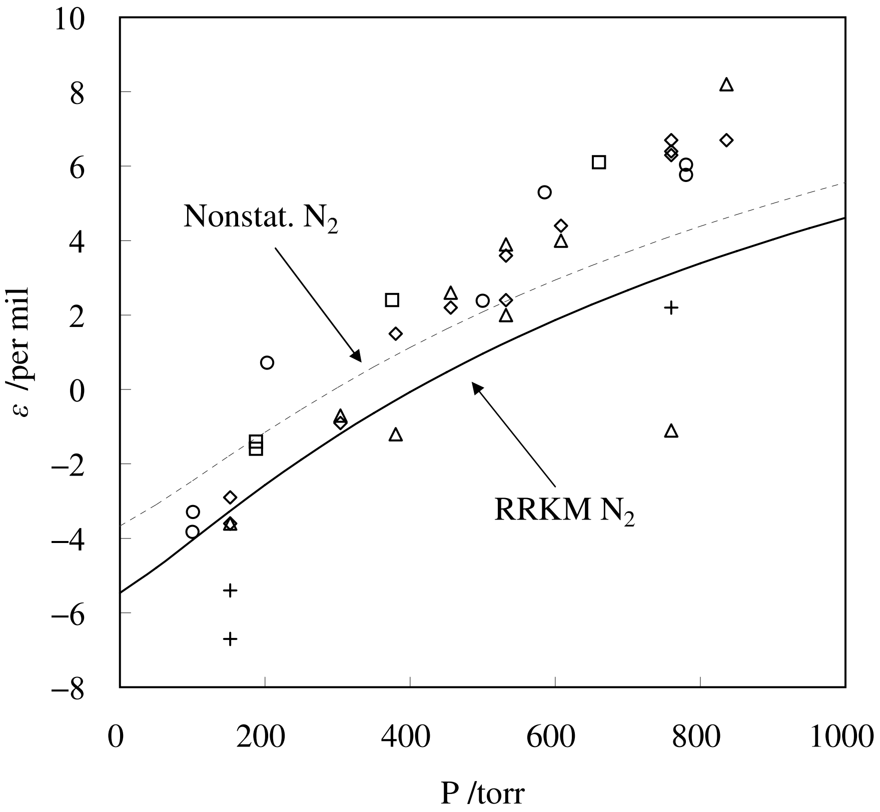

FIG. 4: The ε^{13}CO values for the system of CO+OH given as a function of total pressure at room temperature. The solid lines are calculated using the conventional RRKM theory with a scaling factor 0.95 on the imaginary frequency of TS_2, and the dashed line is obtained with the nonstatistical model with a similar scaling factor, but with value 0.85. Open circles are obtained for N_2 by Smit et al.[54] Black open squares are obtained in N_2 or N_2+O_2, respectively, by Röckmann.[30] Black open triangle, open diamond, and plus symbols are obtained in Ar, air (by measuring products), air, and O_2, respectively, by Grose.[55]

APPENDIX C: CALCULATED $\varepsilon_1^{\mathrm{approx}}$, $\varepsilon_2^{\mathrm{approx}}$, AND ε

The definition of $\varepsilon_1^{\mathrm{approx}}$ is similar to that of $\varepsilon_2^{\mathrm{approx}}$ but with a $k_{N_1}^{\mathrm{approx}}$ similar to $k_{N_2}^{\mathrm{approx}}$ in equation (9), with N_1 instead of N_2 in the integral. At zero pressure, the calculated $\varepsilon_1^{\mathrm{approx}}$, $\varepsilon_2^{\mathrm{approx}}$, and ε of different *ab initio* methods are given in Table VIII. The ε value shifts from $\varepsilon_2^{\mathrm{approx}}$ toward $\varepsilon_1^{\mathrm{approx}}$ when the ratio of thermally weighted N_1 and N_2 decreases. Even with an unreasonably large value of the imaginary frequency in MP2, which gives nearly equal contributions to KIE from both TS_1 and TS_2, the calculated $\varepsilon C^{18}O$ is still positive at zero pressure. Thus, the different methods as well as the argument based on equation (9) yield positive ε values, in contrast to current experiment.

TABLE VIII: Calculated N_1/N_2, $\varepsilon_1^{\text{approx}}$, $\varepsilon_2^{\text{approx}}$, and ε at low pressure limit of different *ab initio* methods[a]

	N_1/N_2[b]	$\varepsilon_1^{\text{approx}}$	$\varepsilon_2^{\text{approx}}$	ε
		CC		
$C^{17}O+OH$	3.80	1.50	3.35	2.60
$C^{18}O+OH$	3.82	−0.77	7.17	4.62
$CO+^{17}OH$	3.77	14.34	8.51	8.58
$CO+^{18}OH$	3.73	33.20	17.35	18.32
		DFT-CC		
$C^{17}O+OH$	5.75	2.68	3.96	4.04
$C^{18}O+OH$	5.77	2.66	7.05	6.49
$CO+^{17}OH$	5.64	16.35	−1.94	2.20
$CO+^{18}OH$	5.54	31.19	−4.79	3.62
		DFT-MP		
$C^{17}O+OH$	2.72	2.19	3.95	3.82
$C^{18}O+OH$	2.73	4.15	7.02	7.13
$CO+^{17}OH$	2.67	16.52	−2.07	5.67
$CO+^{18}OH$	2.62	34.69	−5.03	11.21
		MP2		
$C^{17}O+OH$	1.07	−0.10	3.31	1.31
$C^{18}O+OH$	1.08	−2.37	5.22	1.61
$CO+^{17}OH$	1.08	17.18	21.77	19.72
$CO+^{18}OH$	1.08	33.15	41.85	38.65

[a] The units of $\varepsilon_1^{\text{approx}}$, $\varepsilon_2^{\text{approx}}$, and ε are in per mil.

[b] The ratios of thermally weighted N_1 and N_2 at room temperature is listed in the N_1/N_2 column.

[1] R. P. Wayne, *Chemistry of Atmospheres* (New York: Oxford University Press, 2000), 3rd ed.

[2] A. Miyoshi, H. Matsui, and N. Washida, *J. Chem. Phys.* **100**, 3532 (1994).

[3] C. D. Jonah, W. A. Mulac, and P. Zeglinski, *J. Phys. Chem.* **88**, 4100 (1984).

[4] D. Fulle, H. F. Hamann, H. Hippler, and J. Troe, *J. Chem. Phys.* **105**, 983 (1996).

[5] A. R. Ravishankara and R. L. Thompson, *Chem. Phys. Lett.* **99**, 377 (1983).

[6] V. Lissianski, H. Yang, Z. Qin, M. R. Mueller, and K. S. Shin, *Chem. Phys. Lett.* **240**, 57 (1995).

[7] M. S. Wooldridge, R. K. Hanson, and C. T. Bowman, *Int. J. Chem. Kinet.* **28**, 361 (1996).

[8] M. S. Wooldridge, R. K. Hanson, and C. T. Bowman, in *25th Symp. (Intl.) Combust.* (1994), pp. 741–748.

[9] T. A. Brabbs, F. E. Belles, and R. S. Brokaw, in *13th Symp. (Intl.) Combust.* (1971), pp. 129–136.

[10] M. J. Frost, P. Sharkey, and I. W. M. Smith, *J. Phys. Chem.* **97**, 12254 (1993).

[11] M. J. Frost, P. Sharkey, and I. W. M. Smith, *Faraday Discuss. Chem. Soc.* **91**, 305 (1991).

[12] A. J. Hynes, P. H. Wine, and A. R. Ravishankara, *J. Geophys. Res.* **91**, 11815 (1986).

[13] A. Hofzumahaus and F. Stuhl, *Ber. Bunsenges. Phys. Chem.* **88**, 557 (1984).

[14] R. Forster, M. Frost, D. Fulle, H. F. Hamann, H. Hippler, A. Schlepegrell, and J. Troe, *J. Chem. Phys.* **103**, 2949 (1995).

[15] N. F. Scherer, C. Sipes, R. B. Bernstein, and A. H. Zewail, *J. Chem. Phys.* **92**, 5239 (1990).

[16] D. M. Golden, G. P. Smith, A. B. McEwen, C. L. Yu, B. Eiteneer, M. Frenklach, G. L. Vaghjiani, A. R. Ravishankara, and F. P. Tully, *J. Phys. Chem. A* **102**, 8598 (1998).

[17] H. G. Yu, J. T. Muckerman, and T. J. Sears, *Chem. Phys. Lett.* **349**, 547 (2001).

[18] T. V. Duncan and C. E. Miller, *J. Chem. Phys.* **113**, 5138 (2000).

[19] R. Valero and G. J. Kroes, *J. Chem. Phys.* **117**, 8736 (2002).

[20] R. S. Zhu, E. G. W. Diau, M. C. Lin, and A. M. Mebel, *J. Phys. Chem. A* **105**, 11249 (2001).

[21] J. P. Senosiain, C. B. Musgrave, and D. M. Golden, *Int. J. Chem. Kinet.* **35**, 464 (2003).

[22] R. Valero, D. A. McCormack, and G. J. Kroes, *J. Chem. Phys.* **120**, 4263 (2004).

[23] M. J. Lakin, D. Troya, G. C. Schatz, and L. B. Harding, *J. Chem. Phys.* **119**, 5848 (2003).

[24] D. M. Medvedev, S. K. Gray, E. M. Goldfield, M. J. Lakin, D. Troya, and G. C. Schatz, *J. Chem. Phys.* **120**, 1231 (2004).

[25] W. C. Chen and R. A. Marcus, *J. Chem. Phys.* **123**, 094307 (2005).

[26] W. C. Chen and R. A. Marcus, *J. Chem. Phys.* **124**, 024306 (2006).

[27] M. Brouard, D. W. Hughes, K. S. Kalogerakis, and J. P. Simons, *J. Chem. Phys.* **112**, 4557 (2000).

[28] M. Brouard, I. Burak, D. W. Hughes, K. S. Kalogerakis, J. P. Simons, and V. Stavros, *J. Chem. Phys.* **113**, 3173 (2000).

[29] C. M. Stevens, L. Kaplan, R. Gorse, S. Durkee, M. Compton, S. Cohen, and K. Bielling, *Int. J. Chem. Kinet.* **12**, 935 (1980).

[30] T. Röckmann, C. A. M. Brenninkmeijer, G. Saueressig, P. Bergamaschi, J. N. Crowley, H. Fischer, and P. J. Crutzen, *Science* **281**, 544 (1998).

[31] J. Bigeleisen and M. G. Mayer, *J. Chem. Phys.* **15**, 261 (1947).

[32] J. Bigeleisen, M. G. Mayer, P. C. Stevenson, and J. Turkevich, *J. Chem. Phys.* **16**, 442 (1948).

[33] J. T. Petty, J. A. Harrison, and C. B. Moore, *J. Phys. Chem.* **97**, 11194 (1993).

[34] J. Nolte, J. Grussdorf, E. Temps, and H. G. Wagner, *Z. Naturforsch. A: Phys. Sci.* **48**, 1234 (1993).

[35] G. Poggi and J. S. Francisco, *J. Chem. Phys.* **120**, 5073 (2004).

[36] M. J. Kurylo and A. H. Laufer, *J. Chem. Phys.* **70**, 2032 (1979).

[37] G. D. Greenblatt and C. J. Howard, *J. Phys. Chem.* **93**, 1035 (1989).

[38] K. L. Feilberg, S. R. Sellevag, C. J. Nielsen, D. W. T. Griffith, and M. S. Johnson, *Phys. Chem. Chem. Phys.* **4**, 4687 (2002).

[39] D. H. Volman, *J. Photochem. Photobiol. A-Chem.* **100**, 1 (1996).

[40] Y. Q. Gao and R. A. Marcus, *J. Chem. Phys.* **114**, 9807 (2001).

[41] Although there are other methods treating for collisional energy transfer, such as the exponential-down model, a stepladder model is computationally less intensive for the current purpose of treating small isotope effects. Since the difference of vibrational frequencies and rotational constants between isotopomers are small, the energy grain size for either model needs to be small enough to distinguish the difference between isotopomers. The energy grain size is 1 cm^{-1} in the current work to cover the 8000 cm^{-1} in the E range.[25] Using a

stepladder model with a typical energy transfer parameter α ($\sim$200 cm^{-1}), there are 200 40×40 square matrices to be solved in the master equation. However, in the test calculation the energy grain size for the exponential-down model to reach similar accuracy is around 5 cm^{-1}, requiring, thereby, a single 1600×1600 matrix in the master equation. Although the step-down model needs to have 200 matrices and the exponential-down model has only one, the size of matrix in the exponential down model is considerably larger than those in the stepladder model. Thereby, the stepladder model needed about one order of magnitude less computational resources than the exponential-down model. Test calculations showed that as long as the energy grain size is small enough to describe the properties of isotopomers, both models gave similar pressure dependence for the fractionation. The fractionation at low pressure is, of course, independent of the deactivation model.

[42] C. Eckart, *Phys. Rev.* **35**, 1303 (1930).

[43] The vibrational frequencies and rotational constants of all stationary structures are calculated by the CCSD(T) method with the 6-31G(d,p) basis set.

[44] The difference of rotational constants and most vibraitonal frequencies between our CC and Yu's CCSD(T)/cc-pVTZ[17] in the equlibrium structures is less than 5%. The calculated values of oxygen isotope fractionation by CC is higher than the other by around 0.5 per mil at low pressure and around 1 per mil at 1 atm. Thus, the structures and vibrational frequencies by CC is sufficiently good for the present study.

[45] Compared with the experimental result by Forney *et al.*,[56] the calculated vibrational frequencies in *trans*-HOCO. are larger by less than 5%, except for the OH stretching (6%).

Since the offset is small, no scaling factor of vibrational frequencies was used in calculating the number of states. However, to account approximately for the anharmonicity of the energetic intermediates, the density of states of *trans*- and *cis*-HOCO were increased by a constant factor, 1.5.[57] Again, this factor does not affect the low pressure fractionation.

[46] Recent high level *ab initio* calculations were used for the energies of stationary points in the LTSH potential.[23] Since the imaginary frequency of TS_2 in the LTSH potential is anomalously low, the vibrational frequencies and rotational constants of all stationary structures are calculated instead by *ab initio* methods. Only the energies without ZPE corrections of the stationary structures are obtained from the LTSH potential.

[47] The barrier heights of both TSs are robust with respective to the different calculations. Since the classical barrier of TS_1 at J=0 is lower than that of TS_2, and the structure of TS_2 is more compact than TS_1, the classical barrier of TS_1 is lower than TS_2 at all J. That is, there is no rotational channel switching[58] (change of principal exit channel with J).

[48] S. D. Chambreau, D. Townsend, S. A. Lahankar, S. K. Lee, and A. G. Suits, *Physica Scripta* **73**, C89 (2006).

[49] S. A. Lahankar, S. D. Chambreau, D. Townsend, F. Suits, J. Farnum, X. B. Zhang, J. M. Bowman, and A. G. Suits, *J Chem. Phys.* **125**, 044303 (2006).

[50] D. Townsend, S. A. Lahankar, S. K. Lee, S. D. Chambreau, A. G. Suits, X. Zhang, J. Rheinecker, L. B. Harding, and J. M. Bowman, *Science* **306**, 1158 (2004).

[51] The HO−CO distance of TS_1 optimized by B3LYP is too long, about 2.99 Å in B3LYP, so doubtful frequencies would be expected. A similar result happened when Lin used B3LYP/6-

311G(d,p) to calculate TS_1.[20] The calculated HO−CO distance of TS_1 calculated by CC and MP is 2.03 and 1.95 Å, respectively.

[52] Gaussian 98, Revision A.11.3, M. J. Frisch, G. W. Trucks, H. B. Schlegel, G. E. Scuseria, M. A. Robb, J. R. Cheeseman, V. G. Zakrzewski, J. A. Montgomery, Jr., R. E. Stratmann, J. C. Burant, S. Dapprich, J. M. Millam, A. D. Daniels, K. N. Kudin, M. C. Strain, O. Farkas, J. Tomasi, V. Barone, M. Cossi, R. Cammi, B. Mennucci, C. Pomelli, C. Adamo, S. Clifford, J. Ochterski, G. A. Petersson, P. Y. Ayala, Q. Cui, K. Morokuma, N. Rega, P. Salvador, J. J. Dannenberg, D. K. Malick, A. D. Rabuck, K. Raghavachari, J. B. Foresman, J. Cioslowski, J. V. Ortiz, A. G. Baboul, B. B. Stefanov, G. Liu, A. Liashenko, P. Piskorz, I. Komaromi, R. Gomperts, R. L. Martin, D. J. Fox, T. Keith, M. A. Al-Laham, C. Y. Peng, A. Nanayakkara, M. Challacombe, P. M. W. Gill, B. Johnson, W. Chen, M. W. Wong, J. L. Andres, C. Gonzalez, M. Head-Gordon, E. S. Replogle, and J. A. Pople, Gaussian, Inc, Pittsburgh PA, 2002.

[53] The equlibrium imaginary frequency of TS_2 is $1526i$, $2125i$, and $3176i$ for DFT, CC, and MP2, respectively.

[54] H. G. J. Smit, A. Volz, D. H. Ehhalt, and H. Knappe, in *Stable Isotopes*, edited by H. Schmidt, H. Förstel, and K. Heinzinger (Elsevier Scientific Publishing Company, 1982), pp. 147–152.

[55] C. M. Stevens, L. Kaplan, R. Gorse, S. Durkee, M. Compton, S. Cohen, and K. Bielling, *Int. J. Chem. Kinet.* **12**, 935 (1980).

[56] D. Forney, M. E. Jacox, and W. E. Thompson, *J. Chem. Phys.* **119**, 10814 (2003).

[57] J. Troe, *J. Chem. Phys.* **79**, 6017 (1983).

[58] J. Troe, *J Chem. Soc. Faraday Trans.* **90**, 2303 (1994).

Chapter 4

Isotopomer Fractionation in the UV Photolysis of N_2O: 2. Further Comparison of Theory and Experiment

[This chapter appeared in the *Journal of Geophysical Research-Atmospheres* **113**, D05309 (2008).]

JOURNAL OF GEOPHYSICAL RESEARCH, VOL. 113, D05309, doi:10.1029/2007JD009180, 2008

Isotopomer fractionation in the UV photolysis of N_2O:
2. Further comparison of theory and experiment

Wei-Chen Chen,[1] Meher K. Prakash,[1] and R. A. Marcus[1]

Received 17 July 2007; revised 1 September 2007; accepted 18 December 2007; published 8 March 2008.

[1] Wavelength-dependent fractionation of various isotopomers in the photodissociation of N_2O is studied. The absorption cross sections are calculated by a time-independent reflection principle, related to the Prakash et al. (2005) treatment but now with an inclusion of the NN stretching coordinate and both the $2A'$ and $1A''$ electronic excited states. The added $1A''$ state is found to have little effect on both the absorption cross section and the fractionation. The improvements include more physical details in the photodissociation of N_2O, while maintaining an advantage of a treatment in the work by Prakash et al. (2005) that was not computationally intensive. The present calculated fractionation, without a significant adjustable parameter, gives good agreement with experiments in the absorption cross section in the low-energy region, the important region for the experimentally observed isotopic fractionation.

Citation: Chen, W.-C., M. K. Prakash, and R. A. Marcus (2008), Isotopomer fractionation in the UV photolysis of N_2O: 2. Further comparison of theory and experiment, *J. Geophys. Res.*, *113*, D05309, doi:10.1029/2007JD009180.

1. Introduction

[2] The photolytic dissociation of molecules is important in stratospheric and atmospheric chemistry [e.g., *Wayne*, 2000]. N_2O, in particular, is an effective greenhouse gas and a source of NO_x. Isotopomer fractionation measurements help in determining the sources and sinks of atmospheric gases [*Stevens et al.*, 1972; *Brenninkmeijer et al.*, 2003]. The atmospheric modeling of the N_2O isotopomers [*Popp et al.*, 2002; *Röckmann et al.*, 2003; *McLinden et al.*, 2003; *Morgan et al.*, 2004] and the isotopic fractionation photodissociation behavior of N_2O [*Kim and Craig*, 1990; *Naqvi et al.*, 1998; *Brenninkmeijer et al.*, 2003; *Johnston et al.*, 1995] has been the subject of many studies, including wavelength-dependent measurements [*Zhang et al.*, 2000; *Turatti et al.*, 2000; *Röckmann et al.*, 2000, 2001; *Kaiser et al.*, 2003; *von Hessberg et al.*, 2004]. These studies motivated both empirical [*Blake et al.*, 2003; *Liang et al.*, 2004] and the more theoretical [*Johnson et al.*, 2001; *Nanbu and Johnson*, 2004; *Prakash et al.*, 2005] models to explain the wavelength-dependent fractionation.

[3] Frequently, the process is treated as a two-electronic-state process in which the lower electronic state is excited to the upper state by absorption of radiation [e.g., *Schinke*, 1993]. However, for polyatomic molecules, N_2O being an example, there are usually a number of excited electronic states which are accessible even though the excitation to only one of them may be dominant in the wavelength region of interest. It has been convenient in such work to "broaden" the calculated absorption spectrum as a way of simulating the optical absorption into the other nearby electronic states, as in the treatment of the photolysis N_2O in the work of *Daud et al.* [2005] Analogously, in the work by *Prakash et al.* [2005] (hereinafter referred to as part 1) such a broadening was included tacitly by using a scaling factor for the potential energy curve of the excited electronic state [*Prakash et al.*, 2005]. (The scale used for the excited state in the work by *Prakash et al.* [2005] was 1.57. The broadening there happened inadvertently and was not reported therein.)

[4] In the present paper, we extend the work of part 1 on N_2O by including an effect of the changes in the NN bond length in N_2O, investigating the absorption to an additional electronic state, and using an absorption expression [*Heller*, 1978] that preserves both the momentum and coordinate parts of Franck-Condon principle. The calculated cross section without any broadening factor gives good agreement with experiment in the energy region of interest for the fractionation measurements (apart from a small shift of the absorption maximum). The fractionation of the various isotopomers is then obtained from these calculated absorption cross sections. We use the results of the vibrational analysis in part 1 to calculate the vibrational wave function in the ground state and then invoke the multidimensional reflection principle to calculate the absorption spectrum and the isotopic fractionation factors as a function of wavelength.

2. Theory

2.1. Absorption Cross Section

[5] The theoretical procedure used to obtain absorption cross sections for the N_2O isotopomers is similar to that

---

[1] Noyes Laboratory, California Institute of Technology, Pasadena, California, USA.

0148-0227/08/2007JD009180$09.00

described previously by *Prakash et al.* [2005], but with some additions described below. UV photolysis of N_2O is essentially a direct dissociation, since the shape of the absorption spectrum is a broad envelope with a only weak structure superimposed. Thereby, the time-dependent expression for the absorption cross section can be rewritten in a time-independent form using the reflection principle in conjunction with the Franck-Condon principle [*Heller*, 1978; *Schinke*, 1993]. The absorption cross section σ is given as

$$\begin{aligned}\sigma_{f\nu}(\omega) &= \frac{\pi\omega}{\hbar\epsilon_0 c}\frac{1}{2\pi}\int_{\infty}^{-\infty} dt\langle\Psi_\nu|\vec{e}\cdot\vec{\mu}_{fi}^{\dagger}e^{-iH_f t/\hbar}\vec{\mu}_{fi}\cdot\vec{e}|\Psi_\nu\rangle e^{i(\omega-E_i/\hbar)t}\\ &\approx \frac{\pi\omega}{3\epsilon_0 c}\int d\mathbf{Q}|\Psi_\nu(\mathbf{Q})|^2|\vec{\mu}_{fi}(\mathbf{R})|^2\delta\big(\hbar\omega - V_f(\mathbf{R}) + V_i(\mathbf{R})\big)\\ &\approx \frac{\pi\omega}{3\epsilon_0 c}\int dq_1\ldots dq_{N-1}|\Psi_\nu(\mathbf{Q})|^2|\vec{\mu}_{fi}(\mathbf{Q})|^2/\Delta S, \qquad (1a)\end{aligned}$$

where a change in slope ΔS is given by

$$\Delta S = \big(\partial\big[V_i(\mathbf{Q}) - V_f(\mathbf{Q})\big]/\partial q_N\big)_{q_N^\omega}. \qquad (1b)$$

Here, **R** and **Q** denote internal and normal coordinates, respectively, as before [*Prakash et al.*, 2005], $\mathbf{R} = (q_1, q_2 \cdots q_N)$, $\vec{e}$ is a unit vector, $\vec{\mu}_{fi}(\mathbf{R})$ is the transition dipole moment function for a transition between the ground and the excited electronic states i and f, respectively, $V_f(\mathbf{Q})$ and $V_i(\mathbf{Q})$ denote the potential energy surfaces of the electronic excited and ground states, respectively, and q_N is the repulsive coordinate in the excited state f, along which dissociation happens, while q_N^ω in equation (1b) is the value of q_N where $h\omega$ equals the vertical potential energy difference of the two electronic states:

$$\hbar\omega - V_f\big(q_1,\cdots,q_{N-1},q_N^\omega\big) + V_i\big(q_1,\cdots,q_{N-1},q_N^\omega\big) = 0, \qquad (2)$$

[6] $|\Psi_\nu(\mathbf{Q})|^2$ in equation (1a) is the probability density function of **Q** in the initial nuclear vibrational state ν and ground electronic state i. Using the harmonic approximation for the potential energy V_i as a function of the normal coordinates, the probability density function of the vibrational state ν in the ground electronic state can be written as a product of that of each of the normal vibration modes.

[7] In the present calculation of the absorption cross section in equation (1b), the actual potential of the electronic ground state $V_i(\mathbf{Q})$ at coordinate **Q** is used [*Heller*, 1978], instead of the average potential energy $\langle V_i\rangle$ [*Lee et al.*, 1983; *Prakash et al.*, 2005]. This change corresponds to conserving the momenta in the Franck-Condon principle and enhances the calculated intensity of the absorption cross section on the long-wavelength side of absorption maximum. The result obtained with equation (1a) is shown and discussed later in section 3.1, now without any significant adjustable parameter. (The slope of the excited electronic potential in the work by *Prakash et al.* [2005] was enlarged by the broadening scale, which also increased the width of the absorption cross section.)

[8] The total absorption cross section is temperature-dependent, because of the dependence of $\sigma_{f\nu}$ on the initial vibrational state v and thermal excitation of each vibrational states. The total absorption cross section at temperature T is given by

$$\sigma_{total}(T) = \sum_{f,\nu}\sigma_{f\nu}\exp\left(\frac{-E_\nu}{k_B T}\right)/Q_{vib}(T), \qquad (3)$$

where $Q_{vib}(T)$ is the partition function of the vibrations in the ground electronic state, and E_ν is the vibrational energy of the vibrational state ν. The present calculation for the total absorption cross section of N_2O includes excitation from the ground electronic state to two excited states, $2A'$ (1Δ) and $1A''$ $(1\Sigma^-)$, and all vibrational states that are significantly populated with energy not more than 1500 cm^{-1} above the zero-point energy. It involves the ground state, the first excited state of NO stretching, and the first and second excited states of the N_2O bending. Since the N_2O is linear in the electronic ground state, this bending vibration is doubly degenerate, as discussed in by *Prakash et al.* [2005].

2.2. Potential Energy

[9] The best currently available potential energy and transition dipole moment surfaces appear to be those of *Daud et al.* [2005] However, these surfaces are given in terms of mass-dependent Jacobi coordinates with a fixed NN distance. The present treatment of the potential energy surfaces includes varying the NN distance by expanding it to second-order in terms of a displacement of the equilibrium NN distance of both electronic ground and excited states. The details of the potential difference used in equation (1b) are given in Appendix A.

2.3. Fractionation

[10] The expression for the photodissociation rate at energy $h\omega$ in equation (1a) depends upon three factors: the total absorption cross section $\sigma_{total}(\omega)$ in equation (3), the photon flux, and the quantum yield of the photodissociation. The fractionation $\epsilon(\omega)$ of one isotopomer relative to another due to a direct photodissociation reaction can be defined as the ratio of photodissociation rates. When the upper state is dissociative, the quantum yield equals unity for all the isotopomers. The fractionation then is expressed in terms of the ratio of total absorption cross sections,

$$\epsilon(\omega) = \left[\frac{\sigma'_{total}(\omega)}{\sigma_{total}(\omega)} - 1\right] \times 1000\ ‰. \qquad (4)$$

3. Results and Discussion

3.1. Absorption Cross Section

[11] In the present treatment the potential difference between the ground and excited states in equation (1b) includes all vibrational modes of N_2O in the calculation. A harmonic approximation is used in the NN stretching mode, which was fixed in the best currently available potential [*Daud et al.*, 2005]. The N_2 vibration is expected to be a spectator [*Hanisco and Kummel*, 1993; *Neyer et al.*, 1999] as far as the initial and final NN stretching state are concerned. The NN stretching mode is also expected to cause only a small change in the transition dipole moment of the N_2O molecule. In the excited state, there is never-

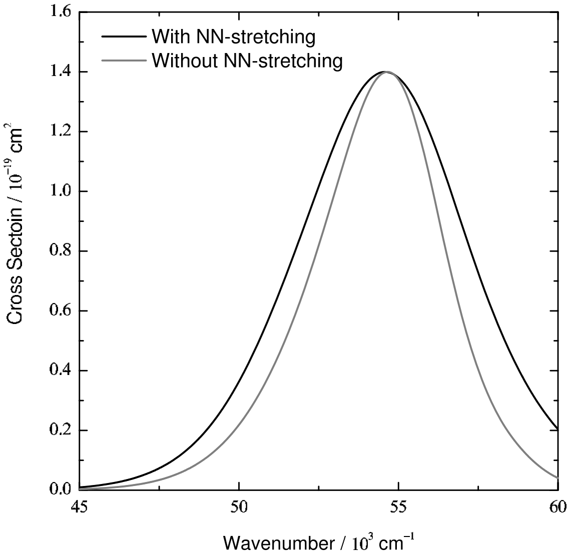

Figure 1. The calculated absorption cross section with (black) and without (gray) the NN stretching mode at 298 K.

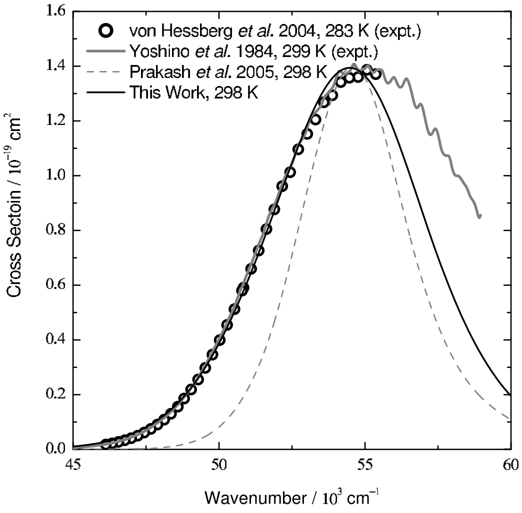

Figure 2. Absorption cross section of $^{14}N^{14}N^{16}O$. The black line is the current calculation result. The gray dashed line is the calculation result obtained by our previous formula [*Prakash et al.*, 2005], but without using any broadening factor. Both calculation results are rescaled and shifted to overlap their maximum absorption cross section at ~55000 cm^{-1}.

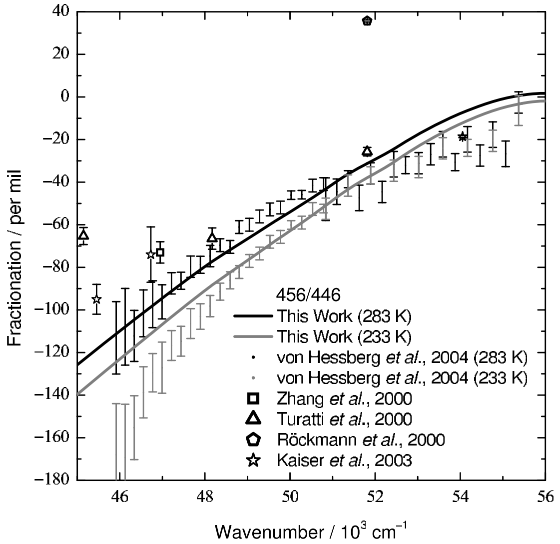

Figure 3. Fractionation of 456 calculated at 233 and 283 K.

theless a transient distortion of the NN coordinate because of the difference in $V_f(\mathbf{R})$ and $V_i(\mathbf{R})$ in this coordinate. Using an approximate method for introducing this distortion in Appendix A, there results a significant broadening effect in the absorption cross section, as shown in Figure 1. In this formalism, the NN stretching mode thus gives a broadening effect on the absorption cross section. The stored vibrational energy at the moment of excitation is relaxed to other modes later. The same Frank-Condon assumption was also used in the very accurate ionization-energy calculations in various molecules [*Cheng et al.*, 1997; *Eberhard et al.*, 1998], where it gives excellent results for the comparison of theory and experiment, now between vibrationally bound states. However, more detailed theoretical and experimental studies are necessary to test this assumption.

[12] The most important spectral region where isotopic fractionation studies of N_2O have been reported is the long-wavelength side of the absorption maximum (180 nm to 220 nm). The calculated absorption cross section of the most abundant isotopomer, 446 (i.e., $^{14}N^{14}N^{16}O$), is compared with experiments [*Yoshino et al.*, 1984; *von Hessberg et al.*, 2004] in Figure 2, where the result calculated by our previous formula [*Prakash et al.*, 2005], but without their broadening factor, is also shown. The calculated properties needed to obtain the absorption cross section are provided in the Appendix C. In the comparison with the experimental spectrum, the calculated peak is red shifted by 1100 cm^{-1} and rescaled by a factor of 0.69. The need for the shift arises from a small error in the difference between the energy of ground and excited electronic states from the ab initio calculations. Such differences are indeed expected. A rescaling in height is also expected since the ab initio calculation of the transition dipole moment $\vec{\mu}_{fi}$ is expected to have some errors [*Borges*, 2006; *Daud et al.*, 2005]. However, the rescaled factor at the absorption maximum has no effect on the isotopic fractionations since the factor cancels in equation (4). The total absorption cross sections for other isotopomers are calculated similarly with the same shift in the peak position as that for 446, since the energy difference between potential energy surfaces is independent of isotopic substitution. The red shifted value at the absorption maximum also has a minor red-shifted effect on the isotope fractionations.

[13] The agreement of calculated and measured absorption cross sections in Figure 2 is seen to be good on the long-wavelength side of absorption maximum, the region of

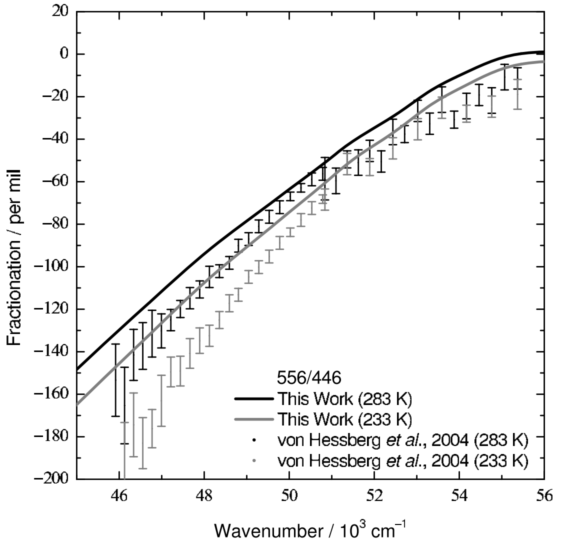

Figure 4. Fractionation of 556 calculated at 233 and 283 K.

most interest. In the short-wavelength side of the absorption spectrum the experimental result has larger cross section than the calculated. A difference is probably due to the presence of electronic excited states of N_2O higher than $2A'$ and $1A''$, and perhaps due to the long tail in the cross section that involves the vibrationally excited NN stretching mode in the excited N_2O. Although that mechanism may broaden the absorption cross section at higher energy, it has little effect for the fractionation at the energies of conventional interest since there is less than 2% of products with the vibrationally excited N_2, *Hanisco and Kummel* [1993], and *Neyer et al.* [1999] both at ~200 nm, where the fractionations are of interests.

3.2. Wavelength-Dependent Fractionation

[14] The calculated wavelength-dependent fractionation of isotopomers 456, 556, and 546 relative to the most abundant isotopomer 446 are shown in Figures 3–5. The calculated values of 456 and 556 agree well with experimental data [*Zhang et al.*, 2000; *Turatti et al.*, 2000; *Röckmann et al.*, 2000, 2001; *Kaiser et al.*, 2003; *von Hessberg et al.*, 2004]. The values of 546 are not so good. Although the calculated fractionation 546 in Figure 5 is higher than the experimental result obtained by *von Hessberg et al.* [2004] at the long-wavelength region, our result is still comparable with the result observed by *Turatti et al.* [2000]. However, *Johnson et al.* [2001], using a completely different model (Hermite propagation method), obtained a fractionation 546 similar to ours. A more detailed theoretical study is necessary to see whether the discrepancy may be due to anharmonicity: the middle atom in 546 is the lightest and becomes the most susceptible to anharmonic effect (larger amplitude).

[15] Comparison with other ab initio values was given in part 1. Since the present calculations neglect the weak structure of the absorption cross section, the calculated fractionation is an averaged curve for comparison with the mean of the experiments. Compared with the previous paper [*Prakash et al.*, 2005], the current results agree better with experiments and now contain no ad hoc broadening factor is used. This improvement in the results over part 1 is expected since the current treatment includes some distortion effect of the NN stretching and also has a physically more understandable expression, equation (1a) and (1b), for the fractionation.

[16] The calculated fractionations 447 and 448 relative to 446 at 283 K is given in Figure 6. The agreement is very good [*Turatti et al.*, 2000; *Röckmann et al.*, 2000, 2001; *Kaiser et al.*, 2003]. Compared with fractionation of isotopomers, the sensitivity of the calculated fractionation to changes in the wavelength is 556 > 456 > 448 > 447 ~ 546. This trend is similar to the difference of the vibrational frequency of the bending mode between 446 and the respective isotopomers since the electronic excitation from the ground state to the excited state is forbidden for a linear N_2O. This transition is allowed only when the molecule is bent. In the experiments [*Zhang et al.*, 2000; *Turatti et al.*, 2000; *Röckmann et al.*, 2000, 2001; *Kaiser et al.*, 2003; *von Hessberg et al.*, 2004] the order is 556 > 456 > 448 ~ 546 > 447.

[17] All Figures 3–6 show a convex curve where the slope of wavelength-dependent fractionation decrease in the high-energy region. This result is different from that obtained by the empirical ZPE model [*Yung and Miller*, 1997], which predicts a straight line, because the model assumes that the slope of the absorption cross section is preserved upon isotope substitution. However, comparing the intensity factors, defined as the integral of the product of the vibrational probability function and the square of transition dipole moment, between 446 and various isotopomers, the factors have only a slight dependence on isotopomers (cf. Table 1). This dependence also should be important in the near leveling-off effect in the fractionation near the peak region of the absorption cross section. A similar calculational result is also discussed by *Johnson et al.* [2001]. (The intensity factor in the work by *Johnson et al.* [2001] is slightly different from ours.)

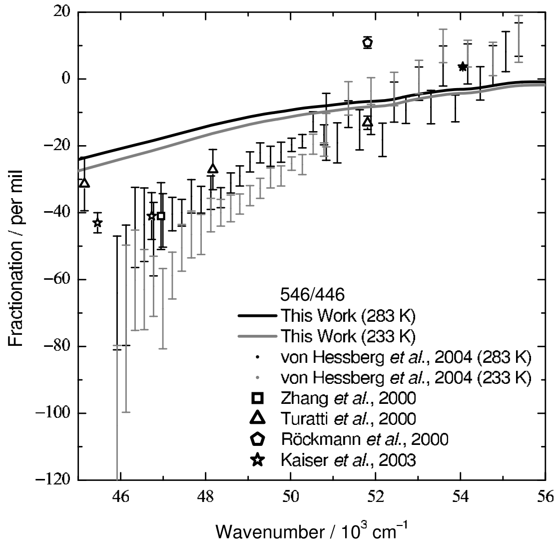

Figure 5. Fractionation of 546 calculated at 233 and 283 K.

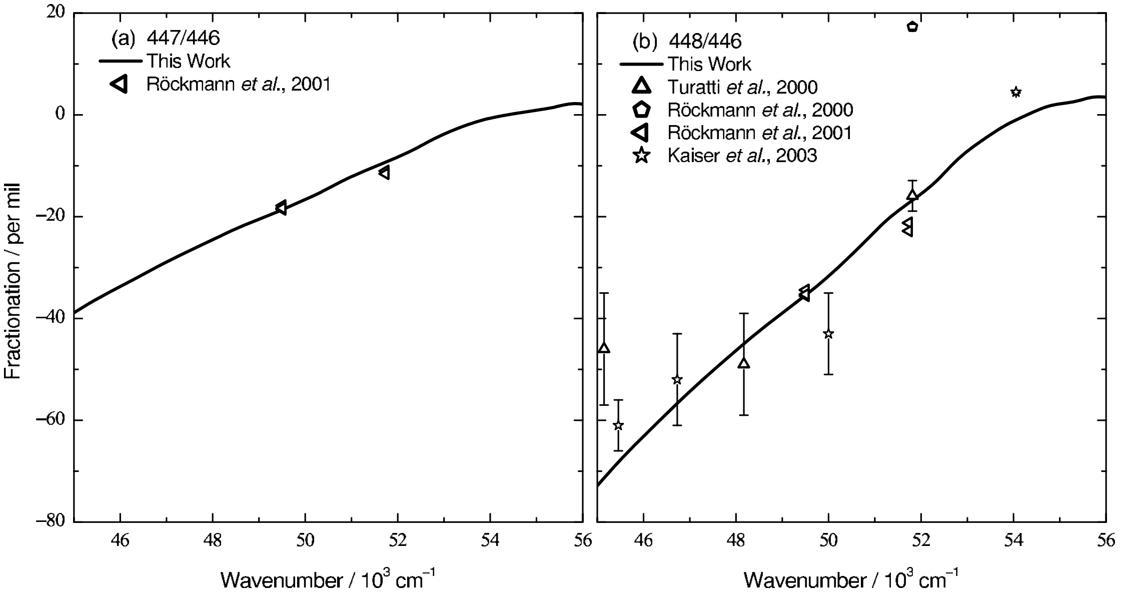

Figure 6. Fractionation of (a) 447 and (b) 448. The calculated values are at 283 K.

[18] There is a mass-dependent fractionation of oxygen isotopes in the current model, that is the same as the previous one [*Prakash et al.*, 2005; *Prakash and Marcus*, 2005]. This model also gives a mass-dependent fractionation in nitrogen fractionation, which is discussed elsewhere (W.-C. Chen and R. A. Marcus, Slopes in three-isotope plots of fractionation in photolysis of N_2O: A theory with reduced-mass approach, manuscript in preparation, 2008). The mass-dependent heavy oxygen isotope enrichment of residual N_2O is also measured by *Johnston et al.* [1995]. The observation of anomalous mass effect of N_2O in troposphere and lower stratosphere [*Cliff and Thiemens*, 1997; *Cliff et al.*, 1999; *Röckmann et al.*, 2001] is due to other chemical reactions, as discussed by *McLinden et al.* [2003] using a global model.

3.3. Excited Electronic States

[19] There are two potential energy surfaces (2A′ and 1A″) included in these calculations. The 1A″ state has a minor contribution in the calculation of absorption cross section since the peak intensity of the 1A″ state is smaller than that of the 2A′ state by a factor of ∼100. The intensity factor of various vibrational states of the isotopomer 446 is shown in Table 1. This difference in intensity is similar to that found in the time-dependent calculation by *Daud et al.* [2005]. It also has a very minor contribution (<2 per mil) to the fractionation of all isotopomers. Since the effect of the 1A″ state is very small, we do not show the results in figures.

4. Conclusions

[20] The absorption cross section of 446 calculated using a computationally simple time-independent treatment with small adjustments for the position of the peak and its amplitude is in reasonable agreement with the broad envelope of the cross section in experiments. (Compared with the wave packet propagation method, the current method requires less computational resources. Both methods depend heavily on accurate transition dipole moment and potential energy surfaces of the electronic ground and excited states, which is not a simple task.) The required computations are similar to that in our previous treatment [*Prakash et al.*, 2005] but there are several improvements in the calculations, including the effect of NN stretching and avoiding the need for an empirical broadening parameter. There is a reasonable agreement in the wavelength-dependent fractionations of the isotopomers. The 2A′ excited state dominates both the absorption cross section and fractionation in the N_2O photodissociation.

Table 1. Intensity Factors of 446 in the Various Vibrational States and the Ratio of Intensity Factors Between 446 and Other Isotopomers[a]

	000	001	002	010
		2A′		
446	7.561	16.58[b]	24.41[c]	8.1493
447/446	0.9934	0.9949	0.9954	0.9923
448/446	0.9880	0.9903	0.9915	0.9858
456/446	0.9708	0.9760	0.9788	0.9714
546/446	0.9923	0.9939	0.9944	0.9895
556/446	0.9637	0.9702	0.9739	0.9614
		1A″		
446	0.08755	0.1489[b]	0.1787[c]	0.1760
447/446	0.9831	0.9848	0.9856	0.9866
448/446	0.9684	0.9713	0.9729	0.9746
456/446	0.9710	0.9764	0.9813	0.9833
546/446	0.9948	0.9963	0.9973	0.9764
556/446	0.9662	0.9727	0.9788	0.9598

[a] The vibrational quantum states are denoted as a three-digit number, such as 001, in which the digits indicate the vibrational quantum number of ν_1, ν_2, and ν_3, respectively. The vibrational frequencies of various isotopomers are listed in Table 2. The unit of intensity factors is 10^{-3} (atomic unit)^2.

[b] An average value of two degenerate vibrational states.

[c] An average value of three degenerate vibrational states.

[21] The current method is useful for studying isotopic fractionation in direct photodissociation systems when accurate transition moment and potential energy surfaces are available. However, other interesting photodissociation reactions, such as ozone, CO_2, and OCS, have a trapped state before dissociation or involve more than one excited states in the photodissociation process. In order to study these more complicated photodissociation, further developments on the current theory are required. When the quantum yield for dissociation is close to unity, then it is possible that the present method can be adapted to these other systems.

Appendix A: Potential Energy Difference

[22] The potential difference in equation (1b) is expanded as

$$\begin{aligned} V_f(\mathbf{R}) - V_i(\mathbf{R}) \approx{} & V_f(\mathbf{\Gamma}) + \frac{1}{2}k_{N_2}\left[(r_{NN} - r_\Delta)^2 - r_\Delta^2\right] \\ & - V_i(\mathbf{\Gamma}) - \frac{1}{2}k_{NN,NN}r_{NN}^2 - \frac{1}{2}k_{NO,NO}r_{NO}^2 - k_{NN,NO}r_{NN}r_{NO}, \end{aligned} \tag{A1}$$

where r_{NN} and r_{NO} are the displacement of the NN and NO distances, respectively, from the equilibrium at the electronic ground state, and r_Δ is the difference in the equilibrium NN distance between N_2 and N_2O. Because in the excited state the N_2 formed a triple bond, and the NO coordinate is a strongly repulsive one, the force constant corresponding to the cross terms of r_{NN} and r_{NO} is assumed to be small compared with these two dominate coordinates on the excited state potential energy surfaces. A further detailed calculation about this coupling on the excited potential energy surface is needed to validate this assumption. In equation (A1), $\mathbf{\Gamma}$ has the same meaning as $\mathbf{R}$, but with the displacement coordinate $r_{NN} = 0$; The integration in equation (1a) is more easily performed in normal coordinates. The relation between internal and normal coordinates satisfies $\mathbf{R} = \mathscr{L}\mathbf{Q}$, where $\mathscr{L}$ is a matrix composed of eigenvectors of the $\mathcal{G}\mathcal{F}$ matrix [*Wilson et al.*, 1955]. The $\mathcal{G}$ and $\mathcal{F}$ matrices of N_2O are given in Appendix B. The potential difference is rewritten as

$$\begin{aligned} V_f(\mathbf{R}) - V_i(\mathbf{R}) &= V_f(\mathbf{Q}) - V_i(\mathbf{Q}) \\ &\approx V_f(0, L_{2,i}q_i, L_{3,3}q_3) + \frac{1}{2}k_{N_2}\left[(L_{1,i}q_i - r_\Delta)^2 - r_\Delta^2\right] \\ &\quad - V_i(0, L_{2,i}q_i, L_{3,3}q_3) - \frac{1}{2}\omega_1^2\left[q_1^2 - \left(L_{1,2}^{-1}L_{2,i}q_i\right)^2\right] \\ &\quad - \frac{1}{2}\omega_2^2\left[q_2^2 - \left(L_{2,2}^{-1}L_{2,i}q_i\right)^2\right], \end{aligned} \tag{A2}$$

where $\sum_{i=1}^{2} L_{j,i}q_i$ are abbreviated as $L_{j,i}q_i$, and $L_{i,j}$ and $L_{i,j}^{-1}$ are the (*i*th, *j*th) elements of the matrices $\mathscr{L}$ and $\mathscr{L}^{-1}$, respectively.

[23] A treatment of the NN distance contribution to the vibration is in one sense different from that of the NO coordinate. Unlike the NO coordinate it is not a dissociative one. However, because of the difference in the NN contribution to the two potential energy functions V_f and V_i in the two electronic states, and the coupling of the motion to the NO coordinate, the NN coordinate is not a bystander, even though the product is formed primarily in the N_2 ground vibrational state, and N_2O is a almost entirely in the lowest NN stretching vibrational state before illumination. For simplicity, we have used the simple Frank-Condon assumption given above and used successfully earlier by *Cheng et al.* [1997] and *Eberhard et al.* [1998] in the studies of the vertical ionization energy (rather than an absorption spectrum). The molecules studied in the neutral and cation state have the same chemical formula (except for the charge of the state), although their equilibrium geometries are slightly different. However, ultimately the model should be compared with more rigorous treatment. The present method recognizes a distortion that occurs in the NN vibration, due to differences in $V_f(\mathbf{R})$ and $V_i(\mathbf{R})$ for that coordinate, and so by this distortion transiently stores energy in that coordinate and so broadens the absorption spectrum.

Appendix B: $\mathcal{G}$ and $\mathcal{F}$ Matrices

[24] The $\mathcal{G}$ and $\mathcal{F}$ matrices of N^1N^2O are defined as [*Wilson et al.*, 1955]

$$\mathcal{G} = \begin{pmatrix} \frac{1}{m_{N^1}} + \frac{1}{m_{N^2}} & \frac{-1}{m_{N^2}} & 0 \\ \frac{-1}{m_{N^2}} & \frac{1}{m_{N^2}} + \frac{1}{m_O} & 0 \\ 0 & 0 & \frac{1}{m_{N^1}\left(r_{NN}^{eq}\right)^2} + \frac{1}{m_{N^2}}\left(\frac{1}{r_{NN}^{eq}} + \frac{1}{r_{NO}^{eq}}\right)^2 + \frac{1}{m_O\left(r_{NO}^{eq}\right)^2} \end{pmatrix}, \tag{B1}$$

$$\mathcal{F} = \begin{pmatrix} k_{NN,NN} & k_{NN,NO} & 0 \\ k_{NN,NO} & k_{NO,NO} & 0 \\ 0 & 0 & k_{\theta,\theta} \end{pmatrix}. \tag{B2}$$

The mass of each isotope are available from *Lide* [2004]. The equilibrium NN and NO distance for N_2O is 1.1273 and 1.1851 Å, respectively, which are obtained experimentally by *Teffo and Chédin* [1989]. The force constants of the $\mathcal{F}$ matrix are given in Appendix C. The $\mathcal{L}$ matrix is obtained by solving the eigenvectors of the $\mathcal{G}\mathcal{F}$ matrix.

Appendix C: Properties of Isotopomers

[25] This appendix provides the parameters used for obtaining the absorption cross section of various isotopomers. The mass of each isotope are available from *Lide* [2004]. The equilibrium bond length for N_2 is 1.09768 Å (http://webbook.nist.gov/cgi/cbook.cgi?Formula=n2&NoIon=on&Units=SI&cDI=on). The force constant in the ground state k_{N2} is 22.948 aJ/Å^2. The force constants for

Table A1. Calculated and Experimental Normal-Mode Frequencies of Various Isotopomers[a]

	$\bar{\nu}_1$	$\bar{\nu}_1^{expt.b}$	$\bar{\nu}_2$	$\bar{\nu}_2^{expt.c}$	$\bar{\nu}_3$	$\bar{\nu}_3^{expt.d}$
446	2224.424	2223.757	1286.003	1284.903	588.729	588.768
447	2221.012	2220.074	1263.532	1264.704	586.264	586.362
448	2218.085	2216.711	1243.136	1246.885	584.074	584.225
456	2176.677	2177.657	1284.090	1280.354	575.272	575.434
546	2201.880	2201.605	1269.392	1269.892	585.225	585.312
556	2153.347	2154.726	1267.940	1265.334	571.685	571.894

[a] Unit is cm^{-1}.
[b] *Toth* [1986].
[c] *Amiot* [1976] and *Jolma et al.* [1983].
[d] *Toth* [1987].

N_2O are $k_{NN,NN}$ = 17.655 aJ/Å^2; $k_{NO,NO}$ = 11.559 aJ/Å^2; $k_{NN,NO}$ = 1.260 aJ/Å^2; and $k_{\theta,\theta}$ = 0.649 aJ/rad^2 [*Csaszar*, 1994]. The force constants are calculated by fitting the experimental vibrational frequencies of various N_2O isotopomers. The difference between calculated and experimental frequencies, as shown in Table A1, are smaller than ±3.7 cm^{-1} in the two stretching modes and ±0.3 cm^{-1} in the bending mode. The force constants used in the present work are slightly different from the experimental values obtained by *Teffo and Chédin* [1989], used in our previous work [*Prakash et al.*, 2005].

[26] **Acknowledgment.** It is a pleasure to acknowledge the support of this research by the National Science Foundation.

References

Amiot, C. (1976), Vibration-rotation bands of $^{15}N_2{}^{16}O$-$^{14}N_2{}^{18}O$, *J. Mol. Spectrosc.*, *59*(3), 380–395.

Blake, G. A., M. C. Liang, C. G. Morgan, and Y. L. Yung (2003), A Born-Oppenheimer photolysis model of N_2O fractionation, *Geophys. Res. Lett.*, *30*(12), 1656, doi:10.1029/2003GL016932.

Borges, I. (2006), Configuration interaction oscillator strengths of the H2O molecule: Transitions from the ground to the B^1A_1, C^1B_1, D^1A_1, and 1^1B_2 excited states, *Chem. Phys.*, *328*(1–3), 284–290.

Brenninkmeijer, C. A. M., C. Janssen, J. Kaiser, T. Röckmann, T. S. Rhee, and S. S. Assonov (2003), Isotope effects in the chemistry of atmospheric trace compounds, *Chem. Rev.*, *103*(12), 5125–5161.

Cheng, B. M., J. Eberhard, W. C. Chen, and C. H. Yu (1997), Photoionization efficiency spectrum and ionization energy of HSO studied by discharge flow photoionization mass spectrometry, *J. Chem. Phys.*, *106*(23), 9727–9733.

Cliff, S. S., and M. H. Thiemens (1997), The $^{18}O/^{16}O$ and $^{17}O/^{16}O$ ratios in atmospheric nitrous oxide: A mass-independent anomaly, *Science*, *278*(5344), 1774–1776.

Cliff, S. S., C. A. M. Brenninkmeijer, and M. H. Thiemens (1999), First measurement of the $^{18}O/^{16}O$ and $^{17}O/^{16}O$ ratios in stratospheric nitrous oxide: A mass-independent anomaly, *J. Geophys. Res.*, *104*, 16,171–16,175.

Csaszar, A. G. (1994), Anharmonic force field of N_2O, *J. Phys. Chem.*, *98*(36), 8823–8826.

Daud, M. N., G. G. Balint-Kurti, and A. Brown (2005), Ab initio potential energy surfaces, total absorption cross sections, and product quantum state distributions for the low-lying electronic states of N_2O, *J. Chem. Phys.*, *122*(5), 054305.

Eberhard, J., W. C. Chen, C. H. Yu, Y. P. Lee, and B. M. Cheng (1998), Photoionization spectra and ionization energies of HSCl, HSSSH, SSCl, and HSSCl formed in the reaction system $Cl/Cl_2/H_2S$, *J. Chem. Phys.*, *108*(15), 6197–6204.

Hanisco, T. F., and A. C. Kummel (1993), State-resolved photodissociation of N_2O, *J. Phys. Chem.*, *97*(28), 7242–7246.

Heller, E. J. (1978), Quantum corrections to classical photo-dissociation models, *J. Chem. Phys.*, *68*(5), 2066–2075.

Johnson, M. S., G. D. Billing, A. Gruodis, and M. H. M. Janssen (2001), Photolysis of nitrous oxide isotopomers studied by time-dependent Hermite propagation, *J. Phys. Chem. A*, *105*(38), 8672–8680.

Johnston, J. C., S. S. Cliff, and M. H. Thiemens (1995), Measurement of multioxygen isotopic ($\delta^{18}O$ and ($\delta^{17}O$) fractionation factors in the stratospheric sink reactions of nitrous-oxide, *J. Geophys. Res.*, *100*, 16,801–16,804.

Jolma, K., J. Kauppinen, and V. M. Horneman (1983), Vibration-rotation spectrum of N_2O in the region of the lowest fundamental ν_2, *J. Mol. Spectrosc.*, *101*(2), 278–284.

Kaiser, J., T. Röckmann, C. A. M. Brenninkmeijer, and P. J. Crutzen (2003), Wavelength dependence of isotope fractionation in N_2O photolysis, *Atmos. Chem. Phys.*, *3*, 303–313.

Kim, K. R., and H. Craig (1990), 2-isotope characterization of N_2O in the Pacific Ocean and constraints on its origin in deep-water, *Nature*, *347*(6288), 58–61.

Lee, S. Y., R. C. Brown, and E. J. Heller (1983), Multidimensional reflection approximation—Application to the photo-dissociation of polyatomics, *J. Chem. Phys.*, *87*(12), 2045–2053.

Liang, M. C., G. A. Blake, and Y. L. Yung (2004), A semianalytic model for photo-induced isotopic fractionation in simple molecules, *J. Geophys. Res.*, *109*, D10308, doi:10.1029/2004JD004539.

Lide, D. R. (Ed.) (2004), *CRC Handbook of Chemistry and Physics*, 84th ed., CRC Press, Boca Raton, Fla.

McLinden, C. A., M. J. Prather, and M. S. Johnson (2003), Global modeling of the isotopic analogues of N_2O: Stratospheric distributions, budgets, and the ^{17}O-^{18}O mass-independent anomaly, *J. Geophys. Res.*, *108*(D8), 4233, doi:10.1029/2002JD002560.

Morgan, C. G., M. Allen, M. C. Liang, R. L. Shia, G. A. Blake, and Y. L. Yung (2004), Isotopic fractionation of nitrous oxide in the stratosphere: Comparison between model and observations, *J. Geophys. Res.*, *109*, D04305, doi:10.1029/2003JD003402.

Nanbu, S., and M. S. Johnson (2004), Analysis of the ultraviolet absorption cross sections of six isotopically substituted nitrous oxide species using 3d wave packet propagation, *J. Phys. Chem. A*, *108*(41), 8905–8913.

Naqvi, S. W. A., T. Yoshinari, D. A. Jayakumar, M. A. Altabet, P. V. Narvekar, A. H. Devol, J. A. Brandes, and L. A. Codispoti (1998), Budgetary and biogeochemical implications of N_2O isotope signatures in the Arabian Sea, *Nature*, *394*(6692), 462–464.

Neyer, D. W., A. J. R. Heck, and D. W. Chandler (1999), Photodissociation of N_2O: J-dependent anisotropy revealed in N_2 photofragment images, *J. Chem. Phys.*, *110*(7), 3411–3417.

Popp, B. N., et al. (2002), Nitrogen and oxygen isotopomeric constraints on the origins and sea-to-air flux of N_2O in the oligotrophic subtropical North Pacific gyre, *Global Biogeochem. Cycles*, *16*(4), 1064, doi:10.1029/2001GB001806.

Prakash, M. K., and R. A. Marcus (2005), Three-isotope plot of fractionation in photolysis: A perturbation theoretical expression, *J. Chem. Phys.*, *123*(17), 174308.

Prakash, M. K., J. D. Weibel, and R. A. Marcus (2005), Isotopomer fractionation in the UV photolysis of N_2O: Comparison of theory and experiment, *J. Geophys. Res.*, *110*, D21315, doi:10.1029/2005JD006127.

Röckmann, T., C. A. M. Brenninkmeijer, M. Wollenhaupt, J. N. Crowley, and P. J. Crutzen (2000), Measurement of the isotopic fractionation of $^{15}N^{14}N^{16}O$, $^{14}N^{15}N^{16}O$ and $^{14}N^{14}N^{18}O$ in the UV photolysis of nitrous oxide, *Geophys. Res. Lett.*, *27*(9), 1399–1402.

Röckmann, T., J. Kaiser, J. N. Crowley, C. A. M. Brenninkmeijer, and P. J. Crutzen (2001), The origin of the anomalous or "mass-independent" oxygen isotope fractionation in tropospheric N_2O, *Geophys. Res. Lett.*, *28*(3), 503–506.

Röckmann, T., J. Kaiser, and C. A. M. Brenninkmeijer (2003), The isotopic fingerprint of the pre-industrial and the anthropogenic N_2O source, *Atmos. Chem. Phys.*, *3*, 315–323.

Schinke, R. (1993), *Photodissociation Dynamics*, Cambridge Univ. Press, New York.

Stevens, C. M., D. Walling, A. Venters, L. E. Ross, A. Engelkem, and L. Krout (1972), Isotopic composition of atmospheric carbon-monoxide, *Earth Planet. Sci. Lett.*, *16*(2), 147–165.

Teffo, J. L., and A. Chédin (1989), Internuclear potential and equilibrium structure of the nitrous-oxide molecule from rovibrational data, *J. Mol. Spectrosc.*, *135*(5), 389–409.

Toth, R. A. (1986), Frequencies of N_2O in the 1100 cm^{-1} to 1440 cm^{-1} region, *J. Opt. Soc. Am. B*, *3*(10), 1263–1281.

Toth, R. A. (1987), N_2O vibration-rotation parameters derived from measurements in the 900–1090 cm^{-1} and 1580–2380 cm^{-1} regions, *J. Opt. Soc. Am. B*, *4*(3), 357–374.

Turatti, F., D. W. T. Griffith, S. R. Wilson, M. B. Esler, T. Rahn, H. Zhang, and G. A. Blake (2000), Positionally dependent ^{15}N fractionation factors in the UV photolysis of N_2O determined by high resolution FTIR spectroscopy, *Geophys. Res. Lett.*, *27*(16), 2489–2492.

von Hessberg, P., J. Kaiser, M. B. Enghoff, C. A. McLinden, S. L. Sorensen, T. Röckmann, and M. S. Johnson (2004), Ultra-violet absorption cross sections of isotopically substituted nitrous oxide species: $^{14}N^{14}NO$, $^{15}N^{14}NO$, $^{14}N^{15}NO$ and $^{15}N^{15}NO$, *Atmos. Chem. Phys.*, *4*(41), 1237–1253.

Wayne, R. P. (2000), *Chemistry of Atmospheres*, 3rd ed., Oxford Univ. Press, New York.
Wilson, E. B., J. C. Decius, and P. C. Cross (1955), *Molecular Vibrations: The Theory of Infrared and Raman Vibrational Spectra*, McGraw-Hill, New York.
Yoshino, K., D. E. Freeman, and W. H. Parkinson (1984), High-resolution absorption cross-section measurements of N_2O at 295 K–299 K in the wavelength region 170–222 nm, *Planet. Space Sci.*, *32*(10), 1219–1222.
Yung, Y. L., and C. E. Miller (1997), Isotopic fractionation of stratospheric nitrous oxide, *Science*, *278*(5344), 1778–1780.
Zhang, H., P. O. Wennberg, V. H. Wu, and G. A. Blake (2000), Fractionation of $^{14}N^{15}N^{16}O$ and $^{15}N^{14}N^{16}O$ during photolysis at 213 nm, *Geophys. Res. Lett.*, *27*(16), 2481–2484.

W.-C. Chen, R. A. Marcus, and M. K. Prakash, Noyes Laboratory 127-72, California Institute of Technology, Pasadena, CA 91125, USA. (cwc@caltech.edu; ram@caltech.edu; meher@caltech.edu)

Chapter 5

Isotopomer Fractionation in the UV Photolysis of N_2O: 3. 3D *Ab Initio* Surfaces and Anharmonic Effects

[This chapter prepared for the *Journal of Geophysical Research-Atmospheres.*]

Abstract

The results for the wavelength-dependent isotopic fractionation of N_2O are calculated extending our previous work[1] in several aspects. The vibrational wavefunctions with anharminicity correction for the ground electronic state are obtained by the variational method. Three-dimensional *ab initio* electronic potential and transition dipole moment surfaces calculated by S. Nanbu and M. S. Johnson[2] are used in calculating the absorption cross sections. The results for the absorption spectrum and for the isotopic fractionation are discussed. Differences between experiments measuring the absorption coefficient[3] and all others, which measured instead the isotopic composition of the remaining reactants of the photodissociation are discussed and predictions are made for further experiments on the quantum yield for wavelengths longer than 200 nm for the 447 and 448 isotopomers.

I. INTRODUCTION

The photolysis of N_2O has been extensively studied in the literature, summarized in Parts 1 and 2.[1,4] In those studies, the results of the vibrational analysis were used to calculate the vibrational wavefunctions in the ground state and, using the multidimensional reflection principle,[5,6] to calculate the absorption spectrum and the isotopic fractionation as a function of wavelength. In the present paper, the method of Part 2 is extended by including the anharmonicity of the ground electronic state, resulting in vibrational wavefunctions with corrections calculated via the variational method. The 3-dimensional *ab initio* electronic potential and transition dipole moment surfaces calculated by Nanbu and Johnson[2] are used. The present treatment improves the calculated absorption cross section in the low energy region ($<$48,000 cm^{-1}) and the wavenumber dependence in photolysis fractionations.

II. THEORY

A. Absorption Cross Section

The theoretical procedure used to obtain absorption cross sections for the N_2O isotopomers is similar to that described previously by Chen et al.,[1] but with the additions described below. UV photolysis of N_2O in the given spectral region of interest is essentially a direct dissociation, since the absorption spectrum is a broad envelope with a only weak structure superimposed. Thereby, as before, the time-dependent expression for the absorption cross section can be rewritten in a time-independent form using the reflection principle in conjunction with the Franck-Condon principle.[5,6] The absorption cross section σ is given as

$$\begin{aligned}
\sigma_{fn}(\omega) &= \frac{\pi\omega}{\hbar\epsilon_0 c}\frac{1}{2\pi}\int_{-\infty}^{\infty} \mathrm{d}t \langle\Psi_n|\vec{\mu}_{fi}^{\dagger}\mathrm{e}^{-iH_f t/\hbar}\vec{\mu}_{fi}|\Psi_n\rangle \mathrm{e}^{i(\omega+E_i/\hbar)t} \\
&\approx \frac{\pi\omega}{3\epsilon_0 c}\int \mathrm{d}\mathbf{Q}\,|\Psi_n(\mathbf{Q})|^2\,|\vec{\mu}_{fi}(\mathbf{R})|^2\,\delta\left(\hbar\omega - V_f(\mathbf{R}) + V_i(\mathbf{R})\right) \\
&\approx \frac{\pi\omega}{3\epsilon_0 c}\int \mathrm{d}q_1\ldots\mathrm{d}q_{N-1}\,|\Psi_n(\mathbf{Q})|^2\,|\vec{\mu}_{fi}(\mathbf{Q})|^2\,/\Delta S(\omega), \qquad (1)
\end{aligned}$$

where a change in slope $\Delta S(\omega)$ of the potential energy difference at ω is given by

$$\Delta S(\omega) = \left(\partial[V_i(\mathbf{Q}) - V_f(\mathbf{Q})]/\partial q_N\right)_{q_N^\omega}. \qquad (2)$$

In equations (1) and (2),[1] **R** and **Q** denote internal and normal coordinates, respectively. The relation between internal and normal coordinates satisfies $\mathbf{R}=\mathscr{L}\mathbf{Q}$, where $\mathscr{L}$ is a matrix composed of eigenvectors of the $\mathscr{G}\mathscr{F}$ matrix.[7] The $\mathscr{G}$- and $\mathscr{F}$-matrices of N_2O are given in appendix A. $\vec{\mu}_{fi}(\mathbf{R})$ is the vector of the transition dipole moment function for a transition between the ground and the excited electronic states i and f, respectively, $V_i(\mathbf{Q})$ and $V_f(\mathbf{Q})$ denote their potential energy surfaces, and q_N is the repulsive coordinate in the excited state f, along which dissociation occurs, while q_N^ω in equation (2) is the value of q_N where $\hbar\omega$ equals the vertical potential energy difference of the two electronic states:

$$\hbar\omega = V_f(q_1,\ldots,q_{N-1},q_N^\omega) - V_i(q_1,\ldots,q_{N-1},q_N^\omega), \qquad (2)$$

The best currently available 3-dimensional *ab initio* potential energy ($V_i(\mathbf{R})$ and $V_f(\mathbf{R})$), and transition dipole moment ($\vec{\mu}_{fi}(\mathbf{R})$) surfaces appear to be those of Nanbu and Johnson.[2] These surfaces are given in terms of mass-dependent Jacobi coordinates that is varied in all degrees of freedom, instead of surfaces with fixed NN distance in our previous treatment.[1] At the ground electronic surfaces obtained by fitting the Nanbu and Johnosn results,[2] the equilibrium NN and NO distance of N_2O is 1.1345 and 1.189 Å, respectively. Both lengths are slightly longer than experimental results, as listed in appendix A. The whole surface is shifted slightly on both bonds to correspond with the experimental results, which are used to obtain the vibrational wavefunctions $\Psi_n(\mathbf{Q})$ in equation (1).

In the present calculation of the absorption cross section, the effect of vibrational anharmonicity in the ground electronic state i is included using a variational method for the vibrational wavefunctions $\Psi_n(\mathbf{Q})$ (section II B), instead of harmonic vibrational wavefunctions used previously in Chen et al.[1] Although anharmonicity has little effect on the total absorption cross section near the peak region, it does affect the absorption cross section in the low energy region and the wavelength dependence in the fractionation there.

The total absorption cross section for any absorption frequency ω is temperature dependent, due to the dependence of the individual $\sigma_{fn}(\omega)$ on the initial vibrational state n and thermal excitation of each vibrational states. The total absorption cross section at temperature T is given by

$$\sigma_{total}(\omega, T) = \sum_{f,n} \sigma_{fn}(\omega) \exp\left(\frac{-(E_n - E_0)}{k_B T}\right) / Q_{vib}(T), \tag{3}$$

where $Q_{vib}(T)$ is the partition function of the vibrations in the ground electronic state, and E_n and E_0 are the vibrational energy of the vibrational state n and zero-point energy, respectively. An anharmonic effect on E_n is also included using the variational method. The vibrational states, n, with energy below 1500 cm^{-1} above the zero-point energy are included. It thus involves the ground state, the first vibrationally excited state of NO stretching, and the first and second excited states of the N_2O bending. Since the N_2O is linear in the electronic ground state, its bending vibration is doubly degenerate, as discussed in Prakash et al.[4] The present calculation for the total absorption cross section of N_2O includes excitation from the ground electronic state to the first excited state, 2A' (1Δ), since the second excited state, 1A" ($1\Sigma^-$), has little effect on the absorption cross section and fractionation, as discussed in Chen et al.[1]

B. Variational Method

As mentioned in the above section, the variational method is used to obtain the vibrational wavefunctions $\Psi_n(\mathbf{Q})$ with the anharmonicity correction in equation (1). The trial functions are a linear combination of the harmonic wavefunctions, such as

$$\Psi_n(\mathbf{Q}) = \sum_m c_{n,m} \Phi_m^{(0)}(\mathbf{Q}), \tag{4}$$

where $\Phi_m^{(0)}(\mathbf{Q})$ are the normalized harmonic wavefunctions of three modes and are given in appendix B. The $c_{n,m}$ coefficients are obtained by the eigenvectors of the secular determinate. Since an orthonormal basis set is used, the secular determinate is

$$\begin{vmatrix} H_{1,1} - E & H_{1,2} & \cdots & H_{1,n} \\ H_{2,1} & H_{2,2} - E & \cdots & H_{2,n} \\ \vdots & \vdots & \ddots & \vdots \\ H_{n,1} & H_{n,2} & \cdots & H_{n,n} - E \end{vmatrix} = 0, \tag{5}$$

where $H_{i,j} = \langle \Phi_i^{(0)} | H | \Phi_j^{(0)} \rangle$. The Hamiltonian H includes the harmonic vibrational operator and all potential terms higher than the quadratic.[8] The jth eigenvalue of equation (5) corresponds the vibrational energy E_j of the Ψ_j state. In the present article, the basis set in the variational method includes six harmonic wavefunctions for each stretching vibration, and four nondegenerate ones for the bending vibration (i.e. 144 harmonic wavefunctions in the orthonormal basis set).

C. Calculated Fractionation

The expression for the photodissociation rate at energy $\hbar\omega$ in equation (1) depends upon three factors: the total absorption cross section $\sigma_{total}(\omega)$ in equation (3), the photon flux, and the quantum yield of the photodissociation. The fractionation $\epsilon(\omega)$ of one isotopomer relative to another due to a direct photodissociation reaction can be defined as the ratio of photodissociation rates. When the upper state is dissociative, the quantum yield equals unity for all the isotopomers. The fractionation $\epsilon(\omega)$ can then be expressed in terms of the ratio of total absorption cross sections,

$$\epsilon(\omega) = \left[\frac{\sigma'_{total}(\omega)}{\sigma_{total}(\omega)} - 1\right] \times 1000\ \text{‰}. \tag{6}$$

III. RESULTS

A. Absorption Cross Section

The current extensions of the absorption cross section calculation contain the use of (i) a 3-dimensional *ab initio* electronic potential and transition dipole moment surfaces,[2] and (ii) variational vibrational wavefunctions that describe the anharmonicity of the ground electronic state (section II B). The energy difference between the ground and first-excited vibrational states of each modes obtained by the variational method is shown Table I. Using

TABLE I: The calculated and experimental energy difference between the ground and first-excited vibrational states in each normal mode of various isotopomers. The unit is cm^{-1}.

	$\bar{\nu}_1$	$\bar{\nu}_1^{expt.19}$	$\bar{\nu}_2$	$\bar{\nu}_2^{expt.20,21}$	$\bar{\nu}_3$	$\bar{\nu}_3^{expt.22}$
446	2222.327	2223.757	1284.932	1284.903	588.356	588.768
447	2218.686	2220.074	1264.698	1264.704	585.962	586.362
448	2215.366	2216.711	1246.833	1246.885	583.836	584.225
456	2176.213	2177.657	1280.409	1280.354	575.027	575.434
546	2200.233	2201.605	1269.923	1269.892	584.915	585.312
556	2153.335	2154.726	1265.381	1265.334	571.501	571.894

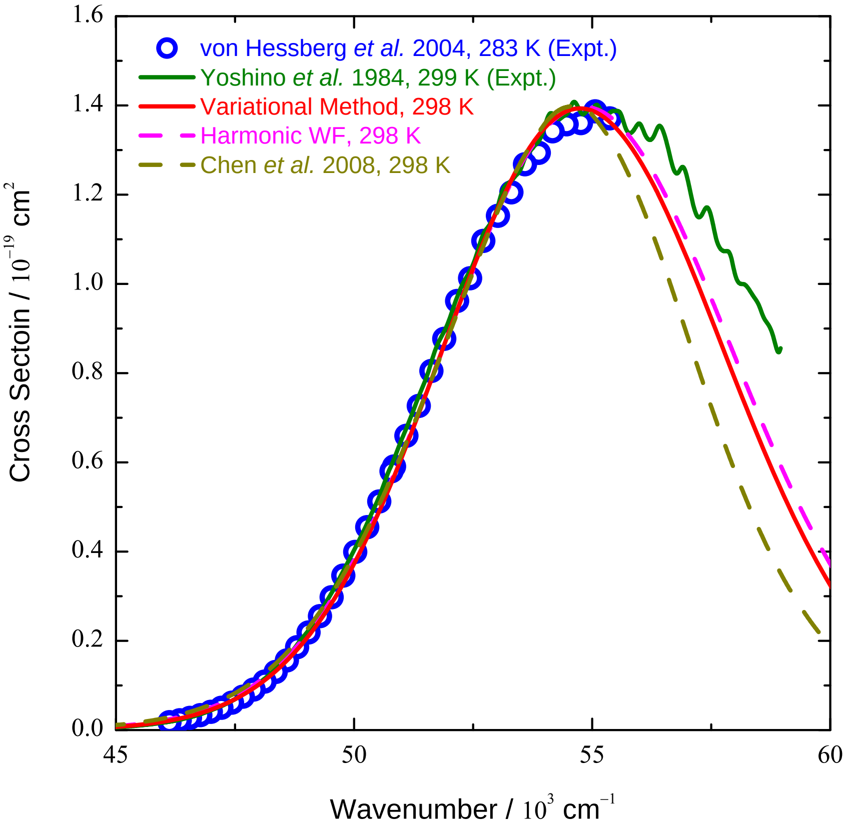

FIG. 1: Absorption cross section of $^{14}\mathrm{N}^{14}\mathrm{N}^{16}\mathrm{O}$. The red line is the current calculation result. The calculation results are rescaled and shifted to overlap with experimental data at the longer wavelength region.

these values of vibrational energy, the calculated absorption cross section with perturbation treatment of the most abundant isotopomer, 446, is shown in Figure 1. The improvement in absorption cross section due to the variational method and the 3-dimensional *ab initio* surfaces is best seen in Figure 2 at the red side of the absorption band.

B. Fractionation

Using equation (6) with the absorption cross section of various isotopomers, the wavelength-dependent fractionation of isotopomers 546, 556, and 456 calculated relative to the most abundant isotopomer 446 is shown in Figures 3–5. The calculated fractionations 447 and 448 relative to 446 at 283 K is given in Figure 6.

IV. DISCUSSION

A. Comparison with Experimental Absorption Cross Section

Without any adjustable parameters, the vibrational energy difference obtained by the variational method of the anharmonicity is in reasonable agreement with experiment (the difference is smaller than 1.5 cm^{-1} in all modes), as seen in Table I. Some of these values are used in equation (3) to obtain the total absorption cross section at various temperatures.

For these comparisons with the experimental spectrum at the long wavelength region (180 to 220 nm) where the isotopic fractionation is of most interest, the calculated peak is redshifted by 800 cm^{-1} and in amplitude rescaled by a factor of 1.59. As mentioned in Chen et al.,[1] the need for the shift arises from a small error in the absolute energy difference

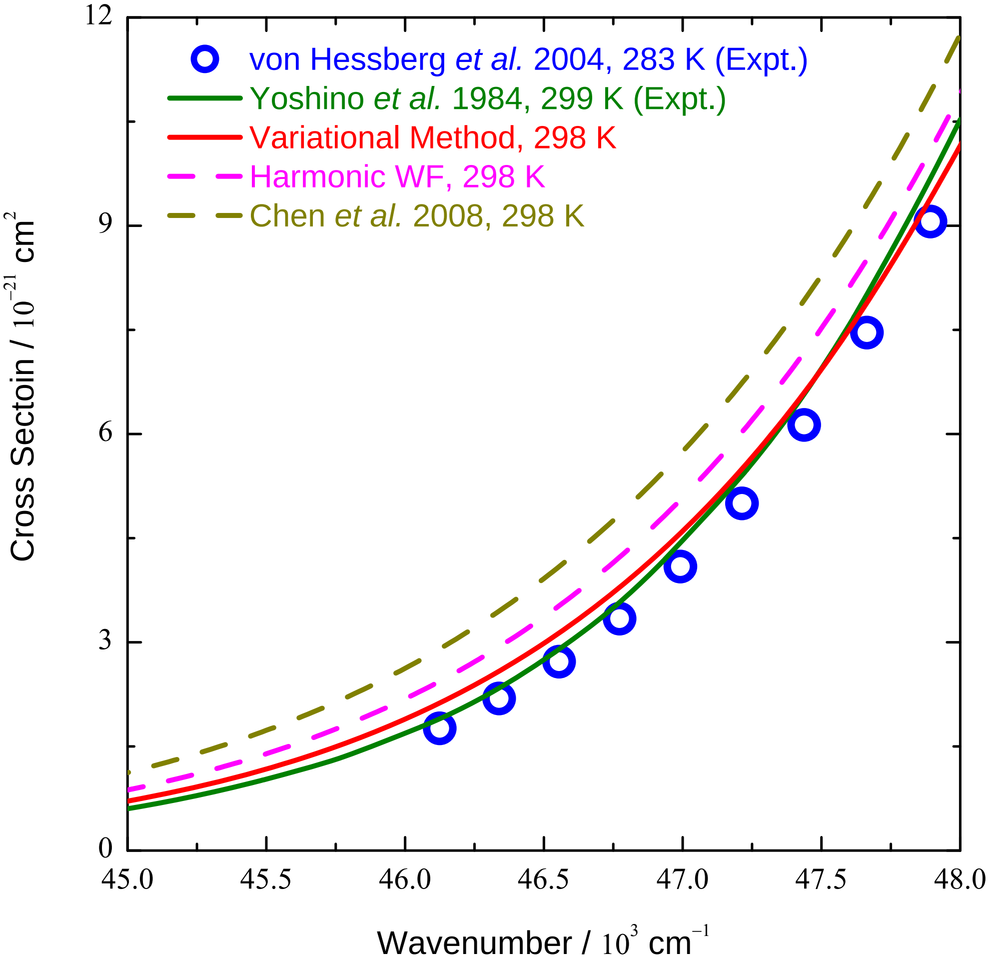

FIG. 2: Absorption cross section of $^{14}N^{14}N^{16}O$ at the lower wavenumber region.

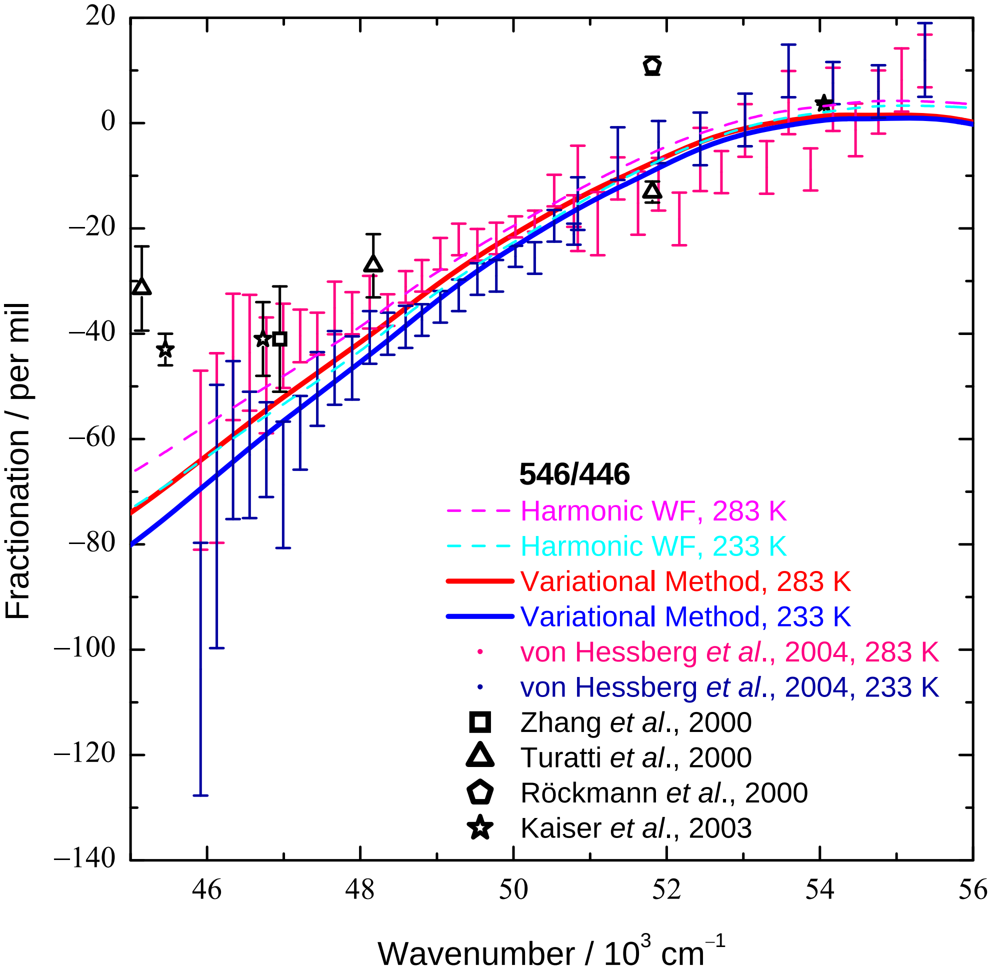

FIG. 3: Fractionation of 546 calculated at 233 and 283 K.

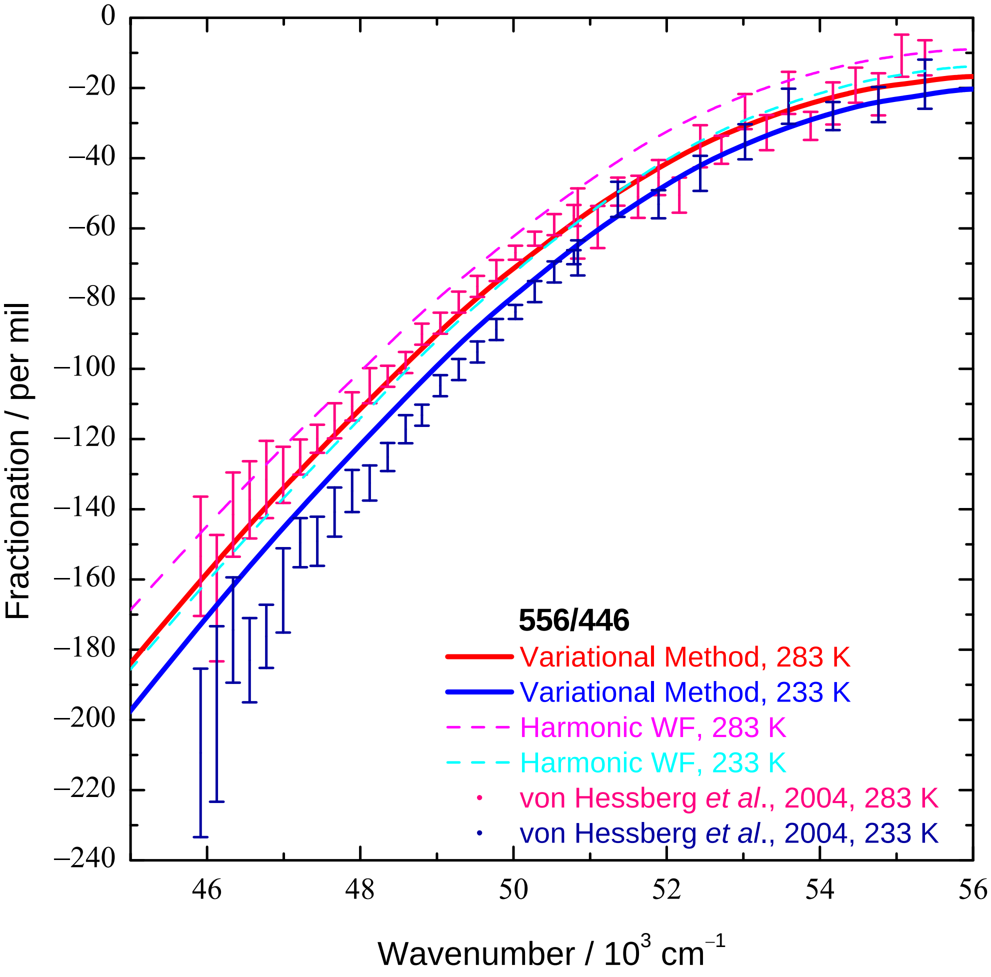

FIG. 4: Fractionation of 556 calculated at 233 and 283 K.

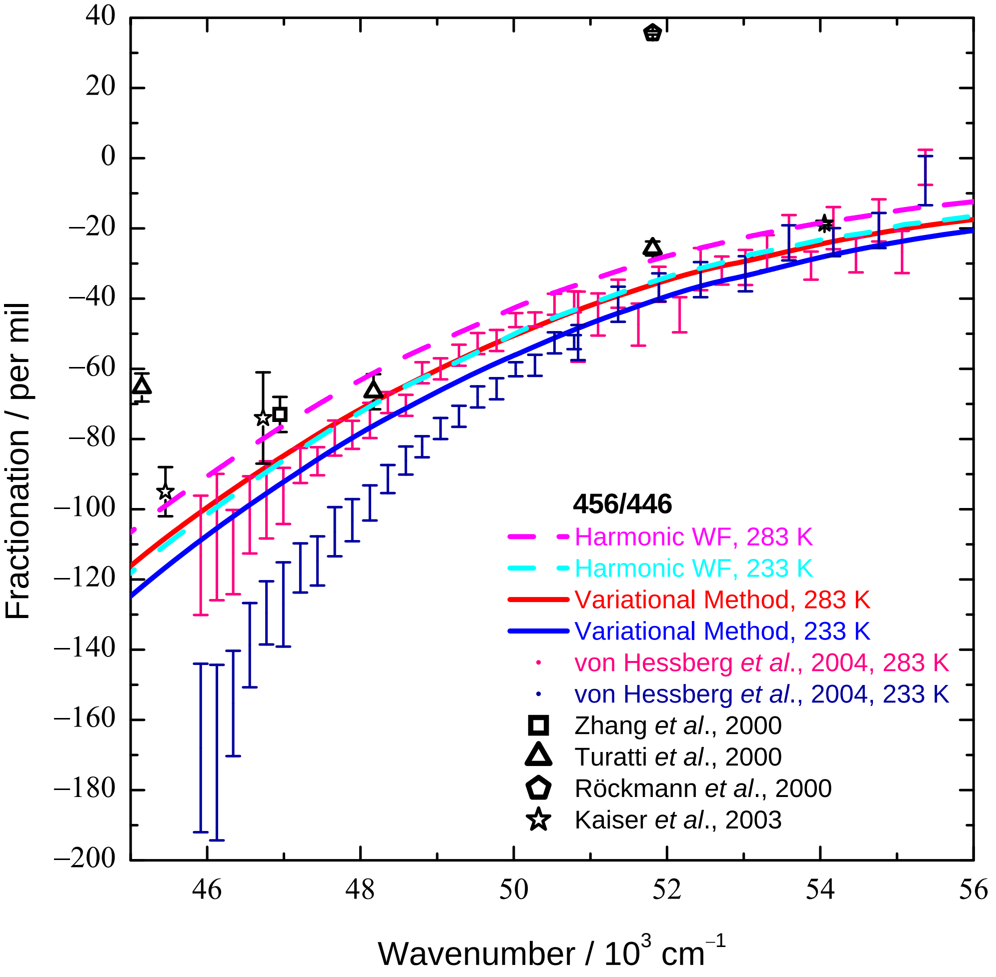

FIG. 5: Fractionation of 456 calculated at 233 and 283 K.

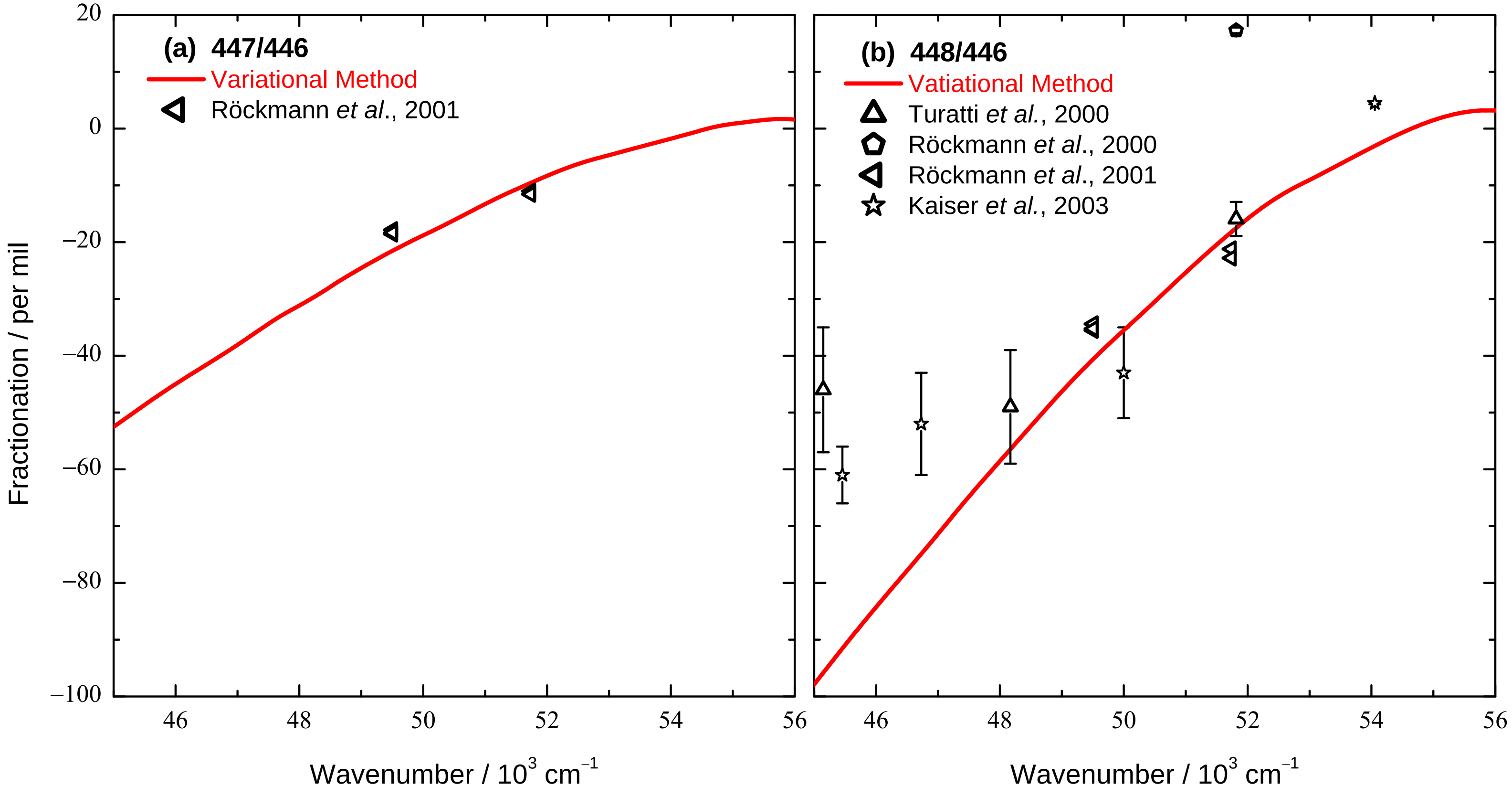

FIG. 6: Fractionation of 447 (a) and 448 (b). The calculated values are at 283 K.

between the energy of ground and excited electronic states, common in *ab initio* calculations. Such differences are indeed expected. A rescaling in height is also reasonable since the *ab initio* calculation of the transition dipole moment $\vec{\mu}_{fi}$ is expected to have some error.[9,10] However, the rescaled amplitude factor at the absorption maximum has no effect on the isotopic fractionations since the factor cancels in equation (6). The total absorption cross sections for other isotopomers are calculated similarly, using the same shift in the peak position as that for 446, since the energy difference between potential energy surfaces is independent of isotopic substitution. The red shifting of the absorption maximum also has a minor effect on the isotopic fractionations.

B. Comparison Between Calculated Absorption Cross Section

In order to test the convergence of the basis set in the variational method, a larger basis set is used to calculate the vibrational wavefunctions in the most abounded isotopomer, 446. The basis set includes eight harmonic wavefunctions for each stretching vibrations, and six nondegenerate ones for the bending vibration. There are 384 orthonormal wavefunctions in the basis set. After rescaled by 1.59 and redshifted by 800 cm^{-1}, there is negligible difference (<0.3%) in the absorption cross section between the larger and smaller basis sets. Therefore, the smaller basis set is also expected to give accurate fractionations.

The absorption cross section obtained by using *ab initio* 3-dimensional surfaces with harmonic wavefunctions are also shown in Figures 1–2. Its rescaled and redshifted parameters are 1.56 and 900 cm^{-1}, respectively. Compared with the absorption cross section obtained by the variational wavefunctions, both give comparable results near peak region, but at the low energy region the harmonic treatment is higher than the variational one, which is closer to experiments,[3,11] as seen in Figure 2.

In Chen et al.[1] the absorption cross section is obtained by using harmonic wavefunctions and approximated 3-dimensional surfaces, which assumes that the NN acts as a spectator in photolysis. Although both harmonic treatments give comparable absorption cross section with experimental values for the long wavelength region, as shown in Figure 1, the treatment with 3-dimensional *ab initio* surfaces gives a significant improvement in the lower energy region, as seen in Figure 2.

C. Experimental Fractionation

In the literature, there are two ways to obtain the experimental wavelength-dependent fractionation. One is by directly measuring the residual N_2O after photolysis at various wavelengths, such as references 12–16. The other measured the relative absorption cross section between isotopomers at various wavelengths, such as reference 3. If the quantum yield were unity at the wavelengths involved, the two types would be the same; then the ratios of photolysis rates and absorption cross sections between isotopomers should be equal. Near the maximum of the absorption cross section, the experimental quantum yield is almost unity.[12] However, in the longer wavelength region, where fractionation is also of interest, the quantum yield may be slightly different between isotopomers if other processes compete because of the smaller internal energy available for direct dissociation. It may be the reason that the fractionation absorption spectrum of 456 and 546 obtained by von Hessberg et al.[3] are lower than other experimental reaction yield fractionation[13–17] at the longer wavelengths.

D. Fractionation

The wavelength-dependent fractionation of isotopomers 546, 556, and 456 calculated relative to the most abundant isotopomer 446 is shown in Figures 3–5. The two types of experimental results are seen to agree with each other and with the calculation for wavelengths longer than 200 nm. For shorter wavelengths, there is a divergence between the two types of experiments,[3,13–17] perhaps for the reason given in the above Section IV C.

Compared with the calculated fractionations in Chen et al.,[1] the current fractionations with the variational method and *ab initio* 3-dimensional surfaces show a much improved agreement for 546 and marginal improvement for 556 in the all the energy region, but slightly worse for 456 at energy lower than 50,000 cm^{-1}. The calculated fractionation for 546, 556 and 456 obtained by using the harmonic wavefunctions are also shown in Figures 3–5. The harmonic treatment gives smaller values of fractionation than the variational one, especially at lower energy region. The variational treatment gives a better agreement with the von Hessberg et al. experiment in all energy region.[3]

The calculated fractionation for 447 and 448 relative to 446 at 283 K is given in Figure 6. At wavelength shorter than 200 nm, both calculational results agree with experiments. There are experimental data for 448 available at longer wavelength. However, the calculated value of the fractionation tends to be larger than experiments, similar to 546 and 456. No absorption spectral data appear to be available for 447 and 448. It would be interesting to measure this wavelength-dependent fractionation of oxygen isotopomers using von Hessberg et al. method.[3] It would also be useful to determine the quantum yields of photodissociation at wavelength longer than 200 nm, as noted earlier.

The NN-stretching was treated as a spectator in the Chen et al. study,[1] and as an active participant in the present calculation. The current results shows that a more accurate treatment. Compared with fractionation of isotopomers, the sensitivity of the calculated fractionation to changes in the wavelength is $556 > 456 > 448 \gtrsim 546 \gtrsim 447$, which is similar to the experiments.[3,13–17]

V. CONCLUSIONS

Building on the previous treatment,[1,4] the current calculations now include 3-dimensional *ab initio* surfaces, and the anharmonicity of the ground electronic potential in the vibrational wavefunctions by the variational method. Compared with the von Hessberg et al. experiment,[3] these improvements in the current theory give improved agreement in the absorption cross section at lower energy region, and notable improvement in fractionation for the 546 isotopomers but marginal changes for 556 and 456.

Quantum yield measurements for wavelength longer than 200 nm, as well as measurements of the relative absorption spectrum between 447/448 and 446 would be useful to understand the difference between the absorption spectra and product yield experimental results.

Acknowledgments

It is a pleasure to acknowledge the support of this research by the National Science Foundation.

APPENDIX A: THE $\mathscr{G}$- AND $\mathscr{F}$-MATRICES

The $\mathscr{G}$- and $\mathscr{F}$-matrices of N^1N^2O are defined as[7]

$$\mathscr{G} = \begin{pmatrix} \frac{1}{m_{N^1}} + \frac{1}{m_{N^2}} & \frac{-1}{m_{N^2}} & 0 \\ \frac{-1}{m_{N^2}} & \frac{1}{m_{N^2}} + \frac{1}{m_O} & 0 \\ 0 & 0 & \frac{1}{m_{N^1}(r_{NN}^{eq})^2} + \frac{1}{m_{N^2}}\left(\frac{1}{r_{NN}^{eq}} + \frac{1}{r_{NO}^{eq}}\right)^2 + \frac{1}{m_O\,(r_{NO}^{eq})^2} \end{pmatrix}, \quad \text{(A1)}$$

$$\mathscr{F} = \begin{pmatrix} k_{NN,NN} & k_{NN,NO} & 0 \\ k_{NN,NO} & k_{NO,NO} & 0 \\ 0 & 0 & k_{\theta,\theta} \end{pmatrix}. \quad \text{(A2)}$$

The mass of each isotope is available from the CRC Handbook.[18] The equilibrium NN and NO distances for N_2O are 1.1273 and 1.1851 Å, respectively, which have been obtained in the literature by minimum residual fitting of the rotational and vibrational spectrum of various isotopomer Teffo and Chédin.[8] The force constants for N_2O in equation (A2) are: $k_{NN,NN} = 18.251$ aJ/Å^2; $k_{NO,NO} = 11.959$ aJ/Å^2; $k_{NN,NO} = 1.028$ aJ/Å^2; and $k_{\theta,\theta} = 0.6659$ aJ/rad^2.[8] The $\mathscr{L}$-matrix is obtained by solving the eigenvectors of the $\mathscr{G}\mathscr{F}$-matrix Wilson et al.[7]

APPENDIX B: HARMONIC VIBRATION WAVEFUNCTIONS

For symmetric and asymmetric stretching, the normalized vibrational wavefunctions are given by

$$\phi_{\nu_i} = \frac{1}{(2^{\nu_i}\nu_i!)^{1/2}}\left(\frac{\alpha_i}{\pi}\right)^{1/4} H_{\nu_i}\left(\alpha_i^{1/2}q_i\right)\exp\left(-\alpha_i q_i^2/2\right), \quad \text{where } \alpha_i = \omega_i/\hbar. \tag{B1}$$

The subscript i equals 1 and 2 for symmetric and asymmetric stretching, respectively. ν_i is the vibrational quantum number. The parameters ω_i and q_i are the vibrational angular frequency and the normal mode coordinate. $H_{\nu_i}(\alpha_i^{1/2}q_i)$ is the Hermite polynomials. The corresponding vibrational energy for ϕ_{ν_i} is $E_{\nu_i} = 2\pi(\nu_i + 1/2)h\omega_i$.

Since the equilibrium structure of N_2O at the ground electronic state is linear, the normalized wavefunctions of degenerated harmonic are given by

$$\phi_{\nu_3,l} = \left[\frac{\alpha_3}{\pi}\frac{\left(\frac{\nu_3-|l|}{2}\right)!}{\left(\frac{\nu_3+|l|}{2}\right)!}\right]^{1/2}\left(\alpha_3 q_3^2\right)^{|l|/2} e^{il\xi} L^{l}_{\frac{\nu_3-|l|}{2}}\left(\alpha_3 q_3^2\right)\exp\left(-\alpha_3 q_3^2/2\right), \tag{B2}$$
$$\text{where } \alpha_3 = \omega_3/\hbar, \text{ and } l = \nu_3,\ \nu_3-2,\ \nu_3-4,\ \ldots,\ -\nu_3,$$

where ξ is an phase angle in the wavefunction, and ω_3 and q_3 are the vibrational angular frequency and the normal mode coordinate for the bending vibration. The quantum numbers ν_3 and l are the vibrational and angular quantum numbers, respectively. $L_n^l(\alpha_3 q_3^2)$ is the Laguerre polynomials. The corresponding vibrational energy is $E_{\nu_3} = 2\pi(\nu_3+1)h\omega_3$.

The unperturbed wavefunction $\Phi_n^{(0)}$ and energy $E_n^{(0)}$ can be expressed as

$$\Phi_n^{(0)} = \Phi^{(0)}_{(\nu_1,\nu_2,\nu_3,l)} = \phi_{\nu_1}\phi_{\nu_2}\phi_{\nu_3,l}, \tag{B3}$$

$$E_n^{(0)} = E^{(0)}_{(\nu_1,\nu_2,\nu_3,l)} = 2\pi h[(\nu_1+1/2)\omega_1 + (\nu_2+1/2)\omega_2 + (\nu_3+1)\omega_3]. \tag{B4}$$

[1] W. C. Chen, M. K. Prakash, and R. A. Marcus, *J. Geophys. Res.-Atmos.* **113**, D05309 (2008).

[2] S. Nanbu and M. S. Johnson, *J. Phys. Chem. A* **108**, 8905 (2004).

[3] P. von Hessberg, J. Kaiser, M. B. Enghoff, C. A. McLinden, S. L. Sorensen, T. Röckmann, and M. S. Johnson, Atmos. Chem. Phys. **4**, 1237 (2004).

[4] M. K. Prakash, J. D. Weibel, and R. A. Marcus, *J. Geophys. Res.-Atmos.* **110**, D21315 (2005).

[5] R. Schinke, *Photodissociation Dynamics* (New York: Cambridge University Press, 1993).

[6] E. J. Heller, *J. Chem. Phys.* **68**, 2066 (1978).

[7] E. B. Wilson, J. C. Decius, and P. C. Cross, *Molecular Vibrations: The Theory of Infrared and Raman Vibrational Spectra* (New York: McGraw-Hill, 1955).

[8] J. L. Teffo and A. Chédin, *J. Mol. Spectrosc.* **135**, 389 (1989).

[9] I. Borges, *Chem. Phys.* **328**, 284 (2006).

[10] M. N. Daud, G. G. Balint-Kurti, and A. Brown, *J. Chem. Phys.* **122**, 054305 (2005).

[11] K. Yoshino, D. E. Freeman, and W. H. Parkinson, Planet. Space Sci. **32**, 1219 (1984).

[12] H. Okabe, *Photochemistry of Small Molecules* (New Jersey: John Wiley, 1978).

[13] H. Zhang, P. O. Wennberg, V. H. Wu, and G. A. Blake, *Geophys. Res. Lett.* **27**, 2481 (2000).

[14] F. Turatti, D. W. T. Griffith, S. R. Wilson, M. B. Esler, T. Rahn, H. Zhang, and G. A. Blake, *Geophys. Res. Lett.* **27**, 2489 (2000).

[15] T. Röckmann, C. A. M. Brenninkmeijer, M. Wollenhaupt, J. N. Crowley, and P. J. Crutzen, *Geophys. Res. Lett.* **27**, 1399 (2000).

[16] T. Röckmann, J. Kaiser, J. N. Crowley, C. A. M. Brenninkmeijer, and P. J. Crutzen, *Geophys. Res. Lett.* **28**, 503 (2001).

[17] J. Kaiser, T. Röckmann, C. A. M. Brenninkmeijer, and P. J. Crutzen, *Atmos. Chem. Phys.* **3**, 303 (2003).

[18] D. R. Lide, editor, *CRC Handbook of Chemistry and Physics* (Boca Raton, FL: CRC Press, 2004), 84th ed.

[19] R. A. Toth, *J. Opt. Soc. Am. B* **3**, 1263 (1986).

[20] C. Amiot, *J. Mol. Spectrosc.* **59**, 380 (1976).

[21] K. Jolma, J. Kauppinen, and V. M. Horneman, *J. Mol. Spectrosc.* **101**, 278 (1983).

[22] R. A. Toth, *J. Opt. Soc. Am. B* **4**, 357 (1987).

Chapter 6

Slopes of Multi-Element Isotope Plots of Fractionation in Photolysis of N_2O: A Mass-Dependent Theory for Isotopomers Where Two Effective Masses Contribute

[This chapter prepared for the *Journal of Chemical Physics*.]

Abstract

A single effective mass usually serves to determine the slope of a multielement isotope plot and to yield approximate agreement between the experimental data and a "mass-dependent" fractionation. The data typically treated are for reactions that involve with little change in total "bond order," one bond broken and another formed. Instead, we treat a photolytic dissociation where the total bond order changes. In the present instance of the photolytic dissociation of N_2O, the computational and experimental results largely agree, but two effective masses are needed to understand intuitively the slopes of the multielement isotope plots, which range from 0.47 to 3.28. A linear combination of the main coordinates for the dissociation provides agreement with these numerical slopes. For the particular case of a multielement isotope plot of 448 vs 447 (which is also a usual three-isotope plot), the two-effective mass result reduces to the usual single mass case, so explaining why the slope value is $\sim$0.5 in this case. The present theory also agrees with the experimental slopes in multielement isotope plots.

I. INTRODUCTION

Customarily, isotopic fractionation plots in the literature are those in which for some series of samples the isotopic enrichment of one isotope is plotted vs that of another, such as $^{17}O/^{16}O$ vs $^{18}O/^{16}O$.[1–3] The slope of the plot is then compared with theory, particularly the well-known Bigeleisen-Mayer theory.[4] Other examples of such plots include those for the sulfur isotopes, and many others.[5,6]

Recently, a related but different kind of fractionation plot has appeared in the literature, one in which the isotopic fractionation of one element is plotted versus that of another, e.g. Park et al.,[7] Bindeman et al.,[8], and Sturchio et al.[9] In one of these multielement isotope plots, the enrichment in an N isotope was plotted versus that for an O isotope.[7] In another case, the enrichment in S and O isotopes of volcanogenic sulfate aerosols was studied.[8] In the other case, the Cl and O isotopic fractionation due to biodegradation of perchlorate was plotted.[9] In the present paper, we explore multielement isotope fractionation plots and for concreteness focus on such a plot for a particular system, N_2O photolysis.

The photolysis of N_2O has been extensively studied in the literature, summarized in Part 1−3.[10–12] Prakash et al. also used a first-order expansion analysis to gain insight into the consequences of the theoretical expression for the slope of the oxygen three-isotope plot in photolytic fractionation of N_2O.[13] The slope obtained by a first-order analysis for the oxygen mass-dependent effect agreed well with that obtained in detailed computations.

In the present article, a first-order analysis similar to that used for the previous result,[13] but extended to other isotopomers is used. Previously 447 and 448 were measured relative to 446 and plotted as the usual three-isotope plot. Only the O isotope was varied. Now the N atoms are also varied yielding a "multielement" isotope fractionation plot. multielement isotope fractionation plots have appeared in the literature in Park et al.,[7] Bindeman et al.,[8], and Sturchio et al.[9] The slopes of multielement isotope plots in the photolysis of N_2O vary from 0.47 to 3.28. We find that a simple single reduced mass no longer suffices to understand the theoretical results. All normal coordinates are now affected in the additional isotopomers in which the central N is varied. The experimental slopes in the multielement isotope plots are very close to the results obtained by the present first-order expansion analysis using reduced masses. To understand the detailed results of the numerical calculations of the slope of the multielement isotope plots for different isotopomers, we consider the physical nature of the photolysis coordinates of the photodissociation of N_2O and give an approximate theoretical expression of the mass effect in the multielement isotope fractionation plots.

II. THEORY

A. Absorption Cross Section

The theoretical procedure used to obtain absorption cross sections for the N_2O isotopomers was described previously,[12] and is briefly summarized here. UV photolysis of N_2O is essentially a direct dissociation, since the absorption spectrum is a broad envelope with a only weak structure superimposed. Thereby, the absorption cross section can be obtained using the multidimensional reflection principle.[14,15] The absorption cross section σ is given by[11]

$$\begin{aligned}\sigma_{f\tilde{n}}(\omega) &= \frac{\pi\omega}{\hbar\epsilon_0 c}\frac{1}{2\pi}\int_{-\infty}^{\infty}\mathrm{d}t\langle\Psi_{\tilde{n}}|\vec{\mu}_{fi}^{\dagger}\mathrm{e}^{-iH_f t/\hbar}\vec{\mu}_{fi}|\Psi_{\tilde{n}}\rangle\mathrm{e}^{i(\omega+E_i/\hbar)t} \\ &\approx \frac{\pi\omega}{3\epsilon_0 c}\int\mathrm{d}\mathbf{Q}\,|\Psi_{\tilde{n}}(\mathbf{Q})|^2\,|\vec{\mu}_{fi}(\mathbf{R})|^2\,\delta\left(\hbar\omega - V_f(\mathbf{R}) + V_i(\mathbf{R})\right) \qquad (1)\end{aligned}$$

where $\mathbf{R}$ and $\mathbf{Q}$ denote internal and normal coordinates, respectively. The transition dipole moment function $\vec{\mu}_{fi}(\mathbf{Q})$ is a transition between the ground and the excited electronic states i and f, respectively. The difference of potential energy surfaces between the electronic excited and ground states is denoted as $V_f(\mathbf{Q}) - V_i(\mathbf{Q})$. The probability density of the initial nuclear vibrational state $\tilde{n}$ in the ground electronic state i is $|\Psi_{\tilde{n}}(\mathbf{Q})|^2\,\mathrm{d}\mathbf{Q}$.

B. Fractionation

Different isotopomers have the same potential energy function but differ in their normal mode frequencies and normal coordinates, and thereby differ in the width of the electronic ground state wave function, $\Psi_{\tilde{n}}(\mathbf{Q})$. Accordingly, they have different absorption cross sections at any wavelength, leading to a fractionation of the isotopomers by photodissociation, particularly in the wings of the absorption band. The photodissociation rate $J(\omega)$ of a molecule is given as

$$J(\omega) = \sigma_{total}(\omega)I(\omega)\phi(\omega), \qquad (2)$$

where $I(\omega)$ is the photo flux at frequency ω and $\phi(\omega)$ is the quantum yield of the reaction at that ω. The quantum yield $\phi(\omega)$ is assumed to be unity in the photolysis of N_2O

due to the direct or nearly-direct nature of the photodissociation. The total absorption cross-section $\sigma_{total}(\omega)$ is obtained by adding the contributions at ω from all vibrational states in the electronic ground state, weighted by their thermal populations according to the Boltzmann distribution. The fractionation factor is dependent upon the ratio of the photolysis rates for the isotopomers A' and A and is written as

$$\epsilon_A^{A'} = \frac{J_{A'}(\omega)}{J_A(\omega)} - 1 = \frac{\sigma_{total}^{A'}(\omega)}{\sigma_{total}^{A}(\omega)} - 1. \tag{3}$$

In a multielement isotope plot the ϵ value of one isotopomer is plotted versus that of another, both relative to the same isotopomer.

C. A First Order Analysis of Mass Dependence

In the present paper, we extend the first-order expansion for the slope of the oxygen three-isotope plot[13] to a more general case. $\vec{\mu}_{fi}(\mathbf{R})$ and $V_f(\mathbf{R})$ in equation (1) are independent of isotopic substitutions since $\mathbf{R}$ is mass independent. We recall that $|\Psi_n(\mathbf{Q})|^2\,\mathrm{d}\mathbf{Q}$ is mass dependent because the $\mathbf{Q}$ are the normal coordinates of a isotopomer and they are mass dependent. A Taylor series expansion of the total absorption cross section, σ_{total}, is used to the first order. If the reduced mass μ_i of the coordinate x_i in the $\mathbf{X}$ coordinate space is changed due to isotopic substitution, the first order expansion treatment for the entire expression of the cross section involves the first order difference in reciprocal masses $\Delta(\mu_i) = \mu_i^{A'} - \mu_i^{A}$ for the two isotopomers, A and A':

$$\sigma_{total}^{A'}(\omega) \approx \sigma_{total}^{A}(\omega) + \sum_i \frac{\partial \sigma_{total}^{A}(\omega)}{\partial \mu_i} \Delta(\mu_i). \tag{4}$$

According to the physical properties of photodissociation of N_2O, in which the N_2 bond length changes only slightly as a result of the photolysis, there are two different reduced masses crucial in the fractionation. Since the photoabsorption is promoted by the bending modes and since the asymmetric stretching mode of N_2O leads to the photolysis products N_2 and O, both motions are important in the dissociation. They can be described in terms of two reduced masses, one being that of the oxygen atom and the nitrogen molecule, and the second being the oxygen atom and the nitrogen atom to which it is bonded, since the NN bond length is not very different in N_2O and N_2. The μ_k that is the best choice to represent this photodissociation is some linear combination of the two reduced masses of the above two coordinates for a molecule labeled as N^1N^2O, $1/\mu_1 = 1/(m_{\mathrm{N}^1}+m_{\mathrm{N}^2})+1/m_{\mathrm{O}}$ and $1/\mu_2 = 1/m_{\mathrm{N}^2} + 1/m_{\mathrm{O}}$.

With this assumption that some linear combination of the μ_is in equation (4), denoted by μ_k, the absorption cross section becomes

$$\sigma^{A'}_{total}(\omega) \approx \sigma^{A}_{total}(\omega) + \frac{\partial \sigma^{A}_{total}(\omega)}{\partial \mu_k}\Delta(\mu_k). \tag{5}$$

Thus, the slope β of the $\epsilon^{A''}_{A}$ vs $\epsilon^{A'}_{A}$ plot based on the above first-order expansion is obtained as

$$\beta = \frac{\mu^{A''}_k - \mu^{A}_k}{\mu^{A'}_k - \mu^{A}_k}, \tag{6}$$

where A usually is the isotopomer with the most abundant isotopes, the A' and A'' isotopomers have isotope substitution on the same element. If there are substitutions on different elements, an experience factor $f^{\mathrm{N}}_{\mathrm{O}}$ should be included since the linear combination of μ_1 and μ_2 would overemphasize the contribution from oxygen. The more general form of equation (6) is

$$\beta = f_{\mathrm{O}}^{\mathrm{N}} \frac{\mu_k^{A''} - \mu_k^{A}}{\mu_k^{A'} - \mu_k^{A}}, \tag{7}$$

where the A' and A'' isotopomers have isotope substitution at oxygen and nitrogen, respectively, and the current fitted $f_{\mathrm{O}}^{\mathrm{N}}$ value is 5.2 in the $\mathrm{N_2O}$ phtolysis. And so the ratio of the relative difference of the reduced masses μ_ks of isotopomers in equations (6) and (7) appears as a slope in each multielement isotope plot.

III. RESULTS AND DSCUSSION

A. Slopes of multielement Isotope Plots of Fractionation

The purpose of the present article is to understand the slopes for the different comparisons of isopotomers, given by the detailed computations in Chen et al.[12] To the tend the approximate perturbation model descried earlier is used.[13] The calculated slopes of a multielement isotope plots for various isotopomers are given in Table I, where the subscript 446 is omitted, the fractionation obtained by the ratio of the absorption cross-section relative to that for this most abundant isotopomer of $\mathrm{N_2O}$. They are compared there with the detailed computational results of Chen et al.[12]

We use weighting factors, 91% and 9%, respectively, to obtain best agreement with the results of the numerical calculations, $\mu_k = 0.91\mu_1 + 0.09\mu_2$. Presumably the derivation of μ_1 here is because the process is mainly a dissociation into $\mathrm{N_2}$+O, while the μ_2 reflects a torque acting on the $\mathrm{N^2}$ due to the large bending angle of the excited $\mathrm{N_2O}$, as well as in part the $\mathrm{N_2}$-O repulsion. The approximate slopes obtained using μ_k and equations (6)

TABLE I: Calculated slopes of multielement isotope plots. The Pearson's coefficient of the linear regression of the theoretical calculations are better than 0.99.

	Lin. Comb. Approx.	233 K[a]	283 K[a]	298 K[a]
	Isotope Substitution at a Single Element			
ϵ^{448} vs ϵ^{447}	0.512	0.537	0.538	0.539
ϵ^{456} vs ϵ^{546}	0.826	0.820	0.829	0.844
ϵ^{556} vs ϵ^{456}	0.559	0.568	0.570	0.572
ϵ^{556} vs ϵ^{546}	0.461	0.471	0.474	0.481
	Isotope Substitution at Both Elements			
ϵ^{448} vs ϵ^{456}	0.993	1.003	0.999	1.003
ϵ^{448} vs ϵ^{546}	0.820	0.850	0.833	0.828
ϵ^{448} vs ϵ^{556}	1.777	1.766	1.756	1.756
ϵ^{447} vs ϵ^{456}	1.937	1.861	1.859	1.867
ϵ^{447} vs ϵ^{546}	1.600	1.577	1.549	1.540
ϵ^{447} vs ϵ^{556}	3.468	3.278	3.267	3.269

[a] The slope is obtained by fitting the result of numerical theory in reference 12.

and (7) are seen in Table I to be very close to the linear fit of the detailed computational results. They are also seen to be very different from the usual 0.5 slope for a fractionation of an isotope with a mass unit difference compared with that for an isotope with two mass units difference.

The use of two coordinates and their combination to describe the mass dependence in a reaction appears to be novel although multielement isotope fractionation plots are given in the literature, such as Park et al.,[7] Bindeman et al.,[8], and Sturchio et al.[9] This case of two effective masses is also closely related to a related reaction coordinate introduced by Klippenstein in variational RRKM to find the transition state of a thermal barrierless unimolecular dissociation reaction.[16] The best reaction coordinate to describe the system was neither the length of the breaking bond (here N^2-O) nor the distance between the center of masses of the dissociation fragments (here, that of N^1-N^2 and O), but rather a linear combination of these two coordinates. The interpretation of the present results for a dissociation invoking two coordinates and two effective masses may also apply to multielement isotope plots for other direct photodissociations, but at this stage of their interpretation would need to be examined on a case by case basis.

In the formation of N_2 and O from N_2O, both bending and asymmetric stretching modes are directly involved in the reaction coordinate of photodissociation. The slopes obtained by μ_k and by the reduced mass of each normal coordinate are compared in Table II with the full theoretical results. Since the symmetric stretching mode has little correlation with the dissociation reaction, its slopes gives strange values in all nitrogen isotopomers (see Table II).

TABLE II: Slopes of multielement isotope plots in isotopic nitrogen substituted istopomers. The slopes obtained by linear combination method of reduced mass (μ_k) and normal coordinates are compared with the full theoretical results.

Method	ϵ^{448} vs ϵ^{447}	ϵ^{556} vs ϵ^{456}	ϵ^{556} vs ϵ^{546}	ϵ^{456} vs ϵ^{546}
Numerical Theory[a]	0.537	0.572	0.471	0.820
Lin. Comb. Approx. (μ_k)	0.512	0.559	0.461	0.826
Asymmetric Stretching	0.535	0.794	0.186	0.234
Symmetric Stretching	0.510	-0.033	1.042	-31.240
Bending	0.527	0.782	0.199	0.254

[a] The temperature is 233 K.

B. Comparison with Experiments

A multielement isotope plots calculated by Chen et al.,[12] are shown in Fig. 1 for ϵ^{448} vs ϵ^{447}, in Fig. 2 for ϵ^{556} vs ϵ^{456}, in Fig. 3 for ϵ^{556} vs ϵ^{546}, and in Fig. 4 for ϵ^{456} vs ϵ^{546}. All computational results show reasonable agreement with available experimental data in laboratories.[17,18] They also give good agreement with the slopes of multielement isotope plots calculated by a first-order approximation with the linear combinate coordinate, as given in Table I.

However, the observations of the slopes of ϵ^{456} vs ϵ^{546}, ϵ^{448} vs ϵ^{456}, and ϵ^{448} vs ϵ^{546} in the stratosphere are listed in Table III.[7,19,20]. The slopes of ϵ^{456} vs ϵ^{546}, and ϵ^{448} vs ϵ^{546} obtained by our linear combination approximation are within the values of some experimental error. However, the linear combination approximation gives a significantly smaller value in ϵ^{448} vs ϵ^{456}. This difference may be due to the anomalous mass effect of N_2O caused by other chemical reactions in troposphere and lower stratosphere, as discussed by McLinden et al. using a global model.[21]

C. Applied to Other Systems

The first-order expansion method with a linear combination of two effective reduced masses give a successful approximation in the slopes of the multielement isotope plots in the N_2O photolysis. This method may be extended to other mass-dependent reactions once the rate is dominated by a single rate-controlling step. For example, a multielement isotope plot of oxygen and chlorite isotopic fractionation is obtained by studying

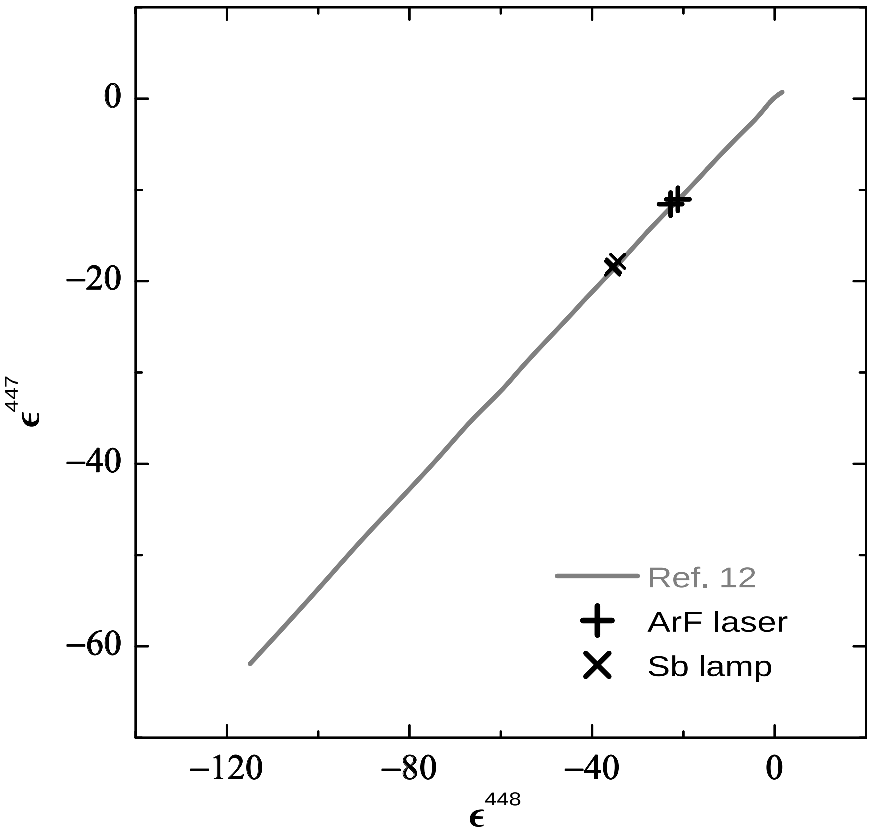

FIG. 1: Three-isotope plot of oxygen isotopologues of N_2O in units of per mil. The experimental data are from Röckmann et al.[17] The linear regression slope of the numerical theory at 233 K obtained by Chen et al.[12] is 0.537.

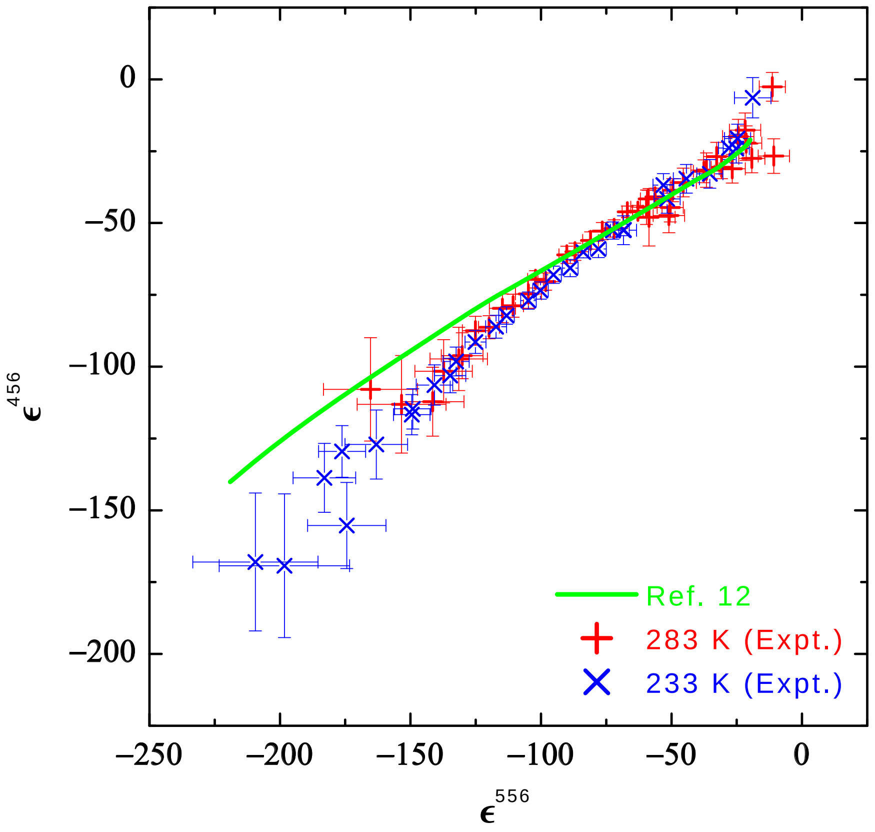

FIG. 2: multielement isotope plot of ϵ^{556} vs ϵ^{456} in units of per mil. The experimental data are from von Hessberg et al.[18] The linear regression slope of the numerical theory at 233 K obtained by Chen et al.[12] is 0.572.

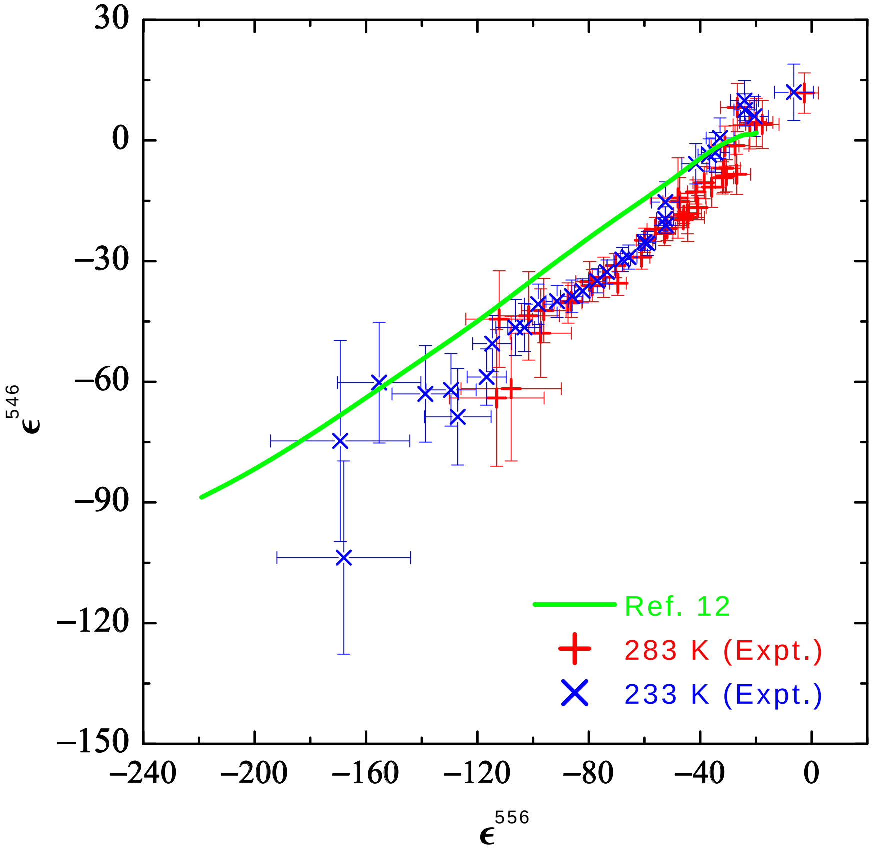

FIG. 3: multielement isotope plot of ϵ^{556} vs ϵ^{546} in units of per mil. The experimental data are from von Hessberg et al.[18] The linear regression slope of the numerical theory at 233 K obtained by Chen et al.[12] is 0.471.

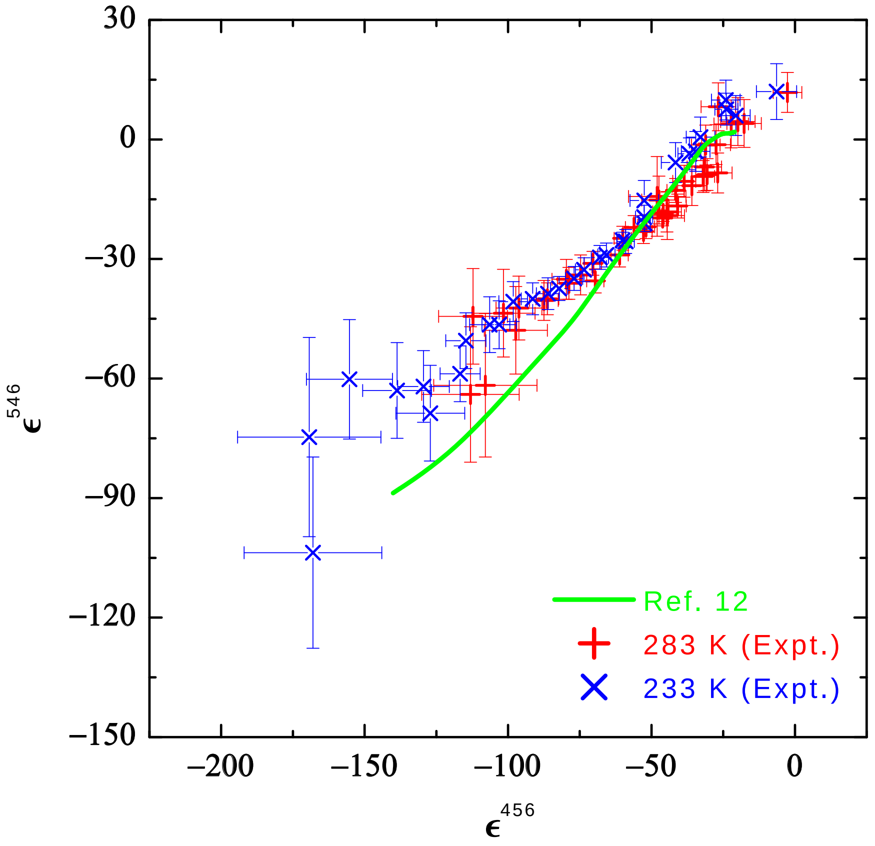

FIG. 4: multielement isotope plot of ϵ^{456} vs ϵ^{546} in units of per mil. The experimental data are from von Hessberg et al.[18] The linear regression slope of the numerical theory at 233 K obtained by Chen et al.[12] is 0.820.

TABLE III: The slopes of multielement isotope plots. The number given in parentheses are the values of 2σ uncertainties in experiments.

	ϵ^{456} vs ϵ^{546}	ϵ^{448} vs ϵ^{456}	ϵ^{448} vs ϵ^{546}
Lin. Comb. Approx.	0.826	0.993	0.820
		Park et al.[7]	
Photolysis	0.42 (±0.03)	1.55 (±0.06)	0.65 (±0.04)
$<$ 200 ppbv SOLVE[a]	0.38 (±0.07)	1.70 (±0.07)	0.64 (±0.12)
$<$ 200 ppbv POLARISII[b]	0.56 (±0.27)	1.58 (±0.21)	0.82 (±0.29)
$<$ 200 ppbv All	0.43 (±0.06)	1.65 (±0.06)	0.68 (±0.20)
$>$ 200 ppbv All	0.38 (±0.14)	1.70 (±0.17)	0.53 (±0.22)
		Toyoda et al.[20] [c]	
$>$ 24.1 km	0.38 (±0.03)	1.66 (±0.13)	0.63 (±0.04)
$<$ 24.1 km	0.38 (±0.13)	1.99 (±0.66)	0.77 (±0.34)
		Röckmann et al.[19] [c]	
All	0.50 (±0.03)	1.54 (±0.07)	0.76 (±0.04)
$>$ 200 ppbv	0.61 (±0.12)	1.51 (±0.24)	0.92 (±0.22)

[a] Stratospheric aerosol and gas experiment III Ozone Loss and Validation Experiment (SOLVE).[23]

[b] Photochemistry of Ozone Loss in the Artic Region in Summer (POLARIS) mission from April and September 1997.[24]

[c] The slopes shown here for the Toyoda et al.[20] and Röckmann et al.[19] data were calculated by Park et al.[7] from their original publications.

the biodegradation of perchlorate.[9] The widely accepted pathway now of biological degradation have been reported as follows: (i) perchlorate (ClO_4^-) is first reduced to chlorate (ClO_3^-) and then to chlorite (ClO_2^-) by the perchlorate reductase, and (ii) the ClO_2^- then undergoes a disproportionation reaction catalyzed by the chlorite dismutase to yield Cl^- and O_2.[22] However, the detailed mechanism at the molecular level is still absent. If the rate-controlling step is the $E_1 \cdot O_x Cl\text{-}O \cdot E_2 \rightarrow E_1 \cdot O_x Cl + O \cdot E_2$ reaction (where E_1 and E_2 are the crucial parts of the enzyme binding with ClO_{x+1} and the charge state is omitted in the reaction equation), two effective reduced mass to describe the mass-dependent properties of the reaction may be $1/\mu_1 = 1/m_{\mathrm{Cl}} + 1/m_{\mathrm{O}}$ and $1/\mu_2 = 1/m_{\mathrm{E_1 \cdot O_x Cl}} + 1/m_{\mathrm{O \cdot E_2}}$. The coefficient for the linear combination of μ_1 and μ_2 can be determined by the fractionation experiments of oxygen or chlorine isotopic substitutions. The slope in the corresponding multielement isotope plot may be estimated by using equation (7).

The observed enrichments in S and O isotopes of volcanogenic sulfate aerosols on the multielement isotope plot by Bindeman et al.[8] are scattered too much to define a slope. It may involves many independent reactions, which would make it very difficult to apply the current method.

IV. CONCLUSIONS

Using a first-order expansion method with a newly defined photolysis reduced mass and coordinate obtained by a linear combination, the slopes of the multielement isotope plots are close to the theoretical detailed calculation of photodissociation fractionation of N_2O, and are similar to experimental results. The concept of photolysis coordinate defined by a linear combination of coordinates is a fruitful one in the present case and can be extended to study the mass-dependent effect of other direct or nearly direct photodissociation reactions or of other chemical reaction with a single rate-controlling step.

Acknowledgments

It is a pleasure to acknowledge the support of this research by the National Science Foundation.

---

[1] R. N. Clayton, L. Grossman, and T. K. Mayeda, Science **182**, 485 (1973).

[2] M. H. Thiemens, Science **283** (1999).

[3] M. H. Thiemens, *Annu. Rev. Earth Planet. Sci.* **34** (2006).

[4] J. Bigeleisen and M. G. Mayer, *J. Chem. Phys.* **15**, 261 (1947).

[5] R. E. Criss and J. Farquhar, *Rev. Mineral. Geochem.* **68** (2008).

[6] S. Amari, L. R. Nittler, E. Zinner, K. Lodders, and R. S. Lewis, *Astrophys. J.* **559** (2001).

[7] S. Y. Park, E. L. Atlas, and K. A. Boering, J. Geophys. Res. - Atmos. **109**, D01305 (2004).

[8] I. N. Bindeman, J. M. Eiler, B. A. Wing, and F. J., *Geochimica et Cosmochimica Acta* **71**, 2326 (2007).

[9] N. C. Sturchio, J. K. Böhlke, A. D. Beloso, Jr., L. J. Heraty, and P. B. Hatzinger, *Environ. Sci. Technol.* **41**, 2796 (2007).

[10] M. K. Prakash, J. D. Weibel, and R. A. Marcus, *J. Geophys. Res.-Atmos.* **110**, D21315 (2005).

[11] W. C. Chen, M. K. Prakash, and R. A. Marcus, *J. Geophys. Res.-Atmos.* **113**, D05309 (2008).

[12] W. C. Chen, R. A. Marcus, and S. Nanbu, **manuscript** (2009).

[13] M. K. Prakash and R. A. Marcus, *J. Chem. Phys.* **123**, 174308 (2005).

[14] E. J. Heller, *J. Chem. Phys.* **68**, 2066 (1978).

[15] R. Schinke, *Photodissociation Dynamics* (New York: Cambridge University Press, 1993).

[16] S. J. Klippenstein, Chem. Phys. Lett. **214**, 418 (1993).

[17] T. Röckmann, J. Kaiser, J. N. Crowley, C. A. M. Brenninkmeijer, and P. J. Crutzen, *Geophys. Res. Lett.* **28**, 503 (2001).

[18] P. von Hessberg, J. Kaiser, M. B. Enghoff, C. A. McLinden, S. L. Sorensen, T. Röckmann, and M. S. Johnson, *Atmos. Chem. Phys.* **4**, 1237 (2004).

[19] T. Röckmann, J. Kaiser, C. A. M. Brenninkmeijer, J. N. Crowley, R. Borchers, W. A. Brand, and P. J. Crutzen, J. Geophys. Res. - Atmos. **106**, 10403 (2001).

[20] S. Toyoda, N. Yoshida, T. Urabe, S. Aoki, T. Nakazawa, S. Sugawara, and H. Honda, *J. Geophys. Res.-Atmos.* **106**, 7515 (2001).

[21] C. A. McLinden, M. J. Prather, and M. S. Johnson, *J. Geophys. Res.-Atmos.* **108** (2003).

[22] J. D. Coates and L. A. Achenbach, *Nature Rev. Microbiol.* **2** (2004).

[23] P. A. Newman, N. R. P. Harris, A. Adriani, G. T. Amanatidis, J. G. Anderson, G. O. Braathen, W. H. Brune, K. S. Carslaw, M. S. Craig, P. L. DeCola, et al., *J. Geophys. Res.-Atmos.* **107** (2002).

[24] P. A. Newman, D. W. Fahey, W. H. Brune, and M. Kurylo, *J. Geophys. Res.-Atmos.* **104**, 26481 (1999).

Chapter 7

Photochemical Fractionation of N_2O: A Comparison of Theory and Laboratory Measurements

[This chapter submitted to *Geophysical Research Letters*.]

Abstract

Using the three-isotope plot formalism given in Prakash and Marcus,[1] and in Chen and Marcus[2] we compare the theory with the laboratory measurements. There is good agreement between the experimental and theoretical results for the fractionation for the limited data. Plots are also given for the wavelength dependence of the ratio of the fractionations and are similarly compared with the available data. The contribution of photodissociation to the observed isotopic anomaly and the motivation for further wavelength dependent fractionation studies are discussed.

I. Introduction

Photodissociation of N_2O and the isotopic fractionation introduced by it are of considerable atmospheric interest.[3] Recently we published theoretical calculations of the absorption cross section of N_2O.[4,5] Detailed wavelength-dependent absorption cross sections of isotopologue 446 (abbreviated form for $^{14}N^{14}N^{16}O$) and wavelength-dependent fractionation factors for the isotopologues 447, 448, 456, 546, 556 all relative to 446 were published in Prakash et al.[4] and in Chen et al.[5] In a separate article[1] a three-isotope plot for isotopologues 446, 447, 448 was given using these calculated fractionation values. In another article[2] a three-isotope plot for various isotopologues, including 456, 546 and 556, was given using these calculated fractionation values. In these articles a perturbation theoretical method using reduced masses to estimate the slope for a nearly direct photodissociation process was also given, and it served to explain why the slope from the numerically calculated photochemical result agreed with the standard thermal result. In the present note we give a graphical comparison between available laboratory measurements, presently very sparse, of fractionation and of three-isotope plots with plots based on fundamental physics-based theory, with an aim of stimulating further experiments.

II. Results

In Chen et al.[5] the time-independent multidimensional reflection principle was used to obtain the absorption cross section σ of N_2O as a function of wavelength λ. Using $\sigma(\lambda)$, the wavelength-dependent fractionation factors such as $\varepsilon_{447}(\lambda)$ were calculated from $\varepsilon_{447}(\lambda) = \sigma_{447}(\lambda)/\sigma_{446}(\lambda) - 1$. When a broadband light source is used for excitation, the wavelength-dependent light source intensity was used as the weighting factor to obtain the averaged value of the fractionation factor.[5]

In Prakash and Marcus[1] a three-isotope plot for the isotopolgues 446, 447, 448 was given using the fractionation values computed in Prakash et al.[4] In Prakash and Marcus[1] the data from the laboratory measurements of Röckmann et al.[6] were not used for a reason given in footnote #30; namely that the error bar in the measurements of 447 and 448 could add up to increase the uncertainty in the measurement of the ratio $\varepsilon_{447}/\varepsilon_{448}$. However, the errors in the measurement of ε_{447} and ε_{448} are usually correlated, (we thank Jan Kaiser for this point) thereby reducing the error bar on the ratio $\varepsilon_{447}/\varepsilon_{448}$. In this paper we compare the laboratory measurements of Röckmann et al.[6] with the theoretical results given in Prakash and Marcus[1] and Chen and Marcus.[2]

Describing the fractionation measurement made in the closed system by a Rayleigh fractionation process the relation between the fractionation ε_{447} and isotopic enrichment δ^{17} is given by:[7]

$$\varepsilon_{447} \ln y = \ln(1 + \delta^{17}) \qquad (1)$$

where y is the fraction of 446 remaining. Using the values given in Table 1 of Röckmann et al.[6] (see also Table 18 of reference 8) the fractionation factors are computed and tabulated in table 1. These values are plotted in figure 1 along with the fractionation factors calculated at 298 K in Chen et al.[5] It can be seen that the calculations are in good agreement with the measurements.

Table 1: Experimental fractionation factors from reference 6.

Light Source	λ (nm)	Conversion (y) (%)	$\delta^{17\,a}$	$\delta^{18\,a}$	$\varepsilon_{447}{}^{a}$	$\varepsilon_{448}{}^{a}$
ArF laser	193.3	71.3%	3.7	7.2	−11.03	−21.21
ArF laser	193.3	51.6%	7.7	15.2	−11.56	−22.80
Sb lamp	185-225	57.6%	10.3	19.8	−18.57	−35.54
Sb lamp	185-225	59.2%	9.4	18.2	−17.83	−34.40
Sb lamp	185-225	29.1%	22.9	44.5	−18.33	−35.27

[a] Unit is per mil.

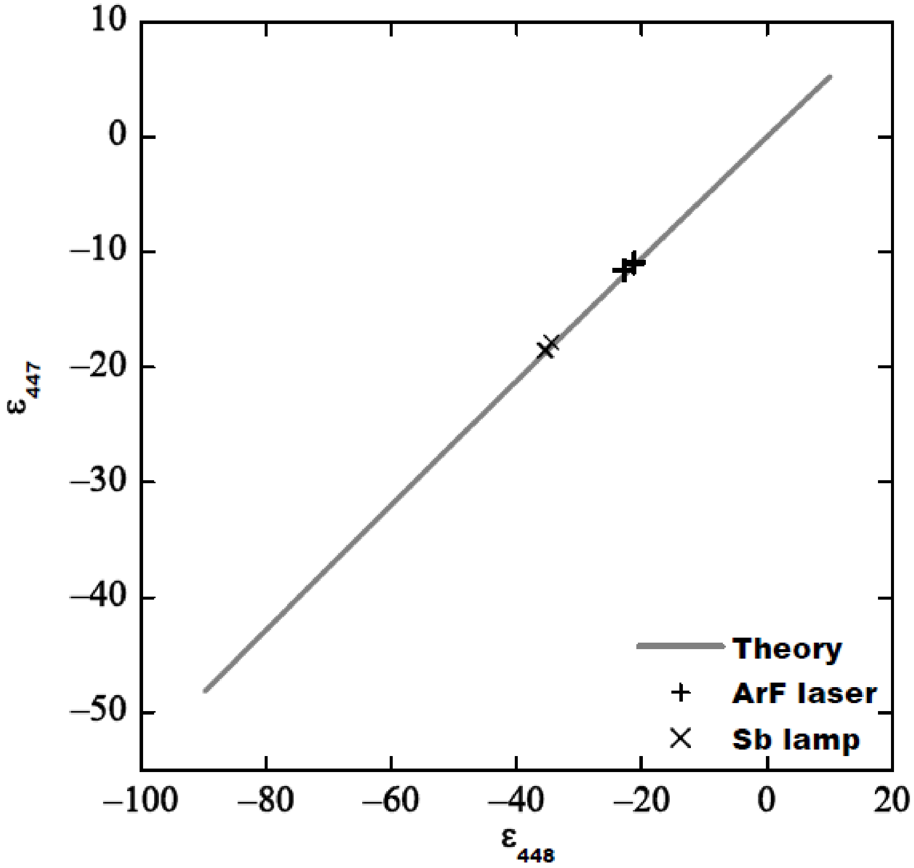

Figure 1: Three isotope plot of oxygen isotopologues of N_2O in units of per mil.

In figure 1 the details of the wavelength dependence of the fractionations are not given but they are shown in figure 2. figure 2 is based on the following calculations of the individual values of fractionation factor for the wavelengths used in measurement. Corresponding to the ArF laser wavelength of 193.3 nm,[6] the fractionation factors $(\varepsilon_{447}, \varepsilon_{448})$ obtained by calculation seen are (−8.85**,** −16.78). They may be compared with the two sets of measured values (−11.03, −21.21) and (−11.56, −22.80).[6] For the Sb source, the averaged values of the fractionation factors were calculated as described in Chen et al.[5] The calculated values of $(\varepsilon_{447}, \varepsilon_{448})$ are (−17.85**,** −33.84), and the measured values for three sets of measurements are (−18.57, −35.54), (−17.83, − 34.40), and (−18.33, −35.27).

A second way of showing the wavelength dependence of the fractionation is by plotting the ratios $\varepsilon_{447}(\lambda)/\varepsilon_{448}(\lambda)$ and $\ln(1+\varepsilon_{447}(\lambda))/\ln(1+\varepsilon_{448}(\lambda))$ as a function of λ, as in figure 1 of Kaiser et al.[7] These plots comparing the experimental data from Röckmann et al.[6] to the detailed computations of Johnson et al.[9] and Chen et al.[5] are shown in the present figure 2. The ratios of fractionations predicted by the two theoretical models[5,9] are nearly similar, as seen in figure 2. It should be noted that while the comparison of the fractionations of ε_{447} and ε_{448} by taking the ratio highlights the wavelength dependence, it can lead to problems with interpretation if a ratio close to the absorption maximum (182 nm) is taken, since ε_{448} approaches zero there and is the reason for very high values of the ratio in that region. The plot of ε_{447} vs. ε_{448} has a small but finite intercept[1,2] meaning that the zeros of ε_{447} and ε_{448} are slightly offset and so the

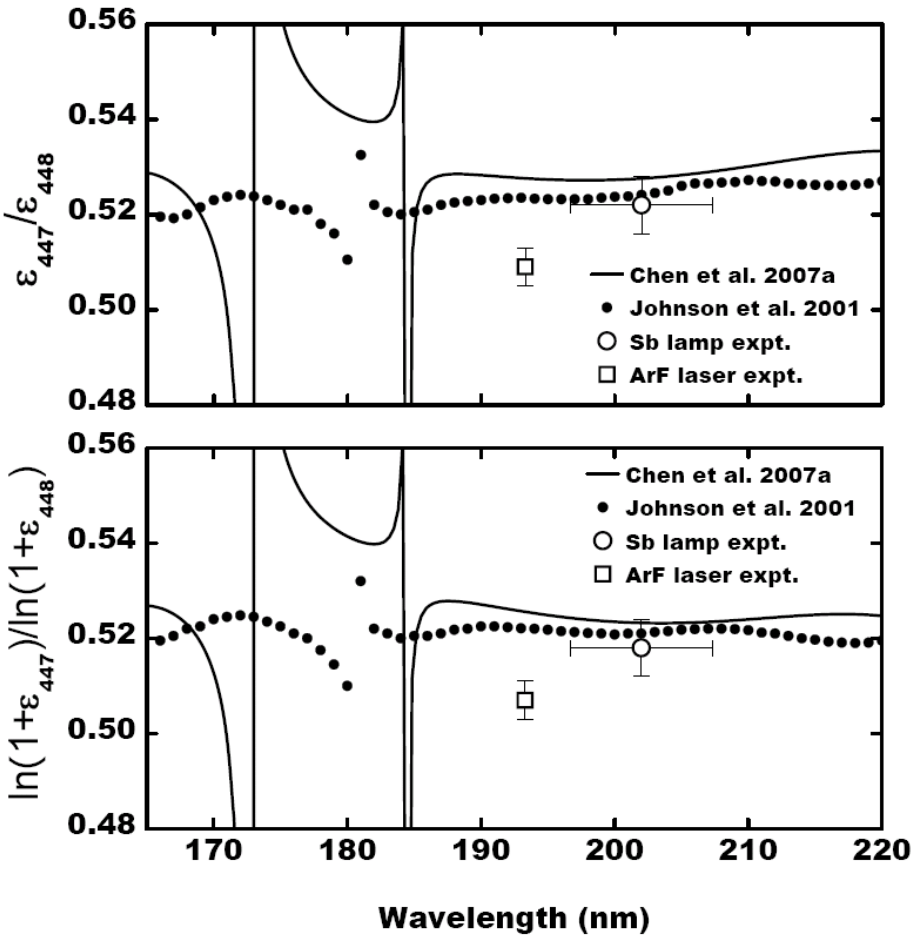

Figure 2: Wavelength dependence of isotopic fractionation ε_{447} relative to ε_{448}.

singularity in the ratio cannot be avoided by using the L'Hôpital's rule. In the former method of comparing the fractionations by making a three-isotope plot this complication is avoided, but the wavelength dependence is not explicit. These two methods–the three-isotope plot and the ratio of fractionations as a function of wavelength–thus complement each other.

III. Discussion

In the data from stratospheric samples[10] an oxygen isotope anomaly Δ^{17} (= δ^{17} – 0.516 δ^{18}) ≈ 1 per mil was observed. To understand this anomaly transport models simulating the effect of various sources and sinks were used.[7,11,12] It was shown by Kaiser et al.[7] after pointing out some details which were overlooked by McLinden et al.[11] that a slope of about 0.525 in the $\ln(1+\varepsilon_{447})$ vs $\ln(1+\varepsilon_{448})$ plot of photolysis contributes less than 0.07 per mil to Δ^{17}.

As can be seen from the present figure 2, our calculations predict a slope of 0.525 in the log-log plot. The slope we obtained was almost independent of temperature in the range 230 K – 300 K[1,2] although the fractionation factors themselves changed with temperature. Experimental measurements of the slope at stratospherically relevant temperatures of 220 K – 273 K[13] are needed to verify our theoretical prediction and to give a correct definition for the calculation of the Δ^{17} in stratosphere. At present there are measurements of only the slope at room temperature.

Our calculations in figure 2 are based on the same theoretical model we used earlier and obtained an agreement with most of the available wavelength-dependent fractionation measurements for other isotopologues better than other detailed computations in the literature.[5] Thus the present figure 2 gives a firmer theoretical basis for the slope of 0.525 used in Kaiser et al.[7] Incidentally the results for 447, 448 obtained by two very different theoretical approaches of Johnson et al.[9] and Chen et al.[5] are very similar although the results for other isotopologues were significantly different.[4]

A theoretical slope of 0.534 we obtained in conjunction with the calculations of Kaiser et al.[7] partially confirms that the contribution of photodissociation of N_2O to Δ^{17} is insignificant. However as noted above, experimental measurement of slopes at different temperatures are needed for a more complete confirmation. Mechanisms other than photodissociation are being studied in the literature to explain the isotopic anomaly.[14,15]

The loss of N_2O by photolysis happens throughout the stratosphere. Over such a wide range of altitudes, the intensity distribution of light ($I(\lambda)$) changes significantly (Plate 4 of reference 16). To quantify the isotopologue fractionations δ^{17}, δ^{18} at these altitudes with different $I(\lambda)$, detailed experimental measurements and theoretical predictions of the absolute values of fractionations at individual wavelengths are needed. This need for wavelength dependent fractionation is unlike the calculation of Δ^{17}. The latter depends mainly on the ratio of the two fractionations rather than on their absolute values. The presently available experimental data for 447, 448[6,17–19] does not have such an exhaustive wavelength dependent study (e.g., cf. Figures 5 of reference 5). Detailed wavelength-dependent fractionation measurements when performed will aid transport computations, besides testing the validity of the theoretical predictions for the isotopologue fractionation factors. For example if δ^{17}, δ^{18} and Δ^{17} are to be estimated as a function of altitude similar to the calculations of Morgan et al.,[12] these wavelength-dependent fractionation measurements of isotopologues will be very useful.

IV. Conclusion

The three-isotope plot obtained by theoretical calculation is compared with the laboratory measurements. The comparison in this plot as well as the ratio of fractionations is found to be good, for the very limited existing available experimental data. We hope that this graphical presentation, based now on fundamental physical theory, will stimulate further experiments for such comparisons.

V. Acknowledgements

We are pleased to acknowledge with the support of this research by the National Science Foundation. We are deeply indebted to Professor Yuk Yung for insightful comments on the atmospheric relevance.

References

1. M. K. Prakash, and R. A. Marcus, *J. Chem. Phys.*, **123**, 174308 (2005).
2. W. C. Chen and R. A. Marcus, **manuscript** (2009).
3. C. A. M. Brenninkmeijer, C. Janssen, J. Kaiser, T. Röckmann, T. S. Rhee, and S. S. Assonov, *Chem. Rev.* **103**, 5125 (2003), and reference therein.
4. M. K. Prakash, J. D. Weibel, and R. A. Marcus, *J. Geophys. Res.-Atmos.*, **110**, D21315 (2005).
5. W. C. Chen, M. K. Prakash, and R. A. Marcus, *J. Geophys. Res.-Atmos.*, **113**, D05309 (2008).
6. T. Röckmann, J. Kaiser, J. N. Crowley, C. A. M. Brenninkmeijer, and P. J. Crutzen, *Geophys. Res. Lett*, **28**, 503 (2001).
7. J. Kaiser, T. Röckmann, and C. A. M. Brenninkmeijer, *J. Geophys. Res.-Atmos.*, **109**, D03305 (2004).
8. J. Kaiser, *Stable Isotope Investigations of Atmospheric Nitrous Oxide*, Ph.D thesis, **2002**, Johannes Gutenberg-University, Mainz, Germany.
9. M. S. Johnson, G. D. Billing, A. Gruodis, and M. H. M. Janssen, *J. Phys. Chem. A*, **105**, 8672 (2001).
10. S. S. Cliff, C. A. M. Brenninkmeijer, and M. H. Thiemens, *J. Geophys. Res.-Atmos.*, **104**, 16171 (1999).
11. C. A. McLinden,; M. J. Prather, and M. S. Johnson, *J. Geophys. Res.-Atmos.*, **108**, 4233 (2003).
12. C. G. Morgan, M. Allen, M. C. Liang, R. L. Shia, G. A. Blake, and Y. L. Yung, *J. Geophys. Res.-Atmos.*, **109**, D04305 (2004).

13. M. Z. Jacobson, *Fundamentals of atmospheric modeling* (New York: Cambridge University Press, **1999**.)
14. J. Kaiser, and T. Röckmann, *Geophys. Res. Lett.*, **32**, 15808 (2005).
15. M. C. Liang, and Y. L. Yung, *J. Geophys. Res.-Atmos.*, **112**, D13307 (2007).
16. T. Röckmann, J. Kaiser, C. A. M. Brenninkmeijer, J. N. Crowley, R. Borchers, W. A. Brand, and P. J. Crutzen, *J.Geophys. Res.-Atmos.*, **106**, 10403 (2001).
17. F. Turatti, D. W. T. Griffith, S. R. Wilson, M. B. Esler, T. Rahn, H. Zhang, and G. A. Blake, *Geophys. Res. Lett.*, **27**, 2489 (2000).
18. T. Rockmann, C. A. M. Brenninkmeijer, M. Wollenhaupt, J. N. Crowley, and P. J. Crutzen, *Geophys. Res. Lett.*, **27**, 1399 (2000).
19. J. Kaiser, T. Röckmann, C. A. M. Brenninkmeijer, and P. J. Crutzen, *Atmos. Chem. Phys.*, **3**, 303 (2003).

Chapter 8

A Theoretical Study of Ozone Isotopic Effects Using a Modified *Ab Initio* Potential Energy Surface

[This chapter appeared in the *Journal of Chemical Physics* **117**, 1536 (2002).]

JOURNAL OF CHEMICAL PHYSICS VOLUME 117, NUMBER 4 22 JULY 2002

A theoretical study of ozone isotopic effects using a modified *ab initio* potential energy surface

Yi Qin Gao, Wei-Chen Chen, and R. A. Marcus[a)]
Noyes Laboratories, California Institute of Technology, Pasadena, California 91125

(Received 12 February 2002; accepted 3 May 2002)

A modified *ab initio* potential energy surface (PES) is used for calculations of ozone recombination and isotopic exchange rate constants. The calculated low-pressure isotopic effects on the ozone formation reaction are consistent with the experimental results and with the theoretical results obtained earlier [J. Chem. Phys. **116**, 137 (2002)]. They are thereby relatively insensitive to the properties of these PES. The topics discussed include the dependence of the calculated low-pressure recombination rate constant on the hindered-rotor PES, the role of the asymmetry of the potential for a general $X+YZ$ reaction $(Y\neq Z)$, and the partitioning to form each of the two recombination products: XYZ and XZY. © *2002 American Institute of Physics.* [DOI: 10.1063/1.1488577]

I. INTRODUCTION

We have treated the unusual isotopic effects[1–28] of ozone formation earlier using both loose and hindered-rotor transition states.[29,30] Because of the lack of an accurate potential energy surface (PES) in the vicinity of the hindered-rotor transition state, a model PES was used for recombination and isotopic exchange reactions.[29,30] This model PES was chosen to fit the experimentally[31] obtained negative temperature dependence of the ozone isotopic exchange rate constant. In the present study a modified[32] *ab initio* PES is used instead and the effect on the calculated rate constant ratios of the many isotopic systems is discussed.

In addition to using a modified *ab initio* PES, a new and more sophisticated way is given for weighting the relative yields of the reaction products XYZ and XZY in the recombination of X and YZ. The method can also be used for more general PES. For simplicity, this weighting factor was assumed earlier[29,30] to be 1/2 for each product. The more general weighting in the present study is obtained by an integration of the squared magnitude of each wave function over the angular space that leads to the desired product. These two methods are then compared in the treatment of ozone isotopic exchange and recombination reactions.

The microscopic rate constants themselves are calculated using a modified RRKM theory with the transition state for each quantum state determined variationally, as before.[29,30] An η effect, which reduces the low-pressure rate constant for the formation of a symmetric molecule more than that for an asymmetric one, is also included.[29,30] The η effect is a small correction $(\sim 15\%)$ and its origin has been described previously.[29,33,34] This correction is apart from symmetry numbers, which are also included.

For the deactivation of the vibrationally excited ozone molecules a master equation formalism is used. It was obtained earlier[30] using a weak collision model. In this weak collisional energy transfer model, the energy transfer is assumed to be stepwise, and a strong collisional angular momentum transfer assumption is used.[30,35] In the low-pressure limit the vibrationally excited ozone molecules with energies above the dissociation threshold can only experience at most a single collision with the bath molecules before redissociation. As a result in a weak collision model only low energy states can be stabilized significantly at low pressures and form stable ozone molecules.[29,30]

One difference between the two exit channels $X+YZ$ and $XY+Z$ for the dissociation of any asymmetric molecule XYZ $(X\neq Z)$ is the difference between the zero-point energies of YZ and YX. At any given energy, this difference of zero-point energies favors the reaction through the channel with the smaller zero-point energy because of the greater number of quantum states in the transition state for that exit channel. This difference between the respective number of quantum states of the transition states for the two exit channels is large at low energies.[30] Since weak collisions sample mainly low energy states, a large difference occurs between the rate constants via the two recombination channels leading to an XYZ at low pressures.[30] Since the zero-point energy difference between YZ and YX depends mainly on the mass difference between Z and X, this weak collision effect leads to a strikingly large mass dependence of individual rate constant ratios when reaction occurs only via one of the two channels (‘‘unscrambled systems’’).[24–28] In particular, in unscrambled experiments vibrationally excited ozone isotopomers XYY^* are formed only from $X+YY\rightarrow XYY^*$ and not from $Y+YX\rightarrow XYY^*$.

In a scrambled system both such channels are allowed since extensive isotopic exchange occurs via XYZ^* between $X+YZ$ and $Z+YX$. As a result, it was shown that the partitioning effect between the two exit channels disappears exactly.[33] Instead, one observes the difference between the formation rates of symmetric and asymmetric molecules and the resulting mass-independent effect (‘‘symmetry driven’’) arises.[29,30,33,34]

The present study was performed to test further the numerical aspects of the theory using a more elaborate ozone

---

[a)] Author to whom correspondence should be addressed. Electronic mail: ram@caltech.edu

0021-9606/2002/117(4)/1536/8/$19.00

PES. We suggested in an earlier paper[30] that the low-pressure results on enrichments and rate constant ratios would be relatively insensitive to the hindered-rotor potential energy surface used. The present study provides a test of this suggestion. The ozone recombination rate constant ratios and the enrichments for different isotopomers are calculated, together with the rate constant of the ozone isotopic exchange reaction $^{16}O+{}^{18}O^{18}O \rightarrow {}^{18}O+{}^{16}O^{18}O$ and its temperature dependence. They are compared with the experimental data and with the previous theoretical results.

The paper is organized as follows: The PES used is summarized in Sec. II. The hindered rotor eigenstates are obtained in Sec. III, and are used to calculate rate constants in Sec. IV. The results are discussed in Sec. V.

II. POTENTIAL ENERGY SURFACE

The underlying *ab initio* ozone PES is that of Morokuma and co-workers,[36] who used the MOLPRO program within the range of $95° \leqslant \alpha \leqslant 135°$, $2.1a_0 \leqslant r_1 \leqslant 3.0a_0$, and $2.1a_0 \leqslant r_2 \leqslant 5.0a_0$, where α is the bond angle and r_1 and r_2 are the bond lengths. This PES was fitted by the same authors to a Murrell–Sorbie analytical function. To be consistent with the experimentally determined negative temperature dependence of the recombination rate constant,[37] an exponential term was added to the Murrell–Sorbie analytical function by Cross and Billing[32] in their molecular dynamic studies of the ozone recombination reaction. It removed a local ~ 0.15 eV maximum in the energy barrier for recombination on the original *ab initio* PES. This modified PES is the one used in the present study.

The reaction coordinate is again taken, for simplicity, as the distance R between the oxygen atom and the center of mass of the oxygen molecule fragment. The modified *ab initio* potential energy surface is written as $V_0(R) + V(R,\theta)$, where $V_0(R)$ is taken as the minimum of the potential energy at R, minimized with respect to θ, and $V(R,\theta)$ is the angular dependence of the PES at the given R; θ is the angle between the oxygen molecular bond and the line connecting the center of mass of this oxygen molecule and the oxygen atom. The $V(R,\theta)$ is fitted to

$$V(R,\theta) = \sum_{i=0}^{d} b_i(R) \cos^i \theta, \tag{1}$$

where d is the highest order of the expansion. Only for a homonuclear fragment YY do all the odd terms in Eq. (1) vanish. The V_0 is given as a function of R in Fig. 1, and $V(R,\theta)$ and a fitting function are depicted for different values of R in Fig. 2. A contour plot of the PES is given as a function of R and θ in Fig. 3.

III. THE HINDERED-ROTOR EIGENSTATES

The orbital and hindered-rotational components of the Hamiltonian for the transition state region for a three body system $X \cdots YZ$ is written as

$$H = \frac{\hbar^2}{2\mu R^2} \mathbf{l}^2 + \frac{\hbar^2}{2I} \mathbf{j}^2 + V(R,\theta,\phi), \tag{2}$$

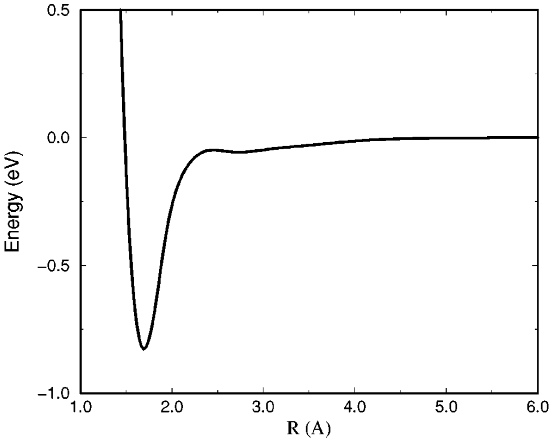

FIG. 1. V_0 as a function of R.

where μ is the reduced mass of $X \cdots YZ$, R is the distance between X and the center of mass of YZ, I the moment of inertia of YZ, $\mathbf{l}\hbar$ the orbital angular momentum operator, and $\mathbf{j}\hbar$ the angular momentum operator for the rotation of the fragment YZ

$$\mathbf{j}^2 = -\frac{1}{\sin\theta} \frac{\partial}{\partial\theta} \left(\sin\theta \frac{\partial}{\partial\theta} \right) + \frac{m^2}{\sin^2\theta}. \tag{3}$$

In Eq. (3) m is the projection of $\mathbf{j}$ onto the axis connecting the X and the center of mass of YZ. The total angular momentum operator $\mathbf{J}$ is then

$$\mathbf{J} = \mathbf{j} + \mathbf{l}, \tag{4}$$

the projection of which along the line connecting the centers of mass is also m.

Combining Eqs. (2) and (4) and neglecting terms off diagonal in m, as discussed in Refs. 30 and 38, one obtains

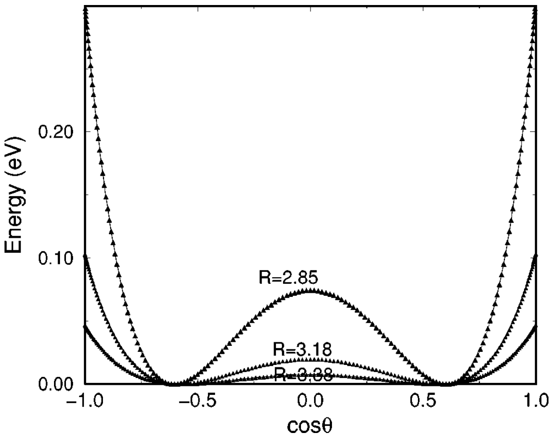

FIG. 2. $V(R,\theta)$ vs $\cos\theta$ for a symmetric fragment $YY+X$, where X may or may not be the same as Y, for different values of R (in units of Å).

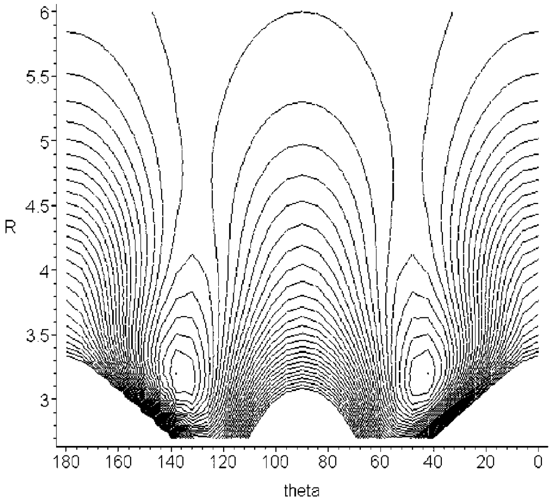

FIG. 3. Contour plot of the potential energy surface as a function of R and θ for ${}^{16}O+{}^{16}O^{16}O$.

$$H=\frac{\hbar^2}{2\mu R^2}\mathbf{J}^2-\frac{\hbar^2}{\mu R^2}m^2+\left(\frac{\hbar^2}{2\mu R^2}+\frac{\hbar^2}{2I}\right)\mathbf{j}^2 +V(R,\theta). \tag{5}$$

(In Appendix A of Ref. 30 m is denoted by Ω.) The first two terms on the right-hand side of Eq. (5) are constants for given J and m. To obtain the eigenvalues of H we focus first on the third and fourth terms on the right-hand side of Eq. (5). Using Eq. (3) these two terms can be written as

$$H_1=-\left(\frac{\hbar^2}{2I}+\frac{\hbar^2}{2\mu R^2}\right)\frac{d}{d\zeta}\left[(1-\zeta^2)\frac{d}{d\zeta}\right] +\left(\frac{\hbar^2}{2I}+\frac{\hbar^2}{2\mu R^2}\right)\frac{m^2}{1-\zeta^2}+V_R(\zeta), \tag{6}$$

where $\zeta=\cos\theta$ and $V_R(\zeta)$ denotes $V(R,\theta)$. The angle when Z in ZY is the closer one to X lies in the interval $(0,\pi/2)$ while when Y is closer to X, θ lies in the interval $(\pi/2,\pi)$.[39]

The solution Ψ_{mj} of $H_1\Psi_{mj}=E_{mj}\Psi_{mj}$ can be written as a linear combination of associated Legendre polynomials P_n^m for the given m

$$\Psi_{mj}(\zeta)=\sum_{k=0}^{\infty} d_k^{mj}P_{m+k}^m(\zeta). \tag{7}$$

Substitution of Eq. (7) into Eq. (6) and using[40]

$$-\frac{d}{d\zeta}\left[(1-\zeta)^2\frac{d}{d\zeta}P_n^m\right]+\frac{m^2}{1-\zeta^2}P_n^m=n(n+1)P_n^m, \tag{8}$$

one obtains

$$\left(\frac{\hbar^2}{2I}+\frac{\hbar^2}{2\mu R^2}\right)\sum_{k=0}^{\infty} d_k^{mj}[(m+k)(m+k+1)-E_{mj}] \times P_{m+k}^m(\zeta)+\sum_{k=0}^{\infty} d_k^{mj}V_R(\zeta)P_{m+k}^m(\zeta)=0. \tag{9}$$

Using the recurrence relation[40]

$$(2n+1)\zeta P_n^m(\zeta)=(n+m)P_{n-1}^m(\zeta) +(n-m+1)P_{n+1}^m(\zeta), \tag{10}$$

and the expansion $V_R(\zeta)=\Sigma_{i=0}^{d}b_i\zeta^i$ the term $V_R(\zeta)P_{m+k}^m(\zeta)$ can be written as a sum of associated Legendre polynomials

$$V_R(\zeta)P_{m+k}^m(\zeta)=\sum_{i=-d}^{d}\alpha_iP_{m+k+i}^m(\zeta). \tag{11}$$

Combining Eqs. (9) and (11) and noting the independence of the P_{m+k}^ms one obtains a set of linear equations for the coefficients d_k^{mj} in Eq. (9)

$$\alpha_{-d}d_{k-d}^{mj}+\cdots+\alpha_{-1}d_{k-1}^{mj}+d_k^{mj} \times[(m+k)(m+k+1)-E_{mj}] +\alpha_1d_{k+1}^{mj}+\cdots+\alpha_dd_{k+d}^{mj}=0. \tag{12}$$

The eigenvalues and the eigenvectors are obtained from Eq. (12). The wave functions of the hindered-rotor states with the quantum number m and all $j\geqslant m$ are then obtained using Eq. (7).

IV. RATE CONSTANTS AND ENRICHMENTS

The rate constant for an exchange reaction, such as

$${}^{16}O+{}^{18}O^{18}O\rightarrow{}^{18}O+{}^{16}O^{18}O \tag{13}$$

can be written as[34]

$$k_{\rm ex}^a=\frac{1}{hQ_a}\sum_J\int_E\frac{N_a(EJ)N_b(EJ)}{N_a(EJ)+N_b(EJ)}e^{-E/k_BT}dE, \tag{14}$$

where Q_a is the partition function of the reacting pair in the center of the mass system of coordinates for channel a, and $N_{a(b)}(EJ)$ is the number of states of the transition state for exit channel $a(b)$ of ozone dissociation at the given E and J. The a denotes the exit channel with the smaller zero-point energy. In the case of the reaction in Eq. (13) it is ${}^{16}O+{}^{18}O^{18}O$. Each of the two exit channels has its own transition state, determined variationally, as discussed later.

Since the reactants $X+YZ$ $(Y\neq Z)$ can lead to two different recombination products, XYZ and XZY, and the phase space for the transition state can be divided into two subspaces, each leading to a different ozone product. A weighting factor $\Phi_{a(b)}$ $(\Phi_a+\Phi_b=1)$ for each quantum state is assigned to each product. The $\Phi_{a(b)}$ is taken as the squared amplitude of the normalized wave functions $\Psi_{mj}(\zeta)$, integrated over half of the θ space, the half that corresponds to the desired product XYZ

$$\Phi_a(mj)=\int_{\zeta=0}^{1}|\Psi_{mj}(\zeta)|^2d\zeta. \tag{15}$$

In the other half of the θ space ζ lies in the interval $(-1,0)$.[39]

When an asymmetric ozone molecule XYZ is formed, it is helpful to distinguish between two different weighting factors: The Φ_a defined in Eq. (15) arises from the fact that when $Y \neq Z$ there exists a competing channel in which the same reactants, $X+YZ$, lead to XZY instead of XYZ. We define a "global" transition state $X \cdots YZ$ as one for the entire θ interval $(0, \pi)$ in which part of this θ interval leads to XYZ and the other part to XZY (cf Fig. 5). On the other hand, for the formation of any product XYZ there also exist two competing entrance channels, one from $X+YZ$ and the other from $XY+Z$ when $X \neq Z$. The weighting factors for the dissociation of XYZ^* into $X+YZ$ and $XY+Z$ were termed partitioning factors[33,34] and denoted by Y_a and Y_b. The Ys are given later by Eq. (18).

This global transition state for any given quantum state (Jjm) in the full θ space (0 to π) is determined by the maximum of its energy $E_{mj}^{J,a}$ along R. The $E_{mj}^{J,a}$ contains three components: the bond fission energy $V_0(R)$, the eigenvalue E_{mj} of the hindered rotor with quantum number (mj), and the centrifugal-type energy $(J(J+1)-2m^2)\hbar^2/2\mu R^2$ in Eq. (5). The vibration frequency of the diatomic fragment is taken to be a constant, although such an approximation is readily removed by the use of a sufficiently accurate PES. The diatomic fragment remains in its ground vibrational state due to the large O_2 vibration frequency. Thereby, $E_{mj}^{J,a}$ also contains the zero-point energy of the oxygen fragment in channel a. The number of states in the transition state for a given (EJ) can then be written as

$$N_a(EJ) = \sum_{mj} (2J+1) h(E - E_{mj}^{J,a}) \Phi_a(mj) \tag{16}$$

with $\Phi_a(mj)$ given by Eq. (15), and $h(E-E_{mj}^{J,a})$ is a unit step function for $E-E_{mj}^{J,a}$. Equations (15) and (16) are next introduced into the appropriate rate expressions.

In the present paper we focus on the isotopic effects for the $O+O_2+M$ recombination reaction at low third-body (M) pressures, rather than considering all pressures. For existing experiments that is the most important pressure region. In the low-pressure limit the recombination rate constant for the $X+YZ \rightarrow XYZ$ $(X \neq Z)$ is given by the following equation, which was derived earlier[30] using the weak collision model:

$$\begin{aligned} k_{bi}^{0,a} = \frac{\omega_d - \omega_a}{Q_a} \Bigg(& \int_0^{\Delta E} \sum_J \rho(EJ) Y_a(EJ) \\ & \times e^{-E/k_B T} \frac{\omega}{\omega_d + \omega_a P^o(E)} dE \\ & + \int_{\Delta E}^{2\Delta E} \sum_J \rho(EJ) Y_a(EJ) \\ & \times e^{-E/k_B T} \frac{\omega_d P^c(E-\Delta E)}{\omega_d + \omega_a P^o(E-\Delta E)} dE + \cdots \Bigg), \end{aligned} \tag{17}$$

where

$$Y_a(EJ) = \frac{N_a(EJ)}{N_a(EJ)+N_b(EJ)} \tag{18}$$

is the partitioning factor[29,33,34] mentioned earlier. A step-ladder energy transfer model and a strong collisional rotational angular momentum transfer assumption were used in deriving Eq. (17). The $P^o(E)$ is the fraction of the quantum states in the global transition state that are "open," i.e., whose Js satisfy $N_a(EJ)+N_b(EJ)>0$ at the given E. We also have for the "closed" states, $P^c(E) = 1 - P^o(E)$.[30]

The quantities appearing in Eqs. (14) and (17) for the rate constants are seen to be the number of states for the hindered rotor, given by Eq. (16), the partition function for the collision pair given by Eqs. (4.8)–(4.12) in Ref. 34, the collision frequencies, and the density of states. The Lennard-Jones collision frequency is used with a unit collision efficiency and is given by Eq. (4.14) of Ref. 34. The density of states for ozone $\rho(EJ)$ is obtained[34] from a convolution[35,41–43] of the rotational and vibrational density of states at each E and J. The vibration frequencies of the ozone isotopomers used in the calculation were obtained using a second-order perturbation formulation, which gives any unknown frequencies to an accuracy of about 1 cm^{-1}.[44] The calculated density of states $\rho(EJ)$ also includes the anharmonicity, which was obtained[30] using experimental vibrational quantum state energies of $^{48}O_3$. The anharmonic count for $\rho(EJ)$ was typically only a factor of 1.5 greater than the harmonic one.

The individual low-pressure rate constants at 300 K for the formation of XYZ molecules were calculated for each channel using Eq. (17). In Tables I–III we give the calculated recombination rate constant ratios for all reactions and com-

TABLE I. Relative rate coefficients of atom plus homonuclear diatomic formation channels ($X+YY \rightarrow XYY$ relative to $X+XX \rightarrow X_3$) at low pressure at 300 K.

Reaction	Expt.[a]	Calc. (present) $\Delta E = 190\ \mathrm{cm}^{-1}$	Calc. (present) $\Delta E = 210\ \mathrm{cm}^{-1}$	Calc. (Ref. 30) $\Delta E = 210\ \mathrm{cm}^{-1}$
$^{16}O+^{36}O_2/^{16}O+^{32}O_2$	1.53 ± 0.03	1.53	1.51	1.53
$^{17}O+^{36}O_2/^{17}O+^{34}O_2$	1.29 ± 0.07	1.34	1.35	1.36
$^{16}O+^{34}O_2/^{16}O+^{32}O_2$	1.23 ± 0.03	1.36	1.35	1.38
$^{17}O+^{32}O_2/^{17}O+^{34}O_2$	1.01 ± 0.05	0.99	1.01	1.01
$^{18}O+^{34}O_2/^{18}O+^{36}O_2$	1.00 ± 0.06	1.06	1.07	1.04
$^{18}O+^{32}O_2/^{18}O+^{36}O_2$	0.90 ± 0.03	0.90	0.92	0.90

[a] From Mauersberger *et al.*, Ref. 25.

TABLE II. Reaction rate coefficients for ozone formation processes relative to $^{16}O+^{32}O_2\rightarrow^{48}O_3$ at low pressure.

Reaction	Expt.[a]	Calc. (present) $\Delta E=190$ cm^{-1}	Calc. (present) $\Delta E=210$ cm^{-1}	Calc. (Ref. 30) $\Delta E=210$ cm^{-1}
$^{16}O+^{16}O^{16}O$	1.00	1.00	1.00	1.00
$^{17}O+^{17}O^{17}O$	1.02	1.03	1.02	1.02
$^{18}O+^{18}O^{18}O$	1.03	1.03	1.03	1.03
$^{18}O+^{16}O^{16}O$	0.93	0.93	0.95	0.93
$^{17}O+^{16}O^{16}O$	1.03	1.02	1.04	1.03
$^{18}O+^{17}O^{17}O$	1.03	1.09	1.10	1.07
$^{17}O+^{18}O^{18}O$	1.31	1.39	1.38	1.39
$^{16}O+^{17}O^{17}O$	1.23	1.36	1.35	1.38
$^{16}O+^{18}O^{18}O$	1.53	1.53	1.51	1.53
$^{16}O+^{16}O^{17}O$[b]	1.17	1.18	1.18	1.19
$^{16}O+^{16}O^{18}O$	1.27	1.25	1.24	1.25
$^{17}O+^{16}O^{17}O$	1.11	1.03	1.04	1.04
$^{17}O+^{17}O^{18}O$	1.21	1.22	1.22	1.20
$^{18}O+^{16}O^{18}O$	1.01	1.00	1.01	0.99
$^{18}O+^{17}O^{18}O$	1.09	1.06	1.07	1.05
$^{16}O+^{17}O^{18}O$	—	1.43	1.41	1.43
$^{17}O+^{16}O^{18}O$	—	1.21	1.21	1.21
$^{18}O+^{16}O^{17}O$	—	1.01	1.03	1.01

[a] From Mauersberger *et al.*, Ref. 25.

[b] This rate constant and those in the subsequent rows are the sum of both channels, $X+YZ\rightarrow XYZ$ and $X+YZ\rightarrow XZY$. Each of the rate constants was calculated separately, with the non-RRKM correction applied to any symmetric channel.

TABLE IV. Calculated and experimental isotopic enrichments at 300 K.

Reaction	Expt.[a]	Calc. (present) $\Delta E=190$ cm^{-1}	Calc. (present) $\Delta E=210$ cm^{-1}	Calc. (Ref. 30) $\Delta E=210$ cm^{-1}
$^{16}O^{16}O^{16}O$	0.0	0.0	0.0	0.0
$^{17}O^{17}O^{17}O$	−1.8	−2.1	−1.6	−2.1
$^{18}O^{18}O^{18}O$	−4.6	−4.3	−4.3	−4.7
$^{16}O^{16}O^{17}O$[b]	11.3	11.5	12.1	12.3
$^{16}O^{16}O^{18}O$	13.0	12.7	12.7	12.7
$^{17}O^{17}O^{16}O$	12.1	11.2	11.2	12.2
$^{17}O^{17}O^{18}O$	9.5	11.7	11.3	10.4
$^{18}O^{18}O^{16}O$	14.4	12.7	12.6	12.7
$^{18}O^{18}O^{17}O$	8.3	9.9	10.3	9.2
$^{16}O^{17}O^{18}O$	18.1	17.2	17.3	17.4

[a] Experimental data at 300 K are from Mauersberger *et al.*, Ref. 25.

[b] Enrichments for this and all following rows are for all possible isotopomers.

pare them there with the experimental values and with the calculated results obtained earlier.[29] The column labeled ‘‘Calc. Ref. 30’’ gives the results obtained before using $\Delta E=210$ cm^{-1}. The column ‘‘Calc. $\Delta E=210$ cm^{-1}’’ gives present results obtained with the same ΔE. The column labeled ‘‘Calc. $\Delta E=190$ cm^{-1}’’ gives the present calculation but where the values of η and of ΔE were chosen, as in Refs. 29 and 30, to fit two experimental low-pressure recombination rate constant ratios, $^{16}O+^{18}O^{18}O/^{16}O+^{16}O^{16}O$ and $^{18}O+^{16}O^{16}O/^{18}O+^{18}O^{18}O$. For the present hindered-rotor transition state the value $\Delta E=190$ cm^{-1} was obtained. An $\eta=1.18$, obtained both in this fit and that in Ref. 30, is used in all the calculations.

The rate constant ratios given in Tables II and III were then used for the calculation of the enrichments of all possible species of ozone. The latter are given in Table IV together with the experimental and previous calculated results. The calculated results were obtained from individual isotopomeric rate constants using Eqs. (4.18a), (4.18b), and (4.26) of Ref. 33.

The rate constant for the isotopic exchange reaction $^{16}O+^{18}O^{18}O\rightarrow^{18}O+^{16}O^{18}O$ was calculated using the modified *ab initio* PES. It is independent of any η and ΔE approximations, but it does assume a loss of ‘‘memory’’ in the intermediate $^{16}O^{18}O^{18}O^*$ formed in the reaction. For the partitioning between the formation of $^{18}O^{16}O^{18}O^*$ and

TABLE III. Reaction rate coefficients for asymmetric and symmetric channels of recombination reactions, relative to $^{16}O+^{16}O_2\rightarrow^{16}O_3$ at low pressure.

Reaction	Expt.[a]	Calc. (present) $\Delta E=190$ cm^{-1}	Calc. (present) $\Delta E=210$ cm^{-1}	Calc. (Ref. 30) $\Delta E=210$ cm^{-1}
Symmetric products				
$^{16}O+^{17}O^{16}O\rightarrow^{16}O^{17}O^{16}O$	—	0.51	0.51	0.51
$^{16}O+^{18}O^{16}O\rightarrow^{16}O^{18}O^{16}O$	0.54±0.01	0.52	0.52	0.52
$^{17}O+^{16}O^{17}O\rightarrow^{17}O^{16}O^{17}O$	—	0.51	0.51	0.51
$^{17}O+^{18}O^{17}O\rightarrow^{17}O^{18}O^{17}O$	—	0.52	0.52	0.51
$^{18}O+^{16}O^{18}O\rightarrow^{18}O^{16}O^{18}O$	0.52±0.01	0.52	0.52	0.52
$^{18}O+^{17}O^{18}O\rightarrow^{18}O^{17}O^{18}O$	—	0.52	0.53	0.52
Asymmetric products[b]				
$^{18}O+^{17}O^{16}O\rightarrow^{18}O^{17}O^{16}O$	—	0.48	0.49	0.47
$^{18}O+^{18}O^{16}O\rightarrow^{18}O^{18}O^{16}O$	0.46±0.03	0.48	0.49	0.47
$^{17}O+^{18}O^{16}O\rightarrow^{17}O^{18}O^{16}O$	—	0.53	0.54	0.52
$^{17}O+^{17}O^{16}O\rightarrow^{17}O^{17}O^{16}O$	—	0.52	0.53	0.53
$^{18}O+^{18}O^{17}O\rightarrow^{18}O^{18}O^{17}O$	—	0.54	0.54	0.53
$^{18}O+^{16}O^{17}O\rightarrow^{18}O^{16}O^{17}O$	—	0.53	0.54	0.53
$^{17}O+^{16}O^{18}O\rightarrow^{17}O^{16}O^{18}O$	—	0.69	0.68	0.70
$^{16}O+^{16}O^{17}O\rightarrow^{16}O^{16}O^{17}O$	—	0.67	0.67	0.68
$^{17}O+^{17}O^{18}O\rightarrow^{17}O^{17}O^{18}O$	—	0.70	0.69	0.70
$^{16}O+^{18}O^{17}O\rightarrow^{16}O^{18}O^{17}O$	—	0.69	0.68	0.69
$^{16}O+^{16}O^{18}O\rightarrow^{16}O^{16}O^{18}O$	0.73±0.02	0.74	0.73	0.74
$^{16}O+^{17}O^{18}O\rightarrow^{16}O^{17}O^{18}O$	—	0.74	0.73	0.74

[a] From Janssen *et al.*, Ref. 26.

[b] Reactions are ordered in sequence of increasing zero-point energy difference.

TABLE V. Calculated and experimental rate constants.

k	Reaction	T (K)	Expt.	Calc. (Ref. 30)	Calc. (present)[c]
$k_{\rm bi}^{0}$[a]	$^{16}O+^{32}O_2+N_2\rightarrow ^{48}O_3+N_2$	130	4[b]	5.2	4.8
		300	0.5[b]	0.76	0.58
	$k_{\rm bi}\propto T^{-n}$	130–300	$n=2.6$	$n=2.3$	$n=2.5$
$k_{\rm ex}$[d]	$^{16}O+^{18}O^{18}O\rightarrow ^{16}O^{18}O+^{18}O$	130	5.6[e]	4.3	2.6[f]
		300	2.9[e]	2.7	1.9[f]
	$k_{\rm ex}\propto T^{-m}$	130–300	$m=0.88\pm0.26$	$m=0.53$	$m=0.36$

[a] Units are 10^{-33} cm^6 s^{-1}.

[b] Experimental data from Hippler *et al.*, Ref. 37.

[c] Calculated using the modified *ab initio* PES and $\Delta E=190$ cm^{-1}. When $\Delta E=210$ cm^{-1} the values are 5.1 and 0.72, respectively.

[d] Units are 10^{-12} cm^3 molecule^{-1} s^{-1}.

[e] Experimental data from Wiegell *et al.*, Ref. 31.

[f] Calculated using the integrated wave function method.

$^{16}O^{18}O^{18}O^*$ from $^{18}O+^{16}O^{18}O$, the partitioning factor was calculated using Eq. (15). For comparison this partitioning was also approximated as 1/2. The integrated wave function method yielded for the isotopic exchange reaction $^{16}O+^{18}O^{18}O\rightarrow ^{18}O+^{16}O^{18}O$ a rate constant of 1.94×10^{-12} cm^{-3} at 300 K and 2.62×10^{-12} cm^{-3} at 130 K. (These values are rounded off in Table V.) When Φ_a and Φ_b are assumed, instead, to be 0.5 these values are virtually unchanged: 1.98×10^{-12} cm^{-3} and 2.74×10^{-12} cm^{-3}, respectively. (The number of "significant figures" is significant for comparison of these numbers with each other and not for comparison with the experiment.) Results for the isotopic exchange reaction and for the recombination reaction are compared with the experimental and previous theoretical results in Table V.

V. DISCUSSION

A modified *ab initio* PES available in the literature was used in the present RRKM calculations for ozone recombination and isotopic exchange rate constants. The ratios of the recombination rate constants agreed with those in our earlier studies[29,30] which employed instead a free-rotor transition state and a hindered-rotor transition state using a model PES. Given the method of choosing the two unknowns ΔE and η from two specific recombination rate constant ratios, the results for the numerous rate constant ratios and enrichments are seen to be virtually unchanged from our previous values.

Although the PES used in the present study is very different in detail from the model PES used in the previous study, as seen from the two potential energy profiles (labeled 000) in Fig. 4, the two surfaces give rather similar results for the isotopic exchange reaction $^{16}O+^{18}O^{18}O\rightarrow ^{18}O+^{16}O^{18}O$: The model PES used in Ref. 30 gives an isotopic exchange rate constant (300 K) about 40% larger than that given by the modified *ab initio* PES. This difference is partly due to the existence of an effective barrier in the present PES at about 2 Å (Fig. 1). It causes the transition state to occur at smaller Rs and thus decreases the value of the calculated rate constant (smaller "cross section") for the recombination collision. If the negative temperature dependence of the rate constant is written as T^{-m}, the experimental value of m is 0.88 ± 0.26. The present calculation yielded a smaller value, 0.36, which is also smaller than the result (0.53) obtained earlier using the model PES.[30] In contrast, the free-rotor transition state is very different from either of the two tight transition states, since it gives[30] a positive temperature dependence of the isotopic exchange rate constant and a rate constant at 300 K more than three times larger than the present result.

The similarity of exchange rate constants obtained using the two very different potential energy surfaces (the model PES used in Ref. 30 and the modified *ab initio* PES used in this study) is not accidental. It occurs because both surfaces were adjusted[30,32] to fit the isotopic exchange rate constants. Although the details of the adiabatic curves for each (JKj) state are very different for the two potential energy surfaces, the effective barrier heights are seen in Fig. 4 to be similar. A reflection of this point is that the sums of quantum states $\Sigma_J N(E,J)$[45] for the transition state are also similar for both potentials (Fig. 5). Also shown in Fig. 5 is the $\Sigma_J N(E,J)$ for a loose transition state. As seen in the comparisons in that Figure (and also from the temperature coefficients discussed above) both hindered rotor-transition states are relatively tight.

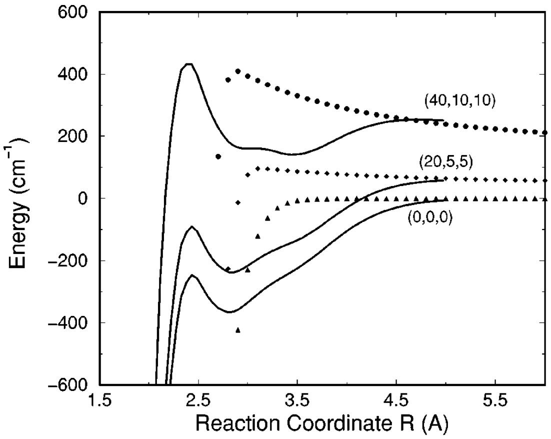

FIG. 4. The energy $E(Jj\Omega;R)$ of a hindered rotor state $(Jj\Omega)$ as a function of R for $^{16}O\cdots{}^{16}O^{16}O$. Symbols are obtained using the model potential (Ref. 30) and lines are obtained using the modified *ab initio* PES.

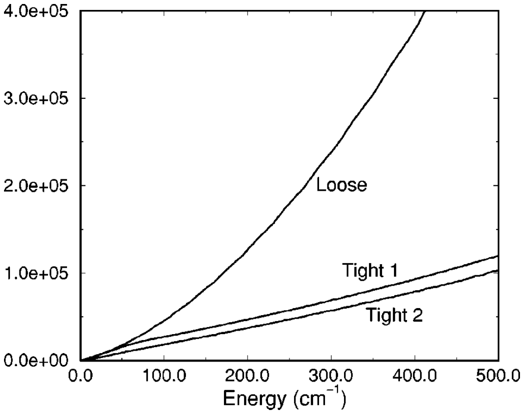

FIG. 5. The number of states $N_E = \Sigma_J N(EJ)$ as a function of E for the recombination reaction $^{16}O + ^{32}O_2 \rightarrow ^{48}O_3$. The curve labeled "Loose" is for a loose transition state, the one labeled "Tight 1" is obtained using the model PES (Ref. 30), and the one labeled "Tight 2" is obtained using the modified *ab initio* PES.

The calculated results for low-pressure recombination rate constants and their ratios are less sensitive to the transition state (and thus to the PES) than the isotopic exchange rate constants. The differences between results obtained using the two tight transition states (this work) and between those obtained using a loose and a tight transition state (Ref. 30) are both small. For example, the model PES gives a low pressure recombination rate constant for $^{16}O + ^{16}O^{16}O \rightarrow ^{48}O_3$ within 10% of that given by the model PES at both 130 and 300 K when the same ΔE is used (footnote c of Table V). The insensitivity of the low-pressure recombination rate constant ratios to the PES is seen clearly in Tables I–III, by comparing the third with the fourth and fifth columns. The third and fifth columns were obtained using a ΔE optimized for each PES and the third and fourth columns were obtained using the same ΔE, which is optimized for the present surface.

The reasons for the weak dependence of the low pressure recombination results on the PES are several-fold: The dependence of the low pressure recombination rate constants for symmetric molecules on the number of states at the transition state, $h(N_a(EJ))$, and that of the recombination rate constant for an asymmetric molecule, $N_a(EJ)/(N_a(EJ) + N_b(EJ))$, are both expected to be weaker than that of the isotopic exchange rate constant. The latter is not only proportional to $N_a(EJ)/(N_a(EJ) + N_b(EJ))$ but also to $N_b(EJ)$, as discussed earlier.[30] In addition, since the ΔE per collision was varied to fit two experimental recombination rate constant ratios and then used to calculate all the other ratios, the differences in the rate constant ratios obtained using the two different surfaces are further reduced. For example, to fit the experimental recombination rate constant ratios, values of 260, 210, and 190 cm^{-1} were chosen for ΔE when the loose transition state and the previous and present tight transition states were used, respectively. Accordingly, the calculated rate constant ratios and thus the enrichments are essentially the same under the three different conditions.

Since a recombination reaction $X + YZ$ $(Y \neq Z)$ can lead to two different products, the partitioning between the two products at the same hindered-rotor transition state is of interest. In earlier studies, it was assumed that half of the quantum states of the transition state in the entrance channel lead to one ozone isotopomer XYZ and half to the other, XZY. In the present study, a more general approach is used, where the assignment of the transition quantum state to each product was determined by an integral of its wave function (squared) over half of the θ space, the space that leads to that particular molecule as in Eq. (15). As noted in Sec. IV, no significant difference between the two sets of results was found for the isotopic exchange rate constants, or for the recombination rate constants, between the approximate $(\Phi_a = \Phi_b = 0.5)$ and the integrated wave function treatment for this partitioning.

It has been pointed out that the large variation in recombination rate constant ratios correlate empirically well with ratios of moment of inertia,[34] differences in zero-point energies,[34,46] and ratios of reduced masses.[34] Indeed, all three quantities are mathematically related to each other[34] and so one cannot determine which of the three factors dominates simply from a plot of the rate constant ratios versus any one of them.[34,47] The theory[29,30] brings out that of the three it is the zero-point energy difference that is the primary source of the large mass-dependent effect in the recombination rate constant ratios, because of its effect on numbers of states in transition states of the two dissociation channels.

ACKNOWLEDGMENT

It is a pleasure to acknowledge the support of this research by the National Science Foundation.

[1] R. N. Clayton, L. Grossman, and T. K. Mayeda, Science **182**, 485 (1973).
[2] J. E. Heidenreich III and M. H. Thiemens, J. Chem. Phys. **78**, 892 (1983).
[3] J. E. Heidenreich III and M. H. Thiemens, J. Chem. Phys. **84**, 2129 (1986).
[4] K. Mauersberger, Geophys. Res. Lett. **14**, 80 (1987).
[5] J. Yang and S. Epstein, Geochim. Cosmochim. Acta **51**, 2011 (1987).
[6] J. Yang and S. Epstein, Geochim. Cosmochim. Acta **51**, 2019 (1987).
[7] M. H. Thiemens and T. Jackson, Geophys. Res. Lett. **14**, 624 (1987).
[8] M. H. Thiemens and T. Jackson, Geophys. Res. Lett. **15**, 639 (1988).
[9] S. M. Anderson, J. Morton, and K. Mauersberger, Chem. Phys. Lett. **156**, 175 (1989).
[10] J. Morton, B. Schueler, and K. Mauersberger, Chem. Phys. Lett. **154**, 143 (1989).
[11] J. Morton, J. Barnes, B. Schueler, and K. Mauersberger, J. Geophys. Res., [Atmos.] **95**, 901 (1990).
[12] M. H. Thiemens and T. Jackson, Geophys. Res. Lett. **17**, 717 (1990).
[13] B. Schueler, J. Morton, and K. Mauersberger, Geophys. Res. Lett. **17**, 1295 (1990).
[14] J. Wen and M. H. Thiemens, Chem. Phys. Lett. **172**, 416 (1990).
[15] J. Wen and M. H. Thiemens, J. Geophys. Res., [Atmos.] **96**, 10911 (1991).
[16] S. M. Anderson, K. Mauersberger, J. Morton, and B. Schueler, ACS Symp. Ser. **502**, (1992).
[17] M. H. Thiemens, ACS Symp. Ser. **502**, (1992).
[18] K. Mauersberger, J. Morton, B. Schueler, J. Stehr, and S. M. Anderson, Geophys. Res. Lett. **20**, 1031 (1993).
[19] D. Krankowsky, F. Bartecki, G. G. Klees, K. Mauersberger, and K. Schellenbach, Geophys. Res. Lett. **22**, 1713 (1995).
[20] J. Sehested, O. J. Nielsen, H. Egsgaard, N. W. Larsen, T. Pedersen, L. K. Christensen, and M. Wiegell, J. Geophys. Res., [Atoms.] **100**, 20979 (1995).
[21] D. Krankowsky and K. Mauersberger, Science **274**, 1324 (1996).

[22] L. K. Christensen, N. W. Larsen, F. M. Nicolaisen, T. Pedersen, G. O. Sørensen, and H. Egsgaard, J. Mol. Spectrosc. **175**, 220 (1996).

[23] J. C. Johnson and M. H. Thiemens, J. Geophys. Res., [Atmos.] **102**, 25395 (1997).

[24] S. M. Anderson, D. Hüsebusch, and K. Mauersberger, J. Chem. Phys. **107**, 5385 (1997).

[25] K. Mauersberger, B. Erbacher, D. Krankowsky, J. Günther, and R. Nickel, Science **283**, 370 (1999).

[26] C. Janssen, J. Günther, D. Krankowsky, and K. Mauersberger, J. Chem. Phys. **111**, 7179 (1999).

[27] J. Guenther, B. Erbacher, D. Krankowsky, and K. Mauersberger, Chem. Phys. Lett. **306**, 209 (1999).

[28] J. Günther, D. Krankowsky, and K. Mauersberger, Chem. Phys. Lett. **324**, 31 (2000).

[29] Y. Q. Gao and R. A. Marcus, Science **293**, 259 (2001).

[30] Y. Q. Gao and R. A. Marcus, J. Chem. Phys. **116**, 137 (2002).

[31] M. R. Wiegell, N. W. Larsen, T. Pedersen, and H. Egsgaard, Int. J. Chem. Kinet. **29**, 745 (1997).

[32] A. Gross and G. D. Billing, Chem. Phys. **217**, 1 (1997).

[33] B. C. Hathorn and R. A. Marcus, J. Chem. Phys. **111**, 4087 (1999).

[34] B. C. Hathorn and R. A. Marcus, J. Chem. Phys. **113**, 9497 (2000).

[35] R. G. Gilbert and S. C. Smith, *Theory of Unimolecular and Recombination Reactions* (Blackwell Scientific, Boston, 1990), and references cited therein.

[36] K. Yamashita, K. Morokuma, F. Le Quere, and C. Leforestier, Chem. Phys. Lett. **191**, 515 (1992); C. Leforestier, F. Le Quere, K. Yamashita, and K. Morokuma, J. Chem. Phys. **101**, 3806 (1994).

[37] H. Hippler, R. Rahn, and J. Troe, J. Chem. Phys. **93**, 6560 (1990).

[38] The neglect of off-diagonal elements ($\Omega' \neq \Omega$) in treating the radial motion of the two reactants has been termed in the collision dynamics literature the ''j_z-conserving,'' ''coupled state,'' or ''centrifugal decoupling'' approximation. See for example, R. B. Walker and J. C. Light, Chem. Phys. **7**, 84 (1975).

[39] Strictly speaking a boundary of the channels leading from $X+YZ$ to XYZ and to XZY does not occur at a θ exactly equal to $\pi/2$ when $Y \neq Z$. An improved boundary would be at a $\theta = \alpha$ where the distance of X to Y equals that from X to Z. The α depends on R and r via $\alpha = \cos^{-1}\{(m_Z - m_Y)/[2(m_Y+m_Z)]r/R\}$, where $m_{Y,Z}$ is the mass of Y (Z). For hindered rotation the typical amplitude tends to be largest in the interior of each θ region rather than at θ near $\pi/2$. We omit the possible refinement of calculating α instead of using $\alpha = \pi/2$. The present treatment permits one to allow for any asymmetry in the wave function between the two θ intervals.

[40] S. Zhang and J. Jin, *Computation of Special Functions* (Wiley, New York, 1996), Chap. 15.

[41] T. Baer and W. L. Hase, *Unimolecular Reaction Dynamics, Theory and Experiment* (Oxford University Press, New York, 1996), and references cited therein.

[42] W. Forst, *Theory of Unimolecular Reactions* (Academic, New York, 1973) and references cited therein.

[43] P. J. Robinson and K. A. Holbrook, *Unimolecular Reactions* (Wiley-Interscience, London, 1972), and references cited therein.

[44] B. C. Hathorn and R. A. Marcus, J. Phys. Chem. A **105**, 2612 (2001).

[45] $\Sigma_J N(EJ)$ does not appear as such in the rate constant in Ref. 30, but for discussion is a reflection of the tightness or looseness of the transition state.

[46] C. Janssen, J. Guenther, K. Mauersberger, and D. Krankowsky, Phys. Chem. Chem. Phys. **3**, 4718 (2001).

[47] R. A. Marcus, Science **294**, 951a (2001); www.sciencemag.org/cgi/content/full/294/5544/951a

Chapter 9

Half- and Full-Integer Power Law for Distance Fluctuations: Langevin Dynamics in One- and Two-Dimensional Systems

[This chapter appeared in *Chemical Physics* **331**, 245 (2007).]

Available online at www.sciencedirect.com
ScienceDirect
ELSEVIER
Chemical Physics 331 (2007) 245–253
Chemical Physics
www.elsevier.com/locate/chemphys

Half- and full-integer power law for distance fluctuations: Langevin dynamics in one- and two-dimensional systems

Wei-Chen Chen *, Jau Tang *

Noyes Laboratory 127-72, California Institute of Technology, Pasadena, CA 91125, USA

Received 6 June 2006; accepted 24 October 2006
Available online 27 October 2006

Abstract

Langevin dynamics of one- and two-dimensional systems with the nearest neighbor couplings is examined to derive the autocorrelation function (ACF) of the distance fluctuations. Understanding of the dynamics of pairwise distance correlation is essential in the studies using single-molecule spectroscopy. For both 1-D cases of an open chain and a closed loop, a power law of $t^{-1/2}$, $t^{-3/2}$ and $t^{-5/2}$ for the ACF are obtained, and for 2-D systems of a sheet and a tube, a power law of t^{-1}, t^{-2} and t^{-3} are found. The different exponent of the power law is shown to depend on the location of the pairwise beads and their topography.

PACS: 33.15.Vb; 34.30.+h; 36.20.Ey

Keywords: Power laws; Langevin dynamics; Single molecule; Rouse model

1. Introduction

Decays in physical systems are usually characterized by pure-exponential or by non-exponential decays. Power-law decays have often been associated with self-similar processes involving fractals [1–7]. For example, in a recent work by Granek and Klafter [1] they showed that power-law decays in distance autocorrelation function (ACF) could arise due to vibrational excitation of fractals. Recently power-law behavior in fluorescence intermittency observed in single quantum dots [8–12] and other organic molecules [13] have generated some interest. It has been shown that diffusion-controlled electron transfer in a Debye and non-Debye dielectric media could lead to the power-law blinking statistics [14,15].

The recent single-molecule experiments by Xie and coworkers [16–18] on fluctuating fluorescence lifetimes were attributed to fluctuations in the distance between a donor and an acceptor attached to a protein chain. The observed $t^{-1/2}$ power law in the lifetime fluctuations and its relationship to chain dynamics have been investigated recently [19–21] using a Rouse model [22]. There are also many other theoretical studies of reaction controlled by barrier fluctuations and diffuse dynamics [1,23–27]. In electron transfer (ET) and fluorescence resonances energy transfer (FRET), the transfer rate depends on the distance R between donor and an acceptor (exponentially for ET and $1/R^6$ for FRET) [28]. If donor–acceptor distance is subjected to fluctuations, the rate constant would also fluctuate in time. In addition to single-molecule techniques, many other experimental techniques have been employed to study these conformational changes, such as NMR [29], neutron scattering [30,31], optical absorption [32], electrophoresis [33], optical tweezers [34] etc. Chain dynamics has been used in these studies.

In this work, we extend previous studies of Rouse model [22] to a long chain and a closed loop, shown in

---

* Corresponding authors. Present address: Center for Ultrafast Science and Technology, California Institute of Technology, Pasadena, CA 91125, USA (Jau Tang).

E-mail addresses: cwc@caltech.edu (W.-C. Chen), jautang@caltech.edu (J. Tang).

0301-0104/$ - see front matter © 2006 Elsevier B.V. All rights reserved.
doi:10.1016/j.chemphys.2006.10.012

the schematic diagrams Fig. 1(a) and (b), respectively, as well as a two-dimensional system of a sheet or a tube, and examine the distance ACF between any pair of beads in such a 1-D or 2-D system. We will show that Langevin dynamics for 1-D chain/loop under some conditions could lead to the less well-know $t^{-3/2}$ and $t^{-5/2}$ power law, in addition to the more familiar $t^{-1/2}$ behavior. In addition to the half-integer power law for the 1-D system, we will also show that for a 2-D system, the ACF decays with a full-integer law (t^{-1}, t^{-2} and t^{-3}), depending on the topological conditions of such a pairwise beads. A ladder system, seen in Fig. 1(c), is also studied and has similar time behaviors of ACF in chain a system. Besides the half-integer laws, the ACF in a ladder also has only exponential (no power laws) decays at certain topological conditions. The main purpose of this work is to show these half- and full-integer power laws can arise and to explain their causes.

2. Theory

We will derive in this section the analytic results for ACF of the distance fluctuation for four different topological categories, *i.e.* an open chain, a closed loop, a sheet, a tube, and a ladder. Their corresponding long time behaviors are also summarized and illustrated.

2.1. An open chain

An ideal chain of N beads with equal couplings to their nearest neighbors and other vibrations have been studied widely [22]. The Langevin equation of over-damped oscillators in such a N-unit Rouse chain can be expressed by [35,36]

$$\zeta \frac{\mathrm{d}}{\mathrm{d}t} Q(t) + \omega^2 \mathbf{R} Q(t) = F(t)/m, \tag{1}$$

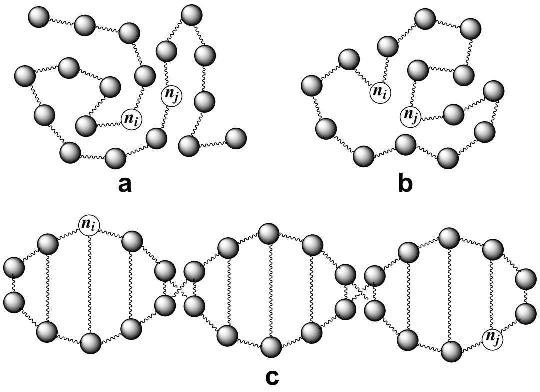

Fig. 1. The schematic diagrams of a Rouse model with a open chain (a), a closed loop (b), and a ladder (c) of beads. A bead interacts with others through the connected springs. The dynamics between n_ith and n_jth beads at various positions are studied in this work.

where ζ is a constant friction coefficient. The $Q(t)$ is a column super vector $(\vec{q}_1, \vec{q}_2, \vec{q}_3 \ldots \vec{q}_N)$, where $\vec{q}_i$ denotes the displacement vector of the ith bead from its equilibrium position. $\mathbf{R}$ is the Rouse coupling matrix. $F(t)$ represents white noise with zero mean and no correlation with $Q(t)$. Therefore, one has the following equations: $\langle F_i^{\mu}(t)\rangle = 0$, $\langle F_i^{\mu}(t) \cdot q_j^{\nu}(\tau)\rangle = 0$, and $\langle F_i^{\mu}(t) \cdot F_j^{\nu}(\tau)\rangle = 2mk_{\mathrm{B}}\ T\zeta\delta(t-\tau)\,\delta_{\mu,\nu}\delta_{i,j}$, where μ and ν represent x, y, or z, whereas i and j represent the bead index. The pairwise correlation of the displacement vectors can be written as [20,21]

$$\begin{aligned}
&\frac{\mathrm{d}}{\mathrm{d}t}\langle \vec{q}_1(t)\cdot\vec{q}_i(0)\rangle + \frac{\omega^2}{\zeta}(\langle \vec{q}_1(t)\cdot\vec{q}_i(0)\rangle - \langle \vec{q}_2(t)\cdot\vec{q}_i(0)\rangle) = 0,\\
&\frac{\mathrm{d}}{\mathrm{d}t}\langle \vec{q}_n(t)\cdot\vec{q}_i(0)\rangle + \frac{\omega^2}{\zeta}(-\langle \vec{q}_{n-1}(t)\cdot\vec{q}_i(0)\rangle + 2\langle \vec{q}_n(t)\cdot\vec{q}_i(0)\rangle\\
&\quad - \langle \vec{q}_{n+1}(t)\cdot\vec{q}_i(0)\rangle) = 0,\\
&\frac{\mathrm{d}}{\mathrm{d}t}\langle \vec{q}_N(t)\cdot\vec{q}_i(0)\rangle + \frac{\omega^2}{\zeta}(-\langle \vec{q}_{N-1}(t)\cdot\vec{q}_i(0)\rangle\\
&\quad + \langle \vec{q}_N(t)\cdot\vec{q}_i(0)\rangle) = 0,
\end{aligned} \tag{2}$$

where $n = 2, 3, \cdots N-1$; $i = 1, 2, \cdots N$; and $\langle \vec{q}_j(t)\cdot\vec{q}_i(0)\rangle$ is the ensemble average of the inner product of $\vec{q}_j(t)$ and $\vec{q}_i(0)$. Using the method described in Appendix C of Ref. [37] the pairwise correlation functions can be simplified as

$$\begin{aligned}
\langle \vec{q}_n(t)\cdot\vec{q}_i(0)\rangle &= \sum_{j=1}^{N} \frac{\langle \vec{q}_j(0)\cdot\vec{q}_i(0)\rangle}{N}\\
&\quad \times \left\{1 + 2\sum_{k=1}^{N-1}\cos\left(\frac{\pi k(n-\frac{1}{2})}{N}\right)\right.\\
&\quad \left.\times \cos\left(\frac{\pi k\left(j-\frac{1}{2}\right)}{N}\right)\exp\left[-4\frac{\omega^2 t}{\zeta}\sin^2\left(\frac{\pi k}{2N}\right)\right]\right\}\\
&= \frac{\langle|\vec{q}_i(0)|^2\rangle}{N}\left\{1 + 2\sum_{k=1}^{N-1}\cos\left(\frac{\pi k(n-\frac{1}{2})}{N}\right)\right.\\
&\quad \left.\times \cos\left(\frac{\pi k\left(i-\frac{1}{2}\right)}{N}\right)\exp\left[-4\frac{\omega^2 t}{\zeta}\sin^2\left(\frac{\pi k}{2N}\right)\right]\right\},
\end{aligned} \tag{3}$$

where $\langle \vec{q}_j(0)\vec{q}_i(0)\rangle = \delta_{i,j}\langle|\vec{q}_i(0)|^2\rangle$ was used. By assuming the distance fluctuation of each bead from its equilibrium position is small, the ACF of the distance deviation, $C_Q(t)$, between the n_1th and n_2th beads from their equilibrium position equals $\langle[\vec{q}_{n_1}(t) - \vec{q}_{n_2}(t)]\cdot[\vec{q}_{n_1}(0) - \vec{q}_{n_2}(0)]\rangle/3$. Using Eq. (3), one obtains [20,21]

$$\frac{C_Q(t)}{C_0} = \sum_{k=1}^{N-1} \frac{\mathrm{e}^{\frac{-4\omega^2 t}{\zeta}\sin^2\left(\frac{\pi k}{2N}\right)}}{N}\left[\cos\left(\frac{\pi k\left(n_1-\frac{1}{2}\right)}{N}\right) - \cos\left(\frac{\pi k\left(n_2-\frac{1}{2}\right)}{N}\right)\right]^2, \tag{4}$$

where C_0 is defined as $C_Q(0)$. The power-law behaviors at long times are depending on the location and separation of the pairwise beads. In a long chain the long time behaviors of the above equation can be classified as

$$\frac{C_Q(t)}{C_0} \propto \begin{cases} t^{-1/2} & \text{as } |n_1 - n_2| \approx N, \\ t^{-3/2} & \text{as } |n_1 - n_2| \ll N, \text{and both } n_1 \;\&\; n_2 \\ & \quad \text{away from ends,} \\ t^{-5/2} & \text{otherwise.} \end{cases} \tag{5}$$

The numerical results are illustrated in Fig. 2(a). The power-laws behaviors are derived in A.1 using asymptotic approximation. More detailed discussion about the causes of different power laws will be discussed in Section 3.

2.2. A closed loop

The pairwise correlation function of displacement vectors in a N-unit loop satisfies

$$\frac{\mathrm{d}}{\mathrm{d}t}\langle \vec{q}_n(t)\cdot\vec{q}_i(0)\rangle + \frac{\omega^2}{\zeta}(-\langle \vec{q}_{n-1}(t)\cdot\vec{q}_i(0)\rangle + 2\langle \vec{q}_n(t)\cdot\vec{q}_i(0)\rangle - \langle \vec{q}_{n+1}(t)\cdot\vec{q}_i(0)\rangle) = 0, \tag{6}$$

where n, $i = 1, \ldots N$. One has the Nth bead connects with the first bead to form a loop, *i.e.* $\vec{q}_0 = \vec{q}_N$ and $\vec{q}_1 = \vec{q}_{N+1}$. Using the method described in Appendix A of Ref. [37], the correlation functions are simplified as

$$\langle \vec{q}_n(t)\cdot\vec{q}_i(0)\rangle = \frac{\langle|\vec{q}_n(0)|^2\rangle}{N}\sum_{k=1}^{N}\cos\left(\frac{2\pi k(n-i)}{N}\right) \times \exp\left[\frac{-4\omega^2 t}{\zeta}\sin^2\left(\frac{\pi k}{N}\right)\right]. \tag{7}$$

With the above equation, the ACF of the distance deviation between the n_1th and n_2th beads from their equilibrium positions can be expressed as

$$\frac{C_Q(t)}{C_0} = \frac{2}{N}\sum_{k=1}^{N}\sin^2\left(\frac{\pi k(n_1-n_2)}{N}\right)\exp\left[\frac{-4\omega^2 t}{\zeta}\sin^2\left(\frac{\pi k}{N}\right)\right]. \tag{8}$$

In a long chain the time power-law behaviors of C_Q can be grouped as

$$\frac{C_Q(t)}{C_0} \propto \begin{cases} t^{-1/2} & \text{when } |n_1 - n_2| \approx N/2, \\ t^{-3/2} & \text{otherwise.} \end{cases} \tag{9}$$

These behaviors of C_Q are also shown in Fig. 2(b). The mathematical asymptotic approximation of the power-law behaviors in Eq. (8) are given in A.1. More detailed discussion about the reasons of change from $t^{-1/2}$ to $t^{-3/2}$ are discussed in Section 3.

2.3. A sheet

Assuming a two-dimensional sheet with $N \times M$ beads where each bead is coupled to the nearest beads, the pairwise correlation of the displacement vectors can be obtained straight forward by introducing another independent dimension to Eq. (2). Extending Eq. (3) to two independent variables along N and M directions, the solution of the correlation of the displacement is given by

$$\begin{aligned} \langle \vec{q}_{n,m}(t)\cdot\vec{q}_{i,j}(0)\rangle = \frac{\langle|q_{n,m}(0)|^2\rangle}{NM}&\left\{1 + 2\sum_{k_x=1}^{N-1}\cos\left(\frac{\pi k_x\left(n-\frac{1}{2}\right)}{N}\right)\right. \\ &\left.\times\cos\left(\frac{\pi k_x\left(i-\frac{1}{2}\right)}{N}\right)\times\exp\left[-4\frac{\omega_x^2 t}{\zeta}\sin^2\left(\frac{\pi k_x}{2N}\right)\right]\right\} \\ &\times\left\{1 + 2\sum_{k_y=1}^{M-1}\cos\left(\frac{\pi k_y\left(m-\frac{1}{2}\right)}{M}\right)\right. \\ &\left.\times\cos\left(\frac{\pi k_y\left(j-\frac{1}{2}\right)}{M}\right)\exp\left[\frac{-4\omega_y^2 t}{\zeta}\sin^2\left(\frac{\pi k_y}{2M}\right)\right]\right\}. \end{aligned} \tag{10}$$

One can derive the ACF of the distance deviation between the beads at the (n_1,m_1)- and (n_2,m_2)-sites as

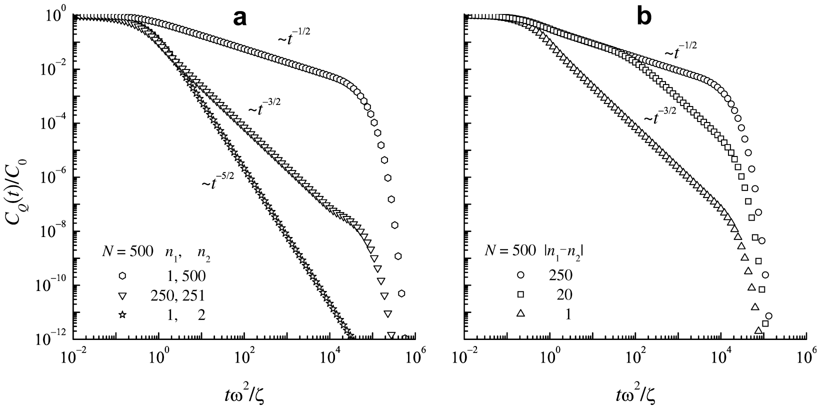

Fig. 2. The calculated $C_Q(t)/C_0$ for the various separations between the pairwise beads for a chain (a) and a loop (b) with $N = 500$. Here a dimensionless $t\omega^2/\zeta$ is used for the x-axis. n_1 and n_2 are the site indices of the pairwise beads. The exponent of the power law, $-1/2$, $-3/2$, and $-5/2$, depends on $|n_1 - n_2|$ and its location. At much longer times, $C_Q(t)/C_0$ becomes a single exponential decay.

$$\frac{C_Q(t)}{C_0} = \frac{1}{NM}\left\{\sum_{k_x=1}^{N-1} \mathrm{e}^{\frac{-4\omega_x^2 t}{\zeta}\sin^2\left(\frac{\pi k_x}{2N}\right)}\left[\cos\left(\frac{\pi k_x\left(n_1-\frac{1}{2}\right)}{N}\right) - \cos\left(\frac{\pi k_x\left(n_2-\frac{1}{2}\right)}{N}\right)\right]^2 + \sum_{k_y=1}^{M-1} \mathrm{e}^{\frac{-4\omega_y^2 t}{\zeta}\sin^2\left(\frac{\pi k_y}{2M}\right)}\right.$$
$$\times\left[\cos\left(\frac{\pi k_y\left(m_1-\frac{1}{2}\right)}{M}\right) - \cos\left(\frac{\pi k_y\left(m_2-\frac{1}{2}\right)}{M}\right)\right]^2 + 2\sum_{k_x=1}^{N-1}\sum_{k_y=1}^{M-1} \mathrm{e}^{\frac{-4t}{\zeta}\left[\omega_x^2\sin^2\left(\frac{\pi k_x}{2N}\right)+\omega_y^2\sin^2\left(\frac{\pi k_y}{2M}\right)\right]}$$
$$\left.\times\left[\cos\left(\frac{\pi k_x\left(n_1-\frac{1}{2}\right)}{N}\right)\times\cos\left(\frac{\pi k_y\left(m_1-\frac{1}{2}\right)}{M}\right) - \cos\left(\frac{\pi k_x\left(n_2-\frac{1}{2}\right)}{N}\right)\cos\left(\frac{\pi k_y\left(m_2-\frac{1}{2}\right)}{M}\right)\right]^2\right\}. \quad (11)$$

At various locations of the pairwise beads, its long time property in a large sheet gives the following asymptotic behaviors.

$$\frac{C_Q(t)}{C_0} \propto \begin{cases} t^{-1} & \text{as } |n_1-n_2| \approx N \text{ and } |m_1-m_2| \approx M \\ t^{-2} & \text{as } |n_1-n_2| \ll N,\ |m_1-m_2| \ll M \text{ and } (n_1,m_1)\text{-} \\ & \&\ (n_2,m_2)\text{-sites are parallel to or far away from} \\ & \text{the boundaries,} \\ t^{-3} & \text{otherwise.} \end{cases} \quad (12)$$

The numerical results are illustrated in Fig. 3(a). More detailed discussions of the behaviors and the analytical asymptotic approximation to obtained the power laws will be presented in Section 3 and A.2, respectively.

2.4. A tube

The differential equations of the pairwise correlation of the displacement vector of a $N \times M$ hollow tube with N-bead in length can be obtained by combining Eq. (2) with N beads and Eq. (6) with M beads. Using the results in Eqs. (3) and (7), the correlation of the displacement $\langle q_{n,m}(t)q_{i,j}(0)\rangle$ and the ACF $C_Q(t)$ between the beats at (n_1,m_1)- and (n_2,m_2)-sites can be derived as

$$\langle \vec{q}_{n,m}(t)\cdot\vec{q}_{i,j}(0)\rangle = \frac{\langle |q_{n,m}(0)|^2\rangle}{NM}\left\{1 + 2\sum_{k_x=1}^{N-1} \mathrm{e}^{\frac{-4\omega_x^2 t}{\zeta}\sin^2\left(\frac{\pi k_x}{2N}\right)} \times\cos\left(\frac{\pi k_x\left(n-\frac{1}{2}\right)}{N}\right)\cos\left(\frac{\pi k_x\left(i-\frac{1}{2}\right)}{N}\right)\right\}$$
$$\times\sum_{k_y=1}^{M} \mathrm{e}^{\frac{-4\omega_y^2 t}{\zeta}\sin^2\left(\frac{\pi k_y}{M}\right)}\cos\left(\frac{2\pi k_y(m-j)}{M}\right). \quad (13)$$

$$\frac{C_Q(t)}{C_0} = \frac{1}{NM}\left\{2\sum_{k_y=1}^{M} \mathrm{e}^{\frac{-4\omega_y^2 t}{\zeta}\sin^2\left(\frac{\pi k_y}{M}\right)}\sin^2\left(\frac{\pi k_y(m_1-m_2)}{M}\right) + \sum_{k_x=1}^{N-1}\sum_{k_y=1}^{M} \mathrm{e}^{\frac{-4t}{\zeta}\left[\omega_x^2\sin^2\left(\frac{\pi k_x}{2N}\right)+\omega_y^2\sin^2\left(\frac{\pi k_y}{M}\right)\right]}\right.$$
$$\times\left[\cos^2\left(\frac{\pi k_x\left(n_1-\frac{1}{2}\right)}{N}\right) + \cos^2\left(\frac{\pi k_x\left(n_2-\frac{1}{2}\right)}{N}\right) - 2\cos\left(\frac{\pi k_x\left(n_1-\frac{1}{2}\right)}{N}\right)\times\cos\left(\frac{\pi k_x\left(n_2-\frac{1}{2}\right)}{N}\right)\right.$$
$$\left.\left.\times\cos\left(\frac{2\pi k_y(m_1-m_2)}{M}\right)\right]\right\}. \quad (14)$$

The long time property of the AFC, shown in Fig. 3(b), similar to the case in a sheet and the asymptotic behaviors are classified as

$$\frac{C_Q(t)}{C_0} \propto \begin{cases} t^{-1} & \text{as } |n_1-n_2| \approx N \text{ and } |m_1-m_2| \approx M/2 \\ t^{-2} & \text{as } |n_1-n_2| \ll N,\ |m_1-m_2| \ll M/2 \text{ and} (n_1,m_1)\text{-} \\ & \&\ (n_2,m_2)\text{-sites are parallel to or far away from} \\ & \text{the boundaries,} \\ t^{-3} & \text{otherwise.} \end{cases} \quad (15)$$

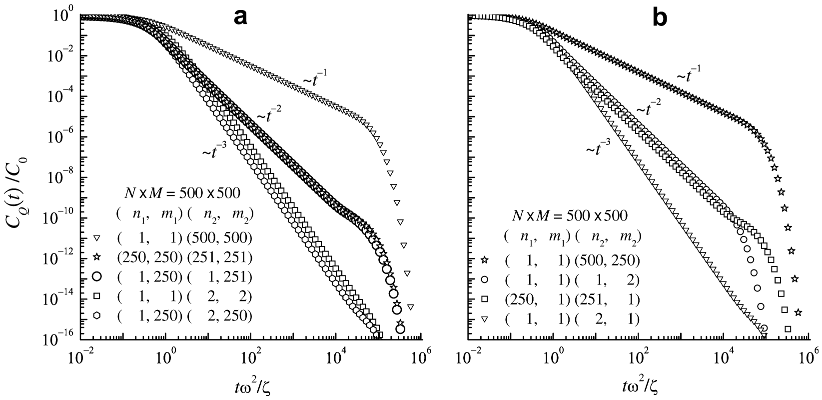

Fig. 3. The calculated $C_Q(t)/C_0$ for the various separations in a sheet (a) and a hallow tube (b) with $\omega = \omega_x = \omega_y$ and $N = M = 500$. The decay follows an full-integer power law, and becomes single exponential decays at much longer time.

The analytical derivations of the asymptotic power-law behaviors can be found in A.2.

2.5. A ladder

Although C_Q of a ladder can be formed by modifying Eq. (11) to an $N \times 2$ sheet, it behaves more like a chain. The numerical results and the analytical asymptotic approximation of Eq. (11) as $N \times 2$ in the long time are shown in Fig. 4 and A.3, respectively. The ACF formed the following behaviors at certain topological conditions:

$$\frac{C_Q(t)}{C_0} \propto \begin{cases} e^{-\alpha t} & \text{as two beads are at the same level } (\textit{i.e. } n_1 = n_2), \\ t^{-1/2} & \text{as } |n_1 - n_2| \approx N, \\ t^{-3/2} & \text{as } |n_1 - n_2| \ll N, \text{and both } n_1 \;\&\; n_2 \text{ away} \\ & \text{from ends,} \\ t^{-5/2} & \text{otherwise.} \end{cases} \tag{16}$$

At the same level of a ladder, the exponential time behavior implies that these two beads have very fast synchronized motions due to the link between them. It may also contribute to the stability in molecules with a ladder structure, such as DNA.

3. Origins for different exponents of the power law

In the one-dimensional cases, the physical origin of the different asymptotic behaviors are given as following: The ACF of distance deviation is proportional to $\langle \vec{q}_{n_1}(t) \cdot \vec{q}_{n_1}(0) + \vec{q}_{n_2}(t) \cdot \vec{q}_{n_2}(0) - \vec{q}_{n_1}(t) \cdot \vec{q}_{n_2}(0) - \vec{q}_{n_2}(t) \cdot \vec{q}_{n_1}(0) \rangle$. The first two terms represent the ACF of distance deviation at the n_1th and n_2th sites, respectively. The last two terms are the correlation function of the displacement vector between the n_1th and n_2th beads. They also correspond to the displacement in a diffusion-like process from one bead to another since the interaction between beads are described by the Langevin equation, Eq. (1). These terms are much smaller than the first two because there is a long separation between beads. Therefore, the C_Q is dominated by the change of the displacement amplitude in itself by diffusion, which results in the usual $t^{-1/2}$ power-law behavior in the 1-D system. By rearranging terms, the C_Q is also proportional to $\langle [\vec{q}_{n_1}(t) - \vec{q}_{n_2}(t)] \cdot \vec{q}_{n_1}(0) + [\vec{q}_{n_2}(t) - \vec{q}_{n_1}(t)] \cdot \vec{q}_{n_2}(0) \rangle$. The $\langle [\vec{q}_{n_1}(t) - \vec{q}_{n_2}(t)] \cdot \vec{q}_{n_1}(0) \rangle$ term represents the difference of the diffused displacement vector (originated from the n_1th bead) between the n_1th and n_2th beads at a time t. If the separation between them is comparable to or smaller than the diffusion distance of the displacement vector, the magnitude of $\langle \vec{q}_{n_2}(t) \cdot \vec{q}_{n_1}(0) \rangle$ is similar to that of $\langle \vec{q}_{n_1}(t) \cdot \vec{q}_{n_1}(0) \rangle$. A difference of these two terms corresponds to a time differential of the displacement vector, *i.e.* $\mathrm{d}\langle \vec{q}_{n_1}(t) \cdot \vec{q}_{n_1}(0) \rangle / \mathrm{d}t$, if the separation between the n_1th and n_2th beads is much smaller than the diffusion distance. Thus, it results in the $t^{-3/2}$ asymptotic behavior for the ACF for a small separation of beads. As the separation of the beads increases, the asymptotic behavior is shown in Fig. 2(b), having $t^{-1/2}$ initially and then becomes $t^{-3/2}$ at later time.

If two beads are close and near an end in a long chain, the ACF yields a $t^{-5/2}$ asymptotic behavior, shown in Fig. 2(a), instead of $t^{-3/2}$ as two close beads in a loop or far from ends in a chain. It is due to boundary conditions at the ends of a chain. Because of the reflection of distance deviation at the end of a chain, the value of $\langle [\vec{q}_{n_1}(t) - \vec{q}_{n_2}(t)] \cdot \vec{q}_{n_1}(0) \rangle$ is similar to taking a second time derivative at $\langle \vec{q}_{n_1}(t) \vec{q}_{n_1}(0) \rangle$ if n_1 and n_2 are close and near the end in an open chain.

Due to the same reason in one 1-D systems, the ACF in 2-D systems has one power smaller in large separation than in short one, shown in Fig. 3. It also means that the interference between the pairwise beads that are close is faster and stronger, which is similar to the 1-D cases. The long-time behavior for close pairwise beads near a corner in a large sheet is t^{-3}, instead of t^{-2} for beads near the center. It is due to the reflection at the boundaries. If the two beads are near the edge but far away from the corner, the ACF of distance deviation can have different long-time behavior, which depends on the orientation of the beads with the edge. If the beads are parallel to the edge and not close to a corner, the reflection of diffusion at the boundary does not affect the ACF of displacement. Therefore, the long-time behavior, shown in Fig. 3, has the t^{-2} character, similar to the case of two beads that are close but both far away from boundaries. If the pairwise beads are not parallel to an edge, the reflection at the boundary does affect the C_Q values. Therefore, the long-time behavior has t^{-3} asymptotic behavior, as seen in Fig. 3(a) and (b) for sheet and tube cases, respectively.

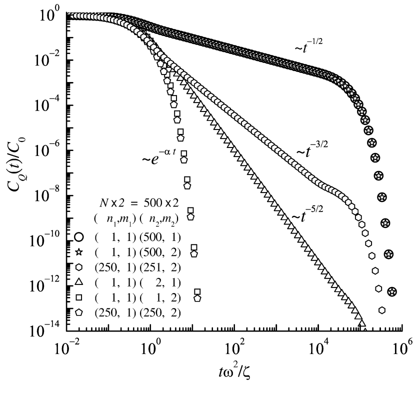

Fig. 4. The calculated $C_Q(t)/C_0$ for the various separations in a ladder with $\omega = \omega_x = \omega_y$ and $N = 500$. The decay is a single exponential if the pairwise beads are at the same level, and follows half-integer power law otherwise. All become single exponential decays eventually.

4. Discussion and conclusions

In this work, we have studied Langevin dynamics for an ideal 1-D and 2-D systems. Several kinds of power-law behavior are obtained and their exponent is found to be dependent on the distance of the pairwise beads such as a donor and an acceptor in electron or energy transfer. Studies of pairwise distance correlation using single-molecule spectroscopy are important in elucidating molecular dynamics. As shown in Figs. 2–4, the power-law behavior lasts for about six decades. Using the typical van der Waals couplings and the experimental values of the friction constant [32,38], the time range to observe such power-law behavior is estimated to cover picosecond to microsecond range.

This work shows that the distance ACF of a distant donor–acceptor pair follows a power law of $t^{-d/2}$ for a simple Rouse model with a d-dimension coupling network. This power-law behavior is very similar to d-dimension diffusion based on the scale invariance argument. The similarity is due to mathematical analogy between the Langevin equation of a Rouse model to a d-dimensional random walk process. However, for a close pair, our work predicts an interesting but different power law than the usual $t^{-d/2}$ dependence. For example, for an adjacent donor-acceptor pair of a 1-D Rouse chain, the power law does not follows the ordinary $t^{-1/2}$ behavior but follow $t^{-3/2}$ or $t^{-5/2}$ behavior, depending on the location of the donor–acceptor pair.

The half-integer power law ($t^{-1/2}$, $t^{-3/2}$ and $t^{-5/2}$) are obtained for the 1-D systems; and the full-integer power law (t^{-1}, t^{-2} and t^{-3}) for the 2-D systems. In 1-D (or 2-D) system, the $t^{-1/2}$ (or t^{-1}) power law is obtained if the pairwise beads have a large separation and very weak interference. The $t^{-3/2}$ (or t^{-2}) power-law behavior is found if the pairwise beads are near but far away from the boundaries. It is also found that if the pairwise beads in a 2-D system are near and parallel the boundaries, the reflection of the interference from the boundaries has no effects on the dynamics. The $t^{-5/2}$ (or t^{-3}) power law is obtained if the close pairwise beads are close to but not parallel to the boundaries.

The Langevin dynamics in a ladder is more special, and it yields both pure exponential and power-law ($t^{-1/2}$, $t^{-3/2}$ and $t^{-5/2}$) behaviors. The conditions and reasons for different power laws are similar to the cases of an open chain. The pure exponential behavior happens if two beads are at the same level of a ladder. It also implies that the distance fluctuation between two beads at the same level decays very fast as compared to those at different ladder levels.

In our treatment we focused on ACF of the distance fluctuations between a donor–acceptor pair. It can be directly applied in electron transfer reactions which have simple exponential distance dependence for the electronic coupling. The temporal behavior of the distance ACF is sensitive to the specific dynamics of the donor–acceptor pair and their interactions with surrounding atoms or molecules. For other processes such as FRET which has different distance dependence ($\sim 1/R^6$) and other dynamics with orientational dependence as occurs in a 2-D rotor [28], a characteristically different temporal behavior for the ACF could arise. In some special cases, power laws may happen for the temporal behavior of the ACF in FRET. With anomalous diffusion in the subdiffusion regime ($\langle x^2 \rangle \propto t^{\alpha}$, $0 < \alpha < 1$), the temporal behavior of the lifetime fluctuation correlation at long time could be written as a summation of six terms with different powers in time [23].

For native proteins and other macromolecules with heavy cross links the simple Rouse model treatment is insufficient. The presence of heavy cross links in native folded proteins could lead to deviation from the simple power law [21]. However, in polypeptides one can treat aperiodic chain by assigning a distribution of non-identical force constants among those springs between beads, except that for such a case with various spring constants a simple analytic solution is no longer available and numerical approaches need to be used. Based on our numerical simulations for such a situation [20], we have found that the power law still applies so long as the root-mean-square deviation for the distribution for the force constant is not too broad. Otherwise, these simple power-law behaviors for a system with a more complicate coupling network could break down.

Here we suggested some experiments to test the power laws of various exponents. If an electron/energy donor and an acceptor are attached to a 1-D system such as polypeptides and polymers, or a 2-D system such as a membrane, or a ladder structure such as DNA, studies of the distance fluctuations between the donor–acceptor pair could provide information about the conformational dynamics of these low-dimensional structures as beautifully illustrated by single-molecule experiments of proteins by Xie's group [16–18]. It would be interesting if the predicted power law of various exponent can be observed with a donor–acceptor pair at different topological conditions. By varying the location and the separation between the donor and the acceptor, one could explore the power law of $t^{-3/2}$, $t^{-5/2}$, in addition to the more well-known $t^{-1/2}$ law.

Acknowledgments

The authors thank Professor R.A. Marcus and Meher Prakash for discussions. It is a pleasure to acknowledge the support of this research by the National Science Foundation and the Office of Naval Research. J.T. thanks the support of James W. Glanville Foundation at the California Institute of Technology when the major part of this work was completed.

Appendix A. The Asymptotic solutions of the power-law behavior

A.1. One-dimensional system

In the limit of a loop with a very large N and a long separation between the n_1th and n_2th beads (*i.e.* $N \to \infty$ and $|n_1 - n_2| \approx N/2$), Eq. (8) can be simplified by an integral [39] as

$$\frac{C_Q(t)}{C_0} \approx \frac{\exp\left(\frac{-2\omega^2 t}{\zeta}\right)}{\pi}\int_0^{\pi} \mathrm{d}x \exp\left(\frac{-2\omega^2 t}{\zeta}\cos x\right) = \mathrm{e}^{\frac{-2\omega^2 t}{\zeta}} I_0\left(\frac{2\omega^2 t}{\zeta}\right), \tag{A.1}$$

where $I_0(z)$ is the modified Bessel function of the first kind. Because of $I_\nu(x) \approx \exp(x)/(2\pi x)^{-1/2}$ at large x [40], Eq. (A.1) has an asymptotic power law, $(4\pi\omega^2 t/\zeta)^{-1/2}$, as shown in Fig. 2(b). The Rouse equation, Eq. (2), is mathematically equivalent to a 1-D diffusion equation. The $t^{-1/2}$ power behavior is expected since the solution of a diffusion equation in 1-D system has a pre-exponential factor proportional to $t^{-1/2}$.

If N of a loop is very large but the separation between the n_1th and n_2th beads is much smaller than $N/2$ (*i.e.* $N \to \infty$ and $|n_1 - n_2| \ll N/2$ or $|n_1 - n_2 - N| \ll N/2$), Eq. (8) can be approximated by an integral that can be simplified as [39]

$$\begin{aligned}\frac{C_Q(t)}{C_0} &\approx \frac{\mathrm{e}^{\frac{-2\omega^2 t}{\zeta}}}{2\pi}\int_0^{2\pi} \mathrm{d}x\{1 - \cos[x(n_1 - n_2)]\}\mathrm{e}^{\frac{2\omega^2 t \cos x}{\zeta}} \\ &= \mathrm{e}^{\frac{-2\omega^2 t}{\zeta}}\left[I_0\left(\frac{2\omega^2 t}{\zeta}\right) - I_{|n_1-n_2|}\left(\frac{2\omega^2 t}{\zeta}\right)\right].\end{aligned} \tag{A.2}$$

If $|z|$ and $|\arg z| \leqslant \pi/2 - \delta$, one has [40]

$$I_\nu(z) = \frac{e^z}{\sqrt{2\pi z}}\left[\sum_{k=0}^{n}(\nu,k)\left(\frac{-1}{2z}\right)^k + \mathrm{O}(|z|^{-n-1})\right],$$
$$\text{where } (\nu,k) = \frac{(4\nu^2 - 1^2)(4\nu^2 - 3^2)\cdots(4\nu^2 - (2k-1)^2)}{2^{2k}k!} \text{ and } (\nu,0) = 1. \tag{A.3}$$

Therefore, at a large t the leading term of Eq. (A.2) is proportional to $t^{-3/2}$. In the loop case, the asymptotic behavior of the distance ACF for a small separation is $t^{-3/2}$, which is different from the $t^{-1/2}$ behavior in a large separation, as seen in Fig. 2(b).

If two beads in a long chain have a short separation and are not close to the ends, the C_Q exhibits $t^{-3/2}$ behavior, as shown in Fig. 2(a). The behavior can also be expressed as Eq. (A.2) in a large loop. If two beads have a long distance separation (*i.e.* $n_1, n_2' \ll N$; $n_2 = N - n_2'$; and $N \to \infty$), the ACF of distance deviation can be written as

$$\begin{aligned}\frac{C_Q(t)}{C_0} &\approx \frac{\mathrm{e}^{\frac{-2\omega^2 t}{\zeta}}}{\pi}\int_0^{\pi} \mathrm{d}x\left\{\cos\left[x\left(n_1 + \frac{1}{2}\right)\right] - \cos\left[x\left(n_2 + \frac{1}{2}\right)\right]\right\}^2 \mathrm{e}^{\frac{2\omega^2 t \cos x}{\zeta}} \\ &= \mathrm{e}^{\frac{-2\omega^2 t}{\zeta}}\left[I_0\left(\frac{2\omega^2 t}{\zeta}\right) + \frac{1}{2}I_{2n_1+1}\left(\frac{2\omega^2 t}{\zeta}\right) + \frac{1}{2}I_{2n_2'-1}\left(\frac{2\omega^2 t}{\zeta}\right)\right].\end{aligned} \tag{A.4}$$

Using Eq. (A.3) the above equation at a large t yields a $t^{-1/2}$ behavior, which is similar to the behavior of two beads having a large separation for a loop case. Eq. (4) can be expressed by integral if N is very large and the beads are close to one end of the open chain (*i.e.* $N \to \infty$ and n_1, $n_2 \ll N$). It can be further simplified [39] as

$$\begin{aligned}\frac{C_Q(t)}{C_0} \approx \mathrm{e}^{\frac{-2\omega^2 t}{\zeta}}\Bigg[&I_0\left(\frac{2\omega^2 t}{\zeta}\right) - I_{n_1+n_2+1}\left(\frac{2\omega^2 t}{\zeta}\right) - I_{|n_1-n_2|}\left(\frac{2\omega^2 t}{\zeta}\right) \\ &+ \frac{1}{2}I_{2n_1+1}\left(\frac{2\omega^2 t}{\zeta}\right) + \frac{1}{2}I_{2n_2+1}\left(\frac{2\omega^2 t}{\zeta}\right)\Bigg].\end{aligned} \tag{A.5}$$

At a large t the leading term of Eq. (A.5) is proportional to $t^{-5/2}$, which is the same as the asymptotic behavior shown in Fig. 2(a).

A.2. Two-dimensional system

The C_Q of a sheet, Eq. (11), between the pairwise beads at (n_1, m_1) and (n_2, m_2) sites with a very large separation in the limit of a very large $N \times M$ (*i.e.* $N \to \infty$, $M \to \infty$, and $|m_1 - m_2| \approx M$) can be simplified as

$$\begin{aligned}\frac{C_Q(t)}{C_0} \approx \mathrm{e}^{-\frac{2t}{\zeta}(\omega_x^2+\omega_y^2)} I_0\left(\frac{2\omega_y^2 t}{\zeta}\right)\Bigg[&I_0\left(\frac{2\omega_x^2 t}{\zeta}\right) + \frac{1}{2}I_{2n_1-1}\left(\frac{2\omega_x^2 t}{\zeta}\right) \\ &+ \frac{1}{2}I_{2n_2-1}\left(\frac{2\omega_x^2 t}{\zeta}\right)\Bigg].\end{aligned} \tag{A.6}$$

Using Eq. (A.3), the leading term of the equation has t^{-1} dependence. The asymptotic behavior at large t is shown in Fig. 3(a). It is similar to the long-time behavior for two largely-separated beads in a very large and long tube, shown in Fig. 3(b), since Eq. (14) can also be approximate as Eq. (A.6). Therefore, the ACF of the distance deviation between widely separated beads in two-dimensional cases yields a t^{-1} asymptotic behavior.

If the separation of beads on a sheet is close and near the center, and $N \times M$ is very large, (*i.e.* n_1, $n_2 \approx N/2$ and m_1, $m_2 \approx M/2$) Eq. (10) can be simplified by an integral [39] as

$$\begin{aligned}\frac{C_Q(t)}{C_0} \approx \mathrm{e}^{\left[-\frac{2t}{\zeta}(\omega_x^2+\omega_y^2)\right]}\Bigg\{&I_0\left(\frac{2\omega_x^2 t}{\zeta}\right)I_0\left(\frac{2\omega_y^2 t}{\zeta}\right) \\ &-I_{|n_1-n_2|}\left(\frac{2\omega_x^2 t}{\zeta}\right)I_{|m_1-m_2|}\left(\frac{2\omega_y^2 t}{\zeta}\right)\Bigg\}.\end{aligned} \tag{A.7}$$

The equation can be expended by using Eq. (A.3), and has a leading term in t^{-2}, which is consistent with the asymptotic behavior shown in Fig. 3(a). This physical origin of one power smaller than in large separation is due to the interaction of the pairwise beads of the ACF through fewer beads, which is similar to the one-dimensional cases. If two beads are near a corner on a large sheet (*i.e.* $n_1, n_2 \ll N$ and $m_1,\ m_2 \ll M$). The ACF of distance deviation can be rewritten as

$$\frac{C_Q(t)}{C_0} \approx \mathrm{e}^{\left[-\frac{2t}{\zeta}(\omega_x^2+\omega_y^2)\right]} \left\{ \frac{1}{2}\left[I_0\left(\frac{2\omega_x^2 t}{\zeta}\right) + I_{2n_1-1}\left(\frac{2\omega_x^2 t}{\zeta}\right)\right] \times \left[I_0\left(\frac{2\omega_y^2 t}{\zeta}\right) + I_{2m_1-1}\left(\frac{2\omega_y^2 t}{\zeta}\right)\right] + \frac{1}{2}\left[I_0\left(\frac{2\omega_x^2 t}{\zeta}\right) + I_{2n_2-1}\left(\frac{2\omega_x^2 t}{\zeta}\right)\right] \times \left[I_0\left(\frac{2\omega_y^2 t}{\zeta}\right) + I_{2m_2-1}\left(\frac{2\omega_y^2 t}{\zeta}\right)\right] - \left[I_{n_1+n_2-1}\left(\frac{2\omega_x^2 t}{\zeta}\right) + I_{|n_1-n_2|}\left(\frac{2\omega_x^2 t}{\zeta}\right)\right] \times \left[I_{m_1+m_2-1}\left(\frac{2\omega_y^2 t}{\zeta}\right) + I_{|m_1-m_2|}\left(\frac{2\omega_y^2 t}{\zeta}\right)\right]\right\}. \tag{A.8}$$

As expected, because of the reflection distance deviations at the boundaries, the long-time behavior is t^{-3}, instead of t^{-2} for beads near the center.

If the pairwise beads on a very long and large tube are close and far away from the edges, the ACF of distance deviation in Eq. (14) can also be expressed as Eq. (A.7). Thus, it also exhibits t^{-2} asymptotic behavior, as seen in Fig. 3(b). If the close pairwise beads are parallel and near an edge (*i.e.* $n_1 = n_2 = n \ll N$, $|\ m_1 - m_2| \ll M/2$, and $N,M \to \infty$), C_Q can be written as

$$\frac{C_Q(t)}{C_0} \approx \mathrm{e}^{\left[-\frac{2t}{\zeta}(\omega_x^2+\omega_y^2)\right]} \left[I_0\left(\frac{2\omega_x^2 t}{\zeta}\right) + I_{2n-1}\left(\frac{2\omega_x^2 t}{\zeta}\right)\right] \times \left[I_0\left(\frac{2\omega_y^2 t}{\zeta}\right) - I_{|m_1-m_2|}\left(\frac{2\omega_y^2 t}{\zeta}\right)\right]. \tag{A.9}$$

According to Eq. (A.3), it yields t^{-2} behavior in Fig. 3(b), which is similar to the results of the pairwise beads parallel to the edge and far away from a corner of a sheet. If the pairwise beads are close and unparallel the edges, the Eq. (14) can be expressed as

$$\frac{C_Q(t)}{C_0} \approx \mathrm{e}^{\left[-\frac{2t}{\zeta}(\omega_x^2+\omega_y^2)\right]} \left\{ I_0\left(\frac{2\omega_y^2 t}{\zeta}\right) \left[I_0\left(\frac{2\omega_x^2 t}{\zeta}\right) + \frac{1}{2} I_{2n_1-1}\left(\frac{2\omega_x^2 t}{\zeta}\right) + \frac{1}{2} I_{2n_2-1}\left(\frac{2\omega_x^2 t}{\zeta}\right)\right] - I_{|m_1-m_2|}\left(\frac{2\omega_y^2 t}{\zeta}\right) \left[I_{n_1+n_2-1}\left(\frac{2\omega_x^2 t}{\zeta}\right) + I_{|n_1-n_2|}\left(\frac{2\omega_x^2 t}{\zeta}\right)\right]\right\}, \tag{A.10}$$

when $|n_1 - n_2| \ll N$ and $|m_1 - m_2| \ll M/2$ in a very large and long tube. The time behavior in Fig. 3 becomes t^{-3} at long time. The power law changes if the pairwise beads change the orientation with respect to the edges. The change is due to the reflection at the boundary having different effects at the different orientation of the pairwise beads. The effects are similar to the results on a sheet.

A.3. A ladder

The analytical expression at the limit of a very large N can be derived by using the integral in Ref. [39]. If $n_1 = n_2 = n$, it can be written as

$$\frac{C_Q(t)}{C_0} \approx \exp\left[-\frac{2t}{\zeta}(\omega_x^2 + \omega_y^2)\right]\left[I_0\left(\frac{2\omega_x^2 t}{\zeta}\right) + I_{2n-1}\left(\frac{2\omega_x^2 t}{\zeta}\right)\right]. \tag{A.11}$$

Using Eq. (A.3), at a large t the asymptotic behavior is $(4\pi\omega_x^2 t/\zeta)^{-1/2}\exp(-2\omega_y^2 t/\zeta)$, as shown in Fig. 4, which is very different from the power-law results in the usual one- or two-dimensional systems. If the pairwise beads on a very long ladder are at a large separation (*i.e.* $|n_1 - n_2| \approx N$, $N \to \infty$), the ACF becomes

$$\frac{C_Q(t)}{C_0} \approx \frac{1}{2}\exp\left(-\frac{2\omega_x^2 t}{\zeta}\right)\left[1 + \exp\left(-\frac{2\omega_y^2 t}{\zeta}\right)\right] I_0\left(\frac{2\omega_x^2 t}{\zeta}\right), \tag{A.12}$$

which exhibits $t^{-1/2}$ in Fig. 4 at longer times. The result is the same as that obtained in both chain and loop cases with a large separation. When the pairwise beads have a short separation and far away from the ends of the very long ladder, C_Q can be simplified by

$$\frac{C_Q(t)}{C_0} \approx \frac{\mathrm{e}^{-\frac{2\omega_x^2 t}{\zeta}}}{2}\left\{\left[1 + \mathrm{e}^{-\frac{2\omega_y^2 t}{\zeta}}\right] I_0\left(\frac{2\omega_x^2 t}{\zeta}\right) - \left[1 \pm \mathrm{e}^{-\frac{2\omega_y^2 t}{\zeta}}\right] \times I_{|n_2-n_1|}\left(\frac{2\omega_y^2 t}{\zeta}\right)\right\} (\text{“}+\text{” if } m_1 = m_2;\ \text{“}-\text{” if } m_1 \neq m_2). \tag{A.13}$$

As curve with the open hexagon symbols in Fig. 4, it yields $t^{-3/2}$ power-law behavior at longer times. It is the same as the 1-D case if the pairwise beads are close and far away from the boundaries.

When the two beads are close and near the ends of the very long ladder, (*i.e.* $n_1 \neq n_2$ and $n_1, n_2 \ll N$), the ACF is expressed as

$$\frac{C_Q(t)}{C_0} \approx \frac{\mathrm{e}^{-\frac{2\omega_x^2 t}{\zeta}}}{2}\left\{\left[1 + \exp\left(-\frac{2\omega_y^2 t}{\zeta}\right)\right]\left[I_0\left(\frac{2\omega_x^2 t}{\zeta}\right) + \frac{1}{2} I_{2n_1-1}\left(\frac{2\omega_x^2 t}{\zeta}\right) + \frac{1}{2} I_{2n_2-1}\left(\frac{2\omega_x^2 t}{\zeta}\right)\right] - \left[1 \pm \exp\left(-\frac{2\omega_y^2 t}{\zeta}\right)\right]\left[I_{n_1+n_2+1}\left(\frac{2\omega_x^2 t}{\zeta}\right) + I_{|n_2-n_1|}\left(\frac{2\omega_x^2 t}{\zeta}\right)\right]\right\} (\text{“}+\text{” if } m_1 = m_2; \text{“}-\text{” if } m_1 \neq m_2). \tag{A.14}$$

Its leading asymptotic term has a power law of $t^{-5/2}$, represented by the open-triangle-curve in Fig. 4, which is the same as obtained by the close pairwise beads near an end of a very long open chain.

References

[1] R. Granek, J. Klafter, Phys. Rev. Lett. 95 (2005) 098106.
[2] K.J. Maloy, L. Furuberg, J. Feder, T. Jossang, Phys. Rev. Lett. 68 (1992) 2161.
[3] T.H. Solomon, E.R. Weeks, H.L. Swinney, Phys. Rev. Lett. 71 (1993) 3975.
[4] M. Sahimi, S. Arbabi, Phys. Rev. Lett. 77 (1996) 3689.
[5] R. Ketzmerick, Phys. Rev. B 54 (1996) 10841.
[6] H. Isliker, L. Vlahos, Phys. Rev. E 67 (2003) 026413.
[7] M. Misawa, I. Dairoku, A. Honma, Y. Yamada, T. Sato, K. Maruyama, K. Mori, S. Suzuki, T. Otomo, J. Chem. Phys. 121 (2004) 4716.
[8] K.T. Shimizu, R.G. Neuhauser, C.A. Leatherdale, S.A. Empedocles, W.K. Woo, M.G. Bawendi, Phys. Rev. B 63 (2001) 205316.
[9] D.S. Novikov, M. Drndic, L.S. Levitov, M.A. Kastner, M.V. Jarosz, M.G. Bawendi, Phys. Rev. B 72 (2005) 075309.
[10] R.M. Clarke, I.H. Chan, C.M. Marcus, C.I. Duruoz, J.S. Harris, K. Campman, A.C. Gossard, Phys. Rev. B 52 (1995) 2656.
[11] M. Kuno, D.P. Fromm, H.F. Hamann, A. Gallagher, D.J. Nesbitt, J. Chem. Phys. 112 (2000) 3117.
[12] M. Kuno, D.P. Fromm, S.T. Johnson, A. Gallagher, D.J. Nesbitt, Phys. Rev. B 67 (2003) 125304.
[13] J. Schuster, F. Cichos, C. von borczyskowski, Appl. Phys. Lett. 87 (2005) 051915.
[14] J. Tang, R.A. Marcus, Phys. Rev. Lett. 95 (2005) 107401.
[15] J. Tang, R.A. Marcus, J. Chin. Chem. Soc. 53 (2006) 1.
[16] S.C. Kou, X.S. Xie, Phys. Rev. Lett. 93 (2004) 180603.
[17] W. Min, G.B. Luo, B.J. Cherayil, S.C. Kou, X.S. Xie, Phys. Rev. Lett. 94 (2005) 198302.
[18] H. Yang, G.B. Luo, P. Karnchanaphanurach, T.M. Louie, I. Rech, S. Cova, L.Y. Xun, X.S. Xie, Science 302 (2003) 262.
[19] P. Debnath, W. Min, S. Xie, B.J. Cherayil, J. Chem. Phys. 123 (2005) 204903.
[20] J. Tang, R.A. Marcus, Phys. Rev. E 73 (2006) 022102.
[21] J. Tang, S.H. Lin, Phys. Rev. E 73 (2006) 061108.
[22] P.E. Rouse, J. Chem. Phys. 21 (1953) 1272.
[23] S.L. Yang, J.B. Witkoskie, J.S. Cao, J. Chem. Phys. 117 (2002) 11010.
[24] J. Wang, P. Wolynes, Chem. Phys. Lett. 212 (1993) 427.
[25] R. Metzler, E. Barkai, J. Klafter, Phys. Rev. Lett. 82 (1999) 3563.
[26] D.J. Bicout, A.M. Berezhkovskii, A. Szabo, J. Chem. Phys. 114 (2001) 2293.
[27] A.V. Barzykin, K. Seki, M. Tachiya, J. Chem. Phys. 117 (2002) 1377.
[28] B.J. Witkoskie, J. Wu, J. Cao, J. Chem. Phys. 120 (2004) 5695.
[29] R. Kimmich, N. Fatkullin, Adv. Polym. Sci. 170 (2004) 1.
[30] G. Zaccai, Science 288 (2000) 1604.
[31] L. Cordone, M. Ferrand, E. Vitrano, G. Zaccai, Biophys. J. 76 (1999) 1043.
[32] A. Ansari, J. Chem. Phys. 110 (1999) 1774.
[33] S. Ferree, H.W. Blanch, Biophys. J. 87 (2004) 468.
[34] T.T. Perkins, D.E. Smith, S. Chu, Science 264 (1994) 819.
[35] M. Doi, S.F. Edwards, The Theory of Polymer Dynamics, Oxford University Press, New York, 1988.
[36] P.G. de Gennes, Scaling Concepts in Ploymer Physics, Cornell University Press, New York, 1985.
[37] J. Tang, S.N. Dikshit, J.R. Norris, J. Chem. Phys. 103 (1995) 2873.
[38] A. Guillermo, J.P.C. Addad, J. Chem. Phys. 116 (2002) 3141.
[39] I.S. Gradshteyn, I.M. Ryzhik, Tables of Integrals, Series and Products, Academic Press, San Diego, 1980.
[40] N.N. Lebedev, Special Function & Applications, Dover Publications, New York, 1972.